Multi-wavelength studies of the interstellar medium and star formation in nearby galaxies

Multi-wavelength studies of the interstellar medium and star formation in nearby galaxies

By
Ryan Chown

A dissertation submitted to the School of Graduate Studies
in partial fulfillment of the requirements
for the degree of
Doctor of Philosophy

McMaster University
Hamilton, Ontario
August 2021

Title: Multi-wavelength studies of the interstellar medium and star formation in nearby galaxies

Author: Ryan Chown, M. Sc., B. Sc. (McGill University)

Supervisors: Christine Wilson, Laura Parker

Number of Pages: xxii, 224

For Patrick.

Multi-wavelength studies of the interstellar medium and star formation in nearby galaxies

Abstract

In this thesis I investigate three key questions about the interstellar medium (ISM) and star formation in nearby galaxies. The first question is, "how do bars and galaxy interactions affect the distribution of cold gas and the level of central star formation in galaxies?" I use publicly-available spatially-resolved images of CO(1-0) emission in a sample of 126 nearby galaxies from the Extragalactic Database for Galaxy Evolution (EDGE) survey to measure molecular gas concentrations, and I use spatially-resolved optical spectroscopy from the Calar Alto Legacy Integral Field Area (CALIFA) survey to measure the level of central star formation enhancement. I find that gas concentration and the level of central star formation enhancement are positively correlated in barred galaxies but not in unbarred galaxies, and that interacting galaxies show signs of a correlation but not in all cases. These results indicate that central star formation enhancement occurs only in barred galaxies and interacting galaxies with high gas concentrations, which supports theories of bar- and interaction-driven galaxy evolution.

The second question is, "what is the relationship between mid-infrared (MIR) emission and molecular gas at spatially-resolved scales in galaxies?" I extend previous work, which found a tight correlation between global MIR emission in the *Wide-field Infrared Survey Explorer*

(*WISE*) 12 μm band and CO emission from single-dish radio telescopes, to spatially-resolved scales using EDGE CO data smoothed to *WISE* 12 μm resolution. I find that these quantities are tightly correlated at ∼kiloparsec scales, and that the correlation shows offsets from galaxy to galaxy. I find that these offsets are explained best by differences in the level of global near- and far-ultraviolet emission, and that the 12 μm-CO correlation is the strongest of all the resolved correlations that I considered. These results suggest that there is a tight physical link between *WISE* 12 μm emission and CO emission on kiloparsec scales, possibly due to a connection between polycyclic aromatic hydrocarbons (PAHs, which dominate the 12 μm emission) and molecular gas. My findings can be used to estimate resolved CO emission based on (easily obtained) *WISE* 12 μm images and a small number of global multi-wavelength measurements. These results also motivate further work exploring the CO-PAH connection in more diverse conditions and at higher resolution.

Finally, the third question is, "what is the ISM content of red star-forming galaxies?" In comparison to blue star-forming galaxies ("blue actives") which lie on or above the star-forming main sequence (SFMS), these "red misfits" tend to lie on or slightly below the SFMS. I find that the main property other than colour that differentiates red misfits from blue actives is their low gas mass fractions. The gas depletion times and gas-to-dust ratios are similar between these populations. My results indicate that the star formation of red misfits is in the act of quenching.

The unifying theme of each of these projects is the approach: studying key questions in nearby galaxies based on their molecular gas content along with other multi-wavelength data, at a variety of resolutions. This approach is enabled by large publicly available multi-wavelength

data sets at a variety of physical resolutions. Surveys of the global gas content of galaxies with accompanying multi-wavelength data will always be larger, and will continue to be an important reference for smaller resolved surveys. I hope that this thesis serves as a useful comparison between the science that can be done on both global and resolved scales, and will motivate future work on the connection between the ISM and star formation in nearby galaxies.

Acknowledgments

First, I would like to thank my supervisors, Dr. Christine Wilson and Dr. Laura Parker, for being amazing mentors. I've learned so much from you both and I have really enjoyed having you as my supervisors. Thank you both for supporting me to pursue the research I found most interesting, sending me around the world for conferences and research, keeping me on track with regular meetings, and for caring about my general well-being. I could not have asked for better supervisors.

Thank you to everyone who is a part of the Department of Physics and Astronomy for making the Department such a stimulating, fun, inclusive, supportive, responsive, and interconnected place to be. Thank you to my softball teammates – we may have had a very low wins-to-losses ratio and frequently employed self-deprecating humour, but we always supported each other and had a great time. Thanks also to my amazing group- and office-mates, and to Dr. Toby Brown for invaluable mentorship.

Thanks to my friends and frequent squash partners, Hao, Lili, and Blake, for those matches that often straddled a line between being simply "very intense" and what some might call "unsportsmanlike." I think we can all agree that squash has been central to our stress management and personal development as graduate students.

Thanks to my Mitacs host supervisor, Dr. Cheng Li, for being such a great mentor and generous host during my visits to Tsinghua University. Thanks also to the many colleagues and friends I met at Tsinghua for making me feel so welcomed and for teaching me so much. I can-

not express how grateful I am for those experiences, and how much they helped me to grow both academically and personally.

Thanks to my parents for everything.

Finally, thank you to the rest of my family, Henry Sun, and Moose for your unwavering support. I could not have done this without you all.

Co-authorship

Chapters 2, 3, and 4 are original research projects that were led by myself. Chapters 2 and 3 appear in the Monthly Notices of the Royal Astronomical Society (MNRAS) journal, while Chapter 4 is in preparation for submission to MNRAS.

The reference to Chapter 2 is Chown, R., Li, C., Athanassoula, E., Li, N., Wilson, C. D., Lin, L., Mo, H., Parker, L. C., and Xiao, T. 2019, MNRAS, 484, 5192-5211. I performed the analysis, wrote most of the paper text, and I generated the supplementary data tables and their documentation. Prof. Cheng Li was my host supervisor during my stay at Tsinghua University under a Mitacs Globalink Award. Prof. Li provided guidance through the analysis and helped write some of the discussion. Prof. E. Athanassoula ran the simulation of a barred galaxy and wrote the text describing that simulation. Dr. Niu Li performed full spectral fitting on the optical IFU data from the CALIFA survey. Profs. Christine Wilson and Laura Parker are my PhD supervisors and provided many helpful suggestions during the analysis and manuscript preparation. The remaining authors provided helpful comments and suggestions on the draft.

The reference to Chapter 3 is Chown, R., Li, C., Parker, L., Wilson, C. D., Li, N., and Gao, Y. 2021, MNRAS, 500, 1261-1278. I performed the analysis, wrote most of the paper text, and I generated the supplementary data tables and their documentation. Profs. Cheng Li, Laura Parker, and Christine Wilson provided guidance through the analysis and writing of the manuscript. Dr. Niu Li performed full spectral fitting on the optical IFU data from the CALIFA survey. Dr. Yang Gao obtained the *WISE* 12 μm images and their uncertainties.

Chapter 4 is original research done by myself in collaboration with Profs. Laura Parker and Christine Wilson. This paper is in preparation for submission to MNRAS.

List of Abbreviations and Symbols

AGN – Active galactic nucleus

BPT – Baldwin, Phillips, and Terlevich (Baldwin et al. 1981)

LI(N)ER – Low-Ionization (Nuclear) Emission Region

CARMA – The Combined Array for Research in Millimeter-wave Astronomy

DGR – Dust-to-gas ratio

EDGE – Extragalactic Database for Galaxy Evolution

FWHM – Full-width at half-maximum (of a Gaussian)

ISM – Interstellar medium

RMS – Root-mean-square

SFR – Star formation rate

SFH – Star formation history

SFMS – The Star-Forming Main Sequence

SSFR – Specific star formation rate

SCUBA-2 – Submillimetre Common-User Bolometer Array 2

JCMT – James Clerk Maxwell Telescope

ALMA – Atacama Large Millimeter/submillimeter Array

MaNGA – Mapping Nearby Galaxies at Apache Point Observatory

MGMS – The Molecular Gas Main Sequence

PAH – Polycyclic aromatic hydrocarbon

CALIFA – Calar Alto Legacy Integral Field Area Survey

IFU – Integral Field Unit

KS Law – Kennicutt-Schmidt Law

KS Test – Kolmogorov-Smirnov Test

Contents

1 Introduction 1

1.1 Galaxies and Their Evolution 1

1.2 The Interstellar Medium 12

1.2.1 Atomic and molecular gas 13

1.2.2 Dust 17

1.3 Star Formation 20

1.4 Key ISM and Star Formation Scaling Relations 25

1.5 This Thesis 29

2 Linking bar- and interaction-driven molecular gas concentration with centrally-enhanced star formation in EDGE-CALIFA galaxies 33

2.1 Introduction 35

2.2 Data and processing 39

2.2.1 The CARMA EDGE and CALIFA surveys 39

2.2.2 Sample selection 41

2.2.3 Morphological classification 45

2.2.4 Maps and radial profiles of recent SFH diagnostics 47

2.2.5 Maps and radial profiles of molecular gas mass 51

2.3 Central star formation and the link to gas concentration 51

2.3.1 Recent central star formation enhancement . . . 53
2.3.2 Recent central star formation vs. molecular gas concentration . . . 57
2.3.3 Linking central star formation enhancement with molecular gas mass profiles . . . 68
2.4 Comparison to an *N*-body simulation . . . 69
2.4.1 Observations . . . 70
2.4.2 Simulations . . . 70
2.4.3 Morphology . . . 72
2.4.4 Age radial profile . . . 74
2.5 Discussion . . . 78
2.5.1 How often do we see a central star formation enhancement? . . . 78
2.5.2 Can bars and mergers together fully account for the central star formation enhancement? . . . 80
2.5.3 Bar-driven central SF enhancement as a long-lived effect . . . 81
2.5.4 Is high c_{mol} a necessary and sufficient condition for central star formation enhancement? . . . 82
2.6 Conclusions and future work . . . 83

Appendices 89

A Tables of galaxy properties . . . 89
A.1 Notes on individual galaxies . . . 92

3 A new estimator of resolved molecular gas in nearby galaxies 103

3.1 Introduction . . . 105

3.2 Data and Data Processing . . . 109

3.2.1 Sample selection . . . 109

3.2.2 *WISE* 12 μm surface density maps . . . 110

3.2.3 H_2 surface density maps at *WISE* W3 resolution . . . 112

3.2.4 Maps of stellar population and ionized gas properties . . . 114

3.2.5 CO-to-H_2 conversion factor . . . 118

3.3 Analysis and Results . . . 120

3.3.1 The degree of correlation between $\Sigma(12\ \mu m)$ and $\Sigma(H_2)$ . . . 120

3.3.2 Bayesian linear regression . . . 121

3.3.3 Spatially resolved estimator of $\Sigma(H_2)$ . . . 126

3.3.4 Dependence of the 12 μm-H_2 relationship on physical scale . . . 138

3.3.5 Testing the estimators for biases . . . 138

3.4 Discussion . . . 142

3.4.1 Comparisons to previous work . . . 145

3.4.2 Why is $\Sigma(12\ \mu m)$ a better predictor of $\Sigma(H_2)$ than Σ_{SFR}? . . . 146

3.5 Conclusions . . . 149

Appendices 153

A Derivation of *WISE* W3 uncertainty . . . 153

B Derivation of CO uncertainty . . . 154

C Definition of the scatter about a fit . . . 155
D The 12 μm-CO relationship assuming a constant α_{CO} . . . 156
E Multi-parameter fits assuming a constant α_{CO} . . . 156

4 The Cold Gas and Dust Properties of Red Star-Forming Galaxies 166
4.1 Introduction . . . 167
4.2 Data and Data Processing . . . 170
4.2.1 Star formation rates, stellar masses, and other basic properties . . . 170
4.2.2 Single-dish CO observations . . . 171
4.2.3 H I observations . . . 174
4.2.4 Dust masses from sub-millimeter observations . . . 175
4.3 Analysis and Results . . . 177
4.3.1 Comparing the gas and dust properties of red misfit and blue active galaxies . . . 178
4.3.2 Scaling relations . . . 185
4.3.3 The Kennicutt-Schmidt Law, and the Molecular Gas Main Sequences . . . 187
4.4 Discussion . . . 192
4.5 Conclusions . . . 194

Appendices 197
A New JCMT CO(2-1) measurements of red misfits . . . 197
B New SCUBA-2 measurements of red misfits . . . 197

5 Summary and Future Work 202

5.1 The role of bars and interactions 203

5.2 The connection between CO and MIR emission 204

5.3 The nature of red star-forming galaxies 205

5.4 Future Work 206

5.4.1 What is driving the correlation between *WISE* 12 μm and CO emission in galaxies? 206

5.4.2 How do bars and interactions affect the resolved cold gas distribution and star formation history of galaxies? 210

References 213

List of figures

1.1 Hubble "tuning fork" . . . 3

1.2 Galaxy colour-magnitude diagram . . . 5

1.3 Galaxy evolution diagram . . . 7

1.4 Star forming main sequence of galaxies . . . 11

1.5 SED of a star-forming galaxy . . . 18

1.6 PAH emission in M51 . . . 21

1.7 The Kennicutt-Schmidt (KS) relationship . . . 27

1.8 Gas depletion time scaling relations . . . 28

1.9 The KS and MGMS relationships . . . 30

2.1 Colour, stellar mass, and BPT diagram of the EDGE sample . . . 40

2.2 Maps and radial profiles of some EDGE galaxies . . . 42

2.3 Observed vs. extrapolated central star formation history indicators . . . 46

2.4 Histograms of central SFH enhancement and cold gas concentration . . . 48

2.5 Central log Σ_{SFR} vs. log M_* . . . 55

2.6 H_2 surface density radial profiles . . . 58

2.7 SFH enhancement vs. molecular gas concentration . . . 61

2.8 Comparison of cold gas concentration definitions . . . 63

2.9 log Σ_{SFR} vs. log Σ_{H_2} for galaxy centers and disks . . . 66

2.10 Comparison between a snapshot of a simulated barred galaxy and a *gri* image of NGC5000 72

2.11 Radial profiles of stellar age in NGC5000 and a simulated barred galaxy 75

A1 Maps and radial profiles of additional example galaxies in our sample 93

3.1 Selected maps for NGC4047 109

3.2 12 μm surface density versus H_2 surface density 122

3.3 Cumulative histograms of 12 μm-H_2, and SFR-H_2 Pearson correlation coefficients 123

3.4 Best-fit slopes and intercepts of the resolved 12 μm-H_2 relationship 127

3.5 H_2 vs. 12 μm for the full sample (luminosities and surface densities) 128

3.6 RMS error of all estimators versus the number of fit parameters 139

3.7 Galaxy-by-galaxy RMS error 140

3.8 Scatter in the 12 μm-H_2 relationship versus area 141

D1 12 μm vs. H_2 for the full sample (luminosities and surface densities) 156

D2 12 μm vs. H_2 (and vice versa) for the full sample (luminosities and surface densities), assuming $\alpha_{CO} = 3.2$ 157

4.1 SSFR vs. $g - r$ colour of local galaxies 172

4.2 Gas-to-stellar mass ratios of red misfits and blue actives as histograms and in the log SFR, log M_* plane 180

4.3 Gas depletion times of red misfits and blue actives as histograms and in the log SFR, log M_* plane 181

4.4 Dust-to-stellar mass ratios and DGRs of red misfits and blue actives as histograms and in the log SFR, log M_* plane 182
4.5 Molecular and total gas depletion times versus offset from the star forming main sequence 189
4.6 Molecular and total gas mass fractions times versus offset from the star forming main sequence 190
4.7 The MGMS and KS relation of red misfits and blue actives 193

List of tables

1.1 Basic properties of the gas in the ISM 13

2.1 Mean molecular gas concentrations and upturn/turnover strengths 52

2.2 Mean gas depletion times and surface densities of H_2 and SFR 67

A1 Basic properties of the galaxies in our sample 90

A2 Quantities derived from spatially-resolved optical IFU and molecular gas maps . 91

3.1 Number of galaxies and pixels in each of the three samples 116

3.2 List of global properties and pixel properties considered in the multi-parameter fits 130

3.3 Best-performing estimators of $\log \Sigma(H_2)$ (metallicity-dependent α_{CO}) 135

3.4 Best-performing estimators of $\log \Sigma(H_2)$ (metallicity-dependent α_{CO}), without IFU properties 136

3.5 Best-performing estimators of $\log \Sigma(H_2)$ (metallicity-dependent α_{CO}), without 12 μm 137

3.6 Catalog of all resolved measurements for each pixel of each galaxy 144

E1 Best-performing estimators of $\log \Sigma(H_2)$ (constant $\alpha_{CO} = 3.2$) 158

E2 Best-performing estimators of $\log \Sigma(H_2)$ (constant $\alpha_{CO} = 3.2$), without IFU data 158

E3 Best-performing estimators of $\log \Sigma(H_2)$ (constant $\alpha_{CO} = 3.2$), without 12 μm 158

4.1 Numbers of galaxies with CO, H I, and 850 μm measurements 174

4.2 Statistical comparisons of gas- and dust-based quantities between red misfits and blue active galaxies 184

A1 Table of new CO(2-1) measurements of red misfits using the JCMT 197

B2 Table of new 850 μm measurements of red misfits using SCUBA-2 198

1 Introduction

1.1 Galaxies and Their Evolution

Galaxies are complex objects made up of gas, stars, dust, and dark matter that come in a wide variety of shapes, colours, and sizes. Galaxies are luminous objects and we can use them as tracers of the large scale structure of the Universe (e.g. Dodelson 2003). Studying galaxies also gives us perspective into how our own galaxy (the Milky Way) came to be, what will happen to it in the future, and how the conditions became just right for our Solar System to form and host a habitable planet. The physical processes occurring in galaxies span many orders of magnitude in energy, physical scale, and time. The breadth of physical and chemical processes are difficult or impossible to study in the laboratory, making detailed observations of their properties critical for understanding their nature.

Before the main ingredients of galaxies were understood, observations of their diverse morphologies motivated further study. Nearly 100 years ago, using optical images of 400 galaxies (which were called "extragalactic nebulae" at the time), Edwin Hubble noticed that the appearances of galaxies can be classified along a sequence ranging from elliptically-shaped to spiral-shaped (Hubble 1926). This "Hubble sequence" is typically represented in a diagram shaped like a tuning fork with ellipticals on the left and spirals on the right (Figure 1.1). Ellipticals are assigned labels E0, E1, and so on to E7, where the integer represents the ellipticity (0 is nearly round, 7 is very elliptical). Spirals are assigned labels Sa, Sb, or Sc, where the lower case letter indicates how compact the spiral arms are ("Sa" are tightly wound, "Sc" are loosely wound). Spirals are further divided into those with bars (an enlongated structure running through the center of the galaxy) and those without. Barred spirals are assigned the symbols SBa through SBc. At the meeting point of these two branches are the S0, or "lenticular" galaxies which have disks bur no visible spiral features. Dwarf galaxies and irregular galaxies are not shown on this diagram.

Elliptical galaxies are typically referred to as "early-type," and Sa or SBa galaxies as "early-type spirals," while Sc and SBc galaxies are referred to as "late-type spirals." This is vestigial nomenclature from when the Hubble sequence was thought to depict how galaxies evolve over time – we now know that this picture is incorrect, but the names have remained.

The galaxies shown in Figure 1.1 are all relatively nearby, but it is important to understand that we live in an evolving universe. Our universe is expanding, and as it expands, the wave-

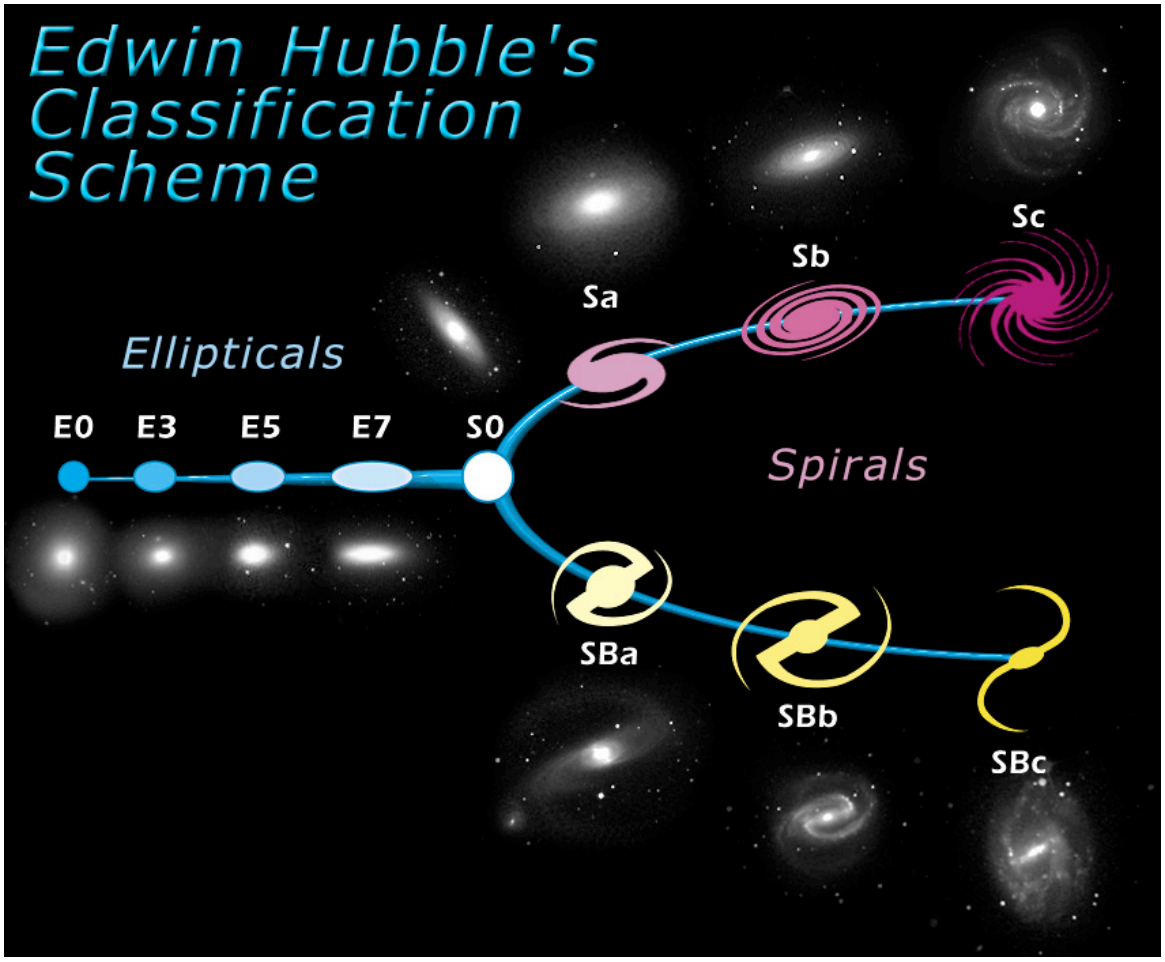

Figure 1.1: The "tuning fork" diagram devised by Edwin Hubble in 1926. On the left are early-type galaxies, and on the right are late-type galaxies. Those without (with) bars are shown in the top (bottom) branches. From left to right in this diagram the bulge component diminishes. Elliptical galaxies can be thought of as a single massive bulge, and Sa galaxies have prominent bulges compared to Sb and Sc galaxies. [Image credit: NASA and ESA; URL:https://esahubble.org/images/heic9902o/].

length of light is stretched in an effect called cosmological redshift. Redshift is defined by

$$z \equiv \frac{\lambda_{\text{observed}}}{\lambda_{\text{emitted}}} - 1, \tag{1.1}$$

where λ_{emitted} is the wavelength of the emitted light and $\lambda_{\text{observed}}$ is that of the observed light. Galaxy redshifts can be measured by comparing the observed wavelengths of spectral lines with their rest-frame wavelengths. Nearby galaxies trace the current epoch and have low redshifts (typically $z < 0.1$), whereas more distant galaxies have large redshifts and trace earlier epochs in the history of the Universe (Dodelson 2003).

How, then, do galaxies evolve over time? The timescales involved are enormous by human metrics, and so it is only possible for us to observe each galaxy in one snapshot of its long history. By observing galaxies at a range of redshifts, observing nearby galaxies in great detail to reconstruct their histories, and by comparing observations with simulations, we have learned a great deal about how galaxies evolve. For example, we now know that the morphological features described above actually represent the spatial distribution of the stars and interstellar medium (ISM) within galaxies, depending on which wavelength the morphology is viewed in (see Sections 1.2 and 1.3). The optical colours of galaxies in the local Universe (Figure 1.2) are bimodally distributed: elliptical galaxies tend to have red colours while spiral galaxies tend to have blue colours (e.g. Strateva et al. 2001; Baldry et al. 2004). Old stars are generally red, while the brightest light from young stars is at blue wavelengths, and since galaxy colours reflect their underlying stellar populations (e.g. Hubble 1936; Strateva et al. 2001), red colours indicate that star formation has mostly stopped, while blue colours indicate that star formation is ongoing.

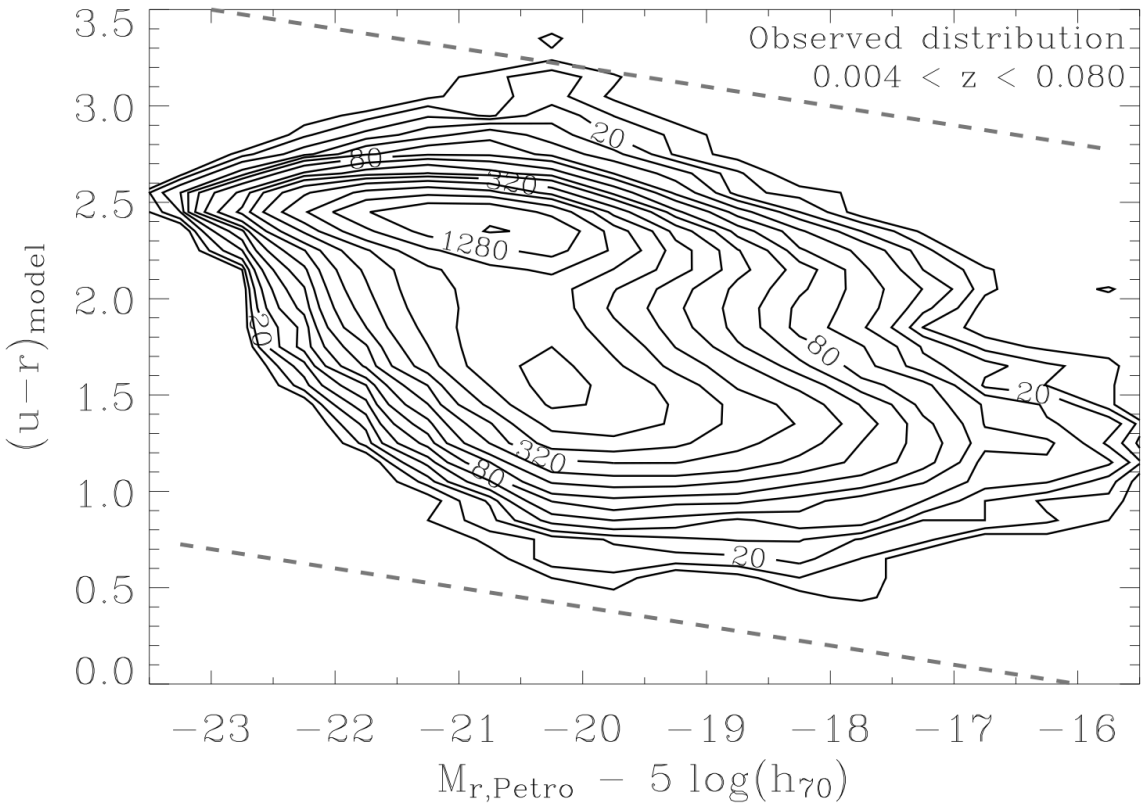

Figure 1.2: The $u - r$ colour vs. r-band Petrosian magnitude diagram for 66,486 galaxies at low redshift from SDSS (Baldry et al. 2004). From bottom to top, colours range from blue to red. Luminosity decreases from left to right. There is a bimodal distribution of red (upper) and blue (lower) galaxies, now referred to as the "red sequence" and "blue cloud." Figure reproduced with permission.

Thus the observed morphology of galaxies is correlated with their star formation (Blanton & Moustakas 2009). Colours are also affected by the presence of dust (Section 1.2.2), and by metals ejected into the ISM by star formation (redder colour indicates higher metallicity; Mo et al. 2010). Below I will review the physical processes which lead to these observed properties.

Figure 1.3 shows the types of processes that drive galaxy evolution, adapted from Kormendy & Kennicutt (2004). These processes can be separated by how quickly they occur (fast or slow), and whether they are driven by processes internal to the galaxy or due to influences from the

external environment. Galaxy evolution, including star formation, metal enrichment and gas recycling, is a result of all of these processes. An important aspect of this field is to understand where and when different transformation mechanisms dominate. Fast processes occur on timescales of about 1 Gyr or faster (this is the orbital timescale for most disk galaxies; Meurer et al. 2018). These processes were dominant in the early Universe, when the first galaxies were forming through protogalactic collapse (the formation of dark matter halos filled with baryons which collapse and cool to form galaxies and stars; Eggen et al. 1962), and when galaxy mergers were much more frequent than today (e.g. Toomre 1977; Patton et al. 2002; Conselice et al. 2003). Externally-driven fast processes include major mergers (e.g. Privon et al. 2013) and ram-pressure stripping (the removal of cold gas from galaxies as they encounter the hot gas in a galaxy cluster; Gunn & Gott 1972). Note that major mergers are generally faster than minor mergers, but major merger timescales can be longer than 1 Gyr (Kitzbichler & White 2008). Galaxy mergers build galaxies with larger stellar masses, and are known to trigger enhanced star formation (if the merger is gas-rich), the formation of bars, and active galactic nuclei (e.g. Mo et al. 2010). Ram pressure is analogous to the drag force one experiences when moving through air (Mo et al. 2010). This can (but doesn't always) dramatically reduce a galaxy's ability to continue forming stars, and can turn a spiral galaxy into a lenticular (e.g. Gunn & Gott 1972; Dressler 1980; Kormendy & Bender 2012).

As the Universe expands mergers become less frequent and slow processes begin to dominate. For example, Conselice et al. (2003) find that up to $z \sim 3$, the fraction of massive galaxies undergoing a major merger scales as $\sim (1+z)^{4-6}$. Slow processes happen over many galaxy rotation

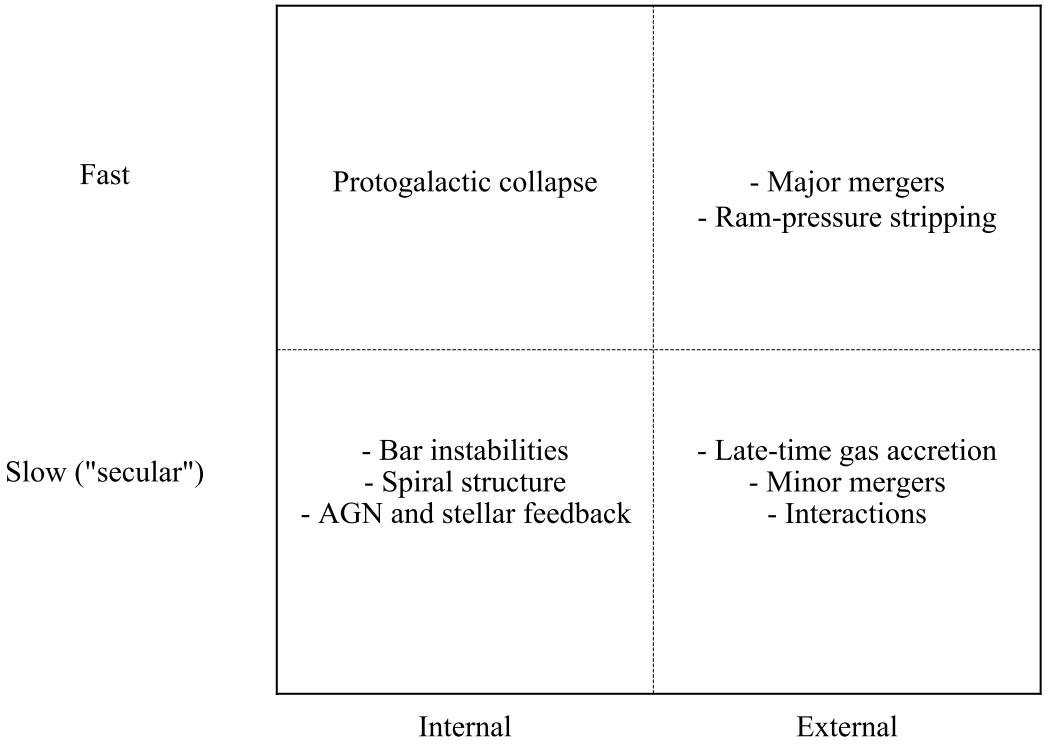

Figure 1.3: Diagram of galaxy evolution processes adapted from Kormendy & Kennicutt (2004). The top row shows fast-evolving processes – these occur on a gravitational collapse timescale. The bottom row shows slowly-evolving processes (often referred to as "secular") which occur over several Gyr (Kormendy & Kennicutt 2004). The left column shows processes which occur within galaxies, while the right column shows processes driven by interactions with other galaxies or interactions unique to high density regions. Galaxy evolution, including star formation, metal enrichment and gas recycling, is a result of all of these processes. An important aspect of this field is to understand where and when different transformation mechanisms dominate.

periods (much longer than 1 Gyr). Like fast processes, they can be grouped into internal and external processes (Figure 1.3). Slow internal processes are those which are driven by the galaxy itself. This type of evolution will occur if there is an effective driving mechanism (Kormendy 2013). Some examples of internal driving mechanisms are:

1. Galactic bars, which are elongated structures extending through the center of a galaxy. About 2/3 of nearby galaxies are barred (Aguerri et al. 2009), and bars started to form at $z \sim 1$ (Kraljic et al. 2012). Gravitational instabilities cause the orbits of some of the stars and gas in the galactic disk to become non-circular. These orbits collect together and when they cross, the gas clouds collide and increase in density, fall inwards, and begin forming stars in the central region (Athanassoula 1992, 1994; Piner et al. 1995; Athanassoula et al. 2013; Sormani et al. 2015).

2. Spiral structure transports mass (such as gas) inward. The inflowing gas can be used to grow the central bulge (Kormendy 2013).

3. Feedback from stars (such as supernova explosions and stellar winds) and accreting supermassive black holes (active galactic nuclei; AGN). These processes inject enormous amounts of energy and metals into the ISM and circumgalactic medium, which affects the gas properties and therefore star formation. The injected energy makes it more difficult for gas to cool and form stars (Hopkins & Hernquist 2006; Mo et al. 2010).

Some examples of slow external mechanisms are galaxy-galaxy tidal interactions and minor mergers (e.g. Barnes & Hernquist 1991; Li et al. 2008; Cox et al. 2008; Lotz et al. 2010; Ellison

et al. 2011; Patton et al. 2013; Lin et al. 2014; Pan et al. 2019), late-time gas accretion (e.g. Fraternali & Binney 2006; Sancisi et al. 2008; Combes 2009), repeated flyby interations (e.g. Richstone 1976; Farouki & Shapiro 1981; Aguilar & White 1985) and the cutting off of gas accretion in a cluster (e.g. Larson et al. 1980; Balogh et al. 2000; Bekki et al. 2002).

All of the processes indicated above leave imprints on galaxy properties. One of these properties is morphology, which is a tracer of galaxy evolution. For example, the type of bulge a galaxy possesses is a fingerprint of the processes that built it: bulges built by fast processes like galaxy mergers are called "classical" bulges, while bulges built by slow processes are called "pseudobulges" (for a detailed comparison between these see Athanassoula 2005; Kormendy 2013). Not only were these two types of bulges built by different processes, they have different appearances. One difference is that pseudobulges tend to appear more disk-like than classical bulges. The correlations between bulge properties and galaxy properties also differ between pseudobulges and classical bulges (Fisher & Drory 2008; Kormendy et al. 2011; Kormendy & Ho 2013).

Other galaxy properties that are affected by the processes in Figure 1.3 include star formation rate, stellar mass, cold gas and dust properties, and metallicity. For example, the effects of these processes can be seen in the colour-magnitude diagram of galaxies. Baldry et al. (2004, 2006) found that $u-r$ colour versus r-band absolute magnitude of nearly 70,000 nearby galaxies from the Sloan Digital Sky Survey (SDSS; York et al. 2000) shows a bimodal distribution (Figure 1.2). r-band absolute magnitude or luminosity are tracers of stellar mass ($M_\star$; e.g. Blanton et al. 2001; Baldry et al. 2006), while u-band absolute magnitude or luminosity are tracers of star formation rate (SFR; e.g. Moustakas et al. 2006), and so $u-r$ colour roughly traces specific star formation

rate (SSFR),

$$\mathrm{SSFR}\,[\mathrm{yr}^{-1}] \equiv \frac{\mathrm{SFR}\,[M_\odot\ \mathrm{yr}^{-1}]}{M_\star\,[M_\odot]}. \tag{1.2}$$

Blue $u - r$ colours indicate galaxies with ongoing star formation, while red colours indicate galaxies that have largely finished forming stars. This bimodality in colour suggests that galaxies tend to spend their time either actively forming stars or being quiescent, and spend little time in between.

More recently, SFR and stellar masses have been estimated for large numbers of galaxies using a variety of techniques (see Section 1.3) including emission lines (for SFR), broad-band photometry, and spectral energy distribution (SED) fitting (for both SFR and M_*; Mitchell et al. 2013; Conroy 2013; Lower et al. 2020). Combining SFR and M_* we can study the SSFR for large samples of galaxies. The bimodality in colour is also seen as a bimodality in SSFR, which is shown in the vertical axis of Figure 1.4. Furthermore, the plot of log SSFR versus log $M_\star$ (Figure 1.4) shows that star-forming galaxies follow a tight relationship, called the "star forming main sequence" (SFMS; Brinchmann et al. 2004; Noeske et al. 2007a,b; Salim et al. 2007; Schiminovich et al. 2007; Speagle et al. 2014; Schreiber et al. 2015; Popesso et al. 2019). The slope of the local SFMS in the SFR vs stellar mass plane ranges from about 0.6 to 1.2 (Speagle et al. 2014), but a similar power-law relationship persists from redshifts $z \sim 0$ to 4 (Brinchmann et al. 2004; Noeske et al. 2007a; Magdis et al. 2010; Schreiber et al. 2015; Mancuso et al. 2016).

The galaxies we observe today are the result of many of the processes outlined above. Galaxy shapes, colours, and star formation properties change as galaxies evolve over cosmic time and are sensitive to the conditions of the ISM within a galaxy. I will first describe some key aspects of

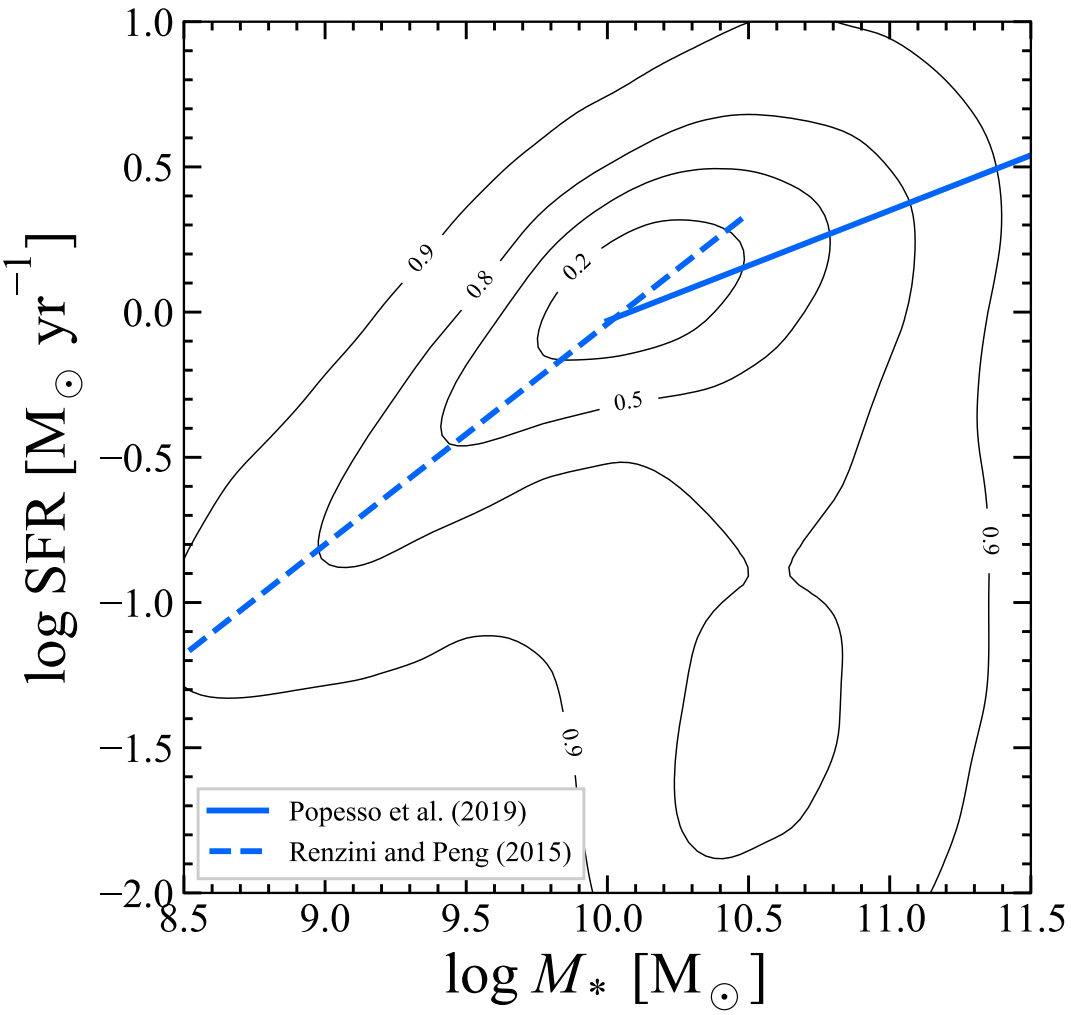

Figure 1.4: Star formation rate versus stellar mass derived from UV-to-optical SED fitting of ∼ 136,000 local ($z < 0.085$) galaxies from the *GALEX*-SDSS-*WISE* M2 catalog (Salim et al. 2016). The solid blue line is the fit to star-forming galaxies with stellar masses between 10^{10} and $10^{11.5}$ $M_\odot$ Popesso et al. (2019), and the dashed blue line is the fit for galaxies with stellar masses between 10^{8} and $10^{10.5}$ $M_\odot$ (Renzini & Peng 2015).

the ISM, and then review key scaling relations between the components of the ISM.

1.2 The Interstellar Medium

The physics and chemistry of the interstellar medium is a rich subject. A wide variety of ingredients comprise the ISM, such as gas, dust, and metals. Typical volume filling factors, temperatures and number densities of the key gaseous components of the ISM are shown in Table 1.1. Neutral gas (mostly H I) exists in two phases: a cool phase and a warm diffuse phase (see Table 1.1 and Draine 2011). By volume, most of this gas is in the warm phase and extends out into the galactic disk. By mass, 40 per cent of the H I in galaxies is in the cool phase while the remaining 60 per cent is in the warm phase (Draine 2011).

Molecular gas (mainly H_2) exists in a cold diffuse phase and a cold dense phase (Table 1.1). Cold, dense molecular regions are the sites of star formation (Goodwin & Whitworth 2004). How molecular clouds form and fragment into sites of star formation is an ongoing area of research – for example, their initial composition is under debate (Elmegreen 2000; Pringle et al. 2001; Dobbs et al. 2012; Dobbs & Pringle 2013).

Regions of dense, hot gas that has been photoionized by nearby hot, massive O stars are called H II regions – most of the Hα emission in galaxies is from H II regions. Most of the ionized gas mass is in a diffuse component ($\sim$ 0.3 cm^{-3}) with a similar temperature to H II regions ($\sim$ 8000 K) but whose ionization source is not understood (Tielens 2008). Both of these components are grouped together as "H II gas" in Table 1.1.

Dust is an essential component of the interstellar medium, and is made up of a variety of

Table 1.1: Basic properties of the gas in the ISM, adapted from Table 1.3 of Draine (2011).

Component	f_V † (%)	T †† (K)	Density (cm^{-3})	Common Tracer(s)
Dense H_2	~ 0.01	$10 - 50$	$10^3 - 10^6$	CO, HCN
Diffuse H_2	~ 0.1	~ 50	~ 100	CO
Cool H I	~ 1.0	~ 100	30	H I 21 cm
Warm H I	~ 40	~ 5000	0.6	H I 21 cm
H II gas ⋆	~ 10	$\sim 10^4$	$0.3 - 10^4$	Optical line emission, thermal radio continuum
Coronal gas	~ 50	$\gtrsim 10^{5.5}$	$\sim 4 \times 10^{-3}$	UV, x-ray emission, radio synchrotron

† Volume filling factor
†† Temperature
⋆ This includes H II regions and diffuse ionized gas.

components such as amorphous carbon, silicates, with sizes ranging from $\sim$ 10 Å to $\sim$ 0.5 μm (see Tielens 2008; Draine 2011). The smallest dust grains are actually large molecules, such as polycyclic aromatic hydrocarbons (PAHs; Allamandola et al. 1985, 1989). The dust-to-gas (H I+ H_2) mass ratio is typically about 1 per cent (Tielens 2008). The effects that dust can have on the ISM depend on its intrinsic properties such as size, charge, structure, chemical composition, and abundance, all of which vary substantially (for a review on dust see Galliano et al. 2018). I now provide an overview of how these key ingredients of the ISM are observed.

1.2.1 Atomic and molecular gas

Neutral hydrogen H I is observed directly through its fine structure line at 21 cm. The relationship between the H I integrated flux density

$$I_{\rm HI}\ [\rm Jy\ km\ s^{-1}] \equiv \int S_v\, dv, \tag{1.3}$$

and corresponding H I mass along the line of sight assuming no opacity is given by

$$M_{\rm HI}\,[{\rm M}_\odot] = 2.343 \times 10^5 (1+z)^{-1} d_L^2\, I_{\rm HI}, \tag{1.4}$$

where d_L is the luminosity distance to the source in Mpc and z is the redshift (equation 8.21 in Draine 2011). Global H I measurements exist for large samples of galaxies such as the *GALEX* Arecibo SDSS Survey (xGASS; Catinella et al. 2018) and the Arecibo Legacy Fast ALFA survey (ALFALFA; Haynes et al. 2018). Obtaining resolved measurements (kiloparsec resolution or better) is quite time consuming. However, there are several smaller resolved H I surveys of nearby galaxies such as The H I Nearby Galaxy Survey (THINGS; Walter et al. 2008) and the VLA Imaging of Virgo in Atomic gas survey (VIVA; Chung et al. 2009). Global H I data exist for samples of galaxies out to redshifts of $\sim$ 0.2 (e.g. Catinella & Cortese 2015; Verheijen et al. 2007), while samples of resolved H I in galaxies at higher redshifts are much smaller and rare. For example, resolved H I measurements of one galaxy at $z \sim 0.3$ required 178 hours of observing time with the Karl G. Jansky Very Large Array (Fernández et al. 2016).

In contrast to H I, molecular hydrogen H_2 is essentially invisible under normal cloud conditions. It has only weak line emission in the MIR and the two lowest-energy transitions in this window require temperatures of $\gtrsim$ 500 and 1000 K to excite (Dabrowski 1984). Rather than directly observing H_2, molecular gas is typically traced indirectly using rotational line emission of CO (for reviews see Solomon & Vanden Bout 2005; Bolatto et al. 2013). CO is the second-most abundant molecule in molecular clouds, and its rotational transitions are easily excited at low temperatures (about 5 K). Conveniently, the ground transition CO($J = 1 \rightarrow 0$), usually

written more concisely as CO(1-0), is at a frequency of 115 GHz, or 2.6 mm, which is in a transparent atmospheric window (Bolatto et al. 2013). While CO is the most widely used molecular gas tracer, an inescapable fact of the use of CO is its high optical depth. As stated by Kennicutt & Evans (2012): "Using CO intensity to estimate the column density of a cloud is akin to using the presence of a brick wall to estimate the depth of the building behind it." CO is not ideal for tracing the cold, dense molecular gas which goes on to form stars – for that, one must use a different tracer such as CN or HCN (e.g. Gao & Solomon 2004; Kauffmann et al. 2017; Wilson 2018).

For a CO(1-0) integrated line flux density $S_{\mathrm{CO}(1-0)}\,\Delta v$ in units of Jy km s^{-1}, the luminosity $L_{\mathrm{CO}(1-0)}$ in units of K km s^{-1} pc^2 is given by

$$L_{\mathrm{CO}(1-0)} = 2453\,\left(S_{\mathrm{CO}(1-0)}\,\Delta v\right)\,d_L^2\,(1+z)^{-1}, \tag{1.5}$$

(Bolatto et al. 2013). There are other versions of this equation for $L_{\mathrm{CO}(1-0)}$ from $I_{\mathrm{CO}(1-0)}$ in K km s^{-1} (e.g. Solomon et al. 1997; Solomon & Vanden Bout 2005). $L_{\mathrm{CO}(1-0)}$ can be converted into an H_2 mass $M_{\mathrm{H_2}}$ or molecular gas mass ($1.36\,M_{\mathrm{H_2}}$, to include the mass contribution of helium) by multiplying by a CO-to-H_2 conversion factor

$$M_{\mathrm{mol}} = \alpha_{\mathrm{CO}}\,L_{\mathrm{CO}(1-0)}. \tag{1.6}$$

For star-forming regions within galaxies, and global CO measurements of star-forming galaxies, $\alpha_{\mathrm{CO}} \simeq 4.3\,\mathrm{M}_\odot\,(\mathrm{K\,km\,s^{-1}\,pc^2})^{-1}$ is typically assumed (Bolatto et al. 2013; Sandstrom et al.

2013); note that this number includes the $\sim$ 36 per cent contribution from helium.

For lines other than CO(1-0), such as CO(2-1), one typically converts the observed luminosity to an equivalent CO(1-0) luminosity by assuming a ratio of the line intensities. For instance, the CO(2-1)/CO(1-0) ratio

$$r_{21} \equiv I_{\mathrm{CO}(2-1)}/I_{\mathrm{CO}(1-0)} \tag{1.7}$$

is observed to be about 0.7 in nearby galaxies (Bigiel et al. 2008; Sandstrom et al. 2013; Leroy et al. 2009, 2013), but variations have been found within and amongst galaxies (e.g. Koda et al. 2020; Yajima et al. 2021; den Brok et al. 2021). There are a number of other assumptions and systematic uncertainties embedded in this approach for estimating M_{mol}, such as the optical depth of the CO line (as previously mentioned), and the dependence of α_{CO} on metallicity (Maloney & Black 1988; Wilson 1995; Genzel et al. 2012), spatial scale, galaxy type, and position within a galaxy (Sandstrom et al. 2013). The systematic uncertainty is roughly a factor of 2.

There are many large samples of global CO measurements in nearby galaxies. Two of the largest are the CO Legacy Database for GASS (xCOLD GASS, $\sim$500 galaxies; Saintonge et al. 2011, 2017) and the James Clerk Maxwell Telescope (JCMT) dust and gas In Nearby Galaxies Legacy Exploration (JINGLE, $\sim$100 galaxies; Saintonge et al. 2018). In the past few years, large samples of spatially-resolved CO measurements of nearby galaxies have been carried out such as the HERA CO-Line Extragalactic Survey (HERACLES, 48 galaxies; Leroy et al. 2009), the JCMT Nearby Galaxies Legacy Survey (NGLS, 155 galaxies; Wilson et al. 2012) and the Extragalactic Database for Galaxy Evolution (EDGE, 167 galaxies; Bolatto et al. 2017), and the Physics

at High Angular Resolution in Nearby GalaxieS ALMA survey (PHANGS, 90 galaxies; Leroy et al. 2021). Several of these resolved CO surveys (like EDGE and PHANGS) are accompanied by spatially-resolved multi-wavelength data, which has opened many exciting opportunities for science which ties cold gas with stellar populations, dust, etc.

1.2.2 Dust

Dust scatters and absorbs visible and UV light (e.g. that from stars and H II regions) causing the light to redden. The effect of dust can be qualitatively seen by performing fits to the spectral-energy distribution (SED) of a galaxy from the UV to the FIR and comparing how bright the stellar light should appear without dust versus how bright it is actually observed to be (represented by the hatched region in Figure 1.5). Following Cardelli et al. (1989) and Galliano et al. (2018), extinction is usually parameterized by A_V with

$$A_\lambda = 1.086 \left\{ \left[\kappa_{\rm abs}(\lambda) + \kappa_{\rm scat}(\lambda) \right] \Sigma_{\rm dust} \right\}, \tag{1.8}$$

where $\kappa_{\rm abs} + \kappa_{\rm scat}$ is the total opacity (which comes from absorption and scattering), $\Sigma_{\rm dust}$ is the dust mass surface density, and everything between curly brackets is the optical depth $\tau(\lambda)$. From UV to the MIR the shape of the A_λ / A_V versus λ curve in different environments exhibits some common features. The features in these curves come from different types of dust that are present. For example, the 217.5 nm bump is thought to be due to small grains such as PAHs, and there is a knee in the optical due to scattering from large grains (Cardelli et al. 1989; Galliano et al. 2018).

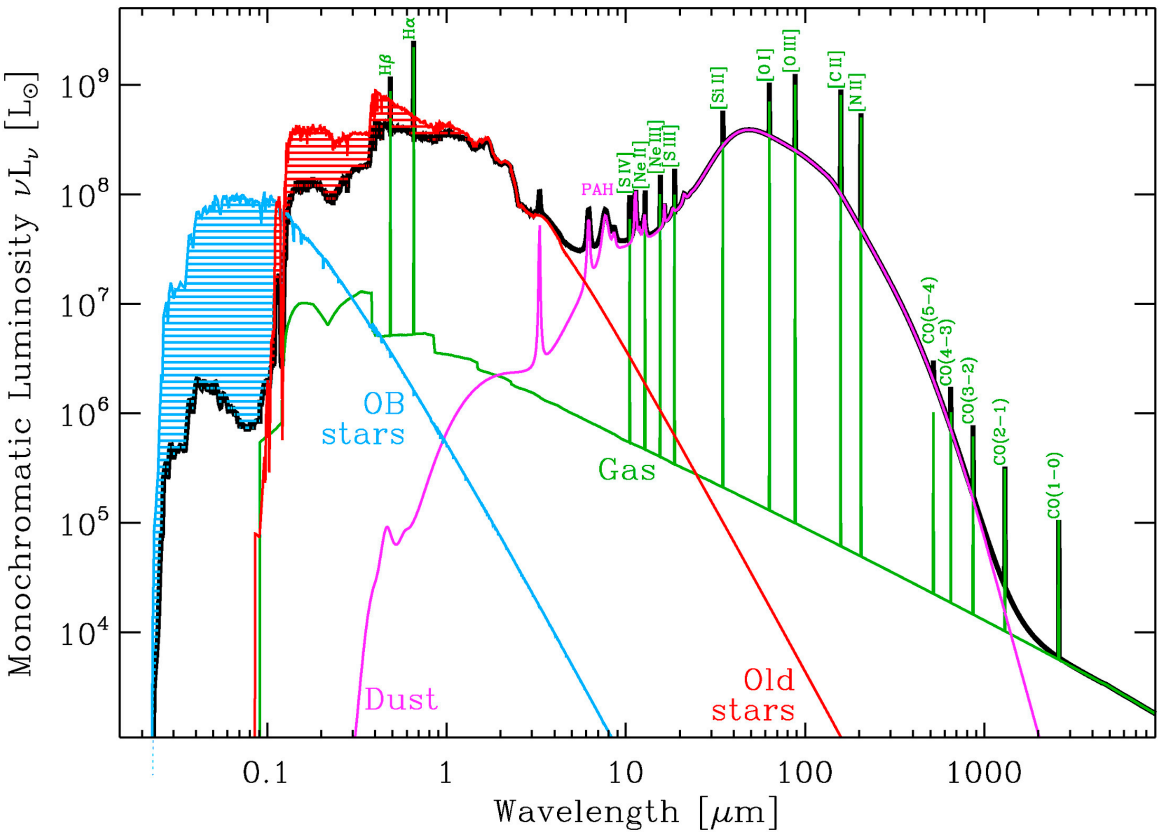

Figure 1.5: UV-to-radio spectral energy distribution (black) for the star-forming galaxy NGC 1569 along with its best-fit model spectrum (coloured curves), taken from Galliano (2017). The model SED is based on that presented in Galliano et al. (2008) with the addition of commonly-observed gas emission lines, then re-fit using the `cloudy` code (Ferland et al. 2013). The blue and red hatched regions show the light from young stars and old stars, respectively, that was absorbed by dust and re-emitted in the infrared. Note the break in the spectrum at around 4000 Å, the Hα and Hβ emission lines, PAH emission, the dust spectrum (which dominates the SED), CO lines, and the continuum at radio wavelengths from synchrotron emission. Figure reproduced with permission from the publisher.

Dust also absorbs visible and UV light and re-emits in the infrared. Infrared emission from dust dominates the spectral energy distributions of many galaxies, re-radiating 30 per cent of the output from stars, even though dust accounts for $\lesssim 1$ per cent of the mass of the ISM (Galliano et al. 2018). This monochromatic luminosity $L_\nu(\lambda)$ of dust is usually approximated as a modified blackbody (or multiple modified blackbodies if there are multiple populations of dust), which is given by

$$L_\nu(\lambda) = M_{\rm dust}\,\kappa(\lambda_0)\left(\lambda_0/\lambda\right)^\beta 4\pi B_\nu(\lambda, T_{\rm dust}), \tag{1.9}$$

where $M_{\rm dust}$ is the dust mass, $T_{\rm dust}$ is the dust temperature, $B_\nu(\lambda, T_{\rm dust})$ is the Planck function, and $\kappa_0\left(\lambda_0/\lambda\right)^\beta$ is the opacity (Galliano et al. 2018). The dust SED of an example galaxy is shown by the pink curve in Figure 1.5. Dust mass and molecular gas mass or H I + molecular gas mass have been known for years to be correlated. This has led to dust being used as a gas mass tracer in galaxies (Hildebrand 1983; Devereux & Young 1990; Leroy et al. 2011; Scoville et al. 2016; Davies et al. 2019; Casasola et al. 2020).

Very small dust grains that are actually large carbon-rich molecules with 10-100 carbon atoms called "polycyclic aromatic hydrocarbons" (PAHs; Allamandola et al. 1985, 1989). MIR emission from PAHs accounts for up to 20 per cent of all IR emission in nearby galaxies (Smith et al. 2007). Despite their complexity, there are a number of prominent PAH emission features commonly found in the spectra of astronomical objects (virtually anywhere there is dust that is being illuminated by UV photons) at 3.3, 6.2, 7.7, 8.6, 11.2, 12.7, and 16.4 μm (Tielens 2008; Galliano et al. 2008). These features can be clearly seen in the mid-infrared region of the SED in Figure 1.5. The well-known MIR emission features arise from the de-excitation of the stretching

and bending vibrational modes of PAHs after being excited by a FUV photon (Tielens 2008).

Observationally, PAH emission is found preferentially in photodissociation regions (PDRs), which are the largely neutral transition regions between ionized and molecular gas on the surfaces of molecular clouds (Li 2020). Photoelectrons from PAHs may collide with nearby neutral gas, causing it to increase its temperature – in fact, this is the dominant heating mechanism in the neutral ISM (Draine 1978; Wolfire et al. 1995). Note that this emission mechanism is IR fluorescence, which is different from the thermal IR emission from other dust grains. Obtaining spatially-resolved mid-infrared spectroscopy for galaxies is an observational challenge. Figure 1.6 shows a map of PAH emission in M51 obtained using a method of extracting spatially-resolved spectra from *Spitzer*/IRS data (Zhang et al. 2021). The *James Webb Space Telescope* (*JWST*) will be used to produce high spatial-resolution MIR data cubes for galaxies, which will allow us to study PAHs in galaxies in much greater detail. For a review on the current status of PAHs from the *Spitzer* perspective see Li (2020).

1.3 Star Formation

Measuring the SFR is a challenge, owing to the complexity of the star formation process and of converting observables into SFRs. Nearly every feature of a galaxy SED (Figure 1.5) is affected by star formation, and there are ways of extracting an SFR from many of these features. SFR tracers can be broadly grouped into direct tracers (light from the stars themselves, also called unobscured) and indirect tracers (light from other sources, also called obscured). I will not review all of these tracers (instead, see Kennicutt & Evans 2012), but I will describe the most relevant

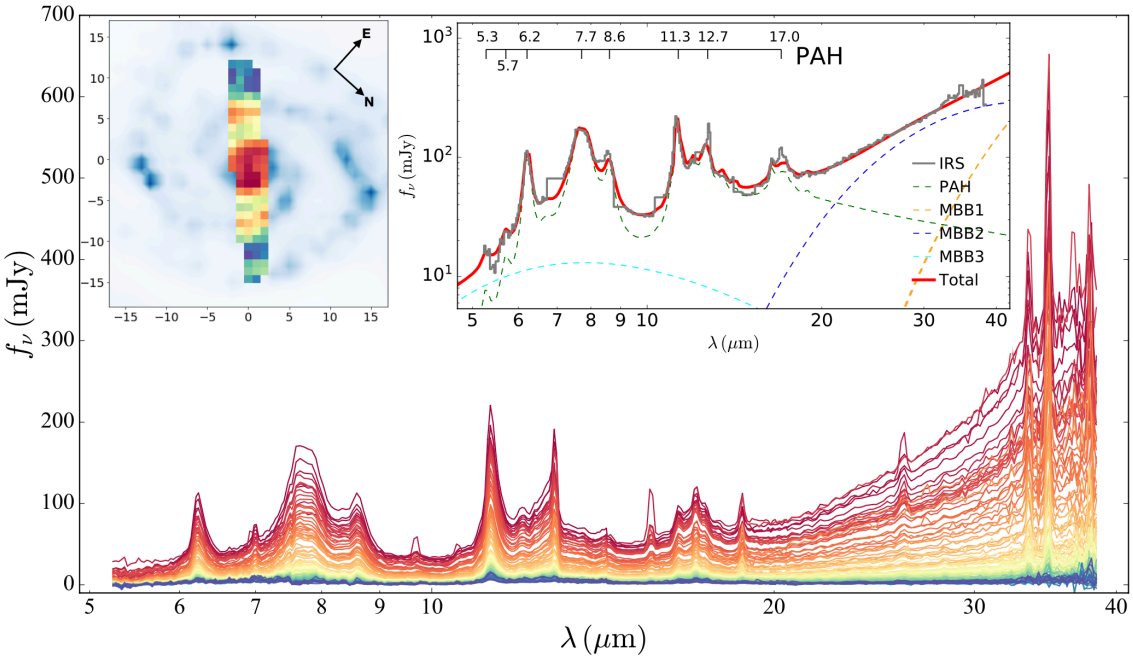

Figure 1.6: Spatially-resolved PAH emission in the galaxy M51 extracted from *Spitzer*/IRS data (Zhang et al. 2021). One can see the many mid-infrared emission features and how their intensities vary with position in this galaxy. The pixels (top left) and PAH spectra of each pixel (bottom) are colour coded from blue to red by the integrated flux from 5 to 20 μm. The inset in the upper right shows the total MIR spectrum for one pixel and the best-fit component spectra. Figure reproduced with permission.

ones for this thesis. I will start from the UV and end in the IR (left to right in Figure 1.5).

Direct (unobscured) tracers of star formation, such as UV emission, miss emission that is absorbed by dust (30 per cent or more, as previously mentioned). The luminosity at UV wavelengths (e.g. as measured by *GALEX*) can be converted into SFR (Kennicutt & Evans 2012), but one must estimate the amount of dust extinction at UV wavelengths. This estimate can be done using global optical and/or MIR measurements and fitting an SED, as was done with the *GALEX*-SDSS-*WISE* Legacy Catalog (GSWLC; Salim et al. 2016). More recently, Leroy et al. (2019) have produced spatially-resolved maps of SFR using UV images from *GALEX* and MIR images from *WISE* for ∼16,000 nearby galaxies ($d_L \lesssim 50$ Mpc).

One of the most widely-used and well-understood SFR tracers is the luminosity of the Hα λ6563 (i.e. 6563 Å) recombination line (Moustakas et al. 2006). This tracer was first investigated by Kennicutt (1983). Radiation from short-lived massive (≥ 10 M$_\odot$) stars (whose collective emission forms the blue curve in Figure 1.5) ionizes the surrounding hydrogen gas, such that the Hα luminosity is proportional to the stellar radiation, and it traces the nearly instantaneous SFR (Kennicutt 1998; Moustakas et al. 2006). This emission line is not from stars themselves, but rather from the ionized gas in an H II region, and so this is an indirect tracer and is also affected by dust attenuation.

Typically, the level of dust reddening is estimated using the "Balmer decrement." Referring again to Figure 1.5, one can see that the Hα and Hβ lines are close to each other. The Balmer decrement is the ratio between the luminosities of these two lines Hα/Hβ. To correct the Hα luminosity, one usually assumes an intrinsic value of this ratio, which depends on the temper-

ature and electron density. The value of the Balmer decrement assuming a temperature of 10^4 K, an electron density of 100 cm^{-3}, and case-B recombination (which means that the region is optically thick to ionizing radiation) is $\left(\mathrm{H}\alpha/\mathrm{H}\beta\right)_{\mathrm{int}} = 2.86$ (Osterbrock & Ferland 2006). The colour excess is given by

$$E(\mathrm{H}\beta - \mathrm{H}\alpha) \equiv -2.5 \log \left[\frac{\left(\mathrm{H}\alpha/\mathrm{H}\beta\right)_{\mathrm{int}}}{\left(\mathrm{H}\alpha/\mathrm{H}\beta\right)_{\mathrm{obs}}} \right], \tag{1.10}$$

where $\left(\mathrm{H}\alpha/\mathrm{H}\beta\right)_{\mathrm{obs}}$ is the observed value of the Balmer decrement. In order to deredden the Hα luminosity we need to convert $E(\mathrm{H}\beta - \mathrm{H}\alpha)$ into an $E(\mathrm{B}-\mathrm{V})$ colour excess, which requires us to assume a reddening curve (Section 1.2.2). These are related by

$$E(\mathrm{B}-\mathrm{V}) \equiv \frac{E(\mathrm{H}\beta - \mathrm{H}\alpha)}{k\left(\mathrm{H}\beta\right) - k\left(\mathrm{H}\alpha\right)}, \tag{1.11}$$

where $k(\lambda) \equiv A(\lambda)/E(\mathrm{B}-\mathrm{V})$ from the assumed reddening curve. Assuming a Milky Way reddening curve (Calzetti et al. 2000), we get

$$E(\mathrm{B}-\mathrm{V}) = 1.97 \, \log \left(\frac{\mathrm{H}\alpha/\mathrm{H}\beta}{2.86} \right), \tag{1.12}$$

$$A\left(\mathrm{H}\alpha\right) = 3.33 \, E(\mathrm{B}-\mathrm{V}), \tag{1.13}$$

and the extinction-corrected Hα flux is

$$F\left(\mathrm{H}\alpha\right)_{\mathrm{corr}} = F\left(\mathrm{H}\alpha\right)_{\mathrm{obs}} 10^{0.4\, A(\mathrm{H}\alpha)}. \tag{1.14}$$

Now I move on to dust-based SFR tracers. As I have already discussed, dust absorbs about 30 per cent of the light from stars, and re-emits in the infrared. The total infrared luminosity $L_{\rm TIR}$, that is, the integrated luminosity over 3 to 1000 μm can be used as a reliable SFR tracer (Hao et al. 2011; Murphy et al. 2011; Kennicutt & Evans 2012). It is sensitive to about a 0-100 Myr timescale, and an average stellar age of 5 Myr (Hao et al. 2011; Murphy et al. 2011; Kennicutt & Evans 2012), although the average age varies depending on the value of the SFR.

Mid-infrared emission has also proven to be a fruitful regime in the search for star formation rate tracers (Calzetti et al. 2007). Since PAHs absorb a significant fraction of the UV energy from massive stars, some individual emission features have been calibrated as SFR tracers (Peeters et al. 2004). Tracers based on *WISE* fluxes are also used, as these bands capture PAH emission along with warm dust (Jarrett et al. 2013). *Spitzer*/MIPS 24 μm and 70 μm fluxes are also widely used as SFR tracers (Calzetti et al. 2007; Li et al. 2010).

The SFR tracers described above have advantages and weaknesses. One way of alleviating weaknesses is to use a composite tracer, such as UV and TIR (Kennicutt & Evans 2012), or another combination of unobscured and obscured tracers as was done in Leroy et al. (2019). To add in the obscured SFR, they used the *WISE* MIR SFR calibration from Jarrett et al. (2013). There is, however, another SFR tracer which does not suffer from dust obscuration and does not depend on dust in order to work – namely, centimeter-wavelength radio continuum emission (the regime in the far right in Figure 1.5). Radio-wavelength synchrotron emission from galaxies is from accelerating charged particles ejected by supernovae (Kennicutt & Evans 2012).

1.4 Key ISM and Star Formation Scaling Relations

As mentioned above, a major goal in the study of galaxy evolution is to understand the physical reasons for the observed star-forming main sequence (SFMS). What processes lead to the SFMS? Why are there so few galaxies in between the SFMS and the red sequence (Figure 1.4)? How do galaxies move in this plane, and what is happening with their ISM and star formation histories as they do so?

Over the past few decades, research on the relationship between the ISM and star formation in nearby galaxies has been from two approaches: small samples of galaxies (of order 1-100 galaxies) with kiloparsec or sub-kiloparsec resolution, or large samples of galaxies (hundreds or more) with limited resolution. A major result from the small sample, high resolution work is the tight correlation between the surface density of SFR (Section 1.3) and the surface density of gas (Section 1.2.1). This correlation was first identified in the Milky Way by Schmidt (1959), which motivated extragalactic work such as Kennicutt (1989) who used Hα as an SFR tracer, and a combination of H I and CO to trace the total cold gas. The Kennicutt-Schmidt relation (Figure 1.7) follows a power law (above $\Sigma_{\rm gas} \sim 10\,M_{\odot}\,{\rm pc}^{-2}$)

$$\Sigma_{\rm SFR} \propto \Sigma_{\rm gas}^{N}, \tag{1.15}$$

where $\Sigma_{\rm SFR}$ is the SFR surface density in $M_{\odot}\,{\rm kpc}^{-2}$, $\Sigma_{\rm gas}$ is the total gas (H I + H_2) surface density in $M_{\odot}\,{\rm pc}^{-2}$, and $N \simeq 1.4$ for H I + H_2 or 1.0 if only H_2 is included (Kennicutt 1989; Kennicutt et al. 2007; Bigiel et al. 2008; Leroy et al. 2008, 2013; de los Reyes & Kennicutt 2019; Ken-

nicutt & De Los Reyes 2021). Other versions of this relationship have been proposed, such as the modified Schmidt law (Shi et al. 2011, 2018), and the Silk-Elmegreen law (Elmegreen 1997; Silk 1997). On galaxy-integrated scales, many studies have also found tight relationships between cold gas and star formation (e.g. Gao & Solomon 2004; Liu et al. 2015; Saintonge et al. 2017, 2018).

Large samples of cold gas measurements in nearby galaxies such as xCOLD GASS and JINGLE, xGASS, and ALFALFA (Section 1.2.1) have made it possible to study the gas content and gas depletion time as functions of position relative to the SFMS (e.g. Saintonge et al. 2016; Feldmann 2020; Sánchez et al. 2021). Gas content is usually quantified as a mass ratio (often called the gas mass fraction)

$$f_{\rm gas} \equiv \frac{M_{\rm gas}}{M_\star}, \tag{1.16}$$

where $M_{\rm gas}$ can be either H I, H_2, or H I+H_2. Gas depletion time $t_{\rm gas}$ is

$$t_{\rm gas} \equiv \frac{M_{\rm gas}}{\rm SFR}, \tag{1.17}$$

where $M_{\rm gas}$ can be either H I, H_2, or H I+H_2, depending on the analysis. The reciprocal of $t_{\rm gas}$ is usually called "star formation efficiency" in extragalactic studies, not to be confused with the true star formation efficiency which is the fraction of a molecular cloud which forms stars before it dissipates (see Kennicutt & Evans 2012). One finding of note is that molecular gas depletion times and total gas depletion times steadily increase from above to below the SFMS (Figure 1.8; Feldmann 2020).

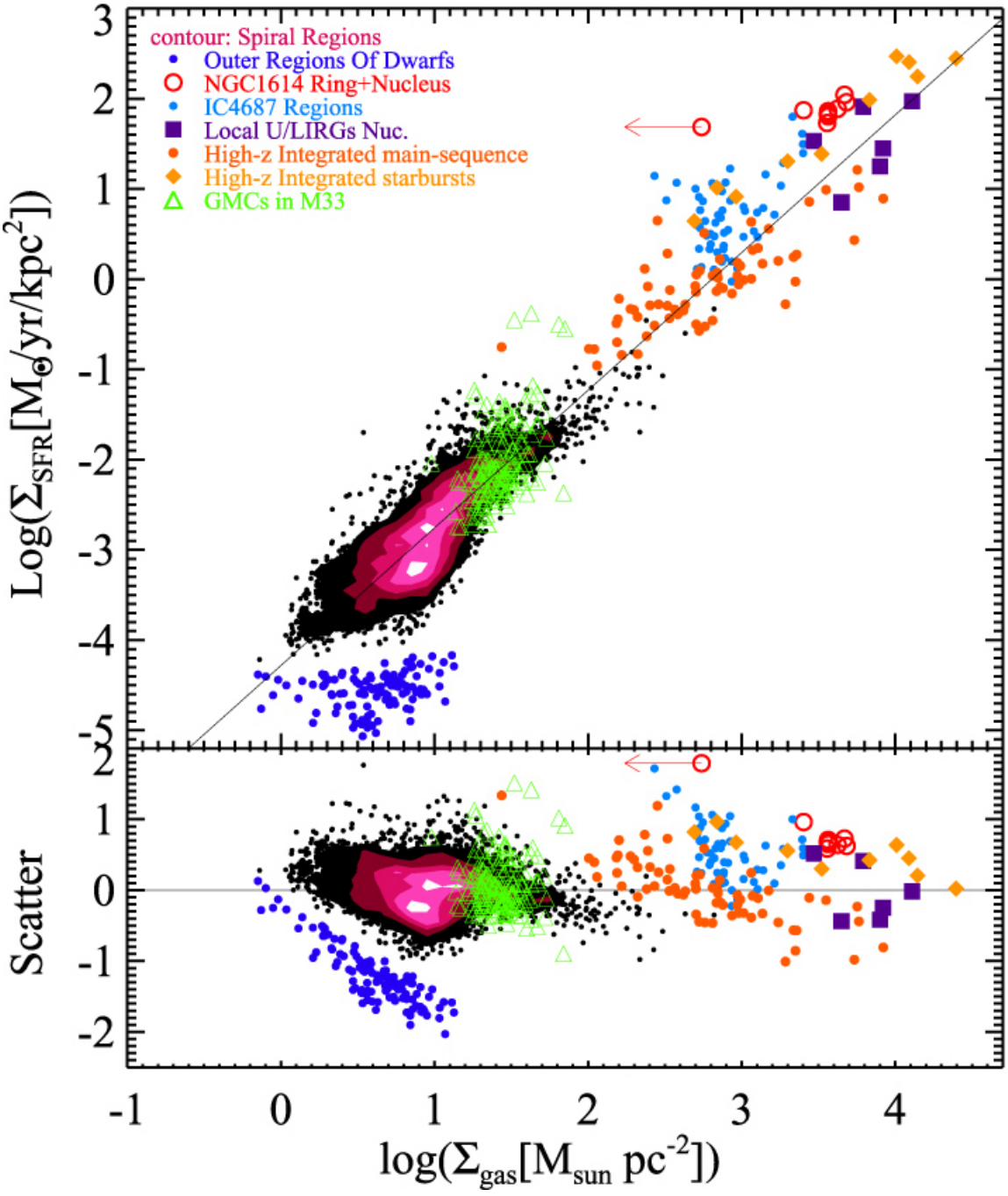

Figure 1.7: The Kennicutt-Schmidt relationship (Shi et al. 2018). Regions within a wide range of galaxy types at low and high redshifts lie on or near the main relation. Figure reproduced with permission.

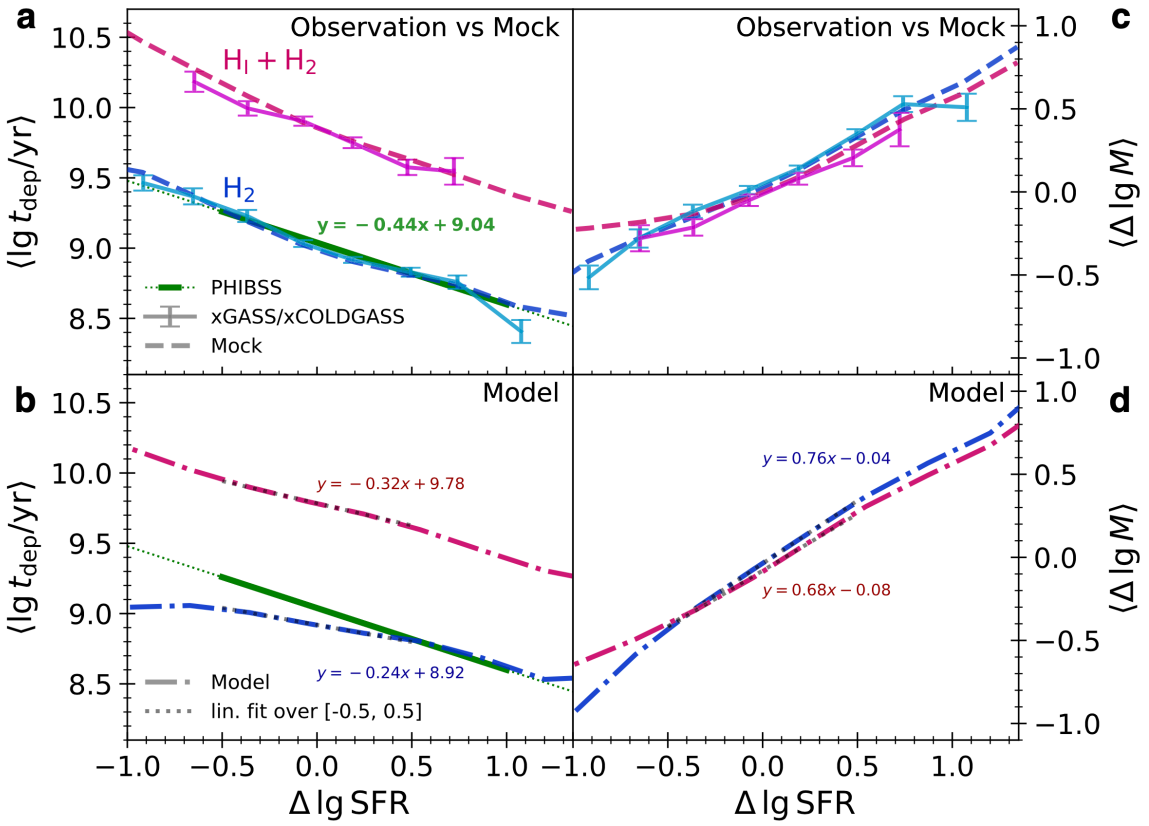

Figure 1.8: The relationship between average gas depletion time (left) or average gas mass (right) and offset from the SFMS (Feldmann 2020). The xCOLD GASS sample was used for CO data, and the xGASS sample was used for HI. The top row shows depletion times before correcting for non-detections and selection effects. The points with error bars are the mean of detections only from the real data. The "mock" curves are the mean relations from only detected data points from simulated data sets. The bottom row shows the best estimate ("model") of the mean scaling relations without biases from non-detections and selection effects. The left column shows depletion times while the right panel shows the average gas masses relative to the peak gas masses for each respective sequence. Figure reproduced from Feldmann (2020) under a Creative Commons CC BY license.

In the past few years, large samples of galaxies (of order 100) with spatially-resolved cold gas and spatially resolved optical spectroscopy have emerged such as EDGE (Bolatto et al. 2017), the ALMA MaNGA Quenching and Star-Formation Survey (ALMaQUEST; Lin et al. 2019), and PHANGS (Leroy et al. 2021). These samples have investigated the KS law and the star forming main sequence at small scales with a large number of galaxies. It has recently been proposed to view the KS law, the SFMS and the molecular gas main sequence (MGMS; Lin et al. 2019) as a three-dimensional space. These three relationships are shown together using the ALMaQUEST sample in Figure 1.9. They find that the MGMS and the KS laws have the strongest correlations, and that the resolved SFMS may simply be a consequence of the KS and MGMS relations. From this perspective we can learn about how quickly the gas is being depleted (from the intercept on the KS law), as well as the ratio of gas to stars (from the intercept on the MGMS). Examining the relative importance of gas depletion time and gas mass fraction in determining position and evolution in the SFMS has become a major interest.

1.5 This Thesis

In this thesis I explore relationships between the ISM and star formation in galaxies using a variety of tracers, and at a variety of spatial resolutions.

In Chapter 2, I study the effects of galactic bars and galaxy-galaxy interactions on the spatial distribution of molecular gas and star formation history in the center of galaxies (Chown et al. 2019). To accomplish this I use spatially-resolved CO data from the Extragalactic Database for Galaxy Evolution (EDGE) survey (Bolatto et al. 2017) and optical integral-field spectroscopy

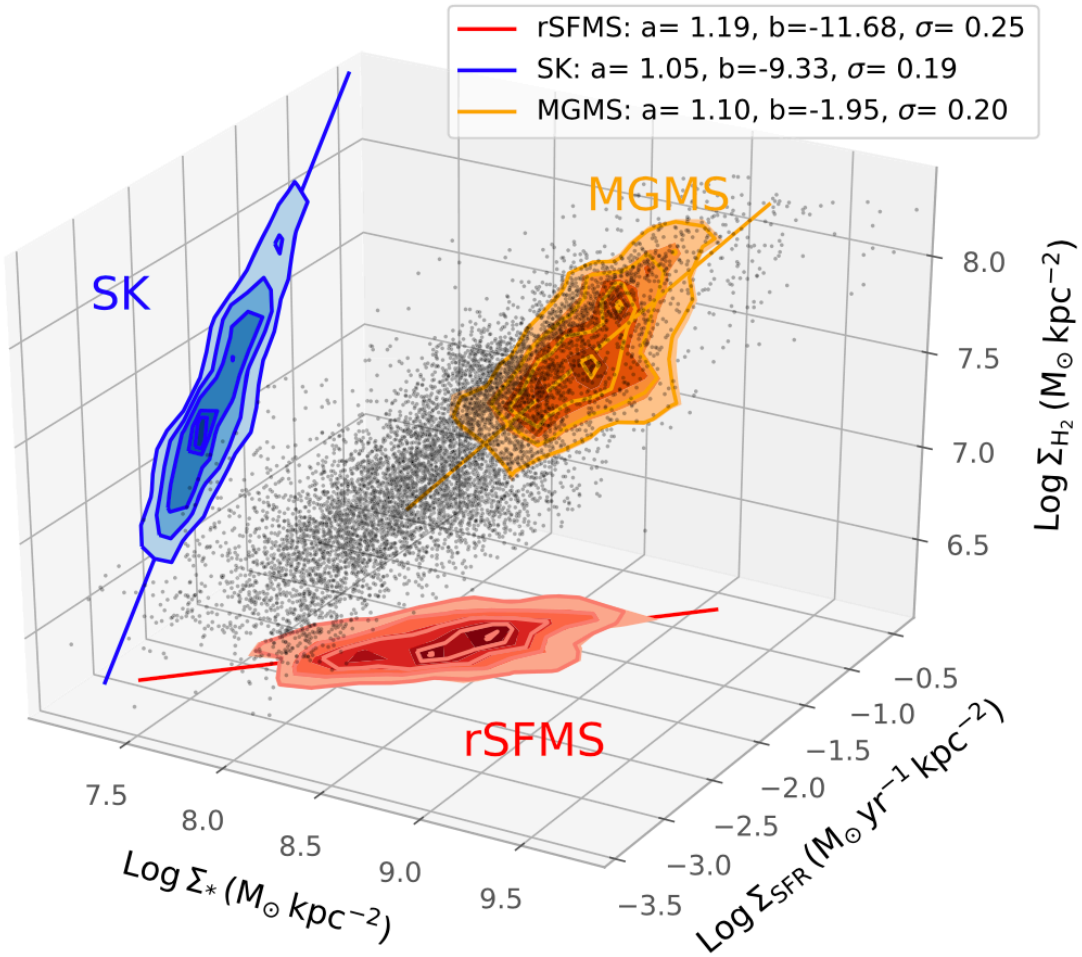

Figure 1.9: The Kennicutt-Schmidt (SK) relation, resolved molecular gas main sequence (MGMS), and resolved star-forming main sequence (rSFMS) can be viewed as a trend in three-dimensional space (Lin et al. 2019). The black points show individual pixels from the ALMaQUEST sample, and the coloured contours show the projected distributions on each of the three planes. The best-fit lines are shown in each plane, and the best-fit parameters ($y = a\,x+b$) are shown in the legend. The resolved SFMS shows the greatest amount of scatter (σ in the legend), suggesting that it is the least fundamental of the three sequences (Lin et al. 2019). Figure reproduced with permission.

from the CALIFA survey (Sánchez et al. 2012, 2016). The main finding is that molecular gas concentration and the level of central star-formation enhancement is correlated among barred galaxies but not among isolated unbarred galaxies. This result confirms previous findings that many (but not all) barred galaxies have enhanced gas concentrations and enhanced central star formation, but for the first time in a sample of galaxies with both resolved gas and star formation measurements.

In Chapter 3, I study the relationship between *WISE* 12 μm emission and CO emission at $\sim$ kpc scales in nearby galaxies using EDGE CO data (Chown et al. 2021). The goals of this work were to determine whether the correlation that was previously found at galaxy-wide scales (Jiang et al. 2015; Gao et al. 2019) holds at smaller scales, and to use multi-wavelength data to better understand its origins. I found for the first time that the 12 μm-CO correlation holds at kiloparsec scales, and that the best-fit power law varies from galaxy to galaxy. I used a machine learning technique to develop spatially-resolved estimators of H_2 surface density within galaxies, based on a wide variety of multi-wavelength data including optical integral-field spectroscopy, and global galaxy properties from UV to FIR wavelengths.

In Chapter 4, I study the gas (H_2 and H I) and dust properties (traced by SCUBA-2 850 μm emission) of a population of red star-forming galaxies called "red misfits," which were originally identified in Evans et al. (2018). The goal here was to characterize the ISM in this unique population of galaxies (e.g. are they more dusty?), and to see what they can tell us about galaxy evolution. My main findings are that, compared to blue star forming galaxies ("blue actives"), red misfits have slightly longer gas depletion times, significantly lower gas mass fractions, lower

dust-to-stellar mass ratios, similar dust-to-gas ratios, and a flatter slope in the ($\log\ M_{\rm mol}$, $\log\ M_{\star}$) plane. These results indicate that red misfits are actually *less* dusty than blue actives, and are likely in the act of quenching.

In Chapter 5, I provide a summary of my key results, broader implications, an outline of future work. For example, I plan on using the PHANGS CO data set to study the cold gas properties in barred galaxies in comparison to resolved data from other wavelengths such as the Multi Unit Spectroscopic Explorer (MUSE; Bacon et al. 2010) and the *Hubble Space Telescope* (*HST*). I will investigate the 12 μm-CO relationship in more detail in the Virgo Environment Traced in CO survey (VERTICO). I also plan on investigating the spatially-resolved correlation between PAH emission using *JWST* and CO emission using ALMA in a variety of systems ranging from star-forming regions in the Milky Way to nearby galaxies.

2

Linking bar- and interaction-driven molecular gas concentration with centrally-enhanced star formation in EDGE-CALIFA galaxies

This chapter contains the following article:

"Linking bar- and interaction-driven molecular gas concentration with centrally-enhanced star formation in EDGE-CALIFA galaxies"

Published in the Monthly Notices of the Royal Astronomical Society (MNRAS): Vol. 484, pp. 5192-5211, 2019.

Authors: Chown, R., Li, C., Athanassoula, E., Li, N., Wilson, C. D., Lin, L., Mo, H., Parker,

L. C., and Xiao, T.

Abstract

We study the spatially resolved star formation history and molecular gas distribution of 58 nearby galaxies, using integral field spectroscopy from the CALIFA survey and CO $J = 1 \rightarrow 0$ intensity mapping from the CARMA EDGE survey. We use the 4000 Å break ($D_n(4000)$), the equivalent width of the Hδ absorption line (EW(Hδ_A)), and the equivalent width of the Hα emission line (EW(Hα)) to measure the recent star formation history (SFH) of these galaxies. We measure radial profiles of the three SFH indicators and molecular gas mass surface density, from which we measure the level of centrally enhanced star formation and the molecular gas concentration. When we separate our galaxies into categories of barred (17 galaxies), unbarred (24 galaxies), and merging/paired (17 galaxies) we find that the galaxies which have centrally-enhanced star formation (19/58) are either barred (13/19) or in mergers/pairs (6/19) with relatively high molecular gas concentrations. A comparison between our barred galaxies and a snapshot of a hydrodynamic *N*-body simulation of a barred galaxy shows that the current theory of bar formation and evolution can qualitatively reproduce the main features of the observed galaxies in our sample, including both the sharp decrease of stellar age in the galactic center and the gradual decrease of age with increasing distance from center. These findings provide substantial evidence for a picture in which cold gas is transported inward by a bar or tidal interaction, which leads to the growth and rejuvenation of star formation in the central region.

2.1 Introduction

Bars play an essential role in the secular evolution of galaxies. Simulations have shown that the growth of a bar causes gas to either form a ring structure or fall inwards and trigger central star formation (Athanassoula 1992b, 1994; Piner et al. 1995; Athanassoula et al. 2013; Sormani et al. 2015). Minor mergers and tidal interactions have a similar effect as bars, as these events also tend to drive molecular gas inward (Barnes & Hernquist 1991). The subsequent star formation from these processes leads to the growth of the central disky pseudobulge (Kormendy & Kennicutt 2004; Athanassoula 2005, and references therein). Internal processes can quench star formation, such as feedback from an active galactic nucleus (AGN), or the growth of the central bulge which can stabilize the gas disk (Martig et al. 2009). Bars can counteract these quenching mechanisms by transporting gas to the center which can fuel subsequent central star formation.

The most commonly-used tracer of molecular gas mass in the interstellar medium is line emission of the CO molecule, e.g. CO $J = 1 \rightarrow 0, J = 2 \rightarrow 1$, etc. (Bolatto et al. 2013, and references therein). Observational studies of CO have found elevated molecular gas concentrations in barred galaxies compared to their unbarred counterparts (e.g., Sakamoto et al. 1999; Sakamoto 2000; Jogee et al. 2005; Sheth et al. 2005; Regan et al. 2006; Kuno et al. 2007). It is also known that star formation rates (SFRs) are higher in the central region of barred galaxies compared to unbarred galaxies (e.g, Hawarden et al. 1986; Devereux 1987; Puxley et al. 1988; Ho et al. 1997; Ellison et al. 2011; Oh et al. 2012; Zhou et al. 2015). Minor mergers and galaxy-galaxy interactions have also been found to correlate with increased central star formation (e.g., Li et al. 2008; Ellison et al. 2011; Wang et al. 2012; Lin et al. 2014). Interaction-induced enhance-

ment of star formation is found mainly in galaxies with projected separations less than $\sim$ 100 kpc (Li et al. 2008; Patton et al. 2013; Ellison et al. 2013). A number of recent studies have used both molecular gas tracers and star formation indicators to study central star formation and cold gas in interacting galaxies (e.g., Saintonge et al. 2012; Stark et al. 2013; Kaneko et al. 2013; Violino et al. 2018), finding lower gas depletion times and enhanced gas content in these galaxies. Galaxies in dense environments also tend to have more centrally-concentrated molecular gas and enhanced star formation (e.g., Mok et al. 2017).

Most earlier optical studies of galaxies used single-fiber measurements from the Sloan Digital Sky Survey (SDSS; York et al. 2000). Integral-field unit (IFU) surveys such as the Calar Alto Legacy Integral Field Area (CALIFA) survey (Sánchez et al. 2012; Walcher et al. 2014; Sánchez et al. 2016), the SDSS-IV Mapping nearby Galaxies at Apache Point Observatory Survey (MaNGA; Bundy et al. 2015; Blanton et al. 2017), and the Sydney-AAO Multi-object Integral field spectrograph (SAMI; Croom et al. 2012) have provided spatially resolved spectroscopy for thousands of galaxies in the local Universe, enabling detailed studies of the correlation of internal structure of galaxies with their star formation properties.

Of particular interest for the present work, Lin et al. (2017) analyzed 57 nearly face-on spiral galaxies using CALIFA IFU data. They measured the recent star formation history (SFH) using three parameters extracted from the CALIFA data: the 4000 Å-break $D_n(4000)$, and the equivalent widths (EW) of the Hα emission line logEW(Hα) and Hδ absorption line EW(Hδ_A). A considerable fraction of their galaxies (17/57) had a central drop ("turnover") in the $D_n(4000)$, and a central upturn in logEW(Hα) and EW(Hδ_A), indicating recent star formation in the cen-

ter. Interestingly, almost all of these "turnover" galaxies are barred, while only half of the barred galaxies in their sample present a turnover feature, suggesting that a bar is a *necessary but not sufficient* condition for central star formation enhancement. The only parameter found to be correlated with the level of central star formation is the bar length, an indicator of bar strength. Together with the results of Kuno et al. (2007), for example, who found a correlation between bar strength and molecular gas concentration, one might expect enhanced central star formation to be associated with molecular gas concentration. Observations of the cold gas within galaxies, with spatial resolution comparable to the optical IFU data, are needed in order to clearly examine the correlation of the two components.

Uniform samples of high-sensitivity (detections of $\Sigma_{H_2} \sim 1\, M_\odot\ \mathrm{pc}^{-2}$), high spatial resolution (sub-kpc) cold gas measurements of nearby galaxies are available, however the sample sizes range from a few up to 30-50 galaxies. Although a sample of 30-50 galaxies is sufficient for many purposes, the effective sample size can quickly become much lower after selection cuts (on redshift, stellar mass, etc.) and/or dividing the galaxies into different categories for comparison (e.g. barred or unbarred). Some notable studies and surveys are Kennicutt et al. (2007), Bigiel et al. (2008), the H I Nearby Galaxy Survey (THINGS; Walter et al. 2008), and the HERA CO-Line Extragalactic Survey (HERACLES; Leroy et al. 2009). At slightly lower spatial resolution, recent surveys have obtained spatially resolved CO spectra for significantly larger samples, such as the James Clerk Maxwell Telescope (JCMT) Nearby Galaxies Legacy Survey (NGLS; 155 galaxies, ∼50% detected; Wilson et al. 2012), the Combined Array for Research in Millimeter-wave Astronomy (CARMA) Extragalactic Database for Galaxy Evolution (EDGE) CO survey (126

galaxies, 82% detected; Bolatto et al. 2017), and the CO Multi-line Imaging of Nearby Galaxies survey (COMING; 127 galaxies; Sorai, K., et al. 2018, in preparation). Galaxies in the CARMA EDGE survey were selected from the CALIFA survey, and were observed in CO $J = 1 \rightarrow 0$ with a similar field-of-view and angular resolution ($\sim 4.5''$) as the CALIFA data ($\sim 2.5''$). The similar resolution and field-of-view were intended to enable joint analyses of the stellar populations and cold gas content of nearby galaxies. Recent work by Utomo et al. (2017) found, using EDGE and CALIFA data, that barred and interacting galaxies tend to have smaller center-to-disk gas depletion time ratios than unbarred, isolated galaxies.

In this paper we extend the work of Lin et al. (2017) by explicitly linking the central SFH and resolved gas properties in barred, unbarred, and interacting galaxies. We have used spatially resolved maps of CO $J = 1 \rightarrow 0$ from EDGE and SFH indicators from CALIFA to accomplish this goal. We find that molecular gas concentrations are indeed associated with centrally-enhanced star formation, and this link is seen in both barred galaxies and interacting galaxies. Our main result is that the level of centrally-enhanced star formation in barred galaxies is positively correlated with molecular gas concentration (correlation coefficient $r = 0.64$), while unbarred galaxies show little-to-no centrally-enhanced star formation and no correlation ($r = 0.09$). Some merger/pair galaxies have centrally enhanced star formation, but the correlation between the level of enhanced star formation and gas concentration is weak ($r = 0.26$). In addition, we have compared these observational results with an N-body simulation of the gas and stellar distributions of a barred galaxy. The similarities between the simulation and the real galaxy suggest that the current theory of bar formation can qualitatively reproduce the key

features of real galaxies.

The structure of this paper is as follows. In §2.2 we describe the data used and how they are processed. We present our observational results in §2.3 and the comparison with the *N*-body simulation in §2.4. We discuss some questions in light of our results and highlight interesting individual galaxies in §2.5. Finally, we summarize our work in §2.6. Tables of galaxy properties and a discussion of a few unusual galaxies are given in the Appendix. Throughout this paper we assume a ΛCDM cosmology with parameters $H_0 = 67.7\,\mathrm{km\,s^{-1}\,Mpc^{-1}}$, $\Omega_\Lambda = 0.693$, and $\Omega_{\mathrm{m},0} = 0.307$, following the results from the *Planck* satellite (Planck Collaboration et al. 2016).

2.2 Data and processing

2.2.1 The CARMA EDGE and CALIFA surveys

CARMA EDGE (Bolatto et al. 2017) is a survey of CO emission in 126 nearby galaxies carried out using the CARMA interferometer (Bock et al. 2006). The CARMA EDGE sample was selected from the CALIFA sample with high fluxes in the 22μm band from the *Wide-field Spectroscopic Explorer* (*WISE*) survey. The requirement for high mid-infrared flux means that the sample is mainly gas-rich and actively star-forming, given the correlation between the mid-infrared luminosities from *WISE* and the molecular gas mass (e.g. Jiang et al. 2015). The sample consists of galaxies imaged in ^{12}CO and ^{13}CO with sensitivity, angular resolution and field-of-view well-matched to CALIFA data. The typical 3σ molecular gas mass surface density sensitivity is $11\,M_\odot\mathrm{pc}^{-2}$, and the typical angular resolution is $4.5''$ (Bolatto et al. 2017). We use the publicly available ^{12}CO $J = 1 \rightarrow 0$ integrated flux maps from CARMA EDGE. Specifically,

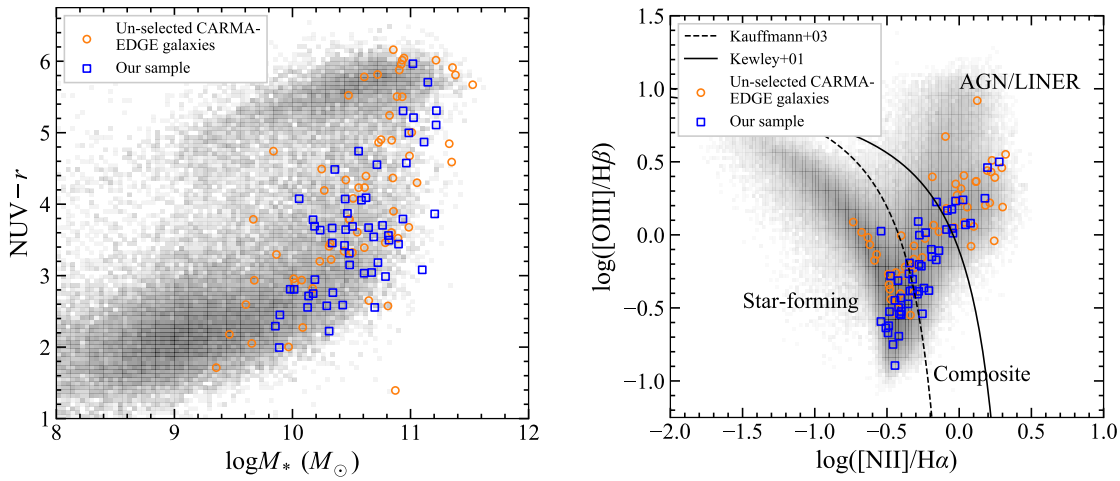

Figure 2.1: *Left:* NUV$-r$ vs. log(M$_*$/M$_\odot$) for the sample used in this work (blue squares), the remaining galaxies in the CARMA EDGE survey (orange circles), and a volume-limited sample of low-redshift galaxies with $0.003 \leq z \leq 0.03$ from the NASA-Sloan Atlas (grey). *Right:* our sample and the unselected CARMA EDGE galaxies shown on the BPT diagram, overlaid on a volume-limited sample selected from the MPA-JHU catalog (grey). Points lying between the lines of Kewley et al. (2001) and Kauffmann et al. (2003c) are composites, while points toward the lower left are star-forming, and points toward the upper right are LINER. These figures show that our sample consists of mostly star-forming galaxies with stellar masses above $\sim 10^{10} M_\odot$, and are mainly star-forming/composite according to the BPT diagram. We use the spatially-resolved BPT diagrams for each of our galaxies to exclude spaxels from our analysis which are classified as composite or LINER. Note that some galaxies are excluded from the left panel if they do not have NUV data in the NSA, and some galaxies are excluded from the right panel if the signal-to-noise is less than 3.0 in any of the relevant emission lines.

we chose the version of these maps made by creating a mask using a smoothed version of the data cubes, and applying this mask to the original (un-smoothed) cubes before integrating. The maps are sampled with $1'' \times 1''$ pixels.

We use optical IFU data from the 3rd data release (DR3) of the CALIFA survey (Sánchez et al. 2012). The CALIFA survey consists of about 600 galaxies observed with the PMAS/PPak integral-field spectrograph at the Calar Alto Observatory (Roth et al. 2005; Kelz et al. 2006). The CALIFA datacubes are available in three spectral setups: (1) a low-resolution setup with 6 Å spectral resolution (V_{500}), (2) a medium-resolution setup with 2.3 Å resolution (V_{1200}), and (3) the combination of V_{500} and V_{1200} cubes (called COMBO). The mean angular resolution of CALIFA is 2.5″, which is similar to SAMI and MaNGA. The maps are sampled with $1'' \times 1''$ pixels. We used the COMBO data cubes from CALIFA DR3 where available. For the 8 CARMA EDGE galaxies with no COMBO datacubes available, we used the V_{500} datacubes instead.

2.2.2 Sample selection

Starting with all 126 CARMA EDGE galaxies, we remove galaxies which are close to edge-on by requiring the minor-to-major axis ratio to be $b/a > 0.3$. For our analysis we need to be able to measure radial profiles of the molecular gas mass density, so we exclude galaxies which are not detected in CO emission, which would prevent us from measuring a radial profile. We use same definition of "detection" as Bolatto et al. (2017), namely a cube which has at least one beam with at least a 5σ detection in at least one velocity bin ($\delta v = 10$ km/s). Furthermore, we remove four galaxies from our sample which are classified as Seyferts according to the SIMBAD

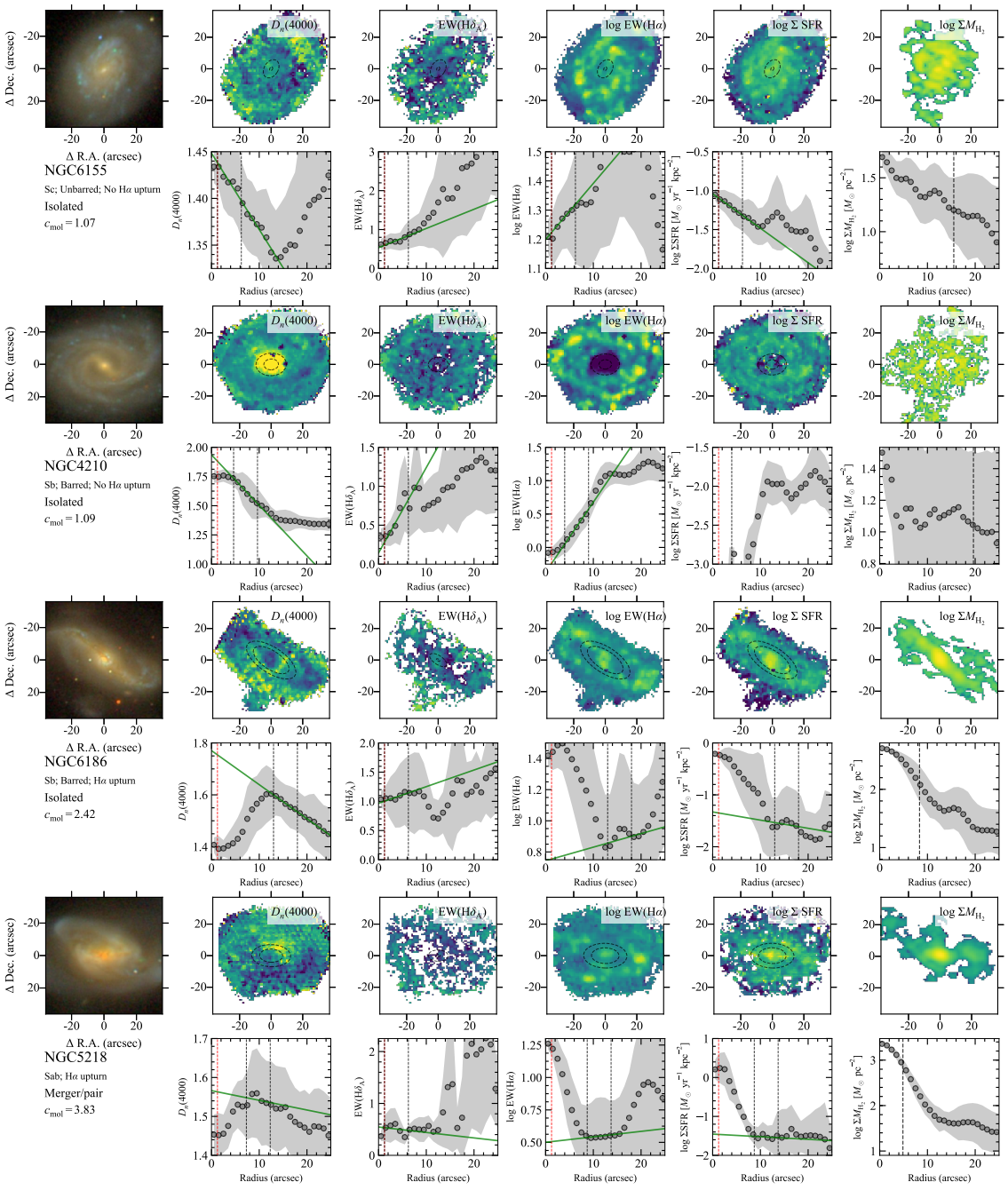

Figure 2.2: (Caption on following page.)

Figure 2.2: (Previous page.) Maps and radial profiles for example galaxies in our sample. For each galaxy, the upper and lower panels on the left show the optical *gri* image from SDSS, the Hubble type and subtype (from CALIFA), an indication of whether it has a central upturn in logEW(Hα) (described in Sec. 2.3.1), and isolated or merger/pair status (described in Sec. 2.2.3). The maps and radial profiles of $D_n(4000)$, EW(Hδ_A), logEW(Hα), log Σ_{SFR}, and log Σ_{H_2} are shown on the right. On each image or map, ellipses are plotted with semi-major axis of the inner and outer regions where the linear fits are performed. The vertical lines in the radial profiles match the corresponding ellipses. The vertical line in the Σ_{H_2} profile is the half-gas-mass radius, which is used to calculate gas concentration; the value of the concentration index is indicated below the *gri* image. The innermost vertical black lines in the middle four panels are determined by eye for each quantity separately ($D_n(4000)$, EW(Hδ_A), logEW(Hα)), and the outermost lines are placed 5″ beyond these lines. The fitting regions are the same for logEW(Hα) and Σ_{SFR}. Any peaks/troughs in the radial profiles at larger radii than where the fitting was performed (e.g. at $\sim$ 12″ in $D_n(4000)$ for NGC 6155) were identified with disk-like structure in the optical images, and so are not classified as the turnover/upturn radii. In the 4 middle radial profiles, if the CALIFA beam half-width at half maximum is smaller than the inner fit radius, it is shown as the red dashed line. The green lines show the linear fits which are done between the two vertical black lines. If no green lines are shown in Σ_{SFR}, the signal-to-noise was insufficient to fit a line to the radial profile. More details can be found in the text.

database, since we suspect such galaxies may have different central star formation properties (and perhaps molecular gas properties) than non-AGN. We remove an additional 6 galaxies which we classify as AGN based on their BPT diagrams. We would like to emphasize that the correlation of nuclear activity with cold gas concentration is an interesting topic by itself, but this is outside the scope of the current paper.

These requirements leave us with 58 galaxies. Some basic properties of the sampled galaxies are listed in Table A1. The galaxies in our sample are located between 24 and 128 Mpc away, or 68 Mpc on average. The angular resolutions of CALIFA ($\sim$2.5″) and CARMA ($\sim$4.5″) at these distances correspond to physical diameters of 0.27-1.5 kpc and 0.5-2.8 kpc respectively. The pixel scale of 1″ corresponds to a physical scale of 0.1-0.6 kpc.

Figure 2.1 shows our sample (blue squares) in the NUV$-r$ vs. log($M_*/M_\odot$) plane on top of

a volume-limited sample ($0.003 \leq z \leq 0.03$) selected from the NASA-Sloan Atlas* (NSA), version 0.1.2. The NUV magnitudes in the NSA catalog are from the *Galaxy Evolution Explorer* (*GALEX*) (Martin et al. 2005), and the stellar masses are estimated by Blanton & Roweis (2007) based on SDSS *ugriz* Petrosian magnitudes; see Blanton et al. (2005a,b, 2011) for details on the NSA. As can be seen, our sample covers a wide range of global properties from the star forming main sequence (the lower part of the plane) through the green valley and into the red sequence, and is roughly representative of the CARMA EDGE survey (the orange circles plus our sample). Compared to the volume-limited sample, galaxies in the EDGE sample have relatively high stellar masses with $M_* \gtrsim 3 \times 10^9 M_\odot$, and are predominately blue or green in colour with some extending into the red sequence. Their mostly-blue NUV$-r$ colours (indirectly) suggests that they have mainly high molecular gas mass fractions according to the tight empirical relation between H_2 mass fraction and NUV$-r$ (Saintonge et al. 2017). This is expected, given the requirement for high 22-μm *WISE* luminosity in the EDGE sample selection.

Figure 2.1 also shows our sample on the Baldwin, Phillips and Terlevich (BPT) diagram (Baldwin et al. 1981). For reference, we show the BPT diagram for a volume-limited sample from the MPA-JHU catalog derived from SDSS DR8 data. For this plot we have measured the fluxes of the four emission lines in the central 3″ of all CARMA EDGE galaxies using the processed CALIFA data. Our galaxies fall mainly in the star-forming and composite regions, with some extending to the LINER region. Compared to the full EDGE sample (orange + blue), our sample lacks Seyfert galaxies which is a consequence of our sample selection as described above. Note that some galaxies are not shown on this diagram, because the signal-to-noise is required

*NSA: http://www.nsatlas.org

to be greater than 3.0 in all four emission lines.

In a later section we analyze the gas content and star formation rate surface density in the nuclei of our galaxies. For that analysis we require at least 50 percent of the pixels in the central 500 pc (radius) to be detected in CO, and not be classified as LINER. 31/58 galaxies from our primary sample satisfy these more stringent requirements. This smaller sample (which we call our "reduced" sample) is used in §2.3.3.

2.2.3 Morphological classification

We visually classify all of the galaxies in our sample (done by the first two authors) as either barred or unbarred, and we cross-check our results with two or three independent classifications from the literature. First, we use the morphological classification by the CALIFA team (Walcher et al. 2014), who classify the galaxies as barred, unbarred, or uncertain. The CALIFA morphological classification is done by-eye by the CALIFA collaboration using *r*- and *i*-band SDSS DR7 images, as described in Walcher et al. (2014). Next, we cross-match our sample with the SIMBAD database (Wenger et al. 2000) to get morphological types and references for each. Additionally, there are 19 galaxies in our sample that overlap with the sample of Lin et al. (2017), who performed a reliable bar classification by applying the IRAF task `ELLIPSE` to the background-subtracted *r*-band images from SDSS. For most galaxies in our sample, these two (or three where available) cross-checks on the bar status agree. Our final classification of barred or unbarred is our best judgment of the CALIFA, SIMBAD, Lin et al. (2017) and our own by-eye classification.

Next, each galaxy is classified as either isolated or interacting with another galaxy (mergers

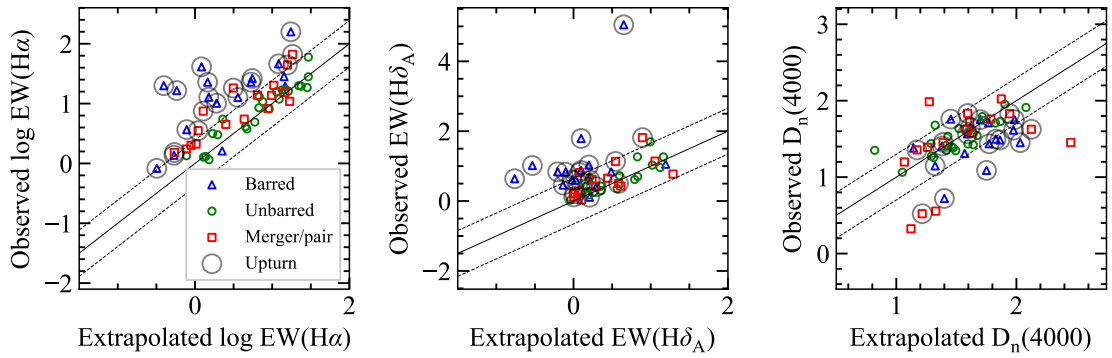

Figure 2.3: Comparison between the observed central value and extrapolated central value of the three star formation history indicators used. In each panel, a 1:1 relation and the 1σ scatter around this relation (not the scatter about the mean) are shown. As in Lin et al. (2017), we define "upturn" galaxies as those which lie above the $+1\,\sigma$ line in the left panel. Upturn galaxies are indicated with grey circles.

or pairs). Galaxies which are classified by the CALIFA team as mergers or isolated are initially put into these two categories. There are a small number of galaxies with uncertain merger status based on their classification. We then cross-check all isolated/merger classifications with the SIMBAD database, which resolves the uncertain cases, and moves some galaxies classified as isolated into the paired category. Galaxies in SIMBAD are classified as interacting if they belong to catalogues of interacting galaxies such as Vorontsov-Velyaminov et al. (2001); galaxies are classified as pairs if they belong to any of the available catalogues of paired galaxies (e.g., Karachentsev 1972; Turner 1976; Barton Gillespie et al. 2003).

We visually examine the SDSS *gri* images of all galaxies classified as pairs, and in a small number of cases, the companion galaxies are too far away to affect the central star formation (greater than $\sim$ 200 kpc as discussed in §2.1, and/or at significantly different redshifts). Such cases are moved into either the isolated barred or isolated unbarred category.

These classifications are used to group the galaxies into three categories: isolated barred, isolated unbarred, and merger/pair/interacting. Note that pair galaxies may be barred or unbarred. In summary, we have 17 isolated barred galaxies, 24 isolated unbarred galaxies, and 17 merger or interacting pair galaxies. The reduced sample mentioned in the previous section consists of 11 barred galaxies, 13 unbarred galaxies, and 7 merger/pair galaxies.

The means and standard deviations of the distances of the barred, unbarred and merger/pair categories are 73 ± 32 Mpc, 66 ± 27 Mpc, and 66 ± 24 Mpc, respectively. Given the similarity of these distributions, we do not expect any distance-related biases to affect the physical resolution of our data. Furthermore, we compare the populations using distance-independent quantities.

2.2.4 Maps and radial profiles of recent SFH diagnostics

We measure three spectral indices, which together tell us the recent SFH for a given spaxel of our galaxies (Bruzual & Charlot 2003; Kauffmann et al. 2003b; Li et al. 2015; Lin et al. 2017):

EW(Hα)— Equivalent width (EW) of the Hα emission line. This quantifies the ratio of the current star formation rate (0-30 Myr; Kennicutt & Evans 2012) to the recent past star formation rate.

EW(Hδ_A)— EW of the Hδ absorption line (the subscript indicates absorption). A strong Hδ_A line indicates a burst of star formation which ended 0.1 to 1 Gyr ago (Kauffmann et al. 2003a).

$D_n(4000)$— The 4000 Å break. This index is sensitive to stellar populations formed 1-2 Gyr ago. In practice, if $D_n(4000) \lesssim 1.6$, there has been star formation in this time frame (Li

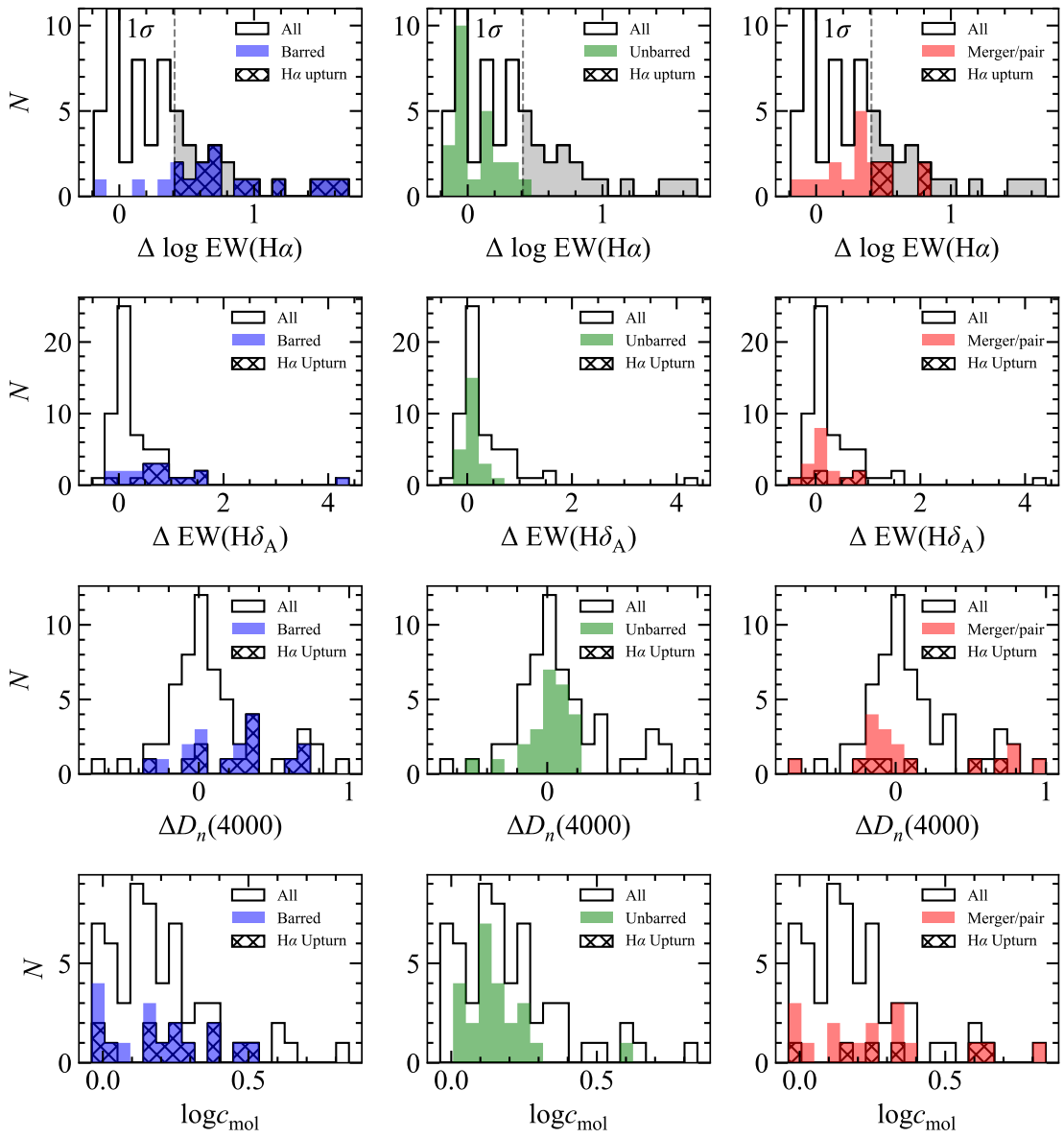

Figure 2.4: Panels from top to bottom are histograms of the logEW(Hα) upturn strength, EW(Hδ_A) upturn strength, D$_n$(4000) turnover strength, and log $c_{\rm mol}$ for barred (blue), unbarred (green) and merger/pair galaxies (red). In each row, the histogram of the corresponding parameter for the full sample is plotted and repeated in the three panels as the black histogram. In the top row the vertical line indicates the 1σ scatter (0.410 dex) of all the points from the 1:1 relation of the observed value of log EW(Hα) at the center to the extrapolated value. Galaxies with Δ logEW(Hα) $\geq$ σ (those lying above the $+1\sigma$ line in Fig. 2.3) are classified as having a central upturn (shown in the grey histogram in the top panels). The distribution of the upturn galaxies in each panel is plotted as the hatched histogram. This figure immediately shows that the upturn galaxies are either barred or mergers/pairs, and none of the unbarred galaxies have an logEW(Hα) upturn.

et al. 2015).

For each galaxy in our sample, we perform full spectral fitting to each spaxel in the CALIFA DR3 COMBO data cube (or V_{500} for the few galaxies which do not have COMBO datacubes), using the Penalized Pixel-Fitting code[†] (pPXF) (Cappellari & Emsellem 2004; Cappellari 2017). The Bruzual & Charlot (2003) simple stellar populations (SSP) and the Calzetti et al. (2000) reddening curve were used during the fitting. The result of the full spectral fitting is a best-fit model spectrum representing the stellar component of the spaxel (continuum plus absorption lines) which is a linear combination of the SSPs, plus a color excess $E(B-V)$ quantifying the overall dust extinction. Both the observed spectrum and the model spectrum are corrected for dust extinction according to this $E(B-V)$. The equivalent width of H$\delta_{\rm A}$ and D$_n$(4000) are then measured from the model spectrum. In addition, we obtain the luminosity-weighted age of the spaxel based on the luminosity and coefficient of the SSPs that form the best-fit spectrum.

The model spectrum is then subtracted from the observed one, and we measure both the dust-corrected flux and the equivalent width for the Hα emission line. We correct for the dust extinction based on the Balmer Decrement measured from the observed spectrum. For this we have assumed a temperature of 10^4 K, an electron density of 10^2 cm^{-3} in the H II regions, an intrinsic Hα-to-Hβ flux ratio of 2.86 in case-B recombination (Osterbrock & Ferland 2006), as well as a Calzetti et al. (2000) reddening curve. The dust-corrected Hα flux is converted to a luminosity using the distance assuming the adopted cosmological parameters §2.1. A star forma-

[†] http://www-astro.physics.ox.ac.uk/~mxc/software

tion rate (SFR) is then estimated by multiplying the Hα luminosity by $5.3 \times 10^{-42} M_{\odot}$ yr^{-1} (erg s^{-1})$^{-1}$ as in Murphy et al. (2011); Hao et al. (2011); Kennicutt & Evans (2012). This SFR calibration adopts the stellar initial mass function (IMF) from Kroupa & Weidner (2003).

We compute radial profiles of each quantity by azimuthally averaging the maps in elliptical annuli separated by 1″ along the semi-major axis. The position angles and minor-to-major axis ratios are taken from the CALIFA DR3 supplementary tables (Walcher et al. 2014). Partial pixel overlap within each annulus is taken into account, and pixels with signal-to-noise ratio less than 1 are set to zero in the averages. Using a 1σ value instead of zero does not significantly affect the radial profiles at the radii used in our analysis. The SDSS *gri* images and the processed maps of $D_n(4000)$, EW(Hδ_A) and logEW(Hα), as well as their radial profiles are shown in Figure 2.2 for four example galaxies from our sample: an unbarred galaxy in the top (NGC6155), followed by two barred galaxies (NGC4210 and NGC6186) and a merging galaxy (NGC5218). The first two galaxies present similar radial profiles in the recent SFH indicators in the sense that, from galactic center to larger radii, $D_n(4000)$ decreases while both logEW(Hα) and EW(Hδ_A) increase. This radial profile shape indicates a relatively old stellar population in the inner region, and less star formation in the recent past in this region. Large samples of IFU observations such as MaNGA have shown that radial profiles like this are typical for the general population of galaxies in the local Universe, although the amplitudes and slopes of the profiles depend on galaxy stellar mass (e.g. Wang et al. 2018).

Different from the top two galaxies in Figure 2.2, the bottom two galaxies in the same figure show a significant upturn in logEW(Hα) and/or a significant turnover in $D_n(4000)$ in their

innermost region, indicating star formation has been recently enhanced in the central region. Galaxies with a central turnover in $D_n(4000)$ were called "turnover" galaxies in Lin et al. (2017). Those authors found that almost all turnover galaxies are barred. We note that the two galaxies in Figure 2.2 with a turnover feature are a barred galaxy and a merger.

2.2.5 Maps and radial profiles of molecular gas mass

We take the integrated flux CO $J = 1 \rightarrow 0$ maps from the public CARMA EDGE data release, convert them from their native units of Jy km/s beam^{-1} to K km/s, and then convert to H_2 gas mass surface densities Σ_{H_2} in units of $M_\odot$ pc^{-2} by assuming a constant CO-to-H_2 conversion factor $\alpha_{CO} = 3.1\ M_\odot\ \mathrm{pc}^{-2}\ (\mathrm{K\ km/s})^{-1}$ (Bolatto et al. 2013; Sandstrom et al. 2013). The α_{CO} conversion factor has been found to be lower by a factor of about 2 (i.e. $\alpha_{CO} = 1.55 M_\odot\ \mathrm{pc}^{-2} (\mathrm{K\ km/s})^{-1}$) in the central kpc of nearby galaxies (Sandstrom et al. 2013). For simplicity, we adopt $\alpha_{CO} = 3.1\ M_\odot\ \mathrm{pc}^{-2}\ (\mathrm{K\ km/s})^{-1}$ but we do consider the impact of the central α_{CO} on our results in later sections. Radial profiles of Σ_{H_2} for our sample are computed in the same way as in the previous section. Pixels without CO detections are set to zero in the averages. As a result, Σ_{H_2} is slightly underestimated at large radii where the fraction of detected pixels is small. However, the fraction of missing flux in the CO maps is small, so this is a good approximation to the true radial profiles (Bolatto et al. 2017). Maps and radial profiles of Σ_{H_2} for our example galaxies are shown in the right-most column in Figure 2.2.

2.3 Central star formation and the link to gas concentration

Table 2.1: Mean molecular gas concentrations and upturn/turnover strengths for our full sample

Category	N [a]	$\log c_{\rm mol}$ [b] (dex)	$\Delta \log \mathrm{EW}(\mathrm{H}\alpha)$ [c] (dex)	$\Delta \mathrm{EW}(\mathrm{H}\delta_{\mathrm{A}})$ [d] (Å)	$\Delta \mathrm{D_n}(4000)$ [e]
			Barred		
All	17	0.19 ± 0.04	0.75 ± 0.12	0.88 ± 0.26	0.20 ± 0.07
Upturn	13	0.23 ± 0.05	0.92 ± 0.12	1.13 ± 0.30	0.26 ± 0.08
No upturn	4	0.05 ± 0.04	0.17 ± 0.12	0.08 ± 0.10	0.01 ± 0.10
			Unbarred		
All	24	0.17 ± 0.02	0.06 ± 0.03	0.08 ± 0.04	-0.00 ± 0.03
Upturn	0	...	...	...	...
No upturn	24	0.17 ± 0.02	0.06 ± 0.03	0.08 ± 0.04	-0.00 ± 0.03
			Merger/pair		
All	17	0.27 ± 0.06	0.32 ± 0.06	0.18 ± 0.08	0.13 ± 0.11
Upturn	6	0.32 ± 0.10	0.58 ± 0.06	0.41 ± 0.16	0.14 ± 0.16
No upturn	11	0.23 ± 0.07	0.18 ± 0.05	0.04 ± 0.07	0.13 ± 0.15

[a] Number of galaxies in category.
[b] Mean and uncertainty on the mean of the molecular gas concentration index (Eq. 2.3).
[c] Mean and uncertainty on the mean of the logEW($\mathrm{H}\alpha$) upturn strength (Eq. 2.1).
[d] Mean and uncertainty on the mean of the EW($\mathrm{H}\delta_A$) upturn strength (Eq. 2.1).
[e] Mean and uncertainty on the mean of the $\mathrm{D}_n(4000)$ turnover strength (Eq. 2.2).

2.3.1 Recent central star formation enhancement

Our identification and measurement of centrally elevated star formation is similar to the procedure described in Lin et al. (2017). First we calculate radial profiles of logEW(Hα), EW(Hδ_A), $D_n(4000)$, and log $\Sigma_{\rm SFR}$, and plot them next to the *gri* composite image from SDSS. We then inspect each profile in the inner region of each galaxy (inside of the spiral arms), and judge whether or not the central region shows an *upturn* (for logEW(Hα), EW(Hδ_A) and log $\Sigma_{\rm SFR}$) or a *drop* (for $D_n(4000)$) in the slope of the profile in the innermost region. The inner region corresponds to a by-eye estimate of the radius of the transition between bulge and disk. Note that Lin et al. (2017) had performed photometric decomposition on the optical images, allowing for a precise measurement of these radii, but we do not have that information for all galaxies in our sample so we estimate the inner region by eye. The by-eye estimate of the inner radius is not used in the following analysis. If such an upturn or turnover is identified, we mark by eye the radius at which it occurs.

Next, for each galaxy, and for a given star formation history indicator, we fit a line to the radial profile between $r = r_t$ and $r = r_t + 5''$, where r_t is the turn-up/turnover radius determined by eye in the first step. This is what was done in Lin et al. (2017). Those authors found that this radial range provided a sufficient fit to the general profile in the inner region without being contaminated by spiral arms or the transition region. For radial profiles which are not visually classified as having an upturn/turnover, we still perform the linear fitting, but we set r_t to half of the point-spread function (PSF) size of CALIFA (roughly 1.25″; Walcher et al. 2014). In Figure 2.2, the linear fits are plotted as green solid lines for the four example galaxies. In each panel

the radial range used for the linear fitting is indicated by the two vertical, dotted lines. By our definition, the value of logEW(Hα) or EW(Hδ_A) at the center may be lower than where the fitting is performed (e.g. the logEW(Hα) profiles of NGC4210 in Fig. 2.2), or it may be greater (as in the logEW(Hα) profiles of NGC6186 and NGC5218 in Fig. 2.2). In either of these scenarios, the value of the SFH indicator in the center is greater than expected from extrapolating the linear fit to the center.

The upturn/turnover strength of each galaxy, for each of the star formation history indicators, is then quantified by the difference between the observed and extrapolated value in the central region, as measured above. Specifically, for logEW(Hα), EW(Hδ_A) and log $\Sigma_{\rm SFR}$, the upturn strength is defined as

$$\Delta Y \equiv Y(r=0) - Y_{\rm extrap}(r=0), \tag{2.1}$$

where $Y(r=0)$ is the value of Y in the central radial bin, and $Y_{\rm extrap}(r=0)$ is the best-fit line extrapolated to $r=0$. For D$_n$(4000), the turnover strength is defined as

$$\Delta D_n(4000) \equiv D_n(4000)_{\rm extrap}(r=0) - D_n(4000)(r=0). \tag{2.2}$$

Note that larger values of $\Delta D_n(4000)$ (ΔY) correspond to stronger turnovers (upturns). The upturn and turnover strengths of each galaxy in our sample are listed in Table A2.

In Figure 2.3, which shows the central observed value of each star formation history indicator compared to the value of the line extrapolated to the center for all the galaxies in our sample.

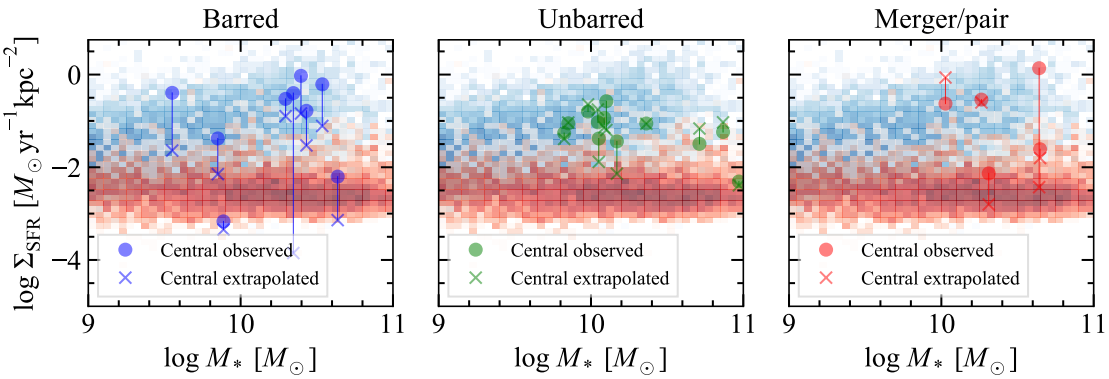

Figure 2.5: Observed central average (in the inner 3″) of log Σ_{SFR} (circles) and the linear fit extrapolated to the center (crosses) as a function of stellar mass in the SDSS fiber (provided in CALIFA DR3). The galaxies shown in this plot are a subset of our reduced sample (§2.2.2) for which we can perform linear fitting to the radial profiles of Σ_{SFR}. The blue background population are galaxies lying within 0.5 dex of the star-forming main sequence (SFMS; Catinella et al. 2018), and the red background population are galaxies more than 0.7 dex below the SFMS. We have converted the SDSS fiber SFRs to surface densities by dividing by the physical area of the fiber in kpc^2. This figure shows that bars are linked to increases in the central star formation rate surface density.

Barred, unbarred and merging/paired galaxies are plotted as blue triangles, green circles and red squares, respectively. The 1:1 relation represents no difference between the observed and extrapolated values. We divide our galaxies into two sets (those with or without an upturn in logEW(Hα)) by comparing the observed value of the logEW(Hα) profile at $r = 0$ with the value of the fitting line extrapolated to $r = 0$. A galaxy is classified as having an upturn if it lies above the 1:1 relation (the solid line) plus the 1 σ scatter (the dotted lines) on the left panel of Figure 2.3. The scatter is the standard deviation of all points with respect to the 1:1 line. We note that turnover/non-turnover galaxies in Lin et al. (2017) were divided in the same way but using D$_n$(4000) rather than logEW(Hα).

Figure 2.4 shows histograms of the upturn and turnover strengths of our sample, for three

of the star formation history indicators: Δ logEW(Hα), ΔEW(Hδ_A), and ΔD$_n$(4000). Results are shown for the barred (red), unbarred (green) and paired/merging (red) galaxies separately in panels from left to right. The separating value of Δ logEW(Hα) $=$ 0.410 dex, which is determined from the scatter of the points about the 1:1 relation in Fig. 2.3, is shown as the vertical dashed line in the top row of Fig. 2.4. In the second and third rows of the same figure, we show the distributions of our sample in logEW(Hδ_A) and D$_n$(4000), highlighting the logEW(Hα)-upturn galaxies as hatched histograms. The mean and uncertainty on the mean upturn strengths from each SFH indicator are shown in Table 2.1.

Both Figure 2.3 and Figure 2.4 show that none of the unbarred galaxies in our sample are classified as having a logEW(Hα) upturn. The majority of the upturn galaxies are barred (13/19), followed by mergers and pairs (6/19). On the other hand, not all of the barred or paired/merging galaxies have upturns. This result suggests that either a bar or galaxy-galaxy interactions/mergers is necessary, but neither alone is sufficient for the central upturn to occur. In agreement with Lin et al. (2017), we find that most galaxies classified as having a central upturn in logEW(Hα) also have a relatively strong EW(Hδ_A) upturn and D$_n$(4000) turnover. These results suggest an enhancement in both the recent and ongoing star formation at the center of the upturn galaxies.

In Figure 2.5 we compare the central-observed and central-extrapolated log $\Sigma_{\rm SFR}$ as a function of global stellar mass for barred (left panel), unbarred (middle panel) and merger/pair (right panel) galaxies. The galaxies shown in this plot are a subset of our reduced sample (§2.2.2) for which we can perform linear fitting to the radial profiles of $\Sigma_{\rm SFR}$. For reference, in each

panel we show the distribution of the volume-limited galaxy sample selected from the MPA/JHU SDSS database (see above), for which the SFR is measured from the SDSS 3″-fiber spectroscopy. We find that barred galaxies generally have observed values of $\Sigma_{\rm SFR}$ that are significantly higher than expected (by ∼0.5-2 dex), effectively bringing the central $\Sigma_{\rm SFR}$ from values that would be typical of the quiescent population or green valley, up into the star-forming main sequence. For unbarred galaxies, we see little change in the central SFR surface density, as expected. Overall, these results are consistent with the theoretical expectation that the central region may be rejuvenated by star formation enhancement driven by a bar. The merger/pair galaxies appear to either have no enhancement or centrally suppressed star formation, however, this is not representative of merger/pair galaxies as a whole due to the selection cuts.

2.3.2 Recent central star formation vs. molecular gas concentration

Figure 2.6 displays the H_2 gas mass surface density profiles $\Sigma_{\rm H_2}(r)$ for barred (left), unbarred (middle) and merger/pair galaxies (right), and for the subsets of upturn galaxies (upper panels) and non-upturn galaxies (lower panels), as classified above. In this figure we have normalized each profile to the value of $\log \Sigma_{\rm H_2}$ at $r = 0.75r_{50}$, and have scaled the radius r by r_{50}. In each panel we also show the mean profile and the standard deviation around the mean.

The upturn galaxies on average show a centrally-peaked molecular gas profiles. The peak value of the normalized gas profiles relative to $0.75r_{50}$ is $\sim$ 1 dex for upturn galaxies and all merger/pairs, vs. $\sim$ 0.5 dex for unbarred galaxies. Almost all of the non-upturn barred or unbarred galaxies have a molecular gas profile without a central peak. Also, some galaxies show unusual profiles, deviating to varying degrees from the average profile of their type. These out-

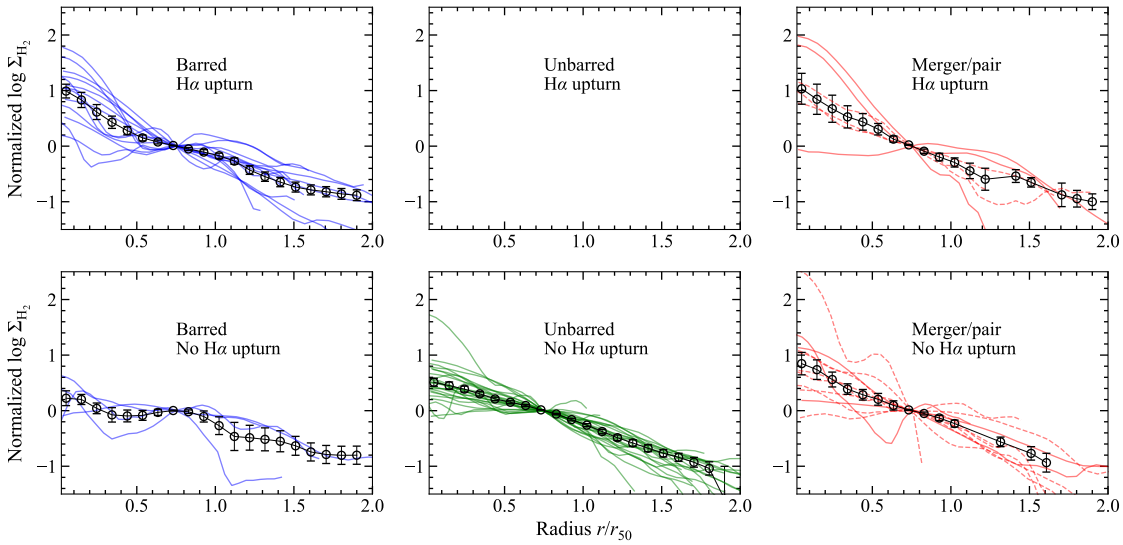

Figure 2.6: Azimuthally-averaged radial profiles of H_2 mass surface density for all galaxies in our sample. Each profile of $\log \Sigma_{H_2}$ has been normalized to the value at $0.75r_{50}$. In the top row, we show galaxies that have been identified as having a central upturn in logEW(Hα) (see Sec. 2.3.1); and in the bottom row are galaxies with no central upturn. Note that the upper middle plot is empty because there are no unbarred galaxies in our sample which show an logEW(Hα) upturn. In each panel, the black circles and error bars are the mean and error in the mean of the profiles in each radial bin. The black profiles show that barred galaxies, mergers and pairs with logEW(Hα) upturns have centrally-peaked profiles with a steeper slope at $r \lesssim 0.5r_{50}$, while non-upturn barred and unbarred galaxies tend to have flatter profiles at these radii. In the right column, barred merger/pair galaxies are shown as solid lines, while unbarred/irregular merger/pairs are shown as dashed lines.

lier galaxies are interesting targets for individual follow-up work.

We measure a molecular gas concentration index for each of our galaxies, defined by

$$c_{\rm mol} \equiv \frac{r_{50}}{r_{50,\rm mol}}, \tag{2.3}$$

where r_{50} is the half-light radius in the SDSS r-band, obtained from the NSA, and $r_{50,\rm mol}$ is the radius enclosing half of the total molecular gas mass. This definition of concentration is similar to the optical concentration index which is commonly used in the SDSS-based studies and defined as $c_r \equiv r_{90}/r_{50}$, where r_{90} is the radius enclosing 90% of the r-band light. A larger value of $c_{\rm mol}$ indicates a higher central concentration of gas mass.

The molecular gas half-mass radius was used in early single-dish surveys such as Young et al. (1995), and was estimated for many but not all (38/58) of the galaxies in our sample by the EDGE-CALIFA team (Bolatto et al. 2017). For completeness, we redo the measurements for all 58 galaxies in our sample. We measure $r_{50,\rm mol}$ by computing the cumulative molecular gas mass radial profile (in linear units, not logarithmic), and determine the radius at which the enclosed mass equals half of the total H_2 mass. We have adopted two different methods to measure the total H_2 mass. In the first method, which is our fiducial method, we ignore non-detections and estimate the total H_2 mass by the sum of the detected pixels. In the second method, we include non-detections as 1σ upper-limits, where σ is the RMS noise in each pixel, obtained from the unmasked CARMA EDGE integrated flux maps. In this case the H_2 mass in each radial bin is the sum of the detections and non-detections, unless the fraction of detected pixels in that bin is less than 0.05, as was done in Mok et al. (2017) when measuring the radial profiles of H_2 for

galaxies in the NGLS (Wilson et al. 2012). In both methods, the enclosed mass as a function of radius is given by the integral of the radial profile of M_{H_2}, and is used to determine the half-mass radius. We find that the two methods lead to almost identical measurements, indicating that non-detection pixels contribute little to the total H_2 mass.

All values of $c_{\rm mol}$ are computed using the first method. Two of the galaxies in the merger/pair category have $r_{50,\rm mol}$ that is $< 2\times$ the CARMA resolution, so we have quoted their concentrations as lower limits. The rest of our galaxies have $r_{50,\rm mol}$ which is significantly larger than the CARMA resolution. The bottom panel of Figure 2.4 shows the distribution of molecular gas concentrations for our sample as a whole and for the subsamples of barred, unbarred and merger/paired galaxies separately. The molecular gas concentrations of the galaxies in our sample are also listed in Table A2.

We have also compared our $r_{50,\rm mol}$ with those of Bolatto et al. (2017), and find the two to agree well, with no systematic differences. The mean absolute differences in $r_{50,\rm mol}$ are 1.6″ and 1.8″ for the two methods adopted in our case, comparable to the 1″ pixel size. In Sheth et al. (2005) the total H_2 masses were obtained from single-dish CO measurements, while the nuclear H_2 mass were obtained from spatially resolved CO maps. We do not have single-dish CO data, but, as discussed in Bolatto et al. (2017), the total flux in the CARMA EDGE maps matches well with expectations based on single-dish CO calibrations from Saintonge et al. (2011). We have also investigated the potential impact of a central drop in the CO-to-H_2 conversion factor $\alpha_{\rm CO}$ in our analysis, and find that the change in $c_{\rm mol}$ is negligible.

In Table 2.1 we show the mean and error on the mean of $\log c_{\rm mol}$ for barred, unbarred, and

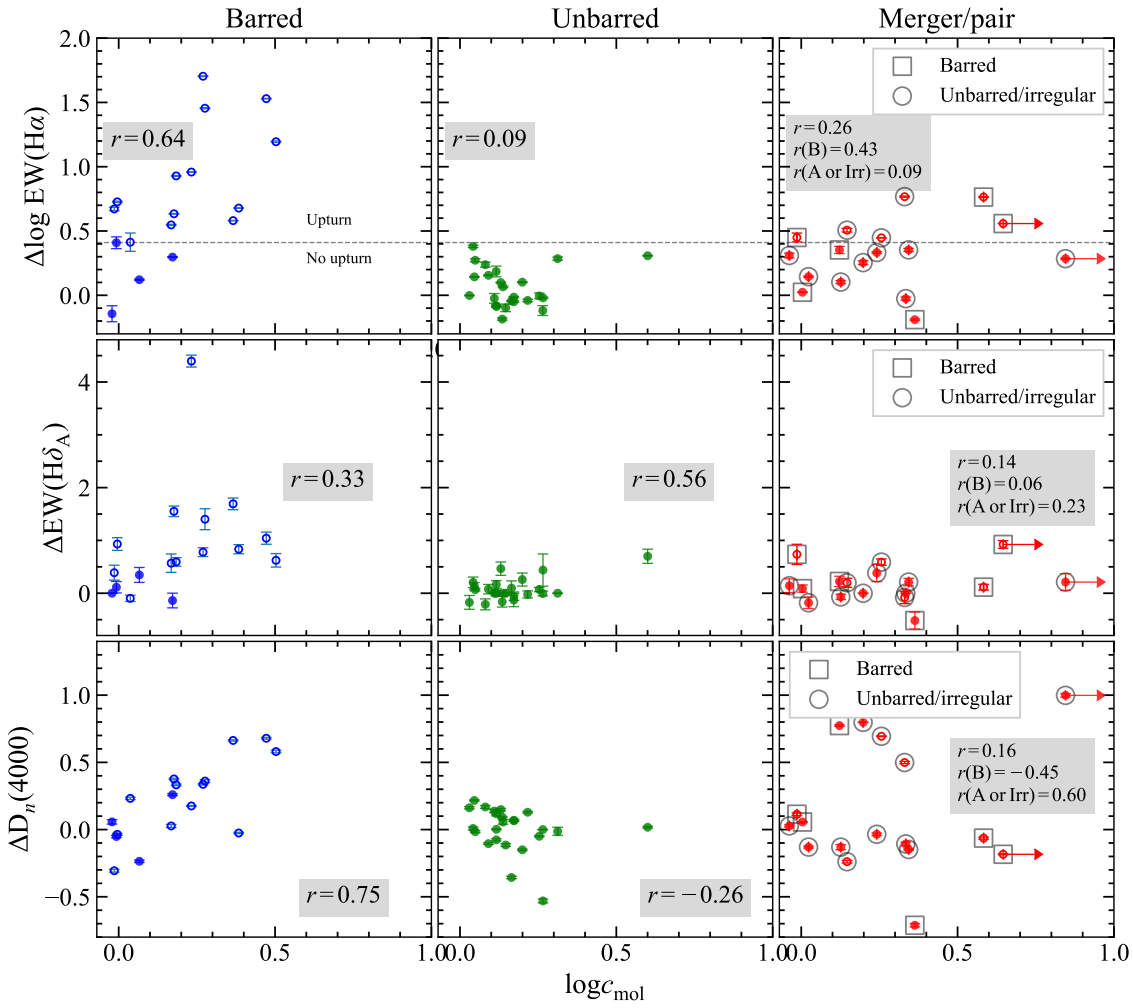

Figure 2.7: log EW(Hα) upturn strength *(top row)*, EW(Hδ_A) upturn strength *(middle row)*, and $D_n(4000)$ turnover strength *(bottom row)* as a function of molecular gas concentration. The open points are those which are classified as having a central logEW(Hα) upturn (see Sec. 2.3.1), while the filled symbols have no upturn. The error bars are the uncertainties on the measured central value of the SFH indicator. The value of Δ logEW(Hα) which divides these two categories is shown by the horizontal line in the top row. The Pearson correlation coefficient r is shown for each panel. This figure shows our main result: galaxies which show centrally enhanced recent star formation are either barred or in a merger/pair, and on average have higher gas concentrations.

merger/pair galaxies. We have calculated these quantities for all galaxies in each category, and the upturn/non-upturn galaxies separately. Galaxies with an upturn (barred or merger/pair) have significantly higher concentrations than unbarred galaxies. Barred galaxies without an upturn have significantly lower concentrations than all other categories. Interestingly, merger/pair galaxies without an upturn have relatively high gas concentrations, which are consistent on average with those with an upturn. These results show that, in order to have an upturn, it is not enough to be a merger/pair with high molecular gas concentration.

In Figure 2.7 we examine the correlation of central star formation enhancement with molecular gas concentration, by showing the Δ logEW(Hα) (first row), ΔEW(Hδ_A) (second row), and ΔD$_n$(4000) (third row) as a function of log $c_{\rm mol}$ for the three main categories (barred, unbarred, and merger/pairs). The Pearson correlation coefficients shown in Fig. 2.7 show that the strongest correlations are between log ΔEW(Hα) and log $c_{\rm mol}$ for barred galaxies, and between ΔD$_n$(4000) and log $c_{\rm mol}$ for barred galaxies. There also appears to be some correlation between ΔEW(Hδ_A) and log $c_{\rm mol}$ for unbarred galaxies. There does not appear to be a significant correlation between upturn strength and concentration in other panels. The lack of correlation between central SF enhancement and $c_{\rm mol}$ in merger/pair galaxies may be suggesting that the enhancement may be episodic. It is interesting that there are some merger/pair galaxies with significant enhancements in D$_n$(4000) but not in EW(Hδ_A) or logEW(Hα) and with relatively low gas concentrations.

Here we briefly remark on why we did not measure a concentration index like $c_{\rm mol}$ for the SFH indicators. The gas concentration is a proxy for how much gas has been transported in-

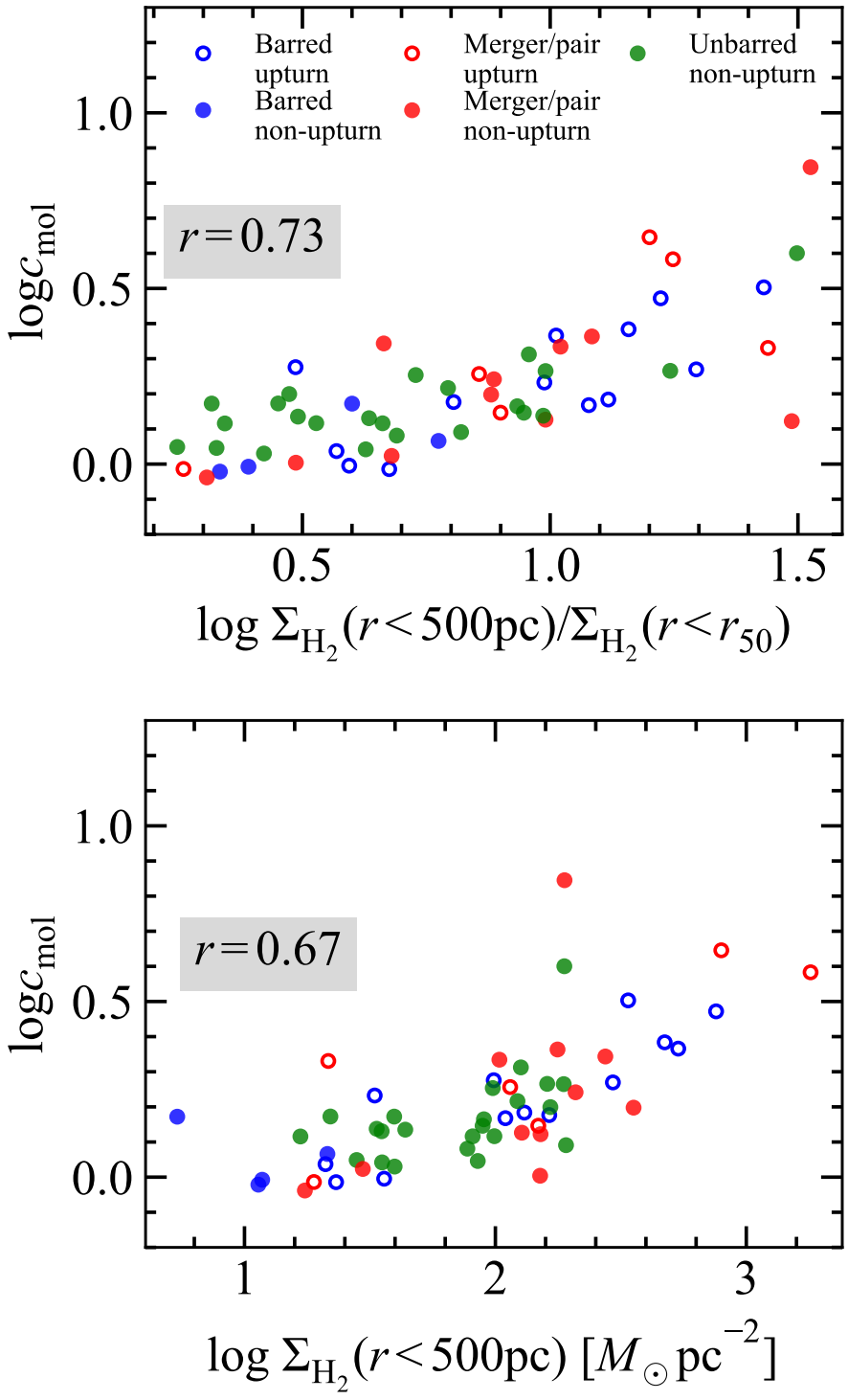

Figure 2.8: *Top:* Correlation between molecular gas concentration and the concentration defined by Sheth et al. (2005), namely Σ_{H_2} calculated in the central 1 kpc divided by Σ_{H_2} calculated over the whole CO disk (which is approximately r_{50}). *Bottom:* Correlation between molecular gas concentration and Σ_{H_2} calculated in the central 1 kpc. The Pearson correlation coefficient r using all galaxies is shown in both panels.

wards. Generally, the gas radial profiles are either flat or with a central peak. This could possibly be due to the lower resolution of the CO data. The case for the SFH indicators is more complex – there are cases where there is clearly a central peak/drop in SFH indicators, but this is sometimes a local peak or drop. A concentration index is sensitive to where most of the gas or SF is happening, and would not pick out a central peak if it is a local one. This problem could be alleviated by calculating a concentration within the inner region only, however this would require a by-eye estimation of the radius of the inner regions since we have not performed photometric decomposition. This is why we decided to measure upturn strengths on the central region specifically.

Now we assess whether such correlations may be due to our particular definition of molecular gas concentration. The top panel of Figure 2.8 shows the comparison between our concentration parameter and an alternative definition from Sheth et al. (2005), namely Σ_{H_2} in the central kiloparsec divided by the total Σ_{H_2}. In their analysis, the total Σ_{H_2} was obtained from single-dish CO measurements, whereas we measure it from the CARMA CO maps. Specifically, we measure the total H_2 mass within r_{50} and divide by the area of the corresponding ellipse. The Pearson correlation coefficient between these quantities is 0.73, indicating a good correlation. Thus, if we were to use this alternative concentration in our analysis, our results would not change significantly. The lower panel of Fig. 2.8 shows our concentration versus Σ_{H_2} calculated in the central kpc (500 pc radius). Again, the correlation coefficient of 0.67 suggests a significant correlation, and our results would also not change significantly if we were to use Σ_{H_2} in the central kpc in place of $c_{\rm mol}$.

We do not find significant correlations between $c_{\rm mol}$ and parameters which quantify the global properties of a galaxy, namely global stellar mass (from the NSA; $r = 0.16$), NUV$-r$ colour (from the NSA; $r = 0.29$), optical concentration (r_{90}/r_{50}, from the NSA; $r = 0.41$), H_2 mass fraction (M_{H_2}/M_*; $r = 0.33$), or H I mass fraction using H I measurements from the ALFALFA 100% catalog (Haynes et al. 2018) or the HyperLeda database (Makarov et al. 2014) ($r = -0.23$). We find a slight correlation between $\log c_{\rm mol}$ and H_2-to-H I mass ratio ($r = 0.48$). In a sense, this quantity is also a gas concentration, because it is a measure of the gas mass in a small area (H_2 tends to be more centrally concentrated) divided by the gas mass in a large region (H I is known to have a larger spatial extent than H_2), so this tentative correlation is not surprising. These results indicate that the gas concentration is indeed caused by bars or mergers, an effect which is independent of galaxy mass, global color or light concentration.

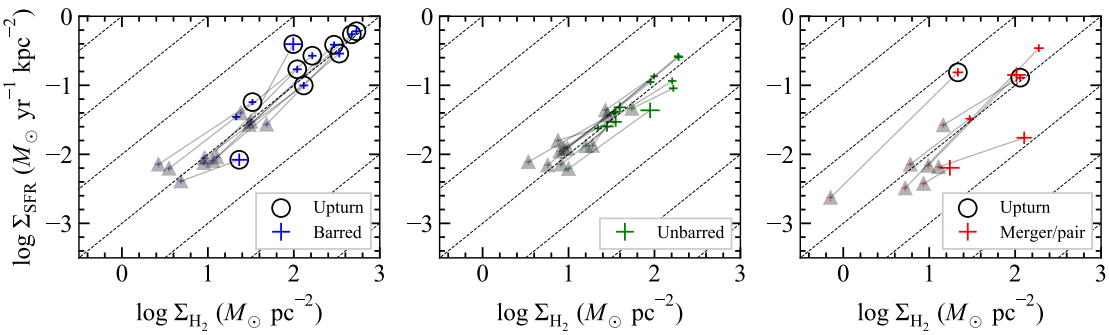

Figure 2.9: log Σ_{SFR} vs. log Σ_{H_2} in the central 0.5 kpc (in semi-major axis; coloured symbols) and over annuli covering 0.5kpc $< r \leq r_{50}$ (in semi-major axis; grey triangles). These two are connected by lines for each galaxy. There are fewer galaxies shown here than in Fig. 2.6 because here we are using the reduced sample, described in §2.2.2 and §2.2.3. Galaxies classified as having a logEW(Hα) upturn are identified with black open circles. The same (Galactic) CO-to-H_2 conversion factor was used for all points – if a lower α_{CO} were used in the central kpc, the central points would shift leftward by 0.3 dex. The diagonal lines indicate constant H_2 depletion times. This plot shows where barred/unbarred/interacting and upturn/non-upturn galaxies lie in terms of their *absolute values* of log Σ_{SFR} and log Σ_{H_2}. It is clear that barred galaxies extend to higher Σ_{SFR} and Σ_{H_2} in the central region than unbarred galaxies. The mean and uncertainty on the mean for each parameter are shown in Table 2.2.

Table 2.2: Mean surface densities of H_2 and SFR, and depletion times for our reduced sample (described in §2.2.2)

Upturn? [a] (Y/N)	N [b]	$\log \Sigma_{H_2}$ [c] ($M_\odot pc^{-2}$)		$\log \Sigma_{SFR}$ [d] ($M_\odot yr^{-1} kpc^{-2}$)		$\log \tau_{depl.}$ [e] (yr)		$\log(\tau_{cen.}/\tau_{disk})$ [f] (dex)
		Center	Disk	Center	Disk	Center	Disk	
Barred								
Y	10	2.16 ± 0.15	1.12 ± 0.12	-0.75 ± 0.18	-1.89 ± 0.11	9.05 ± 0.09	9.15 ± 0.06	-0.10 ± 0.09
N	1	1.33 ± 0.04	0.55 ± 0.04	-1.46 ± 0.05	-2.21 ± 0.04	8.92 ± 0.07	8.89 ± 0.06	0.03 ± 0.09
Unbarred								
Y	0	...	...	...	...	...		
N	13	1.84 ± 0.10	1.08 ± 0.09	-1.17 ± 0.10	-1.85 ± 0.08	9.14 ± 0.04	9.06 ± 0.05	0.07 ± 0.04
Merger/pair								
Y	2	1.70 ± 0.36	0.51 ± 0.66	-0.83 ± 0.42	-2.10 ± 0.53	8.68 ± 0.40	8.74 ± 0.13	-0.06 ± 0.27
N	5	1.82 ± 0.20	0.91 ± 0.07	-0.93 ± 0.32	-2.28 ± 0.07	9.31 ± 0.21	9.32 ± 0.07	-0.02 ± 0.18

Note: a Galactic α_{CO} was assumed, and a 10% calibration uncertainty is included in both Σ_{H_2} and Σ_{SFR}.
Here, "center" refers to $r < 500$ pc, and "disk" refers to 500 pc $\leq r \leq r_{50}$.
[a] Galaxies which have an upturn in logEW(Hα) or not.
[b] Number of galaxies in category.
[c] Mean and uncertainty on the mean of $\log \Sigma_{H_2}$ in the center and disk.
[d] Mean and uncertainty on the mean of $\log \Sigma_{SFR}$ in the center and disk.
[e] Mean and uncertainty on the mean of $\log \tau_{depl.}$ (Eq. 2.4) in the center and disk.
[f] Mean and uncertainty on the mean of the center-to-disk depletion time ratio.

2.3.3 Linking central star formation enhancement with molecular gas mass profiles

For another perspective, rather than comparing the *relative* enhancement in star formation history indicators between barred/unbarred and merger/pair categories, here we compare the absolute values of $\log \Sigma_{\rm SFR}$ and $\log \Sigma_{\rm H_2}$ in these categories. For this analysis we have used the reduced sample (31 galaxies) described in §2.2.2. Figure 2.9 shows $\log \Sigma_{\rm SFR}$ and $\log \Sigma_{\rm H_2}$ for barred (left), unbarred (middle), and merger/pair galaxies (right). For each galaxy we show the means and uncertainties of these surface densities, calculated in the central kpc (500 pc radius, shown as the coloured symbols) and in the disk ($r \leq r_{50}$, triangles). The uncertainties include measurement errors as well as a 10% calibration uncertainty in each quantity. A Galactic $\alpha_{\rm CO}$ was used for all points.

We use these measurements to compute molecular gas depletion times

$$\tau_{\rm depl.} \equiv \frac{\Sigma_{\rm mol}}{\Sigma_{\rm SFR}}, \tag{2.4}$$

where $\Sigma_{\rm mol} = 1.36\Sigma_{\rm H_2}$ (where the factor of 1.36 accounts for the presence of helium). We have measured the mean and uncertainty on the mean of $\log \Sigma_{\rm H_2}$, $\log \Sigma_{\rm SFR}$, $\log \tau_{\rm depl.}$, and $\log(\tau_{\rm cen.}/\tau_{\rm disk})$, all of which are shown in Table 2.2. The measurements for each galaxy are given in Table A2. Table 2.2 shows that barred galaxies with an upturn have a slight drop in depletion time in their centers compared to their disks, while unbarred galaxies have a slight central rise in depletion time. Although $\alpha_{\rm CO}$ in the central kpc may be lower by a factor of 2

(Sandstrom et al. 2013), this would shift all $\log(\tau_{\rm cen.}/\tau_{\rm disk})$ lower by 0.3 dex, without changing their uncertainties. This would turn the central rise in $\tau_{\rm depl.}$ for unbarred galaxies into a slight drop, but would turn the drop for barred galaxies into an even larger drop. However, the *relative* value of these quantities between the barred, unbarred and merger/pair categories should not be affected by such variations in $\alpha_{\rm CO}$.

We would like to emphasize that due to the small number statistics here, we do not interpret these findings as strong evidence. The best statistical comparison we can make is between barred upturn galaxies and unbarred galaxies – we find $\log(\tau_{\rm cen.}/\tau_{\rm disk})$ is lower in barred upturn galaxies than unbarred galaxies by 0.17 ± 0.10 dex. Merger/pair galaxies do not show a statistically significant increase or decrease in depletion times in their centers on average, but from Fig. 2.9, one can see that some of these galaxies have $\log(\tau_{\rm cen.}/\tau_{\rm disk}) \leq 0$, while others have $\log(\tau_{\rm cen.}/\tau_{\rm disk}) > 0$.

These results are similar to those of Utomo et al. (2017), who found $\log(\tau_{\rm cen.}/\tau_{\rm disk})$ for barred and interacting galaxies to be -0.22 ± 0.28 dex and -0.42 ± 0.51 dex respectively. They found this ratio to be -0.03 ± 0.35 dex for unbarred galaxies. Those authors used a slightly different definition of "center" and "disk," which may be the reason for an offset between our ratios and theirs, however the relative difference between barred, unbarred and interacting is similar to what we find.

2.4 Comparison to an *N*-body simulation

2.4.1 Observations

To understand our results better, our observational results are compared to high-resolution *N*-body hydrodynamic simulations. Given the large diversity of properties of our observed barred galaxies (properties of the disc, the bulge(s), the bar as well as of the spirals and rings that the latter may drive, etc.) it is clearly well beyond the scope of this paper to attempt truly quantitative comparisons. We will thus restrain ourselves here to *qualitative* comparisons and to generic properties.

We selected NGC 5000 (Fig. 2.10) as a random galaxy from our sample, using only the rough morphological constraints that the chosen galaxy should have a strong bar, a clear inner ring, and that it be viewed nearly face-on. We then calculated the mass-weighted average age of the stellar population for each IFU spaxel by fitting the corresponding spectrum with a linear combination of simple stellar populations (SSP) of different ages. Then, using simple azimuthal averages, we obtained the corresponding radial age profile (Fig. 2.11). For such fits it is customary to include populations considerably older than the Universe, e.g. up to 18 Gyr, or even more (González Delgado et al. 2015; Scott et al. 2017; Ge et al. 2018, etc.) in order to ensure completeness of templates. Since we want to compare with *N*-body simulations following the formation of discs and of their bars, we limited the age range of our SSPs to 13 Gyr.

2.4.2 Simulations

One of us (EA) has run a number of high resolution *N*-body hydro-dynamic simulations, including star formation, feedback, and cooling. They follow the formation of a disc and of its

components, such as the bar, B/P bulge, lens, spirals, rings etc. We give a very short summary of the simulations here; readers who want more information should refer to Athanassoula et al. (2016, hereafter A16) and Rodionov et al. (2017).

The simulations were run using a code based on Gadget3 (Springel & Hernquist 2002, 2003; Springel et al. 2005), with only a few modifications (A16 and references therein). The initial conditions and the way they were built are also described in that paper. This simulation survey includes galaxies formed and evolved in isolation, as well as galaxies formed from the merging of an isolated pair of protogalaxies, with the merging occurring early on in the run. Compared to most other dynamical simulations, where the disc is already in place and fully developed in the initial conditions of the simulation, they have the big advantage of not starting off with a pre-fabricated disc component, which might unwittingly introduce a bias. Indeed, they start off as single spheroid, composed of dark matter and hot gas, or as a pair of such spheroids. The dark matter is described by 2.2 million collisionless particles and the hot gas by 1.25 million smoothed particle hydrodynamics (SPH) particles. The linear resolution is equal to 50 pc for the dark matter and 25 pc for the baryonic particles.

During the evolution, the gas cools by radiation and accretes onto a plane perpendicular to the initial halo spin axis, thus forming a gaseous disc which, via star formation, becomes partly stellar. This disc forms inside-out, growing with time in radial extent while its gas-to-total-baryonic mass ratio decreases (A16), in good agreement with observations of galaxies at higher and lower redshifts. A stellar bar starts forming and evolves at the same time as the disc.

The various simulations we had at our disposal, as well as most other simulations in the lit-

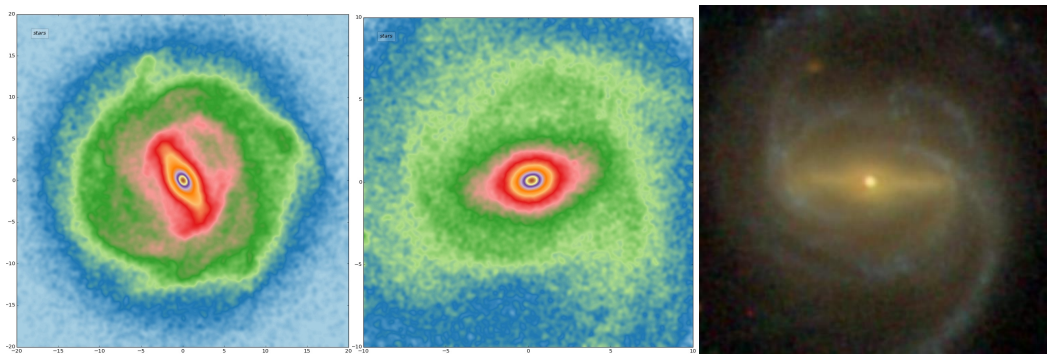

Figure 2.10: The left and middle panels show stellar maps of a snapshot of our simulated galaxy at times 9 and 13 Gyr, respectively. The image dimensions are 40 kpc $\times$ 40 kpc for the former and 20 $\times$ 20 for the latter. The right panel shows the optical *gri* image (29.3 kpc $\times$ 29.3 kpc) of NGC 5000, a galaxy from our sample. These images, and particularly their qualitative similarities, are discussed in Sect. 4.3.

erature, were run for a time span of at most 10 Gyr. Since our goal is to compare the radial age profile of our simulations with that derived from SSP fits to the CALIFA data of NGC 5000, we continued our run to 13 Gyr. We will hereafter call $t = 13$ Gyr the final time of the simulation.

2.4.3 Morphology

None of the simulations at our disposal reproduce well all the morphological features of NGC 5000. Many had a partial success, i.e. reproduced well some features but never all. This is no surprise, given the very large variety of disc galaxy properties. Thus the probability of having a simulation which will reproduce a given observed galaxy is very small, unless we run a large number of simulations specifically for this task, which is well beyond the scope of this paper. Fig. 2.11 shows that the maximum value of the radial age profile for NGC 5000 is around 12.5 Gyr. To reach such ages, we thus need to constrain our comparisons to times as near the final

time as possible and certainly above 12.5 Gyr. This sets very strong restrictions to our choice.

We chose a snapshot in the same way as we had chosen NGC 5000, i.e. a snapshot which has a bar and an inner structure such as a lens or inner ring (Fig. 2.10). It has a clear bar; however, compared to the observations, the simulated bar is less thin, and thus is presumably not as strong. Both the real and the simulated bar are surrounded by a component which is fatter in the equatorial plane. In the real galaxy, however, this component is more ring-like, while in the simulated one it is more lens-like. This relatively minor difference will have some influence on the shapes of the age radial profiles. Outside this structure the observations show a grand design two-armed spiral structure. This exists also in the stellar component of the simulation, but has a much lower amplitude. This difference must be due to the fact that we are looking at times as late as 13 Gyr, so that the bar and, albeit to a lesser extent, the spirals have had ample time to stir up the stars in the region outside the ring and to increase their velocity dispersion considerably, so that no high amplitude spirals can be driven (for a review, see Athanassoula 1984). This could also explain the difference of the bar shape, because horizontally thinner bars can be found in discs with lower velocity dispersions than thicker bars (Athanassoula 1983, 2003, 2018; Bekki & Tsujimoto 2011; Athanassoula et al. 2016; Fragkoudi et al. 2017).

As this comparison is not very satisfactory, most likely due to the late comparison time, we decided to look also at earlier times. We found a much better resemblance between the observed and simulated morphologies. For example, at a time of 9 Gyr (left panel), we find a much thinner bar (although still not as thin as that of NGC 5000), the outline of a partial inner ring (rather than a lens-like enhancement) and much clearer outer spirals. We thus decided to in-

clude this time also in the comparisons, even though this excluded stars older than 9 Gyr from the comparisons, i.e. has a worse completeness of SSP templates.

2.4.4 Age radial profile

In order to compare the two pairs of azimuthally-averaged radial age profiles, we need to calibrate the radii for the data and the simulation. The best calibration is by using physically-motivated lengths, as bars can have considerably different lengths in kpc in the two cases. A good candidate is the radius of one of the main resonances, and the one that is easiest to measure is the corotation or the inner ultra-harmonic resonance. This is one of the reasons we chose a galaxy with a clear inner ring (corresponding to the deepest age minimum), as in that case the radius of the ring can be used as a measuring rod. An inner ring is also easily observed as it is the locus of intense star formation and thus can be seen as a clear minimum in any azimuthally averaged age profile.

We calculated the azimuthally-averaged age radial profile from the simulation both at 9 and 13 Gyr, and we compare them in Fig. 2.11 with two age radial profiles of NGC 5000, calculated with maximum SSP ages of 9 and 13 Gyr. Given that the simulation we use was not specifically run to match NGC 5000, that there are considerable morphological differences between the simulations and observations, and that there are no free parameters to improve the match, we could have expected a very poor fit. Our results, however, are good qualitatively and even acceptable quantitatively.

Over the full radial range used in Fig. 2.11, the average difference between the simulation and the SSP fitted observations is considerably smaller for 9 Gyr than for 13 Gyr (0.625 Gyr for the

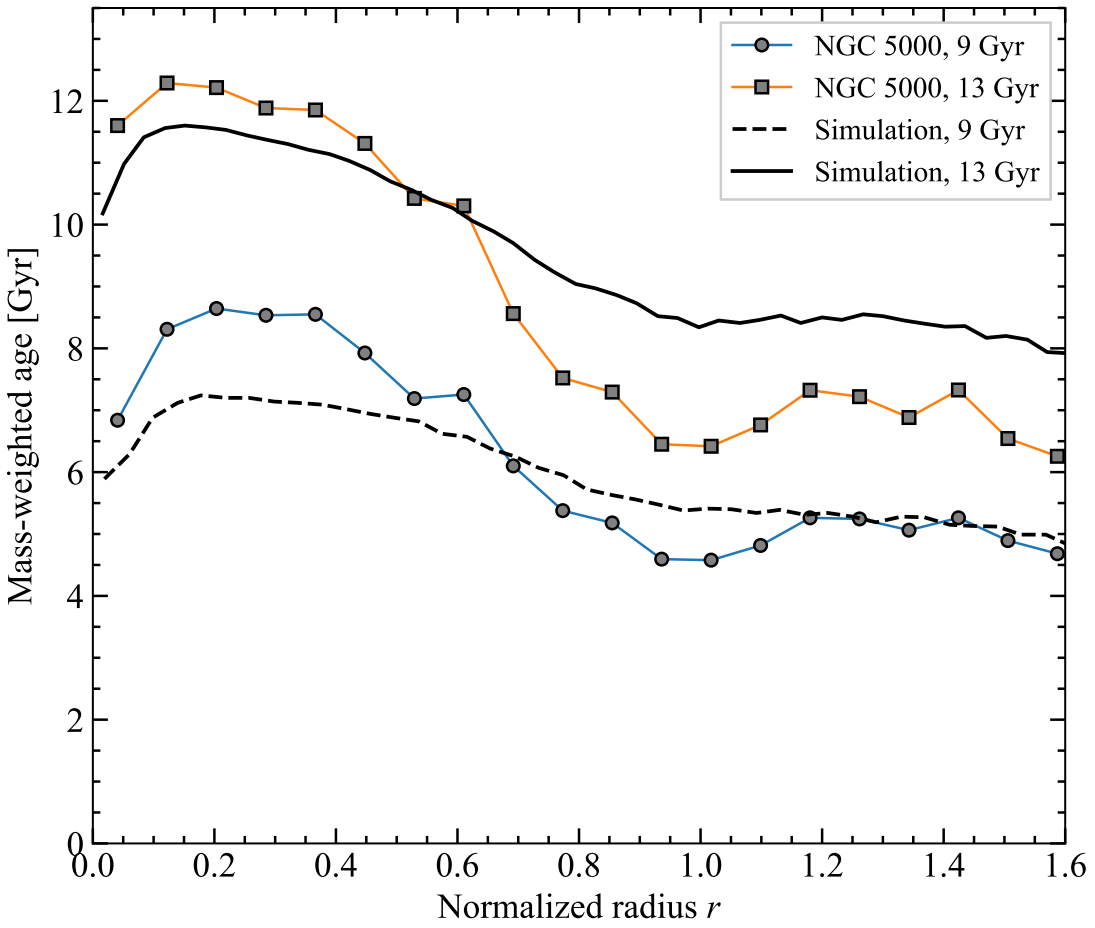

Figure 2.11: Comparison of the azimuthally-averaged mass-weighted stellar age radial profile of NGC 5000 (circle and square symbols) with that of the simulated galaxy. SSPs with ages up to 13 Gyr (squares), or up to 9 Gyr (circles) were used to fit the CALIFA data here. The radii have been normalised to the location of the deepest minimum (corresponding to the inner ring), which is near the end of the bar (the local minimum is at a value of 1.0 on the x-axis). The two main points to note are the central drop in age and the fact that the profile decreases after the end of the drop. The former could be associated with the inner Lindblad resonance of the bar, while the latter is evidence for the disc's and the bar's inside-out formation.

former, compared to 1.127 Gyr for 13 Gyr). Considering separately the part of the disc within a normalised radius of 0.6 and the part beyond that radius, we see that the 13 Gyr model fits better in the former (0.56 Gyr average absolute difference for 13 Gyr, compared to 1.08 for 9 Gyr), while the 9 Gyr model fits better in the region beyond the radius of 0.6 (0.37 Gyr average absolute difference, compared to 1.43 for the 13 Gyr model). If we compare the values of the maximum age in the profile, which are in all cases located in the inner part, the difference between simulations and SSP fits is around 6% for the 13 Gyr case, which is quite good, and better than 20% for the 9 Gyr case, which is acceptable given the differences between morphologies of the simulation and NGC 5000. What is most interesting, however, is that we can see a few generic features, present for both times and for the observations as well as the simulations. Two are most important, namely that the profile has a central dip, and that beyond that dip the age decreases with increasing distance from the centre.

In the central part of all four profiles there is a clear age minimum of relatively small radial extent. The size of this minimum shows a good agreement between observations and simulations. With the help of the simulation used here (but see also previous simulations, e.g. Athanassoula 1992b) it is easy to see how this minimum is formed, as the bar exerts torques on the gas and pushes it inwards. Thus, the gas concentrates in a small central area, where it reaches very high densities. Athanassoula (1992a) showed that the radius of this area is set by the Inner Lindblad Resonance (ILR) radius (i.e. by the extent of the x2 orbits). This radius is more extended for slower rotating bars and for more centrally concentrated mass distributions (see Fig. 6 and 7 in the above mentioned paper). Due to its high gaseous density, this central region will thus be

the locus of high star formation, and therefore the mean stellar age in there will be considerably lower than that of the region immediately surrounding it. The observations also show the same central minimum in age and thus the simulations give a good *qualitative* representation of this feature and allow us to explain its formation and properties.

We have examined the mean stellar age profile for all the galaxies in our observational sample, and find that a central drop is similarly seen in many (but not all) of the barred galaxies, while unbarred galaxies basically show little or no such central features. We similarly examined about half a dozen simulations and found similar results and also could witness the formation of this dip with time. Extensive comparisons with simulations covering a broader spectrum of different galactic types would be able to provide better constraints on models of bar formation and a better understanding of bar-driven secular evolution of galaxies.

Beyond this innermost region, up to one normalised length unit (i.e. roughly up to the end of the bar) the mean age decreases with increasing distance from the centre for both simulated and observed radial profiles. In the simulation, the disc forms inside-out, in good agreement with many observations, and this leads to a negative age gradient. Furthermore, any gas in this region will be pushed inwards by the bar to the region within the ILR and therefore only few new stars will be born, so that any stellar profile at formation will not be modified much at later times.

We also note that the slope of this radial density profile beyond the central dip is not constant with distance from the centre. In the region between the maximum age to about half the bar length, the profile is rather flat. For larger radii, however, the decrease is much stronger,

until a minimum age is reached. This behaviour is very clear in the profile from the CALIFA data, both for 9 and 13 Gyr cases. It is also present for the simulation age profile, although less dramatic. The extent of the two parts, i.e the flatter and the steeper decreasing parts, is also in rather good agreement between observations and simulations.

At the end of this radial range where the age is decreasing, we have a minimum. Again this is much clearer in the profiles obtained from observations, but it can also be seen well in the 13 Gyr simulation profile and, more as a change of slope, for the 9 Gyr one. This difference between observations and simulations is due to a difference in the corresponding morphologies (Fig. 2.11). Namely in NGC 5000 the bar is surrounded by an inner ring, i.e. a structure which is usually gas-rich and a locus of intense star formation (for a review, see Buta & Combes 1996). We thus expect a concentration of young stars and a minimum in the radial age profile. Such inner rings can be seen in a number of other simulations run by one of us (EA) and have the expected properties. However the simulation snapshots analysed here have a clear inner ring only in the gas and young populations (not shown here), but not in the older populations where it has a more lens-like component. Thus there should be less star formation in the simulation and the mean age at these radii should not be much decreased with respect to their surroundings.

2.5 Discussion

2.5.1 How often do we see a central star formation enhancement?

Our sample consists of 58 nearby galaxies, including 41 isolated galaxies with regular morphologies (17 barred and 24 unbarred), and 17 mergers or paired galaxies. A third of all the galaxies

(19/58) in our sample present a significant central upturn in logEW(Hα), including 13 barred isolated galaxies and 6 mergers/pairs. This is a large fraction compared to expectations from the traditional view that spiral galaxies host redder and older galactic centers with less star formation than their outer discs. This result echoes a similar fraction of "turnover" galaxies found in Lin et al. (2017), where 17 out of 57 galaxies were identified as having a central turnover in $D_n(4000)$. We note, however, that Lin et al. (2017) excluded mergers/pairs from their sample. If mergers and pairs are also excluded from our sample, the fraction of upturn galaxies remains similar though slightly higher, 31.7% (13/41).

As discussed in Lin et al. (2017), almost all of the galaxies with a central drop in $D_n(4000)$ present central upturn features in both EW(Hδ_A) and logEW(Hα). Therefore, a higher upturn fraction in our sample should not be attributed to the fact that Lin et al. (2017) used $D_n(4000)$ as the nominal definition of enhanced central star formation rather than logEW(Hα). As pointed out above, by selection the EDGE-CALIFA sample is biased to gas-rich galaxies. Therefore, a higher fraction of upturn galaxies in our sample might imply that the central star formation enhancement happens more frequently in galaxies with more cold gas. As pointed out earlier (§2.2.2), our sample is limited to relatively high-mass galaxies with few below $M_* \sim 10^{10} M_\odot$ (see Fig. 2.1). Therefore, one might expect the upturn galaxy fraction to increase if the sample includes galaxies of lower masses which are more gas-rich.

It is thus natural to conclude that the central star formation enhancement occurs commonly in local galaxies, with a fraction of at least 1/3. The central upturn or turnover in the spectral indices can be observed only when spatially resolved spectroscopy like IFU data is available. Multi-

band imaging should be also useful, and probably more applicable, if one were to study such central features for larger samples. In this case color indices can be used as reasonably good indicators of recent star formation history, although they suffer from dust extinction more seriously than spectral indices. We predict that a large fraction of galaxies must present a central drop in their color maps or profiles, an effect that can be tested with existing/future large-area imaging surveys at different redshifts.

2.5.2 Can bars and mergers together fully account for the central star formation enhancement?

The fact that all galaxies in our sample with a central upturn in logEW(Hα) are either barred, mergers, or pairs, and that no unbarred galaxies (24) present an upturn feature strongly suggests that bars, mergers and pairs fully account for the central star formation enhancement occurring in our sample. On the other hand, 4 of the 17 barred galaxies and 11 of the 17 mergers/pairs present no upturn features in their centers. This result suggests that the presence of a bar or tidal interactions is necessary, but not a sufficient condition for the central star formation enhancement, in agreement with the conclusions of Lin et al. (2017).

Our work extends their findings by including mergers and paired galaxies in the analysis. Bars and mergers appear to respectively account for $\sim$2/3 and $\sim$1/3 of the central upturn phenomenon. Previous studies of large samples from SDSS have examined the correlation of central star formation with both galaxy-galaxy interactions (e.g. Li et al. 2008) and the internal bar structure (e.g. Wang et al. 2012). Li et al. (2008) found $\sim$ 40% of the most strongly star-forming galaxies in the local Universe have a close companion, while Wang et al. (2012) found

that only half of the galaxies with centrally enhanced star formation host a bar. The two studies combine to suggest that bars and interactions can roughly account for the central star formation enhancement occurring in low-redshift galaxies. It is encouraging that the same conclusion is reached by both the SDSS-based studies of large samples, i.e. Li et al. (2008) and Wang et al. (2012) which used single-fiber spectroscopy, the work of Lin et al. (2017), and the current work which uses integral field spectroscopy.

In addition to instabilities driven by bars and tidal interactions, other mechanisms may be invoked, such as driving by spirals or asymmetries, although presumably these may be much less efficient. A common purpose of all these mechanisms is to transport cold gas from the disk to the central kiloparsec, where star formation is triggered due to increased gas density. In this work we have shown that molecular gas is indeed more concentrated when central star formation enhancement is observed (Fig. 2.7). More importantly, our work shows that the star formation enhancement can be substantially explained by bars and mergers, with no need to have additional mechanisms. Again, however, we should emphasize that our sample is biased to relatively high-mass and gas-rich galaxies. Larger samples covering wider ranges of mass and color would be needed if one were to have a complete picture of the physical mechanisms behind the central star formation enhancement.

2.5.3 Bar-driven central SF enhancement as a long-lived effect

Our results suggest that bar-induced central star formation is a long-term process lasting at least 1-2 Gyr. This can be seen from both Fig. 2.4 and Fig. 2.7, where barred galaxies with a central upturn in logEW(Hα) also show a central upturn in EW(Hδ_A) and a central drop in $D_n(4000)$.

We know that a central drop in $D_n(4000)$ indicates that a considerable fraction of young stellar populations were formed in the central region 1-2 Gyr ago, a central upturn in EW($H\delta_A$) reveals the existence of a starburst ending 0.1-1 Gyr ago, and a central upturn in logEW($H\alpha$) indicates ongoing star formation. Therefore, the fact that both a $D_n(4000)$ drop and an EW($H\delta_A$) upturn are associated with barred, logEW($H\alpha$)-upturn galaxies implies that the central star formation induced by the bar started at least 1-2 Gyr ago, and is still happening at the moment.

Krumholz & Kruijssen (2015) showed using simulations that the timescale between bar-induced gas accumulation and a subsequent central starburst is only 10-20 Myr, after which the central region needs to accumulate more gas. The three SFH indicators used in the current work cannot tell whether the SF process is continuous or bursty, if the cycle timescale is only 10-20 Myr. What we can say is that there are young stellar populations; some are younger than a few Myr, and some are younger than 1-2 Gyr. We find that the upturn and turnover strengths are correlated for barred galaxies, with correlation coefficients ranging from 0.50 to 0.54, which supports the conclusion that central SF enhancement is long-lived. The correlations are weaker for merger/pair galaxies, and negligible for unbarred galaxies.

2.5.4 Is high $c_{\rm mol}$ a necessary and sufficient condition for central star formation enhancement?

Our results show that high gas concentration is neither a necessary, nor sufficient condition for enhanced central star formation to occur. This can be seen from both Fig. 2.4 and Fig. 2.7. On the one hand, the upturn galaxies (particularly those with a bar) span the full range of $\log c_{\rm mol}$, although the majority of them have higher gas concentration than non-upturn galaxies, with

$\log c_{\rm mol} \gtrsim 0.3$ in most cases. This result suggests that a highly concentrated gas distribution is an important, but not a necessary condition for the central upturn to occur in our galaxies. On the other hand, we see some galaxies in our sample with high gas concentration $\log c_{\rm mol} > 0.3$ but without a central upturn. This result indicates that high gas concentration alone is not sufficient for the central upturn.

It is interesting that all of the galaxies with no central upturn but with high gas concentration are in the category of mergers/pairs, except for one galaxy, NGC7819, which is an unbarred galaxy with $\log c_{\rm mol} \sim 0.6$ (see § A.1 for more discussion on this galaxy). For barred galaxies, we see that all those with $\log c_{\rm mol} > 0.3$ present a central upturn in logEW(Hα), with no exception, although a central upturn/turnover in EW(Hδ_A) or $D_n(4000)$ is not associated in a few cases. Thus, bars seem to be more efficient than mergers in triggering enhanced star formation in galactic centers, even when cold gas is not highly concentrated. However, star formation may be underestimated in mergers due to high levels of dust extinction. We conclude that high gas concentration is neither necessary, nor sufficient, and that the presence of a bar in most cases or mergers/interactions in other cases appear to be a crucial condition for central star formation enhancement.

2.6 Conclusions and future work

We have studied the spatially-resolved molecular gas and indicators of recent star-formation history for 58 nearby galaxies using CARMA EDGE CO $J = 1 \rightarrow 0$ and CALIFA optical IFU data. We divide our sample of 58 galaxies into three subsamples based on morphology: barred

(17), unbarred (24), and mergers/pairs (17). The resolved gas and star formation history data are used to compare these three subsamples. We use the equivalent width of the Hα emission line logEW(Hα), equivalent width of the Hδ absorption line EW(Hδ_A) and the 4000 Å break D$_n$(4000) to measure the strength of recent star formation in the central region compared to the outer part of the central region (inside the spiral arms). These three parameters allow us to probe the star formation history at three times: 0-30 Myr (EW(Hα)), 0.1-1 Gyr (EW(Hδ_A)), and 1-2 Gyr (D$_n$(4000)). We measure a molecular gas concentration index $c_{\rm mol}$ defined as the ratio of the optical half-light radius to the molecular gas half-mass radius $r_{50,\rm mol}$ measured from radial profiles of the publicly available EDGE CO $J = 1 \rightarrow 0$ maps.

After comparing the central star formation history and molecular gas concentration for subsamples of barred, unbarred and merging/paired galaxies, we reach the following conclusions:

1. Out of the 58 galaxies in our primary sample, 19 show a central upturn in logEW(Hα), of which 13 are barred, none are unbarred, and 6 are mergers/pairs. Galaxies with upturns have higher gas concentrations than barred or unbarred galaxies without upturns (Table 2.1). Merger/pair galaxies without upturns have average concentrations similar to galaxies with upturns.

2. The level of enhanced central star formation is positively correlated with molecular gas concentration for barred galaxies, and in two out of the three SFH indicators. No significant correlations are found for unbarred or merger/pair galaxies (Figure 2.7).

3. Barred galaxies with upturns in logEW(Hα) have significantly higher values of upturn and turnover strengths than merger/pair galaxies with upturns (Table 2.1). The average

gas concentrations are consistent between these two categories. However, barred galaxies with no upturn have significantly lower gas concentrations than merger/pair galaxies with no upturn. These results imply that bars are efficient in enhancing central star formation, which is long-lived (at least 1-2 Gyr).

4. Our observational results provide strong support to the current theory of bar formation in which bars form and grow from inside out. Furthermore, they transport cold gas from the disk to the central region, which leads to significant enhancement in star formation. We compared our results with those from a simulation snapshot (§2.4) and found that the latter successfully reproduce two major features in the azimuthally-averaged radial profiles of mass-weighted age obtained from the data, namely the sharp decrease of stellar age in the galactic center and the gradual decrease of age with increasing distance from center. This qualitative comparison provides evidence for a picture in which cold gas is transported inward due to a bar or tidal driving, which leads to the growth and rejuvenation of the central region.

Some important issues are not yet addressed in the current work, such as the correlation of central upturn strength with bar length and ellipticity (which are commonly used to quantify the strength of a bar), and the distribution of cold gas and star formation indicators along and surrounding the bar. Lin et al. (2017) found a weak correlation between the radius of $D_n(4000)$ turnover and bar length. It would be interesting to examine whether the gas concentration is also somehow correlated with bar properties. Secondly, the merger/pair category may be studied in more detail, e.g. by further splitting the galaxies into subsets according to pair separation

and merger status to examine how the central star formation and gas distribution evolve as the interaction/merger proceeds. It would also be interesting to have more detailed analyses of the exceptional galaxies in our sample, as mentioned in the previous subsection. What are the reasons for variations in the barred galaxies? Do different concentrations indicate different stages of bar-driven gas transport? Finally, one may also want to examine the effects of different environments, such as ram-pressure stripping and tidal stripping that occur in/around massive dark halos and can effectively strip hot/cold gas of satellite galaxies. For this purpose our sample is probably too small, and larger samples with both integral field spectroscopy and CO intensity mapping are needed.

From the theoretical side, it is important to make comparisons for different types of galaxies and for models with different bar strengths, gas properties, feedback, star formation, as and dark matter halo properties. In this work we have focused our observational analysis on stellar populations, while ignoring dynamical properties of our galaxies which can be measured from integral field spectroscopy as well. As mentioned above, the radius where the central upturn/turnover occurs may be related to the mass distribution in the innermost region and the pattern speed of the bar (e.g. Athanassoula 1992b). The latter can be measured by dynamical modelling of the kinematics of stars in the galaxy based on integral field spectroscopy data. Therefore stellar population synthesis and dynamical modelling in combination are expected to provide more powerful constraints on bar formation models.

Acknowledgements

This work is supported by the National Key R&D Program of China (grant Nos. 2018YFA0404502), the National Key Basic Research Program of China (No. 2015CB857004), and the National Science Foundation of China (No. 11233005, 11325314, 11320101002, 11733004). RC acknowledges the support of McMaster University, a Mitacs Globalink Research Award (IT10717), and the China Scholarship Council. EA thanks the CNES for financial support. This work was granted access to the HPC resources of CINES under the allocations 2017-A0020407665 and 2018-A0040407665 attributed by GENCI (Grand Equipement National de Calcul Intensif), as well as the HPC resources of Aix-Marseille University financed by the project Equip@Meso (ANR-10-EQPX-29-01) of the program "Investissements d'Avenir" supervised by the Agence Nationale de la Recherche. HJM acknowledges the support from NSF AST-1517528. The research of CDW is supported by grants from the Natural Sciences and Engineering Research Council of Canada and the Canada Research Chairs program. LL was supported by the National Science Foundation of China (No. 11703063).

This study uses data provided by the CARMA Extragalactic Database for Galaxy Evolution (EDGE) survey (http://www.astro.umd.edu/EDGE/), the Calar Alto Legacy Integral Field Area (CALIFA) survey (http://califa.caha.es/), the NASA-Sloan Atlas (http://www.nsatlas.org/), the Sloan Digital Sky Survey (https://www.sdss.org/), the HyperLeda database (http://leda.univ-lyon1.fr), and the SIMBAD database, operated at CDS, Strasbourg, France. CALIFA is based on observations collected at the Centro Astronómico Hispano Alemán (CAHA) at Calar Alto, operated jointly by the Max-Planck-

Institut für Astronomie and the Instituto de Astrofísica de Andalucía (CSIC).

Supporting Information

Supplementary data are available at MNRAS online.

Table A1. Basic properties of the galaxies in our sample.

Table A2. Quantities derived from spatially resolved optical IFU and molecular gas maps.

Please note: Oxford University Press is not responsible for the content or functionality of any supporting materials supplied by the authors. Any queries (other than missing material) should be directed to the corresponding author for the article.

A Tables of galaxy properties

Table A1 shows basic properties of the galaxies in our sample, and Table A2 shows measurements derived from our analysis.

Table A1: Basic properties of the galaxies in our sample. The full version is available in machine-readable format.

Galaxy	No.	R.A. (J2000)	Dec. (J2000)	z	$\log M_*$ ($M_\odot$)	NUV-r (mag)	r_{50} ($''$)	$\log M_{\rm HI}$ ($M_\odot$)	$\log M_{\rm H_2}$ ($M_\odot$)	Type
(1)	(2)	(3)	(4)	(5)	(6)	(7)	(8)	(9)	(10)	(11)
					Barred					
IC1683	2	20.66220	34.43713	0.016	10.4	4.1	13.1	9.2	9.5	Sb
					Unbarred					
NGC7819	21	1.10211	31.47201	0.017	10.1	2.6	23.8	9.6	9.2	Sc
					Merger/pair					
NGC0523	45	21.33649	34.02495	0.016	10.6	4.1	24.2	10.1	9.5	Sd

(1): Galaxy name.
(3): Right ascension (degrees), from SDSS DR7.
(4): Declination (degrees), from SDSS DR7.
(5): Raw redshift measured from the CALIFA datacubes.
(6): Stellar mass from CALIFA DR3 reanalysis of SDSS DR7 *ugriz* growth curves (Walcher et al. 2014).
(7): NUV$-r$ magnitude from the NASA-Sloan Atlas (NSA).
(8): r-band half-light radius r_{50} from the NSA.
(9): Neutral hydrogen mass from ALFALFA 100% catalog (Haynes et al. 2018) where available, or from the HyperLeda database.
(10): The total detected H_2 mass in the whole CO image.
(11): The morphological type (RC3) provided in CALIFA DR3.

Table A2: Quantities derived from spatially-resolved optical IFU and molecular gas maps. The full table is available in machine-readable format.

Galaxy	Upturn?	$\Delta D_n(4000)$	$\Delta EW(H\delta_A)$ (Å)	Δ logEW(Hα)	$r_{50,mol}$ ($''$)	log c_{mol}	log $\tau_{depl.}$ Center (yr)	log $\tau_{depl.}$ Disk (yr)	log $\tau_{cen.}/\tau_{disk.}$
(1)	(2)	(3)	(4)	(5)	(6)	(7)	(8)	(9)	(10)
Barred									
IC1683	Y	0.66	1.69	0.58	5.63	0.37	8.95 ± 0.07	9.25 ± 0.06	-0.30 ± 0.09
Unbarred									
NGC7819	N	0.02	0.70	0.31	5.96	0.60	8.85 ± 0.07	8.92 ± 0.06	-0.06 ± 0.09
Merger/pair									
NGC0523	N	−0.13	−0.07	0.10	18.05	0.13	9.87 ± 0.10	9.29 ± 0.06	0.57 ± 0.12

Note: galaxies that are not in the reduced sample (§2.2.2) have values of "n/a" in columns 8-10.
(1): Galaxy name.
(2): Does this galaxy have an upturn in logEW(Hα)(§2.3.1)? (Y or N).
(3): $D_n(4000)$ turnover strength.
(4): $EW(H\delta_A)$ upturn strength.
(5): logEW(Hα) upturn strength.
(6): Molecular gas half-mass radius.
(7): Molecular gas concentration index (Eq. 2.3).
(8): Molecular gas depletion time (Eq. 2.4) in the "center" (0.5 kpc semi-major axis).
(9): Molecular gas depletion time in the "disk" (between 0.5 kpc and r_{50}).
(10): Center-to-disk depletion time ratio.

A.1 Notes on individual galaxies

Here we mention a few galaxies which show unusual or extreme behaviours based on Figure 2.7. Their optical images, SFH indicators, molecular gas maps and radial profiles are shown in Fig. A1.

NGC3381: the barred galaxy with a very high $\Delta\mathrm{EW}(\mathrm{H}\delta_A)$ but with only intermediate c_{mol}. This galaxy is blue in colour ($\mathrm{NUV}-r = 2.0$, the bluest of all our barred galaxies), and has a low stellar mass ($10^{9.6} M_{\odot}$; the lowest of all our barred galaxies). This galaxy has an observed value of $\mathrm{EW}(\mathrm{H}\delta_A) = 5.05$Å, the highest in our sample (middle panel of Fig. 2.3), and is consistent with the definition of a post-starburst galaxy.

NGC7819: the unbarred galaxy with the highest c_{mol}. With an $\mathrm{NUV}-r$ of 2.1 mag (the bluest of the unbarred galaxies), this galaxy is clearly blue and star-forming. This galaxy has quite a large optical radius (23.8″), and a relatively small $r_{50,\mathrm{mol}}$. Given this high concentration, why does it not show enhanced central star formation in any of our SFH indicators? With a central $\log \Sigma_{\mathrm{H_2}}$ of $2.27 M_{\odot}\mathrm{pc}^{-2}$ and central $\log \Sigma_{\mathrm{SFR}}$ of $-0.58 M_{\odot}\mathrm{yr}^{-1}\mathrm{kpc}^{-2}$, which are not dissimilar from the central values of these quantities in barred upturn galaxies (Fig. 2.9), it appears that central SFR and $\mathrm{H_2}$ surface densities being similar to barred galaxies, and having a high molecular gas concentration are not sufficient conditions for enhanced central star formation. A bar or galaxy interaction appears to be needed too, as discussed above. It would be interesting to study the dense gas in this system – it could be that the gas is not sufficiently dense to form stars without a bar.

NGC4211NED02: the merger galaxy with the highest c_{mol} but no significant central upturn.

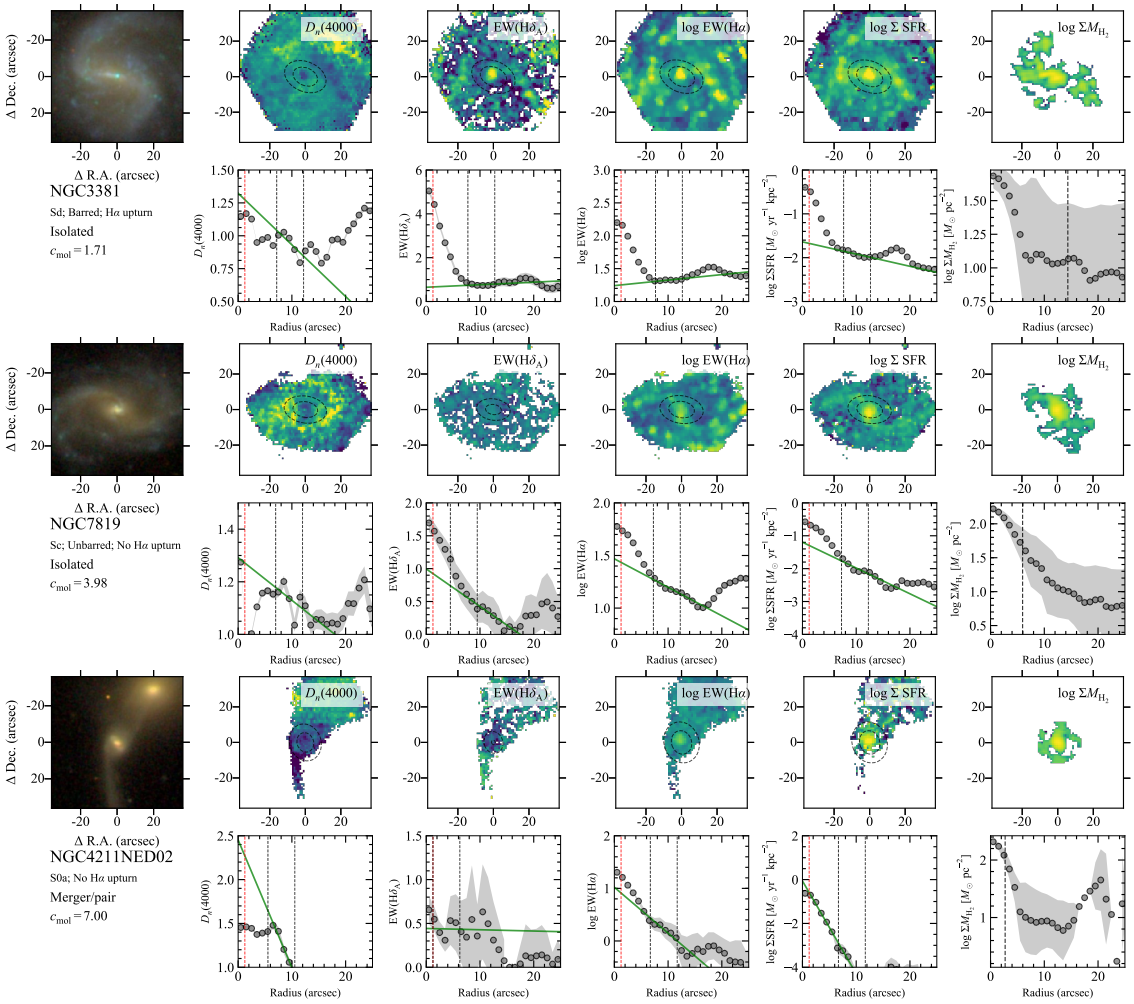

Figure A1: Maps and radial profiles of additional example galaxies in our sample. See caption of Fig. 2.2 for description of quantities.

This galaxy has NUV$-r$ of 3.7, and stellar mass of $10^{10.0} M_{\odot}$. It is in a close pair with NGC4211A (not in our sample), with a projected separation of approximately 16 kpc. The CO emission for this galaxy is very compact, and since $r_{50,\mathrm{mol}}$ is less than twice the CARMA beam scale, c_{mol} should be considered a lower limit (as indicated in Table A2). This galaxy does not show an upturn, however it shows a significant $D_n(4000)$ turnover (see the bottom-right panel of Fig. 2.7). The turnover strength for this particular galaxy should be interpreted with caution, because the size of the central region of this galaxy is quite close to the resolution of CALIFA. Although the optical radius of this galaxy is 19″, this is likely due to the irregular morphology. The size of the inner region is much smaller, which makes our fitting less reliable.

References

Athanassoula E., 1983, in Athanassoula E., ed., IAU Symposium Vol. 100, Internal Kinematics and Dynamics of Galaxies. pp 243–250

Athanassoula E., 1984, Phys. Rep., 114, 321

Athanassoula E., 1992a, MNRAS, 259, 328

Athanassoula E., 1992b, MNRAS, 259, 345

Athanassoula E., 1994, in Shlosman I., ed., Mass-Transfer Induced Activity in Galaxies. p. 143

Athanassoula E., 2003, MNRAS, 341, 1179

Athanassoula E., 2005, MNRAS, 358, 1477

Athanassoula E., 2018, in Chiappini C., Minchev I., Starkenburg E., Valentini M., eds, IAU Symposium Vol. 334, Rediscovering Our Galaxy. pp 65–72 (arXiv:1801.07720), doi:10.1017/S1743921317008778

Athanassoula E., Machado R. E. G., Rodionov S. A., 2013, MNRAS, 429, 1949

Athanassoula E., Rodionov S. A., Peschken N., Lambert J. C., 2016, ApJ, 821, 90

Baldwin J. A., Phillips M. M., Terlevich R., 1981, PASP, 93, 5

Barnes J. E., Hernquist L. E., 1991, ApJ, 370, L65

Barton Gillespie E., Geller M. J., Kenyon S. J., 2003, ApJ, 582, 668

Bekki K., Tsujimoto T., 2011, MNRAS, 416, L60

Bigiel F., Leroy A., Walter F., Brinks E., de Blok W. J. G., Madore B., Thornley M. D., 2008, AJ, 136, 2846

Blanton M. R., Roweis S., 2007, AJ, 133, 734

Blanton M. R., et al., 2005a, AJ, 129, 2562

Blanton M. R., Eisenstein D., Hogg D. W., Schlegel D. J., Brinkmann J., 2005b, ApJ, 629, 143

Blanton M. R., Kazin E., Muna D., Weaver B. A., Price-Whelan A., 2011, AJ, 142, 31

Blanton M. R., et al., 2017, AJ, 154, 28

Bock D. C.-J., et al., 2006, in Society of Photo-Optical Instrumentation Engineers (SPIE) Conference Series. p. 626713, doi:10.1117/12.674051

Bolatto A. D., Wolfire M., Leroy A. K., 2013, ARA&A, 51, 207

Bolatto A. D., et al., 2017, ApJ, 846, 159

Bruzual G., Charlot S., 2003, MNRAS, 344, 1000

Bundy K., et al., 2015, ApJ, 798, 7

Buta R., Combes F., 1996, Fundamentals Cosmic Phys., 17, 95

Calzetti D., Armus L., Bohlin R. C., Kinney A. L., Koornneef J., Storchi-Bergmann T., 2000, ApJ, 533, 682

Cappellari M., 2017, MNRAS, 466, 798

Cappellari M., Emsellem E., 2004, PASP, 116, 138

Catinella B., et al., 2018, MNRAS,

Croom S. M., et al., 2012, MNRAS, 421, 872

Devereux N., 1987, ApJ, 323, 91

Ellison S. L., Nair P., Patton D. R., Scudder J. M., Mendel J. T., Simard L., 2011, MNRAS, 416, 2182

Ellison S. L., Mendel J. T., Patton D. R., Scudder J. M., 2013, MNRAS, 435, 3627

Fragkoudi F., Di Matteo P., Haywood M., Gómez A., Combes F., Katz D., Semelin B., 2017, A&A, 606, A47

Ge J., Yan R., Cappellari M., Mao S., Li H., Lu Y., 2018, MNRAS, 478, 2633

González Delgado R. M., et al., 2015, A&A, 581, A103

Hao C.-N., Kennicutt R. C., Johnson B. D., Calzetti D., Dale D. A., Moustakas J., 2011, ApJ, 741, 124

Hawarden T. G., Mountain C. M., Leggett S. K., Puxley P. J., 1986, MNRAS, 221, 41P

Haynes M. P., et al., 2018, ApJ, 861, 49

Ho L. C., Filippenko A. V., Sargent W. L. W., 1997, ApJ, 487, 591

Jiang X.-J., Wang Z., Gu Q., Wang J., Zhang Z.-Y., 2015, ApJ, 799, 92

Jogee S., Scoville N., Kenney J. D. P., 2005, ApJ, 630, 837

Kaneko H., Kuno N., Iono D., Tamura Y., Tosaki T., Nakanishi K., Sawada T., 2013, PASJ, 65, 20

Karachentsev I. D., 1972, Soobshcheniya Spetsial'noj Astrofizicheskoj Observatorii, 7

Kauffmann G., et al., 2003a, MNRAS, 341, 33

Kauffmann G., et al., 2003b, MNRAS, 341, 54

Kauffmann G., et al., 2003c, MNRAS, 346, 1055

Kelz A., et al., 2006, PASP, 118, 129

Kennicutt R. C., Evans N. J., 2012, ARA&A, 50, 531

Kennicutt Robert C. J., et al., 2007, ApJ, 671, 333

Kewley L. J., Dopita M. A., Sutherland R. S., Heisler C. A., Trevena J., 2001, ApJ, 556, 121

Kormendy J., Kennicutt Jr. R. C., 2004, ARA&A, 42, 603

Kroupa P., Weidner C., 2003, ApJ, 598, 1076

Krumholz M. R., Kruijssen J. M. D., 2015, MNRAS, 453, 739

Kuno N., et al., 2007, PASJ, 59, 117

Leroy A. K., et al., 2009, AJ, 137, 4670

Li C., Kauffmann G., Heckman T. M., Jing Y. P., White S. D. M., 2008, MNRAS, 385, 1903

Li C., et al., 2015, ApJ, 804, 125

Lin Y., Cervantes Sodi B., Li C., Wang L., Wang E., 2014, ApJ, 796, 98

Lin L., Li C., He Y., Xiao T., Wang E., 2017, ApJ, 838, 105

Makarov D., Prugniel P., Terekhova N., Courtois H., Vauglin I., 2014, A&A, 570, A13

Martig M., Bournaud F., Teyssier R., Dekel A., 2009, ApJ, 707, 250

Martin D. C., et al., 2005, ApJ, 619, L1

Mok A., Wilson C. D., Knapen J. H., Sánchez-Gallego J. R., Brinks E., Rosolowsky E., 2017, MNRAS, 467, 4282

Murphy E. J., et al., 2011, ApJ, 737, 67

Oh S., Oh K., Yi S. K., 2012, ApJS, 198, 4

Osterbrock D. E., Ferland G. J., 2006, Astrophysics of gaseous nebulae and active galactic nuclei. University Science Books

Patton D. R., Torrey P., Ellison S. L., Mendel J. T., Scudder J. M., 2013, MNRAS, 433, L59

Piner B. G., Stone J. M., Teuben P. J., 1995, ApJ, 449, 508

Planck Collaboration et al., 2016, A&A, 594, A7

Puxley P. J., Hawarden T. G., Mountain C. M., 1988, MNRAS, 234, 29P

Regan M. W., et al., 2006, ApJ, 652, 1112

Rodionov S. A., Athanassoula E., Peschken N., 2017, A&A, 600, A25

Roth M. M., et al., 2005, PASP, 117, 620

Saintonge A., et al., 2011, MNRAS, 415, 61

Saintonge A., et al., 2012, ApJ, 758, 73

Saintonge A., et al., 2017, ApJS, 233, 22

Sakamoto K., 2000, in Combes F., Mamon G. A., Charmandaris V., eds, Astronomical Society of the Pacific Conference Series Vol. 197, Dynamics of Galaxies: from the Early Universe to the Present. p. 73 (arXiv:astro-ph/9910226)

Sakamoto K., Okumura S. K., Ishizuki S., Scoville N. Z., 1999, ApJ, 525, 691

Sánchez S. F., et al., 2012, A&A, 538, A8

Sánchez S. F., et al., 2016, A&A, 594, A36

Sandstrom K. M., et al., 2013, ApJ, 777, 5

Scott N., et al., 2017, MNRAS, 472, 2833

Sheth K., Vogel S. N., Regan M. W., Thornley M. D., Teuben P. J., 2005, ApJ, 632, 217

Sormani M. C., Binney J., Magorrian J., 2015, MNRAS, 454, 1818

Springel V., Hernquist L., 2002, MNRAS, 333, 649

Springel V., Hernquist L., 2003, MNRAS, 339, 289

Springel V., Di Matteo T., Hernquist L., 2005, ApJ, 620, L79

Stark D. V., Kannappan S. J., Wei L. H., Baker A. J., Leroy A. K., Eckert K. D., Vogel S. N., 2013, ApJ, 769, 82

Turner E. L., 1976, ApJ, 208, 20

Utomo D., et al., 2017, ApJ, 849, 26

Violino G., Ellison S. L., Sargent M., Coppin K. E. K., Scudder J. M., Mendel T. J., Saintonge A., 2018, MNRAS, 476, 2591

Vorontsov-Velyaminov B. A., Noskova R. I., Arkhipova V. P., 2001, Astronomical and Astrophysical Transactions, 20, 717

Walcher C. J., et al., 2014, A&A, 569, A1

Walter F., Brinks E., de Blok W. J. G., Bigiel F., Kennicutt Robert C. J., Thornley M. D., Leroy A., 2008, AJ, 136, 2563

Wang J., et al., 2012, MNRAS, 423, 3486

Wang E., et al., 2018, ApJ, 856, 137

Wenger M., et al., 2000, Astronomy and Astrophysics Supplement Series, 143, 9

Wilson C. D., et al., 2012, MNRAS, 424, 3050

York D. G., et al., 2000, AJ, 120, 1579

Young J. S., et al., 1995, ApJS, 98, 219

Zhou Z.-M., Cao C., Wu H., 2015, AJ, 149, 1

3

A new estimator of resolved molecular gas in nearby galaxies

This chapter contains the following article:

"A new estimator of resolved molecular gas in nearby galaxies"

Published in the Monthly Notices of the Royal Astronomical Society (MNRAS): Vol. 500, pp. 1261-1278, 2021.

Authors: Chown, R., Li, C., Parker, L., Wilson, C. D., Li, N., and Gao, Y.

ABSTRACT

A relationship between dust-reprocessed light from recent star formation and the amount of star-forming gas in a galaxy produces a correlation between *WISE* 12 μm emission and CO line emission. Here we explore this correlation on kiloparsec scales with CO(1-0) maps from EDGE-CALIFA matched in resolution to *WISE* 12 μm images. We find strong CO-12 μm correlations within each galaxy and we show that the scatter in the global CO-12 μm correlation is largely driven by differences from galaxy to galaxy. The correlation is stronger than that between star formation rate and H_2 surface densities ($\Sigma(H_2)$). We explore multi-variable regression to predict $\Sigma(H_2)$ in star-forming pixels using the *WISE* 12 μm data combined with global and resolved galaxy properties, and provide the fit parameters for the best estimators. We find that $\Sigma(H_2)$ estimators that include $\Sigma(12\ \mu m)$ are able to predict $\Sigma(H_2)$ more accurately than estimators that include resolved optical properties instead of $\Sigma(12\ \mu m)$. These results suggest that 12 μm emission and H_2 as traced by CO emission are physically connected at kiloparsec scales. This may be due to a connection between polycyclic aromatic hydrocarbon (PAH) emission and the presence of H_2. The best single-property estimator is $\log \frac{\Sigma(H_2)}{M_\odot\ pc^{-2}} = (0.48 \pm 0.01) + (0.71 \pm 0.01) \log \frac{\Sigma(12\ \mu m)}{L_\odot\ pc^{-2}}$. This correlation can be used to efficiently estimate $\Sigma(H_2)$ down to at least 1 $M_\odot\ pc^{-2}$ in star-forming regions within nearby galaxies.

3.1 Introduction

Stars form out of molecular hydrogen in cold, dense regions of the interstellar medium (ISM). Empirically this picture is supported by correlations between tracers of cold gas and the radiation output from young stars such as the Kennicutt-Schmidt (KS) law

$$\Sigma(\mathrm{SFR}) \propto \Sigma(\mathrm{gas})^{N}, \tag{3.1}$$

where $\Sigma(\mathrm{SFR})$ is the star formation rate (SFR) surface density ($M_{\odot}\,\mathrm{kpc}^{-2}$), $\Sigma(\mathrm{gas})$ is the atomic (H I) + molecular (H_2) gas surface density ($M_{\odot}\ \mathrm{pc}^{-2}$), and N is a power-law index of $\simeq 1.4$, or $\simeq 1.0$ if only H_2 is included (Kennicutt 1989; Kennicutt et al. 2007; Bigiel et al. 2008; Leroy et al. 2008, 2013). Within the scatter of the KS law, there are systematic variations between galaxies and sub-regions within galaxies, suggesting that this law may not be universal (Shetty et al. 2013). For instance, below $\Sigma(\mathrm{gas}) \simeq 10\ M_{\odot}\ \mathrm{pc}^{-2}$ and $\Sigma(\mathrm{SFR}) \lesssim 10^{-3}\ M_{\odot}\mathrm{yr}^{-1}\mathrm{kpc}^{-2}$, the stellar mass surface density Σ_* becomes important in regulating the star formation rate ($\Sigma(\mathrm{SFR}) \propto [\Sigma_*^{0.5}\Sigma(\mathrm{gas})]^{1.09}$) (Shi et al. 2011, 2018). Another example of a modification to the KS law is the Silk-Elmegreen law, which incorporates the orbital dynamical timescale $\Sigma(\mathrm{SFR}) \propto t_{\mathrm{dyn}}^{-1}\Sigma(\mathrm{gas})$ (Elmegreen 1997; Silk 1997). On the galaxy-integrated ("global") side, Gao & Solomon (2004) found a strong correlation between global measurements of HCN luminosity (a dense molecular gas tracer) and total infrared luminosity (a SFR tracer) ranging from normal spirals to ultraluminous infrared galaxies, again supporting a picture in which stars form in cold dense gas. The physical interpretation of these relationships requires an un-

derstanding of the limitations and mechanisms behind the tracers used to measure $\Sigma(\mathrm{SFR})$ and $\Sigma(\mathrm{gas})$ (e.g. Krumholz & Thompson 2007).

One manifestation of the KS law is the correlation between 12 μm luminosity, measured with the *Wide-field Infrared Survey Explorer* (*WISE*; Wright et al. 2010), and CO luminosity measured by ground-based radio telescopes. The 12 μm (also called W3) band spans mid-infrared (MIR) wavelengths of 8 to 16 μm. In nearby galaxies, 12 μm emission traces SFR (e.g. Donoso et al. 2012; Jarrett et al. 2013; Salim et al. 2016; Cluver et al. 2017; Salim et al. 2018; Leroy et al. 2019), vibrational emission lines from polycyclic aromatic hydrocarbons (PAHs), and warm dust emission (Wright et al. 2010). PAHs are excited primarily by stellar UV emission via the photoelectric effect, and the main features appear at wavelengths of 3.3, 6.2, 7.7, 8.6, 11.3, 12.7 and 16.4 μm (Bakes & Tielens 1994; Tielens 2008). Where and how PAHs form is a topic of ongoing debate, but PAH emission is associated with star formation (e.g. Peeters et al. 2004; Xie & Ho 2019; Whitcomb et al. 2020) as well as CO emission (e.g. Regan et al. 2006; Sandstrom et al. 2010; Pope et al. 2013; Cortzen et al. 2019; Li 2020). Galaxy-integrated 12 μm luminosity is strongly correlated with CO(1-0) and CO(2-1) luminosity in nearby galaxies (Jiang et al. 2015; Gao et al. 2019). Gao et al. (2019) find

$$\log\left(\frac{L_{\mathrm{CO}(1-0)}}{\mathrm{K\ km\ s^{-1}\ pc^2}}\right) = N\log\left(\frac{L_{12\ \mu\mathrm{m}}}{\mathrm{L_\odot}}\right) + \log C, \tag{3.2}$$

with $N = 0.98 \pm 0.02$ and $\log C = -0.14 \pm 0.18$, and scatter of 0.20 dex. The correlation between *WISE* 22 μm luminosity, which is dominated by warm dust emission, and CO luminosity is weaker (0.3 dex scatter) than that between 12 μm and CO (0.2 dex scatter), imply-

ing that 12 μm luminosity is a better indicator of CO luminosity than 22 μm (Gao et al. 2019). Since the prominent 11.3 μm PAH feature lies in the *WISE* 12 μm band, it is possible that the 12 μm-CO correlation is strengthened by a combination of the Kennicutt-Schmidt relation (since PAH emission traces SFR) and the link between CO emission and PAH emission. The scatter in the global 12 μm-CO fit is reduced to 0.16 dex when $g - r$ colour and stellar mass are included as extra variables in the fit (Gao et al. 2019). Empirical relationships such as these are useful for predicting molecular gas masses in galaxies, since 12 μm images are easier to obtain than CO luminosities. Mid-infrared tracers of cold gas will be particularly useful upon the launch of the *James Webb Space Telescope*, which will observe the MIR sky with better resolution and sensitivity than *WISE*.

Optical extinction A_V estimated from the Balmer decrement Hα/Hβ has also been used as an H_2 mass tracer in nearby galaxies (Güver & Özel 2009; Barrera-Ballesteros et al. 2016; Concas & Popesso 2019; Yesuf & Ho 2019; Barrera-Ballesteros et al. 2020; Yesuf & Ho 2020). The correlation between extinction (measured either by stellar light absorption A_V or gas absorption Hα/Hβ) and H_2 is due to the correlation between dust and H_2. This method is convenient since spatially resolved extinction maps are available for large samples of galaxies thanks to optical integral-field spectroscopy surveys. However, unlike 12 μm, extinction as measured by the Balmer decrement is only valid over a range that is limited by the signal-to-noise ratio of the Hβ emission line. With extreme levels of extinction, e.g. in local ultra-luminous infrared galaxies, the Hβ line becomes invisible, so this method cannot be used.

It is not yet known whether the correlation between 12 μm and CO holds at sub-galaxy

scales, or how it compares with the resolved SFR-H_2 and A_V-H_2 correlations. Comparing these correlations at resolved scales may give insight into the factors driving the 12 μm-CO correlation. The *WISE* 12 μm beam full-width at half-maximum (FWHM) is 6.6 arcsec (Wright et al. 2010), which corresponds to $\leq$ 1 kpc resolution for galaxies closer than 31 Mpc. This resolution and distance range is well-matched to the Extragalactic Database for Galaxy Evolution survey (EDGE; Bolatto et al. 2017). EDGE is a survey of CO(1-0) in 126 nearby galaxies with 4.5 arcsec spatial resolution using the Combined Array for Research in Millimeter-wave Astronomy (CARMA). One of the main goals of EDGE was to allow studies of resolved molecular gas and optical integral-field spectroscopy data in a large sample of nearby galaxies.

In this study, we use the EDGE CO and *WISE* data to measure the 12 μm and CO(1-0) correlation within individual galaxies. We find that the best-fit parameters describing this relation vary significantly among galaxies. We perform multivariate linear regression using a combination of global galaxy measurements and quantities derived from spatially resolved optical spectroscopy from the Calar Alto Legacy Integral Field Area Survey (CALIFA; Sánchez et al. 2012; Walcher et al. 2014; Sánchez et al. 2016). This yields a set of linear functions with $\log \Sigma(H_2)$ as the dependent variable which can be used as spatially resolved estimators of H_2 surface density. These estimators can predict H_2 surface density with an RMS accuracy of $\simeq$ 0.2 dex in galaxies for which 12 μm data are available.

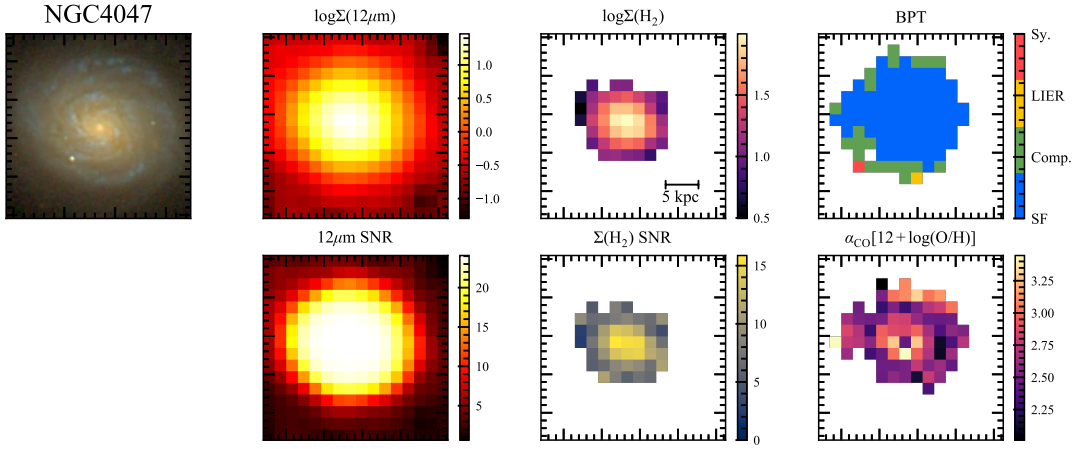

Figure 3.1: Selected maps for an example galaxy. Top row (left to right): Sloan Digital Sky Survey (SDSS; Blanton et al. 2017) *gri* thumbnail; *WISE* 12 μm surface density ($L_\odot$ pc^{-2}); H_2 mass surface density ($M_\odot$ pc^{-2}) at 6.6 arcsec resolution and assuming $\alpha_{CO} = 3.2$ $M_\odot$ (K km s^{-1} pc^2)$^{-1}$; BPT diagram for each pixel constructed from the processed CALIFA data (Section 3.2.4). The pixel size is 6 arcsec, and the cutouts are 96-by-96 arcsec. Bottom row: signal-to-noise ratio (SNR) of the 12 μm and H_2 surface density maps, and the metallicity-dependent α_{CO} values in units of $M_\odot$ (K km s^{-1} pc^2)$^{-1}$ (Equation 3.18).

3.2 Data and Data Processing

3.2.1 Sample selection

The sample is selected from the EDGE survey (Bolatto et al. 2017, hereafter B17). The typical angular resolution of EDGE CO maps is 4.5 arcsec, and the typical H_2 surface density sensitivity before deprojecting galaxy inclination is 11 $M_\odot$ pc^{-2} (B17). Every EDGE galaxy has optical integral field unit (IFU) data from CALIFA, allowing joint studies of the content and kinematics of cold gas (H_2), ionized gas, and stellar populations, all with ∼kpc spatial resolution. We processed the CO data for all 126 EDGE galaxies, and as a starting point we selected the 95 galaxies which had at least one detected pixel after smoothing to 6.6 arcsec resolution and regridding the moment-0 maps with 6 arcsec pixels (Section 3.2.3). We then selected those galaxies

with inclinations less than 75 degrees, leaving 83 galaxies. Inclination angles were derived from CO rotation curves where available (B17), and otherwise were taken from the HyperLEDA database (Makarov et al. 2014). Redshifts z (from CALIFA emission lines) and luminosity distances D_L were taken from B17. A flat ΛCDM cosmology was assumed ($h = 0.7$, $\Omega_m = 0.27$, $\Omega_\Lambda = 0.73$).

3.2.2 *WISE* 12 μm surface density maps

We downloaded 2 degree by 2 degree cutouts (pixel size 1.375 arcsec) of *WISE* 12 μm (W3) flux $F_{\rm W3}$ and uncertainty for each galaxy from the NASA/IPAC Infrared Science Archive. The background for each galaxy was estimated using the IDL package Software for Source Extraction (SExtractor; Bertin & Arnouts 1996), with default parameters and with the corresponding W3 uncertainty map as input. The estimated background was subtracted from each cutout. The background-subtracted images were reprojected with 6 arcsec pixels to avoid over-sampling the 6.6 arcsec beam. These maps were originally in units of Digital Numbers (DN), defined such that a W3 magnitude $m_{\rm W3}$ of 18.0 corresponds to $F_{\rm W3} = 1.0$ DN, or

$$F_{\rm W3} = 10^{-0.4(m_{\rm W3} - {\rm MAGZP})}\ {\rm DN}, \tag{3.3}$$

where the zero-point magnitude MAGZP $=$ 18.0 mag. We converted the maps from their original units to flux density in Jy, given by

$$S_{\mathrm{W3}} = S_0 10^{-0.4 m_{\mathrm{W3}}} \tag{3.4}$$

$$= S_0 10^{-0.4\mathrm{MAGZP}} F_{\mathrm{W3}} \tag{3.5}$$

$$= \left(\frac{31.674}{10^{7.2}} \ \mathrm{Jy\ DN^{-1}} \right) F_{\mathrm{W3}} \tag{3.6}$$

$$= \left(1.998 \times 10^{-6} \ \mathrm{Jy\ DN^{-1}} \right) F_{\mathrm{W3}}, \tag{3.7}$$

where the isophotal flux density $S_0 = 31.674$ Jy for the W3 band is from Table 1 of Jarrett et al. (2011). Luminosity in units of $\mathrm{L}_\odot$ is given by

$$L_{12\ \mu\mathrm{m}} = 4\pi D_L^2 \Delta\nu S_{\mathrm{W3}} \tag{3.8}$$

$$= 7.042 F_{\mathrm{W3}} \left(\frac{D_L}{\mathrm{Mpc}} \right)^2 \mathrm{L}_\odot \tag{3.9}$$

where $\Delta\nu = 1.1327 \times 10^{13}$ Hz is the bandwidth of the 12 μm band (Jarrett et al. 2011), and D_L is the luminosity distance. Luminosities were then converted into surface densities $\Sigma(12\ \mu\mathrm{m})$ ($\mathrm{L}_\odot\ \mathrm{pc}^{-2}$) by

$$\frac{\Sigma(12\ \mu\mathrm{m})}{\mathrm{L}_\odot\ \mathrm{pc}^{-2}} = 7.042 \left(\frac{F_{\mathrm{W3}}}{\mathrm{DN}} \right) \left(\frac{D_L}{\mathrm{Mpc}} \right)^2 \left(\frac{A_{\mathrm{pix}}}{\mathrm{pc}^2} \right)^{-1} \cos i, \tag{3.10}$$

where i is the galaxy inclination, and A_{pix} is the pixel area in pc^2.

The uncertainty in each pixel of the rebinned surface density maps is the quadrature sum of the instrumental uncertainty and the 4.5 per cent uncertainty in the zero-point magnitude

(Appendix A). Maps for an example galaxy are shown in Figure 3.1.

3.2.3 H_2 surface density maps at *WISE* W3 resolution

The original CO(1-0) datacubes were downloaded from the EDGE website,* converted from their native units of K km s^{-1} to Jy beam^{-1} km s^{-1}, and then smoothed to a Gaussian beam with FWHM $=$ 6.6 arcsec using the Common Astronomy Software Applications (CASA; McMullin et al. 2007) task `imsmooth` to match the *WISE* resolution. The cubes have a velocity resolution of 20 km s^{-1}, and span 44 channels (880 km s^{-1}). Two methods were used to obtain CO integrated intensity (moment-0) maps $S_{\rm CO}\Delta v$:

> Method 1: an iterative masking technique for improving SNR, described in Sun et al. (2018), shown in Figure 3.1, and
>
> Method 2: integrating the flux along the inner 34 channels (680 km s^{-1} total). In this "simple" method, the first 5 and last 5 channels were used to compute the root-mean-square (RMS) noise at each pixel.

Method 1 is used for all results in this work, while Method 2 is used as a cross-check and to estimate upper limits for non-detected pixels.

In Method 1 (described in Sun et al. 2018) a mask is generated for the datacube to improve the signal-to-noise of the resulting moment-0 map. A "core mask" is generated by requiring SNR of 3.5 over 2 consecutive channels (channel width of 20 km s^{-1}), and a "wing mask" is generated by requiring SNR of 2.0 over 2 consecutive channels. The core mask is dilated within

*https://mmwave.astro.illinois.edu/carma/edge/bulk/180726/

the wing mask to generate a "signal mask" which defines detections. Any detected regions that span an area less than the area of the beam are masked. The signal mask is then extended spectrally by ± 1 channels. Method 2 gives a map with lower signal-to-noise, but is useful for computing upper-limits for pixels which are masked in Method 1, and for cross-checking results.

The moment-0 maps were then rebinned with 6 arcsec pixels, and the units were converted to integrated intensity per pixel

$$\frac{S_{\rm CO}\,\Delta v}{\rm Jy\ km\ s^{-1}\ pixel^{-1}} = \left(\frac{S_{\rm CO}\,\Delta v}{\rm Jy\ beam^{-1}\ km\ s^{-1}}\right)\frac{4\theta_{\rm pix}^2\ln 2}{\pi {\rm FWHM}^2}, \tag{3.11}$$

where the beam FWHM $= 6.6$ arcsec, and the pixel size $\theta_{\rm pix} = 6$ arcsec.

The total noise variance in each pixel is the sum in quadrature of the instrumental noise which we assume to be the same for both moment-0 map versions, and calibration uncertainty which depends on the moment-0 method (Appendix B). Instrumental noise maps were computed by measuring the RMS in the first five and final five channels at each pixel (Method 2 above). The instrumental noise maps were rebinned (added in quadrature, then square root) into 6 arcsec pixels. To obtain the *total* noise for each moment-0 map, a calibration uncertainty of 10 per cent (B17) of the rebinned moment-0 map (both versions described above) was added in quadrature with the instrumental uncertainty. The sensitivity of the CO data is worse than that of *WISE* W3, and so upper limits for undetected pixels are calculated with the second moment-0 map-making method. All pixels detected at less than 3σ in CO were assigned an upper limit of 5 times the noise at each pixel.

The CO(1-0) luminosity and noise maps (in units of K km s^{-1} pc^2) were computed via (Bo-

latto et al. 2013)

$$L_{\mathrm{CO}(1-0)} = \frac{2453(S_{\mathrm{CO}}\Delta v)D_L^2}{1+z}, \tag{3.12}$$

where z is the redshift. The luminosity maps were converted to H_2-mass surface density $\Sigma(H_2)$ using a CO-to-H_2 conversion factor α_{CO}

$$\Sigma(\mathrm{H_2}) = \frac{\alpha_{\mathrm{CO}} L_{\mathrm{CO}} \cos i}{A_{\mathrm{pix}}}, \tag{3.13}$$

where i is the galaxy inclination angle, and A_{pix} is the pixel area in pc^2. In normal star-forming regions a CO-to-H_2 conversion factor of $\alpha_{\mathrm{CO}} = 3.2\ \mathrm{M_\odot (K\ km\ s^{-1}\ pc^2)^{-1}}$ (multiply by 1.36 to include helium) is often assumed (Bolatto et al. 2013). We consider both a constant α_{CO} and a spatially-varying metallicity-dependent α_{CO} (Section 3.2.5).

3.2.4 Maps of stellar population and ionized gas properties

In the third data release (DR3) of the CALIFA survey there are 667 galaxies observed out to at least two effective radii with $\simeq$ 2.5 arcsec angular resolution over wavelengths 3700-7500 Å (Sánchez et al. 2012, 2016). The observations were carried out in either a medium spectral resolution mode ("V_{1200}," $R \simeq 1700$, 3700-4200 Å, 484 galaxies) or a low spectral resolution mode ("V_{500}," $R \simeq 850$, 3750-7500 Å, 646 galaxies). Cubes using data from both V_{1200} and V_{500} were made by degrading the spectral resolution of the V_{1200} cube to that of V_{500} and averaging the spectra where their wavelength coverage overlaps, and using only V_{1200} or V_{500} for the remaining wavelength bins between 3700-7140 Å (Sánchez et al. 2016). Combined $V_{1200} + V_{500}$

datacubes and V_{500} datacubes were downloaded from the CALIFA DR3 webpage.[†] Of the 95 EDGE galaxies detected in CO, combined $V_{1200} + V_{500}$ datacubes are available for 87 galaxies. V_{500} datacubes were used for the remaining 8 galaxies. We refer to this sample of 8 + 87 galaxies as "Sample A" (Table 3.1).

[†] https://califaserv.caha.es/CALIFA_WEB/public_html/?q=content/califa-3rd-data-release

Table 3.1: Summary of the number of pixels and galaxies at each stage of sample selection. Note that Samples B and C are selected from Sample A. Sample C is the starting point for Section 3.3.2 onwards.

Sample label	Criteria	# pixels	# galaxies	Where used
A	At least one CO-detected pixel,* and have $V_{500} + V_{1200}$ or just V_{500} CALIFA datacubes	2317†	95	
B	A $\cap$ Have at least 4 CO-detected pixels per galaxy and inclination $i < 75$ deg‡	2059	83	Figures 3.3, D2
C	A $\cap$ Have at least 4 CO-detected pixels classified as star-forming per galaxy and $i < 75$ deg	1168	64	Figures 3.2, 3.3, 3.4, 3.5, 3.8

* Using Method 1 (Section 3.2.3).

† CO-detected pixels only.

‡ The reduction in the number of pixels and galaxies when going from Sample A to Sample B is entirely from the inclination cut.

The native pixel size of a CALIFA cube is 1 arcsec. The spaxels were stacked into 6 arcsec spaxels to be compared with the *WISE* and EDGE CO data. Spectral fitting was performed on the stacked spectra using the Penalized Pixel-Fitting (pPXF) Python package (Cappellari 2017) to obtain 2D maps of emission and absorption line fluxes, equivalent widths, and velocity dispersions, as well as stellar population properties such as stellar mass and light-weighted stellar age. A Kroupa initial mass function (IMF) was assumed (Kroupa & Weidner 2003).

Line fluxes were corrected for extinction using the Balmer decrement. Stellar mass was measured from the datacubes after subtracting a dust extinction curve using the method of Li et al. (2020). The unattenuated Hα emission line flux $F_{\mathrm{H}\alpha}$ is related to the observed (attenuated) flux according to

$$F_{\mathrm{H}\alpha} = F_{\mathrm{H}\alpha,\mathrm{obs.}} 10^{0.4 A_V} \tag{3.14}$$

where the extinction is given by

$$A_V = 5.86 \log \left(\frac{F_{\mathrm{H}\alpha,\mathrm{obs.}}}{2.86 F_{\mathrm{H}\beta,\mathrm{obs.}}} \right), \tag{3.15}$$

and $F_{\mathrm{H}\alpha,\mathrm{obs.}}$ and $F_{\mathrm{H}\beta,\mathrm{obs.}}$ are the observed (attenuated) line fluxes. The star formation rate (SFR) surface density is given by

$$\Sigma(\mathrm{SFR}) = \frac{C_{\mathrm{SFR},\mathrm{H}\alpha} L_{\mathrm{H}\alpha}}{A_{\mathrm{pix}}} \tag{3.16}$$

$$= \frac{C_{\mathrm{SFR},\mathrm{H}\alpha} F_{\mathrm{H}\alpha} 4\pi d^2 \cos i}{A_{\mathrm{pix}}}, \tag{3.17}$$

where the Hα luminosity-to-SFR calibration factor $C_{\mathrm{SFR,H}\alpha} = 5.3 \times 10^{-42} \frac{M_\odot\ \mathrm{yr}^{-1}}{\mathrm{erg\ s}^{-1}}$ (Hao et al. 2011; Murphy et al. 2011; Kennicutt & Evans 2012), d is the luminosity distance in cm, and A_{pix} is the pixel area in kpc^2.

The mechanism of gas ionization at each pixel was classified as either star formation (SF), low-ionization emission region (LIER), Seyfert (Sy) or a combination of star formation and AGN ("composite") on a Baldwin, Phillips, and Terlevich (BPT) diagram (Baldwin et al. 1981). It is important to identify non-starforming regions, especially when estimating SFR from Hα flux. BPT classification (Figure 3.1) was done in the [O III] λ5007/Hβ vs. [N II] λ6584/Hα plane using three standard demarcation curves in this space: Eq. 5 of Kewley et al. (2001), Eq. 1 of Kauffmann et al. (2003), and Eq. 3 of Cid Fernandes et al. (2010) (see Figure 7 of Husemann et al. 2013).

3.2.5 CO-to-H_2 conversion factor

The CO-to-H_2 conversion factor α_{CO} increases slightly with decreasing metallicity (Maloney & Black 1988; Wilson 1995; Genzel et al. 2012; Bolatto et al. 2013). At lower metallicities, and consequently lower dust abundance (Draine et al. 2007) and dust shielding, CO is preferentially photodissociated relative to H_2. This process leads to an increase in α_{CO} (Bolatto et al. 2013).

A metallicity-dependent α_{CO} equation (Genzel et al. 2012) was calculated at each star-forming pixel (Figure 3.1)

$$\log\left(\frac{\alpha_{\mathrm{CO}}}{\mathrm{M}_\odot(\mathrm{K\ km\ s^{-1}\ pc^2})^{-1}}\right) = a + b[12 + \log(\mathrm{O/H})], \tag{3.18}$$

where $a = 12 \pm 2$, and $b = -1.30 \pm 0.25$. Gas-phase metallicity $12 + \log(\mathrm{O/H})$ was computed for the star-forming pixels using

$$12 + \log(\mathrm{O/H}) = p + q \log\left(\frac{[\mathrm{N\,II}]\ \lambda 6584}{\mathrm{H}\alpha}\right), \tag{3.19}$$

where $p = 9.12 \pm 0.05$, and $q = 0.73 \pm 0.10$ (Denicoló et al. 2002). Following other works that have used this $\alpha_{\mathrm{CO}}(Z)$ relation (e.g. Genzel et al. 2015; Tacconi et al. 2018; Bertemes et al. 2018), we consciously choose not to include the uncertainty on $\alpha_{\mathrm{CO}}(Z)$ (which comes from the uncertainties in a, b, p, and q) in our analysis, so that the uncertainties on $\log \Sigma(\mathrm{H_2})$ only reflect measurement and calibration uncertainties and not systematic uncertainties in the conversion factor.

The metallicity-dependent $\alpha_{\mathrm{CO}} = \alpha_{\mathrm{CO}}(Z)$ (Eq. 3.18) is our preferred α_{CO} because it is the most physically accurate. This choice of α_{CO} has two effects on the sample:

1. the exclusion of non-starforming pixels; and
2. galaxies that have fewer star-forming pixels with CO detections than a given threshold are removed from the sample.

To assess the impacts of these effects, three α_{CO} scenarios are considered:

1. $\alpha_{\mathrm{CO}} = 3.2$, using all pixels (star-forming or not);
2. $\alpha_{\mathrm{CO}} = 3.2$, only using star-forming pixels; and
3. a metallicity-dependent $\alpha_{\mathrm{CO}} = \alpha_{\mathrm{CO}}(Z)$ (Eq. 3.18).

The impact of only considering star-forming pixels on the total number of pixels and galaxies (Table 3.1) varies depending on how many pixels per galaxy are required. For example, starting from the 95 galaxies in Sample A (Table 3.1), if we require at least 4 CO-detected pixels per galaxy, our sample will consist of 83 galaxies and 2059 pixels (Sample B). If we require at least 4 CO-detected star-forming pixels per galaxy (e.g. to apply a metallicity-dependent α_{CO}), we would have to remove 43% of the pixels and 22% of the galaxies from the sample, and would be left with 1168 pixels and 64 galaxies (Sample C). In the analysis that follows, we use Sample C exclusively except for comparison with Sample B in Section 3.3.1.

3.3 Analysis and Results

3.3.1 The degree of correlation between $\Sigma(12\ \mu m)$ and $\Sigma(H_2)$

Previous work has shown a strong correlation between integrated *WISE* 12 μm luminosity and CO(1-0) luminosity (Jiang et al. 2015; Gao et al. 2019). To determine if this correlation holds at sub-galaxy spatial scales, we matched the resolution of the EDGE CO maps to *WISE* W3 resolution and compared surface densities pixel-by-pixel for each galaxy (Figure 3.2). This comparison indicates that there is a clear correlation between $\Sigma(12\ \mu m)$ and $\Sigma(H_2)$, and that within galaxies, the correlation is strong.

To quantify the strength of the correlation per galaxy, the Pearson correlation coefficient between $\log \Sigma(12\ \mu m)$ and $\log \Sigma(H_2)$ was calculated for each galaxy. The distribution of correlation coefficients across all galaxies was computed separately for each α_{CO} scenario (Section 3.2.5; Figure 3.3). The means for the three distributions are:

1. 0.79 for $\alpha_{\rm CO} = 3.2$, all pixels included;

2. 0.79 for $\alpha_{\rm CO} = 3.2$, star-forming pixels only; and

3. 0.76 for $\alpha_{\rm CO}(Z)$ (Eq. 3.18).

These results indicate that there are strong correlations between $\Sigma(12\ \mu{\rm m})$ and $\Sigma({\rm H_2})$ regardless of the $\alpha_{\rm CO}$ assumed. A minority of galaxies show poor correlations (4 out of 95 galaxies with correlation coefficients < 0.2). Reasons for poor correlations include fewer CO-detected pixels, and small dynamic range in the pixels that are detected (e.g. a region covering multiple pixels with uniform surface density).

For comparison, cumulative histograms of the correlation coefficients between $\log \Sigma_{\rm SFR}$ (Eq. 3.16) and $\log \Sigma({\rm H_2})$ were computed (right panel of Figure 3.3). The same sets of galaxies and pixels were used as in the left panel of Figure 3.3, except the "$\alpha_{\rm CO} = 3.2$, all pix." version is excluded, because $\log \Sigma_{\rm SFR}$ can only be calculated in star-forming pixels. The mean and median correlation coefficients are lower than those in the left panel of Figure 3.3. Since the same pixels are used, this suggests a stronger correlation between $\Sigma(12\ \mu{\rm m})$ and $\Sigma({\rm H_2})$ than between $\Sigma_{\rm SFR}$ and $\Sigma({\rm H_2})$.

3.3.2 Bayesian linear regression

The relationship between 12 μm and CO emission resembles the Kennicutt-Schmidt relation, which also shows variation from galaxy to galaxy (Shetty et al. 2013). We model the relationship

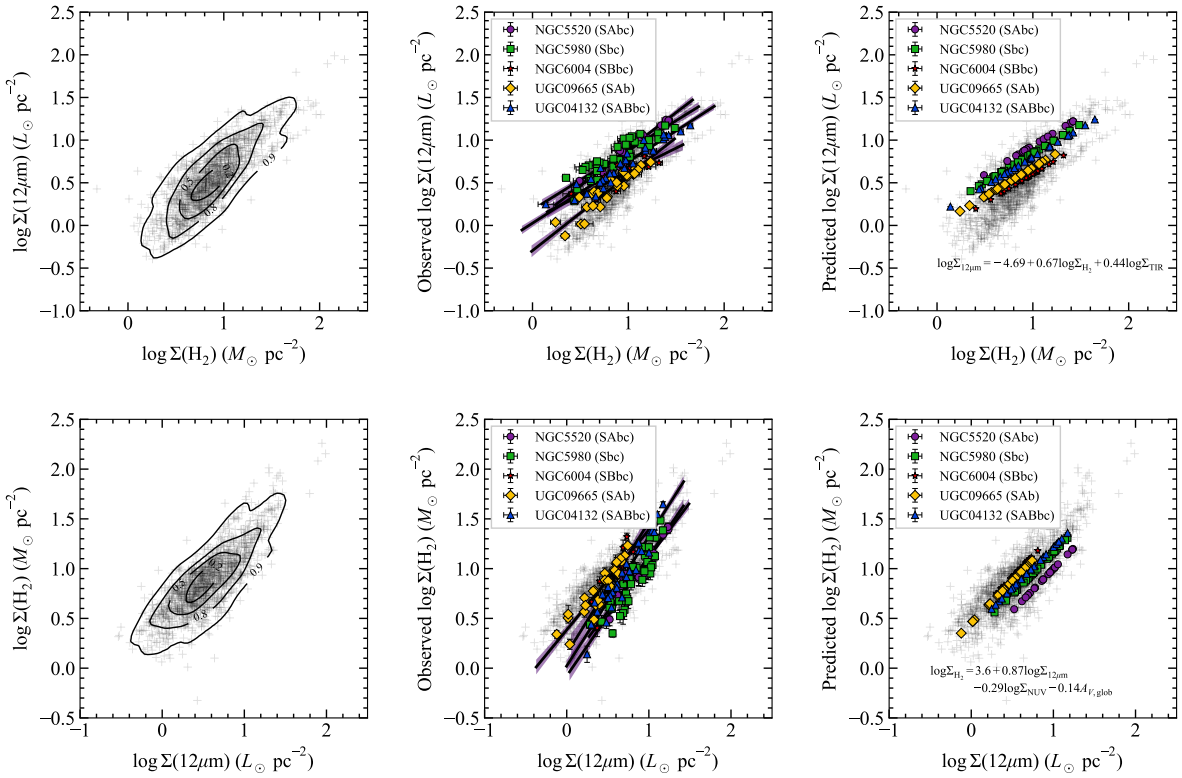

Figure 3.2: 12 μm surface density versus H_2 surface density (*top*) and vice versa (*bottom*) assuming a metallicity-dependent α_{CO} (Section 3.2.5). Only star-forming pixels that are detected in CO are shown. *Left:* The grey points are all pixels, and the fraction of pixels enclosed by each contour are indicated. The grey points are the same in all panels. *Middle:* Observed values of $\log \Sigma(12\ \mu m)$ (top) and $\log \Sigma(H_2)$ (bottom) are shown on the y-axes. The pixel values and best linear fits for five example galaxies from Sample C (Table 3.1) are coloured to illustrate some of the variation in the correlations found. Hubble types from CALIFA DR3 are indicated in the legend for the five selected galaxies. *Right:* Predicted values are shown on the y-axes using selected multi-parameter estimators (Table 3.3). The predictions were made from fits to the pixels from all galaxies except for the galaxy being predicted, to mimic the case where these estimators would be used on a galaxy outside of the sample in this work.

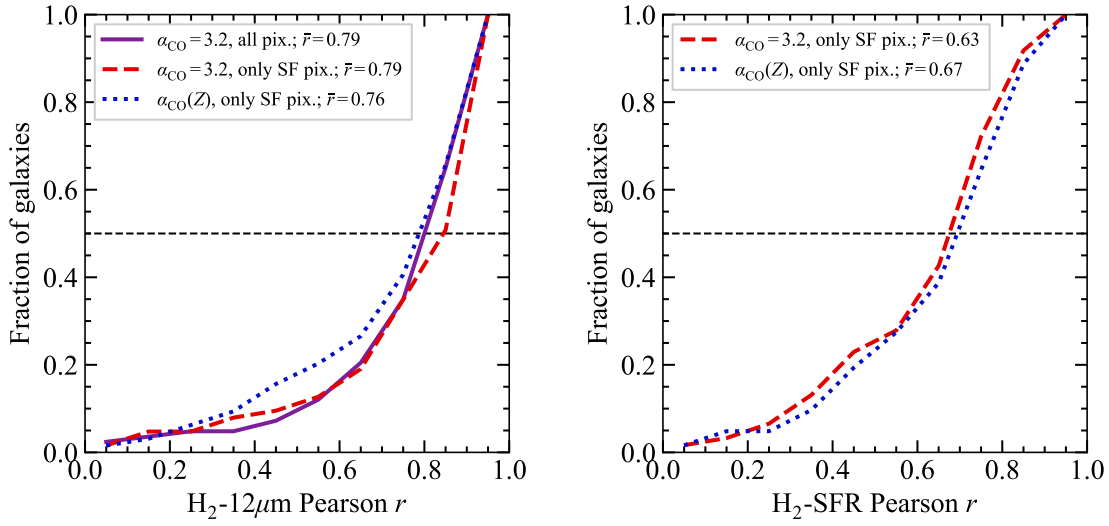

Figure 3.3: *Left:* Cumulative histogram of the Pearson correlation coefficient between $\log \Sigma(H_2)$ and $\log \Sigma(12\ \mu m)$ for each galaxy with a minimum of 4 CO-detected pixels each. *Right:* Same as left except between $\log \Sigma(H_2)$ and $\log \Sigma_{SFR}$. The three colours are for different α_{CO} assumptions: (1) $\alpha_{CO} = 3.2$ and including all pixels, (2) $\alpha_{CO} = 3.2$ including only star-forming pixels, and (3) metallicity-dependent α_{CO} (Eq. 3.18). There are 83, 64, and 64 galaxies shown in the purple, red, and blue histograms respectively. A strong correlation is found for most galaxies, for each α_{CO} assumption; however, the mean and median correlations between Σ_{SFR} and $\Sigma(H_2)$ are not as strong as those between $\Sigma(12\ \mu m)$ and $\Sigma(H_2)$. The same galaxies and pixels were used in both panels, so the differences are not due to a selection effect.

between $\log \Sigma(12\ \mu\mathrm{m})$ and $\log \Sigma(\mathrm{H_2})$ with a power-law

$$\log \Sigma(\mathrm{H_2}) = N \log \Sigma(12\ \mu\mathrm{m}) + \log C. \tag{3.20}$$

To determine whether the 12 μm-CO relation is universal or not, we performed linear fits of $\log \Sigma(\mathrm{H_2})$ against $\log \Sigma(12\ \mu\mathrm{m})$ for each galaxy with at least 4 CO-detected star-forming pixels (Sample C in Table 3.1; middle panel of Figure 3.2). A metallicity-dependent α_{CO} was used in Figure 3.2. These fits were performed using LinMix, a Bayesian linear regression code which incorporates uncertainties in both x and y (Kelly 2007). We repeated the fits for each α_{CO} (Sec. 3.2.5) and with $\log \Sigma(\mathrm{H_2})$ on the x-axis instead.

For a given galaxy, the best-fit parameters do not vary much depending on the α_{CO} assumed, provided there are enough pixels to perform the fit even after excluding non-starforming pixels. The fit parameters are also not significantly different if we include upper limits in the fitting. However, we find significant differences in the slope and intercept from galaxy to galaxy, indicating a non-universal resolved relation. The galaxy-to-galaxy variation in best-fit parameters persists for all three α_{CO} scenarios. The galaxy-to-galaxy variation can be seen in the distribution of slopes and intercepts assuming a metallicity-dependent α_{CO} for example (Figure 3.4). The best-fit intercepts span a range of $\simeq$ 1 dex (-0.31 to 0.87, median 0.41), and the slopes range from 0.20 to 2.03, with a median of 1.13. To quantify the significance of the galaxy-to-galaxy variation in best-fit parameters, residuals in the parameters relative to the mean parameters were computed. For example, if the measurement of the slope for galaxy i is $N_i \pm \sigma_{N_i}$, the residual relative to the average slope over all galaxies $\bar{N}$ is $(N_i - \bar{N})/\sigma_{N_i}$. Similarly, if the measure-

ment of the intercept for galaxy i is $\log C_i \pm \sigma_{\log C_i}$, the residual relative to the average intercept over all galaxies $\overline{\log C}$ is $(\log C_i - \overline{\log C})/\sigma_{\log C_i}$. The residual histograms (Figure 3.4) show that most of the slopes N_i are within $\simeq 1.5\sigma_{N_i}$ of $\bar{N}$, but the intercepts show more significant deviations (many beyond $3\sigma_{\log C_i}$).

To establish how well-fit all pixels are to a single model, linear fits were done on all CO-detected pixels from all 83 galaxies in Sample B (Table 3.1) using LinMix (black crosses in Figure 3.5). The fits were done separately for luminosities ($\log L_{12\ \mu\mathrm{m}}$, $\log L_{\mathrm{CO}}$; left panel of Figure 3.5) and surface densities ($\log \Sigma(12\ \mu\mathrm{m})$, $\log \Sigma(\mathrm{H_2})$; right panel of Figure 3.5). For completeness, the fits were also done with $\mathrm{CO}/\mathrm{H_2}$ on the x-axis (Figure D1). In all cases there are strong correlations (correlation coefficients of $\simeq 0.90$), and good fits (total scatter about the fit $\sigma_{\mathrm{tot}} \simeq 0.19$ dex). By comparing the total scatter σ_{tot} and intrinsic scatter σ_{int} (Appendix C), it is clear that most of the scatter is intrinsic rather than due to measurement and calibration uncertainties. Note that in the right hand panel of Figure 3.5, ignoring the α_{CO} uncertainty means that the $\Sigma(\mathrm{H_2})$ uncertainty has been underestimated, and therefore the intrinsic scatter σ_{int} (derived from σ_{tot} and the uncertainty on $\Sigma(\mathrm{H_2})$, Equation C9) has been overestimated. Also, if we replace $\Sigma(\mathrm{H_2})$ with $\Sigma(\mathrm{CO})$, σ_{tot} decreases by only 0.01 dex and σ_{int} does not change, which indicates that the scatter is dominated by that of the 12 μm-CO surface density relationship. Consequently, σ_{int} in the right hand panel of Figure 3.5 should be interpreted as the intrinsic scatter in the 12 μm-CO surface density relationship.

Similarly, to establish how well-fit all *global values* are to a single model, linear fits were done on the galaxy-integrated values (green diamonds in Figure 3.5) for all 83 galaxies in Sample B

(Table 3.1). The results show good fits overall (correlation coefficients of $\simeq 0.90$, scatter about the fit $\sigma_{\rm tot} \simeq 0.20$ dex). The global values do indeed follow uniform trends (with the exception of one outlier), and the global fits with molecular gas on the x-axis show steeper slopes and smaller y-intercepts than the pixel fits (Figure 3.5). The global fits with 12 μm on the x-axis show shallower slopes and larger y-intercepts than the pixel fits.

3.3.3 Spatially resolved estimator of $\Sigma(H_2)$

To develop an estimator of $\log \Sigma(H_2)$ from $\log \Sigma(12\ \mu m)$ and other galaxy properties, we performed linear regression on all of the star-forming pixels from all galaxies combined. Global properties (from UV, optical, and infrared measurements) and resolved optical properties were included (Table 3.2). The model is

$$\vec{y} = \theta_0 + \sum_i \theta_i \vec{x_i}, \tag{3.21}$$

where each entry of $\vec{y}$ is $\log \Sigma(H_2)$ for each pixel of each galaxy (using the metallicity-dependent $\alpha_{\rm CO}$, Eq. 3.18), the θ are the fit parameters, and the sum is over i properties (a combination of pixel properties or global properties). We used ridge regression, implemented in the Scikit-Learn Python package (Pedregosa et al. 2012), which is the same as ordinary least squares regression except it includes a penalty in the likelihood for more complicated models. The penalty term is the sum of the squared coefficients of each parameter $\delta \sum_i \theta_i^2$. The regularization parameter δ (a scalar) sets the impact of the penalty term. The best value of δ was determined by cross-validation using `RidgeCV`. In ridge regression it is important to standardize the data prior

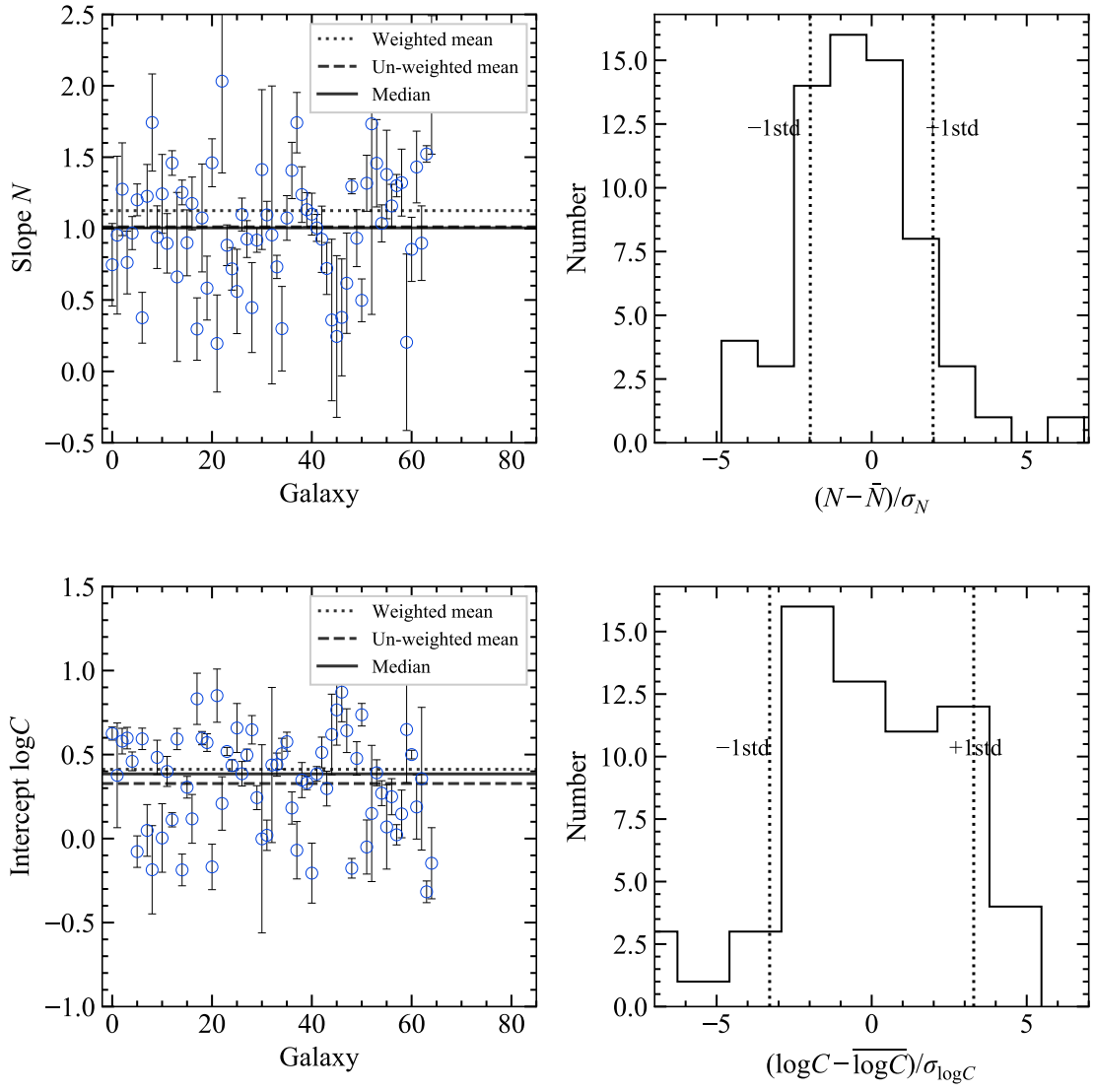

Figure 3.4: Best-fit slope N (top) and intercept log C (bottom) of fits to individual pixel measurements of log $\Sigma(12\ \mu\mathrm{m})$ (x-axis) versus log $\Sigma(\mathrm{H_2})$ (y-axis). Each point is for one galaxy. A metallicity-dependent α_{CO} was used, so only star-forming pixels were used in the fits. At least 4 CO-detected star-forming pixels per galaxy were required (Sample C, Table 3.1). Left: The horizontal lines show the inverse-variance weighted means (dotted), un-weighted means (solid), and medians (dashed). Right: Histograms of the residuals for each galaxy relative to the weighted mean, divided by the uncertainty for each galaxy. The vertical lines indicate ± 1 times the standard deviation of each distribution.

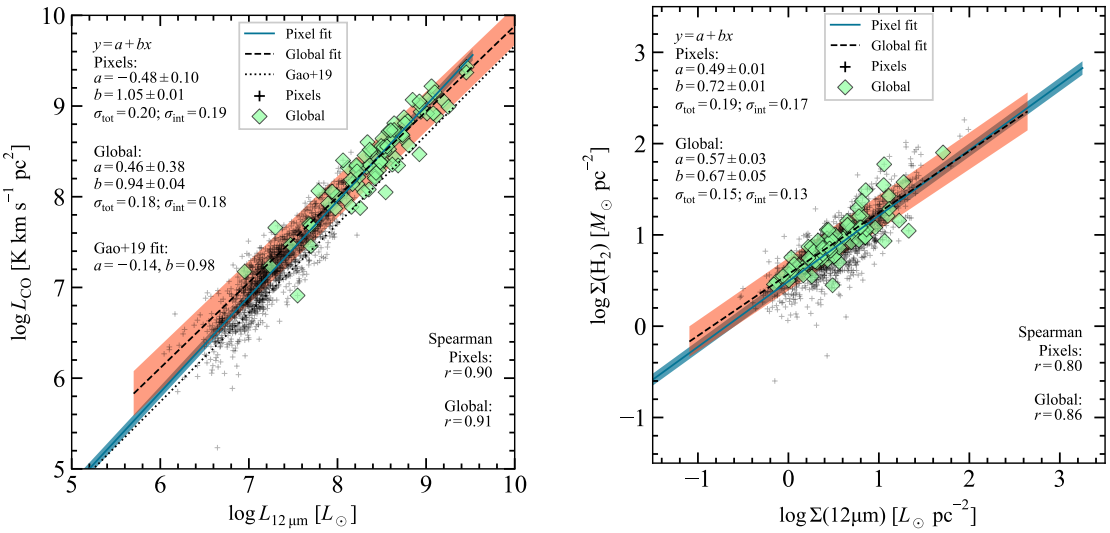

Figure 3.5: Measurements of 12 μm and H_2 (or CO) using all individual pixels from all galaxies in the sample (black crosses), and the galaxy-integrated values (diamonds). The fits (Section 3.3.2) were done separately for the pixel measurements (blue regions) and the global measurements (red regions). Best-fit parameters assuming a power-law model (Equation 3.20), and the total $\sigma_{\rm tot}$ and intrinsic $\sigma_{\rm int}$ scatter (Appendix C) about the fits are indicated. The left and right panels show the fits to luminosities and surface densities respectively. H_2 surface densities were calculated using a metallicity-dependent $\alpha_{\rm CO}$ (Equation 3.18). Note that in the right hand panel, ignoring $\alpha_{\rm CO}$ uncertainty means that the $\Sigma(H_2)$ uncertainty has been underestimated, and therefore the intrinsic scatter $\sigma_{\rm int}$ (derived from $\sigma_{\rm tot}$ and the uncertainty on $\Sigma(H_2)$, Equation C9) has been overestimated. Also, if we replace $\Sigma(H_2)$ with $\Sigma(CO)$, $\sigma_{\rm tot}$ decreases by only 0.01 dex and $\sigma_{\rm int}$ does not change, which indicates that the scatter is dominated by that of the 12 μm-CO surface density relationship. Consequently, $\sigma_{\rm int}$ in the right panel should be interpreted as the intrinsic scatter in the 12 μm-CO surface density relationship. For completeness, versions of these plots using the same data but with the x and y axes interchanged are shown in Figure D1, and versions with a constant $\alpha_{\rm CO}$ and non-starforming pixels included are shown in Figure D2.

to fitting (subtract the sample mean and divide by the standard deviation for all global properties and pixel properties) so that the penalty term is not affected by different units or spreads of the properties. The standardized version of Equation 3.21 is

$$\vec{y} - \text{mean}(\vec{y}) = \sum_i \tilde{\theta}_i \left[\frac{\vec{x_i} - \text{mean}(\vec{x_i})}{\text{std}(\vec{x_i})} \right]. \tag{3.22}$$

Note that it is not necessary to divide $\vec{y} - \text{mean}(\vec{y})$ by $\text{std}(\vec{y})$ because it does not impact the regularization term. After performing ridge regression on the standardized data (which provides $\tilde{\theta}_i$), the best-fit coefficients in the original units are given by

$$\theta_i = \frac{\tilde{\theta}_i}{\text{std}(\vec{x_i})}. \tag{3.23}$$

The intercept θ_0 is given by

$$\theta_0 = \text{mean}(\vec{y}) - \sum_i \tilde{\theta}_i \left[\frac{\text{mean}(\vec{x_i})}{\text{std}(\vec{x_i})} \right]. \tag{3.24}$$

Table 3.2: Global properties (top) and pixel properties (bottom) considered in the multi-parameter fits (Section 3.3.3). The SFR and stellar masses from B17 were both multiplied by 0.66 to convert from Salpeter to Kroupa IMF (Madau & Dickinson 2014). Global SFR, M_*, and luminosities were converted to surface densities by dividing by $2\pi r_{50}^2$, where r_{50} is the i-band half-light radius in kpc from Gilhuly & Courteau (2018).

Label	Units	Reference	Description
			Global Properties
$12 + \log \mathrm{O/H}_{\mathrm{glob}}$	dex	B17	[O III]/[N II]-based gas-phase metallicity
$\log \Sigma_{\mathrm{SFR,glob}}$	$\mathrm{M}_\odot\ \mathrm{yr}^{-1}\ \mathrm{kpc}^{-2}$	B17	Star formation rate surface density ($5.3 \times 10^{-42} L(\mathrm{H}\alpha)/2\pi r_{50}^2$)
$\log \Sigma_{*,\mathrm{glob}}$	$\mathrm{M}_\odot\ \mathrm{kpc}^{-2}$	B17	Stellar mass surface density assuming a Kroupa IMF
$\log \cos i$		B17	Inclination i is either from CO kinematics, Hα kinematics, or LEDA
$\log \Sigma_{\mathrm{NUV}}$	$10^{42}\ \mathrm{erg\ s}^{-1}\ \mathrm{kpc}^{-2}$	(C15)	Near-UV surface density
$\log \Sigma_{\mathrm{FUV}}$	$10^{42}\ \mathrm{erg\ s}^{-1}\ \mathrm{kpc}^{-2}$	(C15)	Far-UV surface density
$\log \Sigma_{\mathrm{TIR}}$	$10^{43}\ \mathrm{erg\ s}^{-1}\ \mathrm{kpc}^{-2}$	(C15)	Total-IR (8-1000μm) surface density
$\log \Sigma_{\mathrm{W4}}$	$10^{42}\ \mathrm{erg\ s}^{-1}\ \mathrm{kpc}^{-2}$	(C15)	*WISE* W4 (22 μm) surface density
$u - r$	mag	B17	Colour from CALIFA synthetic photometry (SDSS filters applied to extinction-corrected spectra)
b/a		(C15)	Minor-to-major axis ratio from CALIFA synthetic photometry
$(B/T)_g$		(C15)	Bulge-to-total ratio from g-band photometry
n_g		(C15)	Sérsic index from g-band photometry
$\log \sigma_{\mathrm{bulge}}$	$\mathrm{km\ s}^{-1}$	G19	Bulge velocity dispersion (5 arcsec aperture)
$A_{V,\mathrm{glob}}$	mag	(C15)	Extinction measured from the Balmer decrement
			Pixel Properties
$12 + \log \mathrm{O/H}_{\mathrm{pix}}$	dex	Eq. 3.19	[O III]/[N II]-based gas-phase metallicity
$\log \Sigma_{\mathrm{SFR,pix}}$	$\mathrm{M}_\odot\ \mathrm{yr}^{-1}\ \mathrm{kpc}^{-2}$	Eq. 3.16	Star formation rate surface density
$\log \Sigma_{*,\mathrm{pix}}$	$\mathrm{M}_\odot\ \mathrm{pc}^{-2}$	Sec. 3.2.4	Stellar mass surface density, assuming a Kroupa IMF
$A_{V,\mathrm{pix}}$	mag	Eq. 3.15	Extinction measured from the Balmer decrement

Our goal was to identify a combination of properties such that the linear fit of $\log \Sigma(\mathrm{H_2})$ vs. these properties (including $\log \Sigma(12\ \mu\mathrm{m})$) was able to reliably predict $\log \Sigma(\mathrm{H_2})$. The $\log \Sigma(\mathrm{H_2})$-predicting ability of the fit to a given parameter combination was quantified by performing fits with one galaxy excluded, and then measuring the mean-square (MS) error of the prediction for the excluded galaxy (the "testing error")

$$\text{MS error} = \frac{1}{N_{\text{pix}}} \sum_{N_{\text{pix}}} (y_{\text{true}} - y_{\text{pred}})^2, \tag{3.25}$$

where N_{pix} is the number of pixels for this galaxy, y_{true} is the true value of $\log \Sigma(\mathrm{H_2})$ in each pixel, and y_{pred} is the predicted value at that pixel using the fit. The RMS error over all test galaxies

$$\text{RMS error} = \sqrt{\frac{1}{N_{\text{galaxies}}} \sum_{\text{galaxy}} \text{MS error}_{\text{galaxy}}} \tag{3.26}$$

was used to decide on a best parameter combination.

To identify the best possible combination of parameters we did the fit separately for all possible combinations with at least one resolved property required in each combination. We did not want to exclude the possibility of parameters other than 12 μm being better predictors of $\mathrm{H_2}$, so we included all combinations even if 12 μm was excluded. To avoid overfitting, we excluded galaxies if the number of CO-detected star-forming pixels minus the number of galaxy properties in the estimator was less than 4 (so there are at least 3 degrees of freedom per galaxy after doing the fit), and only considered models with less than 6 independent variables. We used the metallicity-dependent α_{CO}, so the sample used for these fits was Sample C (Table 3.1); how-

ever, depending on the number of galaxy properties used and the number of CO-detected star-forming pixels, the sample is smaller for some estimators. We require a minimum of 15 galaxies for each estimator.

Here we describe how the pixel selection and fitting method were used to calculate the RMS error for each combination of galaxy properties:

1. Generate all possible sets of pixels such that each set has the pixels from one galaxy left out.

2. For each set of pixels:

   (a) Compute mean($\vec{x_i}$) and std($\vec{x_i}$) of the resolved and global properties $\vec{x_i}$. Use these to standardize the data.

   (b) Perform the multi-parameter fit on the standardized data, which yields $\tilde{\theta}_i$ (Eq. 3.22).

   (c) Compute the un-standardized coefficients θ_i (Eq. 3.23) and zero-point θ_0 (Eq. 3.24).

   (d) Use these θ_0, θ_i to predict $\vec{y}$ of the excluded galaxy (Eq. 3.21).

   (e) Tabulate the mean squared-error (Eq. 3.25).

3. Compute the RMS error (Eq. 3.26) from all of the MS errors. This indicates the ability of this multi-parameter fit to predict new $\vec{y}$. The RMS error for each estimator is shown in Figure 3.6.

In practical applications outside of this work, not all of the global properties and pixel properties will be available. For this reason, we provide several $\log \Sigma(H_2)$ estimators which can be used depending on which data are available. To highlight the relative importance of resolved optical properties vs. 12 μm, the best-performing estimators based on the following galaxy properties are compared:

1. all global properties + IFU properties + 12 μm (Table 3.3),
2. all global properties + 12 μm but no IFU properties (Table 3.4),
3. all global properties + IFU properties but no 12 μm (Table 3.5).

The performance of the estimators was ranked based on their RMS error of predicted $\log \Sigma(H_2)$ (Figure 3.6). The reported estimators are those with the lowest RMS error at a given number of galaxy properties (those corresponding to the stars and squares in Figure 3.6). We estimated the uncertainty on the coefficients in each estimator by perturbing the 12 μm and H_2 data points randomly according to their uncertainties, redoing the fits 1000 times, and measuring the standard deviation of the parameter distributions.

The lack of points below the green curve in Figure 3.6 indicates that there is little to be gained by adding IFU data to the estimators with resolved 12 μm (little to no drop in RMS error). The RMS error of the estimator with only resolved A_V for example (black circle, upper left) performs significantly worse than the fit with only 12 μm (green square, lower left). Estimators with resolved 12 μm but no IFU data perform better than those with IFU data but no resolved 12 μm. There is also no improvement in predictive accuracy of the estimators using global properties

+ resolved 12 μm + no IFU data beyond a four-parameter fit (intercept, $\Sigma(12\,\mu\mathrm{m})$, Σ_{NUV}, and global A_V). The best H_2 estimators all contain $\log \Sigma(12\ \mu\mathrm{m})$, which indicates that this variable is indeed the most important for predicting H_2.

For the fits in the opposite direction, $\log \Sigma(H_2)$ was found to be the most important for predicting 12 μm. The best estimators for 1-5 galaxy properties show that if $\log \Sigma(H_2)$ is already included, there is essentially no improvement in predictive accuracy (little to no drop in RMS error) when resolved optical IFU data are included as variables in the fitting.

We compared how well these multi-parameter estimators perform relative to the one-parameter estimator from the right panel of Figure 3.5:

$$\log \Sigma(H_2) = (0.49 \pm 0.01) + (0.72 \pm 0.01) \log \Sigma(12\,\mu\mathrm{m}). \tag{3.27}$$

Note that this fit, obtained via Bayesian linear regression (Sec. 3.3.2) is consistent with the result from ridge regression (first row of Table 3.3). To compare the performance of each estimator with the fit above, predicted $\log \Sigma(H_2)$ for each pixel was computed from the one-parameter fit, and the RMS error (square root of Eq. 3.25) was computed for each galaxy (Figure 3.7). Most points lie below the 1:1 relation in Figure 3.7, indicating that the multi-parameter fits have lower RMS error per pixel than the single-parameter fit.

Table 3.3: Best-performing estimators of $\log \Sigma(\mathrm{H_2})$ (metallicity-dependent α_{CO}, Sec. 3.2.5) based on global properties + resolved 12 μm + resolved optical IFU properties (Table 3.2). Each successive row adds one galaxy property. For example, the estimator in the second row is $\log \Sigma(\mathrm{H_2}) = 2.54 + 0.78 \log \Sigma(12\ \mu\mathrm{m}) - 0.20 \log \Sigma_{\mathrm{FUV}}$. The RMS error (the accuracy of predicted $\log \Sigma(\mathrm{H_2})$ per pixel, Eq. 3.26), the number of galaxies n_{gal} and pixels n_{pix} used for the fit, and the intrinsic scatter (σ_{int}, Appendix C) are reported. Table E1 shows the best-fit results assuming $\alpha_{\mathrm{CO}} = 3.2$.

					θ_i for pixel properties		θ_i for global properties		
RMS error	n_{gal}	n_{pix}	σ_{int}	Zero-point (θ_0)	$\log \Sigma(12\ \mu\mathrm{m})$	$(12 + \log \mathrm{O/H})$	$\log \Sigma_{\mathrm{FUV}}$	$\log \Sigma_{\mathrm{NUV}}$	$A(\mathrm{H}\alpha)$
0.19	58	1126	0.17	0.48 ± 0.01	0.71 ± 0.01	–	–	–	–
0.17	30	573	0.15	2.54 ± 0.07	0.78 ± 0.01	–	-0.20 ± 0.01	–	–
0.15	27	552	0.15	3.6 ± 0.1	0.87 ± 0.01	–	–	-0.29 ± 0.01	-0.14 ± 0.01
0.14	27	552	0.14	14.6 ± 0.6	0.94 ± 0.01	-1.24 ± 0.07	–	-0.30 ± 0.01	-0.15 ± 0.01

Table 3.4: Same as Table 3.3 but the best-performing estimators based on global properties + resolved 12 μm but no resolved optical IFU properties. Table E2 shows the best-fit results assuming $\alpha_{CO} = 3.2$.

					θ_i for pixel properties	θ_i for global properties		
RMS error	n_{gal}	n_{pix}	σ_{int}	Zero-point (θ_0)	log Σ(12 μm)	log Σ_{FUV}	log Σ_{NUV}	A(Hα)
0.19	58	1126	0.17	0.47 ± 0.01	0.71 ± 0.01	–	–	–
0.17	30	573	0.15	2.54 ± 0.07	0.78 ± 0.01	-0.20 ± 0.01	–	–
0.15	27	552	0.15	3.6 ± 0.1	0.88 ± 0.01	–	-0.29 ± 0.01	-0.14 ± 0.01
0.15	27	552	0.15	3.6 ± 0.1	0.87 ± 0.01	0.03 ± 0.03	-0.31 ± 0.04	-0.14 ± 0.01

Table 3.5: Same as Table 3.3 but the best-performing estimators based on global properties + resolved optical IFU properties but no resolved 12 μm. Table E3 shows the best-fit results assuming $\alpha_{\rm CO} = 3.2$.

					θ_i for pixel properties			θ_i for global properties	
RMS error	$n_{\rm gal}$	$n_{\rm pix}$	$\sigma_{\rm int}$	Zero-point (θ_0)	$\log \Sigma_*$	$(12 + \log {\rm O/H})$	$\log \Sigma_{\rm SFR}$	$\log \Sigma_{\rm NUV}$	$b/a_{\rm disk}$
0.20	58	1126	0.19	2.00 ± 0.01	–	–	0.50 ± 0.01	–	–
0.20	42	942	0.18	1.86 ± 0.01	–	–	0.50 ± 0.01	–	0.22 ± 0.01
0.17	27	552	0.18	1.3 ± 0.1	0.18 ± 0.01	–	0.35 ± 0.01	0.01 ± 0.01	–
0.17	27	552	0.18	8.0 ± 0.6	0.23 ± 0.01	-0.81 ± 0.07	0.32 ± 0.01	0.02 ± 0.01	–

3.3.4 Dependence of the 12 μm-H_2 relationship on physical scale

To establish whether the correlation between global surface densities (12 μm vs H_2) arises from a local correlation between pixel-based surface densities, we computed residuals of the individual pixel measurements from the resolved pixel fit (right panel of Figure 3.5) with varying surface areas (Figure 3.8). For each galaxy, contiguous regions of 1, 4, 7 or 9 pixels were used to compute surface densities (the four columns of Figure 3.8). The contiguous pixels were required to be CO-detected and star-forming, as a metallicity-dependent α_{CO} was used. Each pixel was used in exactly one surface density calculation for each resolution, so all of the black circles are independent. We found that the scatter diminished as the pixel size approached the whole galaxy size. The total scatter about the individual pixel fit declines as pixel area increases, indicating that the global correlation emerges from the local one.

3.3.5 Testing the estimators for biases

To determine whether the best-fit relations are biased with respect to any global or resolved properties (Table 3.2), we performed the following tests for the best-performing H_2 estimators with 1, 2, and 3 parameters from Table 3.3.

For resolved properties, we plotted the residual in predicted vs. true $\log \Sigma(H_2)$ for each pixel versus resolved properties. We computed the Pearson-*r* between the residuals and the resolved quantities. No significant correlations were found for any of the resolved properties. This indicates that the performance of the estimators is not biased with respect to resolved properties.

For global properties, we plotted the RMS error (Equation 3.26) for each galaxy versus global

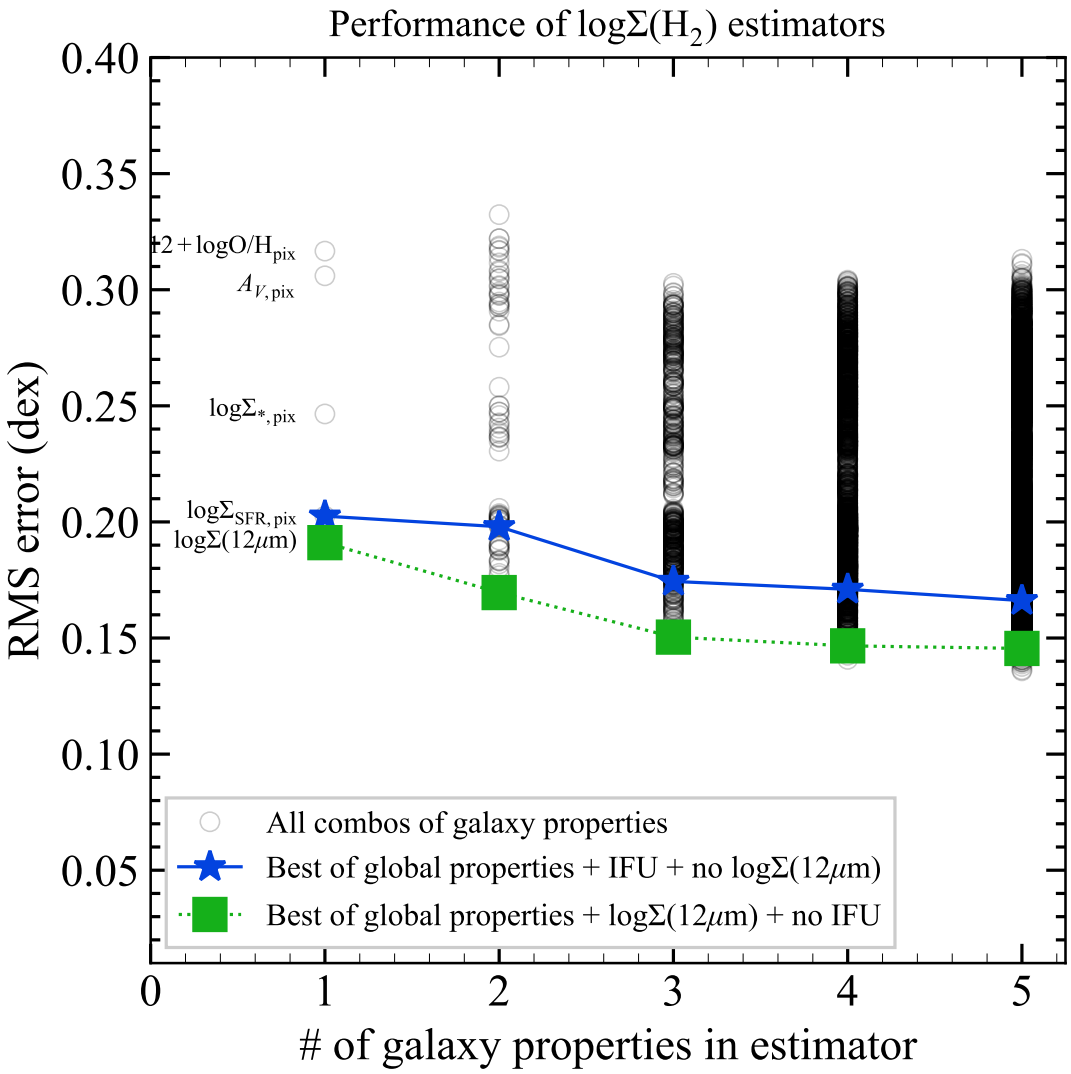

Figure 3.6: RMS error (Equation 3.26) of all estimators. Estimators with smaller RMS errors have better predictive accuracy. The RMS error decreases only slightly as the number of independent variables increases for the fits with resolved 12 μm but no IFU data. The fits with resolved 12 μm but no IFU data have lower RMS errors than those with IFU data. The lack of points below the green curve indicates that there is little to be gained by adding IFU data to the estimators with resolved 12 μm. The RMS error of the estimator with only resolved A_V for example (black circle, upper left) performs significantly worse than the fit with only 12 μm (green square, lower left).

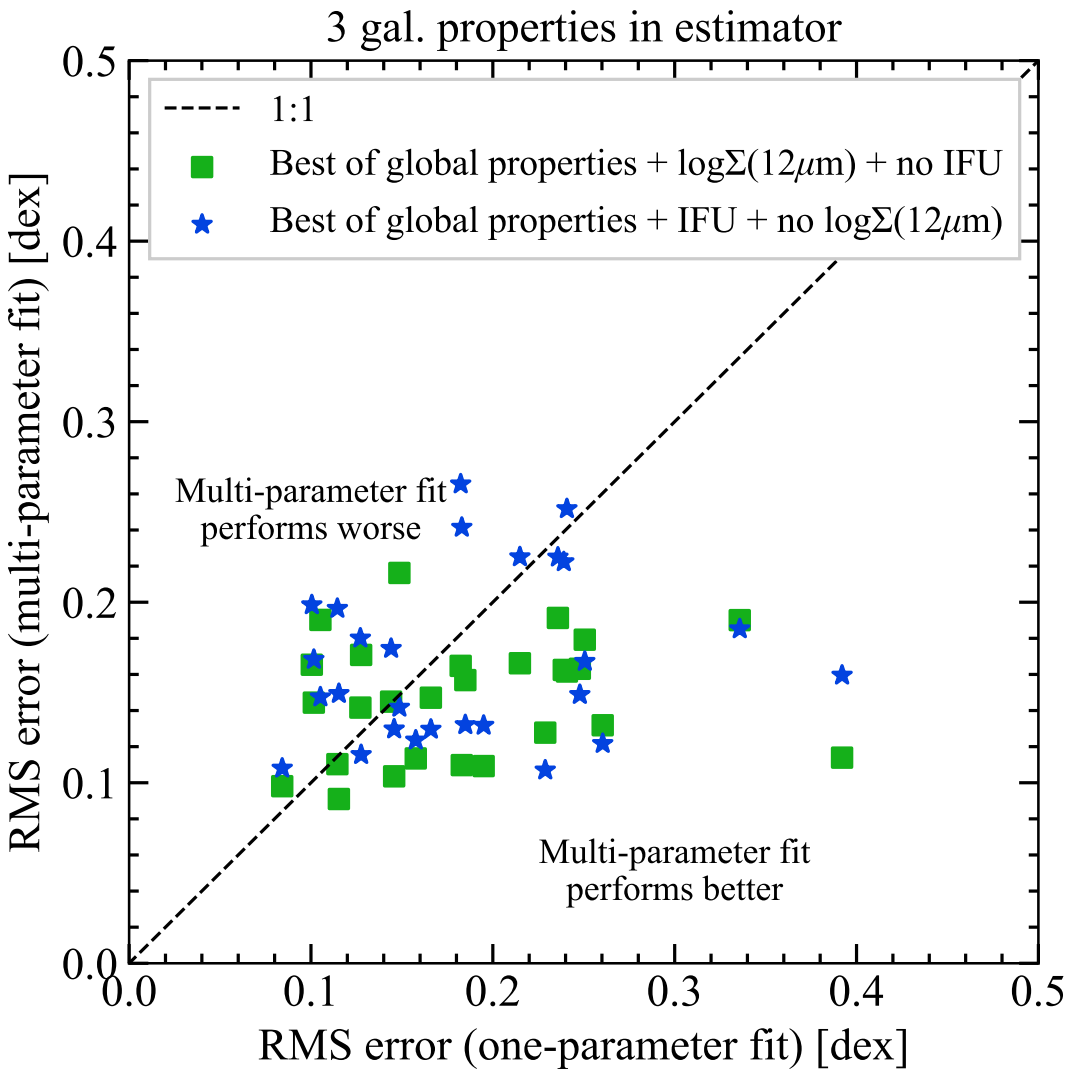

Figure 3.7: Galaxy-by-galaxy RMS error (Equation 3.26) computed from the specified multi-parameter fits with 3 galaxy properties, versus the RMS error computed from the one parameter surface density fit (Figure 3.5). The green squares and blue stars correspond to the green square and blue star in Figure 3.6 at $n = 3$ respectively. The RMS of the y-values of the green squares here gives the RMS error at $n = 3$ in Figure 3.6, and likewise for the blue stars (Equation 3.26).

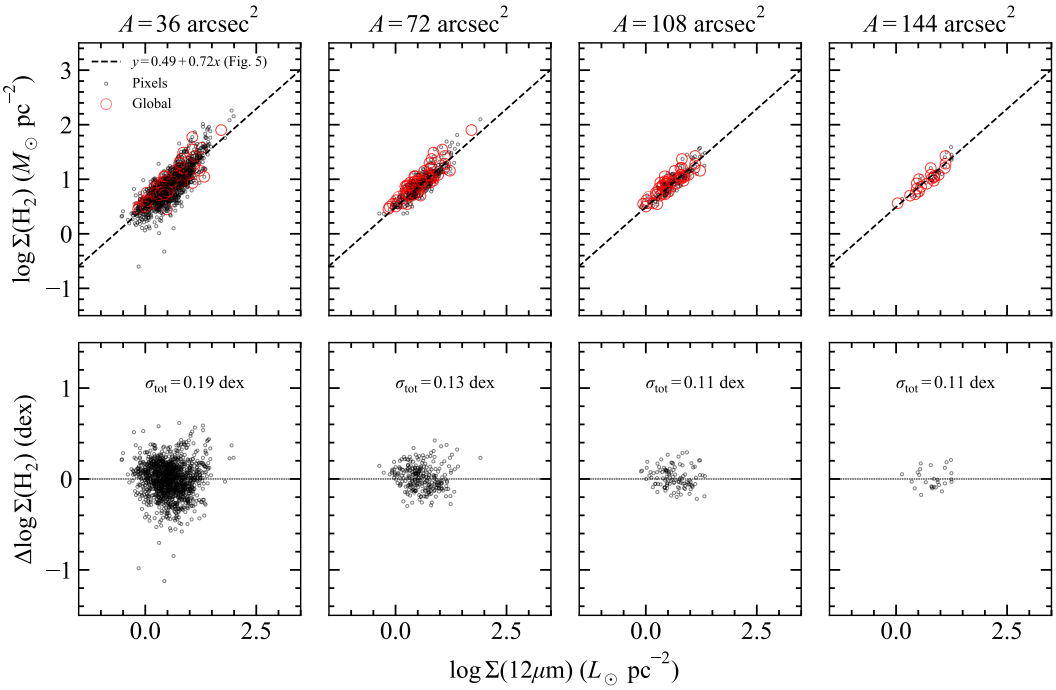

Figure 3.8: Variation of the scatter in the $\Sigma(\mathrm{H_2})$-$\Sigma(12\ \mu\mathrm{m})$ relationship with the area over which surface densities are calculated. *Top:* black points are surface densities computed over area A indicated at the top (36 arcsec^2 is one 6 arcsec pixel). Red circles are the sum of all pixels for each galaxy in the sample, and are the same in all panels in which that galaxy appears. The H_2 surface densities are computed with a metallicity-dependent α_{CO}. For each galaxy, all contiguous CO-detected, star-forming pixels with area A were used. Each pixel was used exactly once in each panel from left to right. The number of galaxies decreases from left to right because some galaxies do not have any contiguous pixels which form the specified area. The fit to individual pixels is the same in all panels. *Bottom:* residuals in 12 μm surface density, relative to the resolved pixel fit (black line) from the bottom right panel of Figure 3.5. The total scatter σ_{tot} about the resolved fit decreases as the surface area approaches the total galaxy area, suggesting that the global correlation (red circles) emerges from the resolved correlation (black circles).

properties for that galaxy. We computed the Pearson-r between the RMS error and global quantities. No significant correlations were found for any of the global properties. This indicates that the performance of the estimators is not biased with respect to global properties.

3.4 Discussion

Our findings show that significant power-law correlations between 12 μm and CO surface densities at kiloparsec scales are responsible for the observed correlation between global (galaxy-wide) measurements (Jiang et al. 2015; Gao et al. 2019). The median correlation coefficient between $\log \Sigma(12\ \mu\mathrm{m})$ and $\log \Sigma(\mathrm{H_2})$ is $\simeq$ 0.86 (per galaxy). Linear fits for each galaxy yield a range of intercepts spanning $\simeq$ 1 dex (-0.31 to 0.87, median 0.41), and a range in slopes (0.20 to 2.03, median 1.13). The 12 μm and CO luminosities computed over the CO-detected area of each galaxy in the sample are well-fit by a single power law, with a larger slope and smaller y-intercept than the fit to all individual-pixel luminosities in the sample. Linear regression on all possible combinations of resolved properties and global properties (Table 3.2) yielded several equations which can be used to estimate $\Sigma(\mathrm{H_2})$ (assuming a metallicity-dependent α_{CO}) in individual pixels. A catalog of all resolved and global properties for each pixel in the analysis is provided in machine-readable format (Table 3.6). The estimators were ranked according to the average accuracy with which they can predict $\Sigma(\mathrm{H_2})$ in a given pixel (RMS error, Eq. 3.26). The best-performing estimators (Tables 3.3, 3.4, 3.5) with 1-4 independent variables are provided, and there is only marginal improvement in prediction error beyond 3 independent variables. Out of all possible parameter combinations considered, the best-performing estimators include

resolved $\Sigma(12\ \mu\mathrm{m})$, indicating that 12 μm emission is likely physically linked to H_2 at resolved scales.

Table 3.6: Selected rows and columns of the catalog of resolved measurements for each pixel considered in the analysis. A full version with more columns and rows is available in machine-readable format. A Python script is provided which shows how to reconstruct two-dimensional images of all quantities in the catalog for each galaxy. The luminosities corresponding to the surface densities in columns 9-12 are provided in the full catalog.

Pixel ID (1)	Galaxy (2)	BPT (3)	$12 + \log \mathrm{O/H_{pix}}$ (4)	α_{CO} (5)	$\log \Sigma_{*,\mathrm{pix}}$ (6)	$\log \Sigma_{\mathrm{SFR,pix}}$ (7)	$A_{V,\mathrm{pix}}$ (8)	$\log \Sigma_{H_2}$ (Simple) (9)	$\log \Sigma_{H_2}$ (Sun) (10)	$\log \Sigma_{H_2}$ (Sun, $\alpha_{CO}(Z)$) (11)	$\log \Sigma(12\ \mu\mathrm{m})$ (12)
1464	NGC5980	Comp.	–	–	2.49	–	–	1.27 ± 0.06	1.24 ± 0.05	–	1.09 ± 0.02
1465	NGC5980	Comp.	–	–	3.13	–	–	1.68 ± 0.05	1.70 ± 0.03	–	1.21 ± 0.02
1466	NGC5980	SF	8.83	2.44	2.48	-1.61 ± 0.03	1.08	1.06 ± 0.11	1.13 ± 0.06	1.01 ± 0.06	1.03 ± 0.02
1467	NGC5980	SF	8.84	2.40	1.60	-2.10 ± 0.02	1.02	< 1.09	0.65 ± 0.07	0.52 ± 0.07	0.65 ± 0.02
1468	NGC5980	Comp.	–	–	0.73	–	–	< 1.12	–	–	0.17 ± 0.02
1469	NGC5980	SF	8.84	2.39	-1.04	-3.77 ± 0.03	-3.02	< 1.24	–	–	-0.29 ± 0.04
24622	NGC4047	SF	8.80	2.70	2.30	-1.51 ± 0.03	1.26	1.58 ± 0.09	1.61 ± 0.04	1.54 ± 0.04	1.17 ± 0.02
24623	NGC4047	SF	8.76	2.97	2.65	-1.30 ± 0.02	1.21	1.78 ± 0.05	1.87 ± 0.03	1.83 ± 0.03	1.35 ± 0.02
24624	NGC4047	SF	8.71	3.45	2.72	-1.20 ± 0.02	1.08	1.88 ± 0.05	1.90 ± 0.03	1.93 ± 0.03	1.41 ± 0.02
24625	NGC4047	SF	8.76	3.02	2.46	-1.40 ± 0.02	1.11	1.81 ± 0.07	1.81 ± 0.03	1.78 ± 0.03	1.36 ± 0.02
24626	NGC4047	SF	8.83	2.47	2.13	-1.65 ± 0.02	1.09	1.47 ± 0.13	1.55 ± 0.04	1.43 ± 0.04	1.20 ± 0.02
24627	NGC4047	SF	8.85	2.32	2.04	-1.82 ± 0.03	1.28	< 1.63	1.20 ± 0.08	1.06 ± 0.08	0.96 ± 0.02
24628	NGC4047	Comp.	–	–	1.41	–	–	< 1.63	–	–	0.63 ± 0.02
24629	NGC4047	SF	8.80	2.64	1.08	-3.01 ± 0.09	0.50	< 1.65	–	–	0.26 ± 0.03
24630	NGC4047	–	–	–	–	–	–	< 1.72	–	–	-0.06 ± 0.05
24631	NGC4047	–	–	–	–	–	–	< 1.86	–	–	-0.30 ± 0.07
24632	NGC4047	–	–	–	–	–	–	< 1.71	–	–	-0.52 ± 0.12
24633	NGC4047	–	–	–	–	–	–	< 1.70	–	–	-0.31 ± 0.08
24634	NGC4047	–	–	–	–	–	–	< 1.79	–	–	-0.02 ± 0.04
24635	NGC4047	SF	8.79	2.73	1.21	-2.34 ± 0.05	1.12	< 1.67	–	–	0.26 ± 0.03
24636	NGC4047	SF	8.84	2.36	1.65	-2.45 ± 0.04	0.86	< 1.58	–	–	0.55 ± 0.02
24637	NGC4047	SF	8.88	2.13	1.90	-2.34 ± 0.04	0.68	< 1.58	1.16 ± 0.06	0.98 ± 0.06	0.90 ± 0.02

(3) BPT classification (Section 3.2.4): starforming ("SF"), composite ("Comp."), low-ionization emission region ("LIER"), or Seyfert ("Sy").
(5) Metallicity-dependent α_{CO} (Eq. 3.18) in units of $\mathrm{M_\odot\,(K\ km\ s^{-1}\ pc^2)^{-1}}$.
(6) Resolved stellar mass surface density (Sec. 3.2.4) in units of $\mathrm{M_\odot\ kpc^{-2}}$.
(7) Resolved SFR surface density (Equation 3.16) in units of $\mathrm{M_\odot\ yr^{-1}\ kpc^{-2}}$.
(8) Resolved extinction derived from the Balmer decrement, in units of mag (Equation 3.15).
(9) H_2 surface density ($\mathrm{M_\odot\ pc^{-2}}$) based on the "Simple" moment-0 map (Method 2, Section 3.2.3). Method 1 is better at improving the SNR in each pixel, so detects more pixels than Method 2. A constant α_{CO} is assumed, and 98% confidence 3σ upper limits are shown for non-detections.
(10) H_2 surface density ($M_\odot\ \mathrm{pc^{-2}}$) from the moment-0 map made using the Sun et al. (2018) method (Method 1), assuming a constant $\alpha_{CO} = 3.2$.
(11) Same as (10) but assuming a metallicity-dependent α_{CO} and only using star-forming pixels.
(12) Resolved 12 μm surface density in units of $\mathrm{L_\odot\ pc^{-2}}$.

3.4.1 Comparisons to previous work

Previous work on the 12 μm-CO relationship has been primarily focused on the total 12 μm luminosity and the total CO luminosity for each galaxy (Jiang et al. 2015; Gao et al. 2019). Our fit of the global CO luminosity versus 12 μm luminosity over the CO-detected area (Figure 3.5) yields a slope of 0.94 ± 0.04 and intercept of 0.46 ± 0.38. Our slope agrees well with Gao et al. (2019) who find 0.98 ± 0.02, but our intercept is significantly greater than their value of -0.14 ± 0.18. Our global CO luminosities are consistent with those reported in B17, which are believed to be accurate estimates of the true total CO luminosities (see Section 3.2 in B17). However, we find that our global 12 μm luminosities (the sum over the CO-detected area) are systematically lower than the true total 12 μm luminosities as measured by the method in Gao et al. (2019). The amount of discrepancy is consistent with the offset in intercept found between this work and Gao et al. (2019). This comparison indicates that 12 μm emission tends to be more spatially extended than CO emission, so by restricting the area to the CO-emitting area, some 12 μm emission is missed, leading to a smaller intercept. The fact that this does not affect the slope indicates that the fraction of 12 μm emission that is excluded by only considering the CO-detected area, is similar from galaxy to galaxy.

When estimating the total CO luminosity in a galaxy, we recommend cross-checking with the Gao et al. (2019) estimators because they take the total 12 μm luminosity as input, whereas our estimators require the 12 μm luminosity *over the CO-detected area*. Since our total CO luminosities agree with the total CO luminosities presented in B17, it is unlikely that these interferometric measurements significantly underestimate the true total CO luminosities. However,

since a comparison of the EDGE total CO luminosities with single-dish measurements for the same sample has not been done, it is not impossible that there is some missing flux.

Our results can be compared to recent work using optical extinction as an estimator of H_2 surface density (Güver & Özel 2009; Barrera-Ballesteros et al. 2016; Concas & Popesso 2019; Yesuf & Ho 2019; Barrera-Ballesteros et al. 2020). We show that resolved 12 μm surface density is better than optical extinction at predicting H_2 surface density by $\simeq$ 0.1 dex per pixel (Figure 3.6). Additionally, a 12 μm estimator does not suffer from a limited dynamic range like A_V traced by the Balmer decrement, which is invalid at large extinctions, and where the SNR of the Hα and Hβ lines are low. In the recent analysis of EDGE galaxies Barrera-Ballesteros et al. (2020) limit their analysis to $A_V < 3$ due to the SNR of the Hβ line. Additionally, the correlation between resolved $\Sigma(12\,\mu\mathrm{m})$ and $\Sigma(H_2)$ is stronger than that between A_V and $\Sigma(H_2)$.

3.4.2 Why is $\Sigma(12\ \mu\mathrm{m})$ a better predictor of $\Sigma(H_2)$ than Σ_{SFR}?

Over the same set of pixels (star forming and CO detected), the correlation between $\log \Sigma(12\ \mu\mathrm{m})$ and $\log \Sigma(H_2)$ per galaxy (left panel, Figure 3.3) is better than the correlation between $\log \Sigma_{SFR}$ and $\log \Sigma(H_2)$ (right panel, Figure 3.3). This is also apparent from our findings that estimators of $\Sigma(H_2)$ based on $\Sigma(12\ \mu\mathrm{m})$ consistently perform better at predicting $\Sigma(H_2)$ than estimators with Σ_{SFR} instead of $\Sigma(12\ \mu\mathrm{m})$ (Section 3.3.3).

Since we have restricted our analysis to star-forming pixels, the 12 μm emission that we see is likely dominated by the 11.3 μm PAH feature. The underlying continuum emission can arise from warm, very small dust grains heated by AGN. This likely does not dominate the 12 μm emission since most ($\sim$ 80 per cent) of the *WISE* 12 μm emission in star-forming galaxies is

from stellar populations younger than 0.6 Gyr (Donoso et al. 2012). However, it is important to rule out any effects of obscured AGN. PAH emission is known to be affected by the presence of an AGN (Diamond-Stanic & Rieke 2010; Shipley et al. 2013; Jensen et al. 2017; Alonso-Herrero et al. 2020), but there is conflicting evidence on the nature of this relationship. For example, Tommasin et al. (2010) find AGN-dominated and starburst-dominated galaxies have roughly the same 11.3 μm PAH flux, while Murata et al. (2014) and Maragkoudakis et al. (2018) find suppressed PAH emission in starburst galaxies relative to galaxies with AGN. In contrast, Shi et al. (2009) and Shipley et al. (2013) find suppressed PAH emission in AGN compared to non-AGN. If there are any obscured AGN in our sample, they would not be identified as AGN from the BPT method. However, since our pixels are 1 to 2 kpc in size, the impact of an obscured AGN would be restricted to the central pixel of the galaxy. To assess the potential impact of obscured AGN on our results, we redid all of our multiparameter fits with the central pixel of each galaxy masked if it was not already masked based on the BPT classification. We found that the 12 μm-H_2 correlation remains stronger than the SFR-H_2 correlation, and that the fit parameters do not change significantly (they are consistent within the quoted uncertainties). Thus we are confident that AGN do not significantly impact our results.

These results have implications for the connection between emission that is traced by the 12 μm band (mostly PAHs) and CO emission. Exactly how and where PAHs are formed is not currently understood (for a recent review from the *Spitzer* perspective see Li 2020), but traditionally PAHs have been modelled to absorb FUV photons through the photoelectric effect and eject electrons into the ISM, which heats the gas (Bakes & Tielens 1994; Tielens 2008).

Since PAHs are excited by stellar UV photons, PAH emission has been considered as an SFR tracer (e.g. Roussel et al. 2001; Peeters et al. 2004; Wu et al. 2005; Shipley et al. 2016; Cluver et al. 2017; Xie & Ho 2019; Whitcomb et al. 2020). Although the PAH-SFR connection breaks down at sub-kpc scales (Werner et al. 2004; Bendo et al. 2020), PAH emission is still used as an SFR tracer on global scales for low-redshift galaxies (Kennicutt et al. 2009; Shipley et al. 2016). *WISE* 12 μm emission has also been examined as a SFR indicator; however its relationship with SFR shows greater scatter than the *WISE* 22 μm-SFR relationship (Jarrett et al. 2013; Cluver et al. 2017; Leroy et al. 2019). Similar to the 8 μm emission vs. SFR relation Calzetti et al. (2007), the complex relationship between thermal dust, PAH emission and star formation activity adds scatter to the correlations between MIR emission and SFR (Jarrett et al. 2013).

Many studies have also found that there is a tight link between PAHs and the contents of the interstellar medium: molecular gas traced by CO (Regan et al. 2006; Pope et al. 2013; Cortzen et al. 2019), and cold ($T \sim 25$ K) dust, which traces the bulk of the ISM (Haas et al. 2002; Bendo et al. 2008; Jones et al. 2015; Bendo et al. 2020). Milky Way studies have found that PAH emission is enhanced surrounding and suppressed within H II regions (e.g. Churchwell et al. 2006; Povich et al. 2007). In addition, the PdBI Arcsecond Whirlpool Survey (PAWS; Schinnerer et al. 2013) of cold gas in M51 with cloud-scale resolution ($\sim$ 40 pc) found that *Spitzer* 8 μm PAH emission and CO(1-0) emission are highly correlated in position but not in flux, and that most of the PAH emission appears to be coming from only the surfaces of giant molecular clouds. These results and others such as Sandstrom et al. (2010) suggest that PAHs are either formed in molecular clouds or destroyed in the diffuse ISM, and that the conditions

of PAH formation and CO formation are likely similar. The suppression of PAH emission in H II regions may be due to decreased dust shielding, analogous to how CO emission is reduced in low-metallicity regions, or to changes in how PAHs are formed and/or destroyed (Sandstrom et al. 2013; Li 2020). It is plausible that our findings support a picture in which PAHs form in molecular clouds or are destroyed in the diffuse ISM; however due to the difference in physical resolution, and the contribution of continuum emission and multiple PAH features to the 12 μm emission, a study focused specifically on 11.3 μm PAH instead of *WISE* 12 μm would be required. Overall it seems likely that the strength of the 12 μm-H_2 correlation in star-forming regions is due to the combination of the Kennicutt-Schmidt relation and a direct link between the 11.3 μm PAH feature and molecular gas as traced by CO.

3.5 Conclusions

We find that *WISE* 12 μm emission and CO(1-0) emission from EDGE are highly correlated at $\sim$ kpc scales in star-forming regions of nearby galaxies after matching the resolution of the two data sets. Using multi-variable linear regression we compute linear combinations of resolved and global galaxy properties that robustly predict H_2 surface densities. We find that 12 μm is the best predictor of H_2, and is notably better than Σ_{SFR} derived from resolved Hα emission. Our results are statistically robust, and are not significantly affected by the possible presence of any obscured AGN or by assumptions about the CO-to-H_2 conversion factor. We interpret these findings as further evidence that 11.3 μm PAH emission is more spatially correlated with H_2 than with H II regions. Although the details of the life cycle and excitation of PAH

molecules are not fully understood, we believe that the strong correlation between 12 μm and CO emission is likely due to the fact that PAH emission is both a SFR tracer and a cold ISM tracer. Additionally, if PAHs are indeed formed within molecular clouds and in similar conditions to CO as previous work suggests, we suspect that the *WISE* 12 μm-CO correlation will persist at molecular-cloud scale resolution.

We present resolved Σ_{H_2} estimators which can be used for two key applications:

1. generating large samples of estimated resolved $\Sigma(H_2)$ in the nearby Universe e.g. to study the resolved Kennicutt-Schmidt law, and

2. predicting $\Sigma(H_2)$ and integration times for telescope observing proposals (e.g. ALMA).

Although the CO-detected pixels in our sample only extend down to $\Sigma(H_2) \sim 1$ $M_\odot$ pc^{-2}, our predictions for $\Sigma(H_2)$ below this are consistent with the upper limits in our data. However, we advise caution when applying the estimator to 12 μm surface densities below about 1 $L_\odot$ pc^{-2}. Since *WISE* was an all-sky survey, in principle these estimators could be applied over the entire sky. In the future, using the MIR data with higher resolution and better sensitivity from the *James Webb Space Telescope* instead of *WISE* 12 μm, and ALMA CO data instead of CARMA CO data, one could produce an H_2 surface density estimator which reaches even lower gas surface densities.

Acknowledgements

We thank the anonymous referee for his/her suggestions that have improved the manuscript.
CL acknowledges the support by the National Key R&D Program of China (grant No. 2018YFA0404502,

2018YFA0404503), and the National Science Foundation of China (grant Nos. 11821303, 11973030, 11673015, 11733004, 11761131004, 11761141012). YG acknowledges funding from National Key Basic Research and Development Program of China (grant No. 2017YFA0402704). LCP and CDW acknowledge support from the Natural Science and Engineering Research Council of Canada and CDW acknowledges support from the Canada Research Chairs program.

This publication makes use of data products from the *Wide-field Infrared Survey Explorer*, which is a joint project of the University of California, Los Angeles, and the Jet Propulsion Laboratory/California Institute of Technology, funded by the National Aeronautics and Space Administration. This research has made use of the NASA/IPAC Infrared Science Archive, which is funded by the National Aeronautics and Space Administration and operated by the California Institute of Technology. This study uses data provided by the Calar Alto Legacy Integral Field Area (CALIFA) survey (http://califa.caha.es/). Based on observations collected at the Centro Astronomico Hispano Aleman (CAHA) at Calar Alto, operated jointly by the Max-Planck-Institut fur Astronomie and the Instituto de Astrofisica de Andalucia (CSIC). We acknowledge the usage of the HyperLEDA database (http://leda.univ-lyon1.fr). This research was enabled in part by support provided by WestGrid (https://www.westgrid.ca) and Compute Canada (https://www.computecanada.ca).

Data Availability

The data underlying this article are available in the article, in its online supplementary material, and at https://lig.astro.tsinghua.edu.cn/astrodata/publication/20/

estimator-resolved-molecular/.

Supporting Information

Supplementary data are available at MNRAS online.

extract_cut-out.py

README.txt

table_global.csv

table_resolved.csv

Please note: Oxford University Press is not responsible for the content or functionality of any supporting materials supplied by the authors. Any queries (other than missing material) should be directed to the corresponding author for the article.

A Derivation of *WISE* W3 uncertainty

The *total* uncertainty in each 6 arcsec pixel is the instrumental uncertainty added in quadrature with the zero-point uncertainty

$$\sigma_{12\ \mu\mathrm{m,\ tot}} = \sqrt{\sigma^2_{\mathrm{inst.,\ final}} + \sigma^2_{\mathrm{ZP}}}. \tag{A1}$$

The instrumental uncertainty in each pixel was measured by taking the uncertainty maps from the *WISE* archive, adding the native pixels in quadrature into 6 arcsec pixels, taking the square root, and multiplying the resulting map by the unit conversion factor in Equation 3.10. The instrumental noise variance in each larger pixel is

$$\sigma^2_{\mathrm{inst.,\ final}} = 5 \sum_{\mathrm{subpixels}} \sigma^2_{\mathrm{inst.,\ natv.}}, \tag{A2}$$

where the factor of 5 correction was estimated from Figure 3 of `http://wise2.ipac.caltech.edu/docs/release/allsky/expsup/sec2_3f.html` (since our 6 arcsec pixels are effectively apertures with radius of $3/1.175 = 2.5$ pixels), and $\sigma_{\mathrm{inst.,\ natv.}}$ is the instrumental uncertainty at the native pixel scale.

There is a 4.5 per cent uncertainty in the W3 zero-point magnitude (Figure 9 of Jarrett et al. 2011), such that

$$\sigma_{\mathrm{MAG}} = \frac{2.5}{\ln 10}\frac{\sigma_F}{F} = 0.045, \tag{A3}$$

or $\sigma_F = 0.0414F$. The zero-point uncertainty is given by

$$\sigma_{\rm ZP} = 0.0414 \sum_{\rm subpixels} F_{\rm natv.}, \tag{A4}$$

where $F_{\rm natv.}$ is the flux at the native pixel scale.

B Derivation of CO uncertainty

A noise map $N(x,y)$ (in Jy beam^{-1} km s^{-1}) is calculated by adding a 10 per cent calibration uncertainty in quadrature with the instrumental uncertainty

$$\frac{N(x,y)}{\rm Jy\ beam^{-1}\ km\ s^{-1}} = \left\{ [0.1 M_0(x,y)]^2 + \sigma(x,y)^2 \frac{N_{\rm pix,beam}}{f_{\rm bin}} \right\}^{1/2}, \tag{B5}$$

where $M_0(x,y)$ is the moment-0 map (Jy beam^{-1} km s^{-1}) with 6 arcsec pixels, the factor of 0.1 is a 10 per cent calibration uncertainty, $N_{\rm pix,beam}$ is the number of pixels per beam in the raw image (prior to any rebinning), $f_{\rm bin}$ is the binning factor (the number of original pixels in the *rebinned* pixels, e.g. since we went from $1'' \times 1''$ to $6'' \times 6''$ pixels, $f_{\rm bin} = 36$), and

$$\frac{\sigma(x,y)}{\rm Jy\ beam^{-1}\ km\ s^{-1}} = \left(\frac{\Delta v_{\rm chan}}{\rm km\ s^{-1}} \right) \sqrt{N_{\rm chan}(x,y)} \left(\frac{\sigma_{\rm chan}}{\rm Jy\ beam^{-1}} \right), \tag{B6}$$

where $\Delta v_{\rm chan} = 20$ km s^{-1} is the velocity width of the channels in the cube, $N_{\rm chan}(x,y)$ is the number of channels used to calculate the moment-0 map (which varies with position), and $\sigma_{\rm chan}$ is the RMS per channel. When calculating upper limits, $N_{\rm chan}(x,y) = 34$ for all pixels.

In a CO cube, $\sigma_{\rm chan}$ is calculated by measuring the RMS of all pixels within a 7 arcsec radius circular aperture in the center of the field in the first 3-5 channels, and again in the last 3-5 channels. $\sigma_{\rm chan}$ is taken to be the average of these two RMSes. Finally, we convert the noise maps into units of luminosity using Equation 3.12.

C Definition of the scatter about a fit

The total scatter about a fit $\sigma_{\rm tot}$ is

$$\sigma_{\rm tot} = \sqrt{\frac{1}{N-m}\sum_i (y_i - \hat{y}_i)^2}, \tag{C7}$$

where N is the number of data points, m is the number of fit parameters, y_i is i'th independent variable, and $\hat{y}_i$ is the estimate of y_i from the fit. $\sigma_{\rm tot}$ can be directly computed from the fit. The total scatter can also be written as the sum in quadrature of random scatter due to measurement uncertainties, and the remaining "intrinsic" scatter $\sigma_{\rm int}$

$$\sigma_{\rm tot} = \sqrt{\frac{1}{N}\sum_i \sigma_i^2 + \sigma_{\rm int}^2}, \tag{C8}$$

where σ_i is the measurement error on y_i. The intrinsic scatter can be computed using

$$\sigma_{\rm int} = \sqrt{\sigma_{\rm tot}^2 - \frac{1}{N}\sum_i \sigma_i^2}. \tag{C9}$$

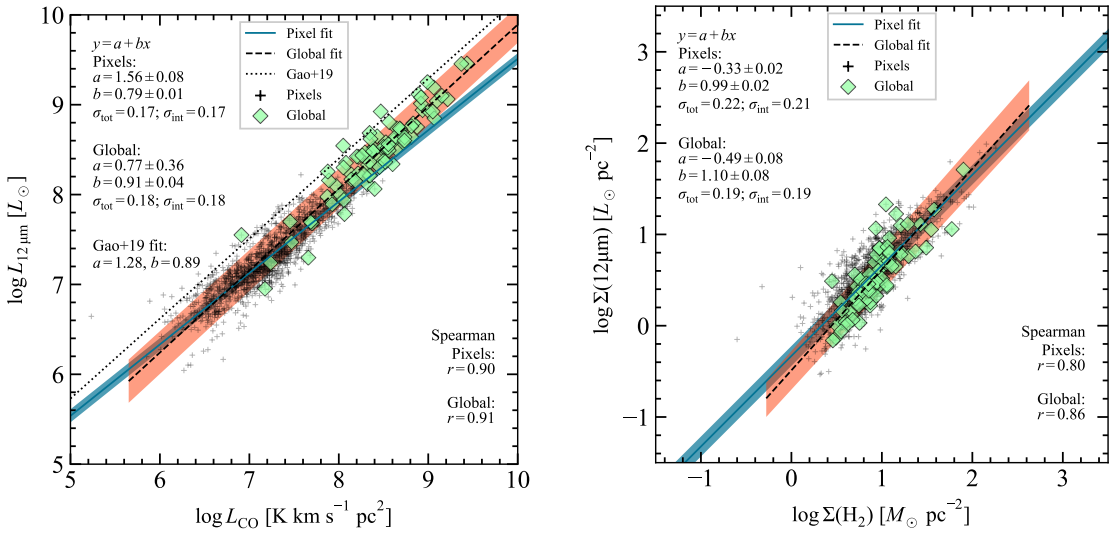

Figure D1: Same as Figure 3.5 but with the x and y axes interchanged.

D The 12 μm-CO relationship assuming a constant α_{CO}

Figure D1 shows the 12 μm vs. CO relationship in terms of luminosities (left) and surface densities (right), as in Figure 3.5 except with the x and y axes interchanged, and the fits redone.

For completeness, Figure D2 shows the relationships and fits as Figure 3.5 except assuming a constant CO-to-H_2 conversion factor $\alpha_{CO} = 3.2\ M_\odot(\mathrm{K\ km\ s^{-1}\ pc^2})^{-1}$, and including all CO-detected pixels (not just star-forming). The changes from Figure 3.5 are slight overall, and are the largest in the lower left panel (however the uncertainties are also larger in that panel).

E Multi-parameter fits assuming a constant α_{CO}

Tables E1, E2, and E3 show the multi-parameter fit results H_2 surface densities were computed assuming $\alpha_{CO} = 3.2\ M_\odot(\mathrm{K\ km\ s^{-1}\ pc^2})^{-1}$.

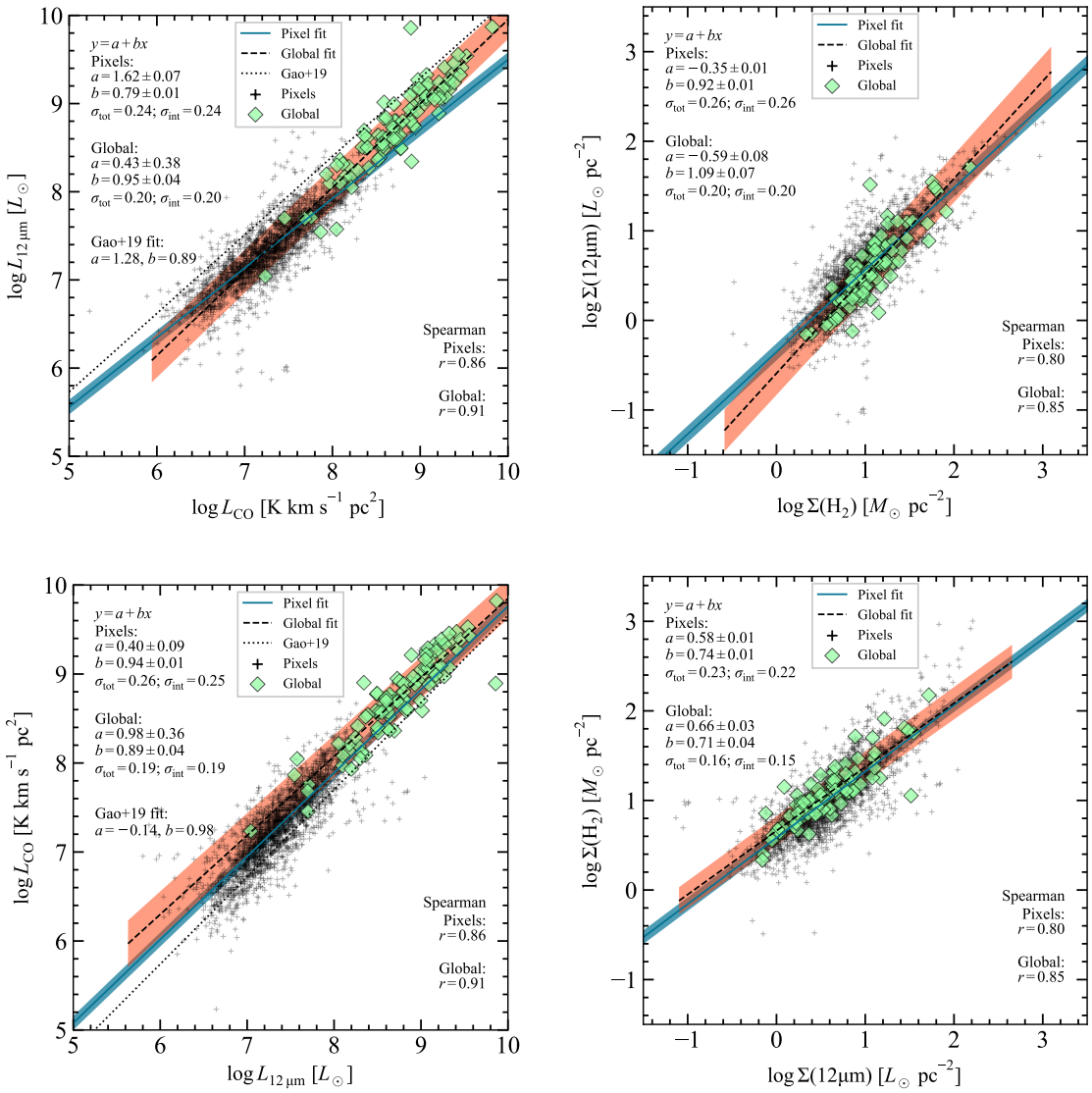

Figure D2: Same as Figure 3.5 except H_2 surface densities were calculated using $\alpha_{CO} = 3.2\ M_\odot (K\ km\ s^{-1}\ pc^2)^{-1}$, and non-starforming pixels were included.

Table E1: Same as Table 3.3 but assuming $\alpha_{CO} = 3.2\ M_\odot (K\ km\ s^{-1}\ pc^2)^{-1}$.

					θ_i for pixel properties		θ_i for global properties		
RMS error	n_{gal}	n_{pix}	σ_{int}	Zero-point (θ_0)	$\log \Sigma(12\ \mu m)$	$(12 + \log O/H)$	$\log \Sigma_{FUV}$	$\log \Sigma_{NUV}$	$A(H\alpha)$
0.18	58	1126	0.16	0.56 ± 0.01	0.73 ± 0.01	–	–	–	–
0.16	30	573	0.14	2.76 ± 0.08	0.85 ± 0.01	–	-0.21 ± 0.01	–	–
0.14	27	552	0.14	3.8 ± 0.1	0.95 ± 0.01	–	–	-0.30 ± 0.01	-0.15 ± 0.01
0.14	27	552	0.14	3.2 ± 0.6	0.94 ± 0.01	0.06 ± 0.07	–	-0.30 ± 0.01	-0.15 ± 0.01

Table E2: Same as Table 3.4 but assuming $\alpha_{CO} = 3.2\ M_\odot (K\ km\ s^{-1}\ pc^2)^{-1}$.

					θ_i for pixel properties	θ_i for global properties		
RMS error	n_{gal}	n_{pix}	σ_{int}	Zero-point (θ_0)	$\log \Sigma(12\ \mu m)$	$\log \Sigma_{FUV}$	$\log \Sigma_{NUV}$	$A(H\alpha)$
0.18	58	1126	0.16	0.56 ± 0.01	0.73 ± 0.01	–	–	–
0.16	30	573	0.14	2.76 ± 0.07	0.85 ± 0.01	-0.21 ± 0.01	–	–
0.14	27	552	0.14	3.8 ± 0.1	0.95 ± 0.01	–	-0.30 ± 0.01	-0.15 ± 0.01
0.14	27	552	0.14	3.5 ± 0.1	0.92 ± 0.01	-0.12 ± 0.03	-0.16 ± 0.03	-0.14 ± 0.01

Table E3: Same as Table 3.5 but assuming $\alpha_{CO} = 3.2\ M_\odot (K\ km\ s^{-1}\ pc^2)^{-1}$.

					θ_i for pixel properties			θ_i for global properties	
RMS error	n_{gal}	n_{pix}	σ_{int}	Zero-point (θ_0)	$\log \Sigma_*$	$(12 + \log O/H)$	$\log \Sigma_{SFR}$	$\log \Sigma_{NUV}$	b/a_{disk}
0.21	58	1126	0.20	2.07 ± 0.01	–	–	0.50 ± 0.01	–	–
0.20	42	942	0.18	1.92 ± 0.02	–	–	0.49 ± 0.01	–	0.21 ± 0.02
0.17	27	552	0.18	0.8 ± 0.1	0.26 ± 0.01	–	0.30 ± 0.01	0.03 ± 0.01	–
0.17	27	552	0.18	-3.1 ± 0.6	0.23 ± 0.01	0.47 ± 0.07	0.32 ± 0.01	0.02 ± 0.01	–

References

Alonso-Herrero A., et al., 2020, A&A, 639, A43

Bakes E. L. O., Tielens A. G. G. M., 1994, ApJ, 427, 822

Baldwin J. A., Phillips M. M., Terlevich R., 1981, PASP, 93, 5

Barrera-Ballesteros J. K., et al., 2016, MNRAS, 463, 2513

Barrera-Ballesteros J. K., et al., 2020, MNRAS, 492, 2651

Bendo G. J., et al., 2008, MNRAS, 389, 629

Bendo G. J., Lu N., Zijlstra A., 2020, MNRAS, 496, 1393

Bertemes C., et al., 2018, MNRAS, 478, 1442

Bertin E., Arnouts S., 1996, A&AS, 117, 393

Bigiel F., Leroy A., Walter F., Brinks E., de Blok W. J. G., Madore B., Thornley M. D., 2008, AJ, 136, 2846

Blanton M. R., et al., 2017, AJ, 154, 28

Bolatto A. D., Wolfire M., Leroy A. K., 2013, ARA&A, 51, 207

Bolatto A. D., et al., 2017, ApJ, 846, 159

Calzetti D., et al., 2007, ApJ, 666, 870

Cappellari M., 2017, MNRAS, 466, 798

Churchwell E., et al., 2006, ApJ, 649, 759

Cid Fernandes R., Stasińska G., Schlickmann M. S., Mateus A., Vale Asari N., Schoenell W., Sodré L., 2010, MNRAS, 403, 1036

Cluver M. E., Jarrett T. H., Dale D. A., Smith J. D. T., August T., Brown M. J. I., 2017, ApJ, 850, 68

Concas A., Popesso P., 2019, MNRAS, 486, L91

Cortzen I., et al., 2019, MNRAS, 482, 1618

Denicoló G., Terlevich R., Terlevich E., 2002, MNRAS, 330, 69

Diamond-Stanic A. M., Rieke G. H., 2010, ApJ, 724, 140

Donoso E., et al., 2012, ApJ, 748, 80

Draine B. T., et al., 2007, ApJ, 663, 866

Elmegreen B. G., 1997, in Franco J., Terlevich R., Serrano A., eds, Revista Mexicana de Astronomia y Astrofisica Conference Series Vol. 6, Revista Mexicana de Astronomia y Astrofisica Conference Series. p. 165

Gao Y., Solomon P. M., 2004, ApJ, 606, 271

Gao Y., et al., 2019, ApJ, 887, 172

Genzel R., et al., 2012, ApJ, 746, 69

Genzel R., et al., 2015, ApJ, 800, 20

Gilhuly C., Courteau S., 2018, MNRAS, 477, 845

Güver T., Özel F., 2009, MNRAS, 400, 2050

Haas M., Klaas U., Bianchi S., 2002, A&A, 385, L23

Hao C.-N., Kennicutt R. C., Johnson B. D., Calzetti D., Dale D. A., Moustakas J., 2011, ApJ, 741, 124

Husemann B., et al., 2013, A&A, 549, A87

Jarrett T. H., et al., 2011, ApJ, 735, 112

Jarrett T. H., et al., 2013, AJ, 145, 6

Jensen J. J., et al., 2017, MNRAS, 470, 3071

Jiang X.-J., Wang Z., Gu Q., Wang J., Zhang Z.-Y., 2015, ApJ, 799, 92

Jones A. G., et al., 2015, MNRAS, 448, 168

Kauffmann G., et al., 2003, MNRAS, 346, 1055

Kelly B. C., 2007, ApJ, 665, 1489

Kennicutt Robert C. J., 1989, ApJ, 344, 685

Kennicutt R. C., Evans N. J., 2012, ARA&A, 50, 531

Kennicutt Robert C. J., et al., 2007, ApJ, 671, 333

Kennicutt Robert C. J., et al., 2009, ApJ, 703, 1672

Kewley L. J., Dopita M. A., Sutherland R. S., Heisler C. A., Trevena J., 2001, ApJ, 556, 121

Kroupa P., Weidner C., 2003, ApJ, 598, 1076

Krumholz M. R., Thompson T. A., 2007, ApJ, 669, 289

Leroy A. K., Walter F., Brinks E., Bigiel F., de Blok W. J. G., Madore B., Thornley M. D., 2008, AJ, 136, 2782

Leroy A. K., et al., 2013, AJ, 146, 19

Leroy A. K., et al., 2019, ApJS, 244, 24

Li A., 2020, Nature Astronomy, 4, 339

Li N., Li C., Mo H., Hu J., Zhou S., Du C., 2020, ApJ, 896, 38

Madau P., Dickinson M., 2014, ARA&A, 52, 415

Makarov D., Prugniel P., Terekhova N., Courtois H., Vauglin I., 2014, A&A, 570, A13

Maloney P., Black J. H., 1988, ApJ, 325, 389

Maragkoudakis A., Ivkovich N., Peeters E., Stock D. J., Hemachandra D., Tielens A. G. G. M., 2018, MNRAS, 481, 5370

McMullin J. P., Waters B., Schiebel D., Young W., Golap K., 2007, in Shaw R. A., Hill F., Bell D. J., eds, Astronomical Society of the Pacific Conference Series Vol. 376, Astronomical Data Analysis Software and Systems XVI. p. 127

Murata K. L., et al., 2014, ApJ, 786, 15

Murphy E. J., et al., 2011, ApJ, 737, 67

Pedregosa F., et al., 2012, arXiv e-prints, p. arXiv:1201.0490

Peeters E., Spoon H. W. W., Tielens A. G. G. M., 2004, ApJ, 613, 986

Pope A., et al., 2013, ApJ, 772, 92

Povich M. S., et al., 2007, ApJ, 660, 346

Regan M. W., et al., 2006, ApJ, 652, 1112

Roussel H., Sauvage M., Vigroux L., Bosma A., 2001, A&A, 372, 427

Salim S., et al., 2016, ApJS, 227, 2

Salim S., Boquien M., Lee J. C., 2018, ApJ, 859, 11

Sánchez S. F., et al., 2012, A&A, 538, A8

Sánchez S. F., et al., 2016, A&A, 594, A36

Sandstrom K. M., Bolatto A. D., Draine B. T., Bot C., Stanimirović S., 2010, ApJ, 715, 701

Sandstrom K. M., et al., 2013, ApJ, 777, 5

Schinnerer E., et al., 2013, ApJ, 779, 42

Shetty R., Kelly B. C., Bigiel F., 2013, MNRAS, 430, 288

Shi Y., et al., 2009, in Wang W., Yang Z., Luo Z., Chen Z., eds, Astronomical Society of the Pacific Conference Series Vol. 408, The Starburst-AGN Connection. p. 209

Shi Y., Helou G., Yan L., Armus L., Wu Y., Papovich C., Stierwalt S., 2011, ApJ, 733, 87

Shi Y., et al., 2018, ApJ, 853, 149

Shipley H. V., Papovich C., Rieke G. H., Dey A., Jannuzi B. T., Moustakas J., Weiner B., 2013, ApJ, 769, 75

Shipley H. V., Papovich C., Rieke G. H., Brown M. J. I., Moustakas J., 2016, ApJ, 818, 60

Silk J., 1997, ApJ, 481, 703

Sun J., et al., 2018, ApJ, 860, 172

Tacconi L. J., et al., 2018, ApJ, 853, 179

Tielens A. G. G. M., 2008, ARA&A, 46, 289

Tommasin S., Spinoglio L., Malkan M. A., Fazio G., 2010, ApJ, 709, 1257

Walcher C. J., et al., 2014, A&A, 569, A1

Werner M. W., et al., 2004, ApJS, 154, 1

Whitcomb C. M., Sandstrom K., Murphy E. J., Linden S., 2020, ApJ, 901, 47

Wilson C. D., 1995, ApJ, 448, L97

Wright E. L., et al., 2010, AJ, 140, 1868

Wu H., Cao C., Hao C.-N., Liu F.-S., Wang J.-L., Xia X.-Y., Deng Z.-G., Young C. K.-S., 2005, ApJ, 632, L79

Xie Y., Ho L. C., 2019, ApJ, 884, 136

Yesuf H. M., Ho L. C., 2019, ApJ, 884, 177

Yesuf H. M., Ho L. C., 2020, arXiv e-prints, p. arXiv:2007.14004

4

The Cold Gas and Dust Properties of Red Star-Forming Galaxies

This chapter contains the following article which is in preparation for submission to the Monthly Notices of the Royal Astronomical Society:

"The Cold Gas and Dust Properties of Red Star-Forming Galaxies"

Authors: Chown, R., Parker, L., and Wilson, C. D.

Abstract

We study the cold gas and dust properties for a sample of red star forming galaxies called "red misfits," to understand what this population can tell us about galaxy evolution. To do this

we collect single-dish CO observations and H I observations from representative samples of low-redshift galaxies, as well as our own JCMT CO observations of red misfits. We also obtain SCUBA-2 850 μm observations for a subset of these galaxies. With these data we compare the molecular gas, total cold gas, and dust properties of red misfits against those of their blue counterparts ("blue actives") taking non-detections into account using a survival analysis technique. We also compare these properties at fixed position in the log SFR-log M_* plane, as well as versus offset from the star-forming main sequence. Compared to blue actives, red misfits have slightly longer molecular gas depletion times, similar total gas depletion times, significantly lower molecular- and total-gas mass fractions, lower dust-to-stellar mass ratios, similar dust-to-gas ratios, and a significantly flatter slope in the log $M_{\rm mol}$-log M_* plane. Our results suggest that red misfits as a population are actively quenching.

4.1 Introduction

A key finding from large surveys of the local universe such as the Sloan Digital Sky Survey (SDSS; York et al. 2000) is that the vast majority of galaxies in the nearby universe tend to fall into one of two categories: a blue and star forming "main sequence" (MS) where star formation rate (SFR) and stellar mass M_* are well-correlated, or the quiescent "red cloud" where SFRs are low and not well-correlated with M_*. A small but significant number of galaxies lie in the so-called "green valley" between the main sequence and red cloud (e.g Salim 2014).

Studying the relationship between galaxy properties and galaxy position in the SFR-M_* plane has provided insight into which physical processes are responsible for evolution in this plane.

One approach to tackle this question is to focus on populations with intermediate specific SFR (SSFR), which may be evolving away from or toward the star-forming MS, such as the green valley (e.g. Salim 2014; Schawinski et al. 2014; Smethurst et al. 2015; Salim et al. 2018; Li et al. 2015; Belfiore et al. 2017; Lin et al. 2017; Eales et al. 2018; Coenda et al. 2018; Mancini et al. 2019; Lin et al. 2020; Brownson et al. 2020). However, some works argue that the green valley exists due to observational biases rather than physical processes (Schawinski et al. 2014; Eales et al. 2018).

We investigate a population of galaxies selected from SDSS to be optically red and actively forming stars (Evans et al. 2018). This population, called "red misfits," appears to have no preference for environment, has an elevated fraction of active galactic nuclei (AGN), and accounts for about 20 per cent of low redshift galaxies across stellar masses from $\log M_* = 9.5$ to 11.5. The primary goal of this work is to study the cold gas and dust properties of these galaxies. Although Evans et al. (2018) found that their red $g - r$ colours are not due to dust extinction, we wish to compare their dust, gas, and stellar properties to understand them.

According to the gas-regulator model (Lilly et al. 2013), processes which affect inflows, outflows, and consumption of gas determine the star formation rate of a galaxy. Gas depletion time $t_{\rm gas}$

$$t_{\rm gas}\ [\rm yr] \equiv \frac{M_{\rm gas}\ [\rm M_\odot]}{\rm SFR\ [M_\odot\ yr^{-1}]} \tag{4.1}$$

is the time it would take for a gas reservoir to turn into stars assuming that none of this gas dissipates (and not returned to the ISM via stellar evolution) and that the SFR is constant over time. Although these assumptions are not physically realistic, it is useful to use $t_{\rm gas}$ as a proxy for the

theoretical star formation efficiency $\varepsilon_{\rm SF}$, namely the fraction of a gas reservoir that forms stars before it dissipates. In the literature, the reciprocal of gas depletion time is often referred to as "star formation efficiency" (SFE, e.g. Leroy et al. 2008; Saintonge et al. 2017). To avoid confusion with the true star formation efficiency or the more commonly-used efficiency per free fall time, in this work we will write $t_{\rm gas}^{-1}$ instead of "SFE."

Observations of the total cold molecular and atomic gas reservoirs in large samples of nearby galaxies such as the CO Legacy Database for GASS (xCOLD GASS; Saintonge et al. 2011, 2017), the James Clerk Maxwell Telescope (JCMT) dust and gas In Nearby Galaxies Legacy Exploration (JINGLE; Saintonge et al. 2018), and the *GALEX* Arecibo SDSS Survey (xGASS; Catinella et al. 2018) have found that $t_{\rm gas}$ is correlated with offset from the star forming MS such that $t_{\rm gas}$ decreases with increasing offset from the main sequence

$$\Delta\mathrm{MS}\ [\mathrm{dex}] \equiv \log \frac{\mathrm{SFR}}{\mathrm{SFR}_{\mathrm{MS}}}. \tag{4.2}$$

Tacconi et al. (2018) find that this trend persists from $z = 4$ to 0. Colombo et al. (2020) find that declining molecular gas mass fractions drive galaxies off of the MS, and that once a galaxy is quenched, $t_{\rm gas}^{-1}$ is more important in determining the SFR. With the ALMA-MaNGA QUEnching and STar formation (ALMaQUEST) sample, Ellison et al. (2020) find that $t_{\rm gas}$ drives regions away from the spatially-resolved MS. Brownson et al. (2020) study seven green valley galaxies, and find that $t_{\rm gas}$ and $f_{\rm gas}$ are equally important in driving departures from the MS. A recent analysis of xCOLD GASS and xGASS data (Feldmann 2020) found that after accounting for selection effects (e.g. stellar mass, SFR) and observational uncertainties the correlation

between $\log t_{\rm mol}$ and ΔMS flattens significantly, from $\log t_{\rm mol} \propto -0.5\Delta$MS to $\log t_{\rm mol} \propto -0.24\Delta$MS. In other words, they find that $t_{\rm mol}$ is nearly independent of offset from the MS after accounting for selection effects and observational uncertainties.

In this work we use a combination of two of the largest samples of CO in the local universe (xCOLD GASS and JINGLE), and sub-millimeter observations of a large number of them (from JINGLE and our own observations), as well as H I measurements from xGASS and the Arecibo Legacy Fast ALFA (ALFALFA) $\alpha.100$ catalog (Haynes et al. 2018) to compare the interstellar medium in red misfits with their blue counterparts ("blue actives") and to try to understand the nature of red misfits.

4.2 Data and Data Processing

4.2.1 Star formation rates, stellar masses, and other basic properties

Optical colours and specific star formation rates are required to select red misfits. Star formation rates and stellar masses are also required to compute gas and dust-based quantities such as gas depletion times. These optical data are taken from the following sources:

1. $g-r$ colours that have been extinction-corrected and inclination-corrected, taken from Evans et al. (2018). Some galaxies with CO measurements in our sample were not included in Evans et al. (2018). For this subset we computed SDSS $g-r$ colours using the same method.

2. SFR and stellar masses from UV + optical spectral energy distribution (SED) fitting taken from the GSWLC-M2 catalog (Salim et al. 2018). The medium-depth (M2) mea-

surements are ideal for star-forming galaxies, which are the focus of this work. Where available we use the M2 catalog, and for a small subset of galaxies we use the A2 catalog.

The distribution of all 118,769 galaxies in the intersection of the Evans et al. (2018) catalog and GSWLC-M2, in the log SSFR vs. $g-r$ colour plane ($0.01 \leq z \leq 0.12, 9.0 \leq \log\ M_* \leq 11.9$) is shown in Figure 4.1. We used the GSWLC-M2 star formation rates and stellar masses to compute the dividing line between star-forming and passive galaxies (the horizontal line at $\log\ \mathrm{SSFR}\ [\mathrm{yr}^{-1}] = -11.3$). This cut was determined by fitting the $\log\ \mathrm{SSFR}$ histogram with a double-Gaussian and calculating where the two Gaussians intersect. In this work we focus on star forming galaxies, namely red misfits (upper right quadrant of this figure) and "blue actives" (upper left quadrant). Red misfits are defined as galaxies that are star forming (above the horizontal line) and red in colour ($g-r \geq 0.67$; Evans et al. 2018).

4.2.2 Single-dish CO observations

We use CO observations from the following three sources:

1. JCMT CO(2-1) measurements from the JINGLE survey (Saintonge et al. 2018). JINGLE is a representative sample of galaxies ranging from just below the star forming main sequence to the starburst regime. The entire JINGLE sample was observed with SCUBA-2, while a subset of about 75 galaxies were observed in CO(2-1). Molecular gas mass is related to CO(2-1) luminosity $L_{\mathrm{CO}(2-1)}$ by

$$M_{\mathrm{mol}}\ [\mathrm{M}_\odot] = r_{21}^{-1}\,\alpha_{\mathrm{CO}} L_{\mathrm{CO}(2-1)}\ [\mathrm{K\ km\ s^{-1}\ pc^2}], \tag{4.3}$$

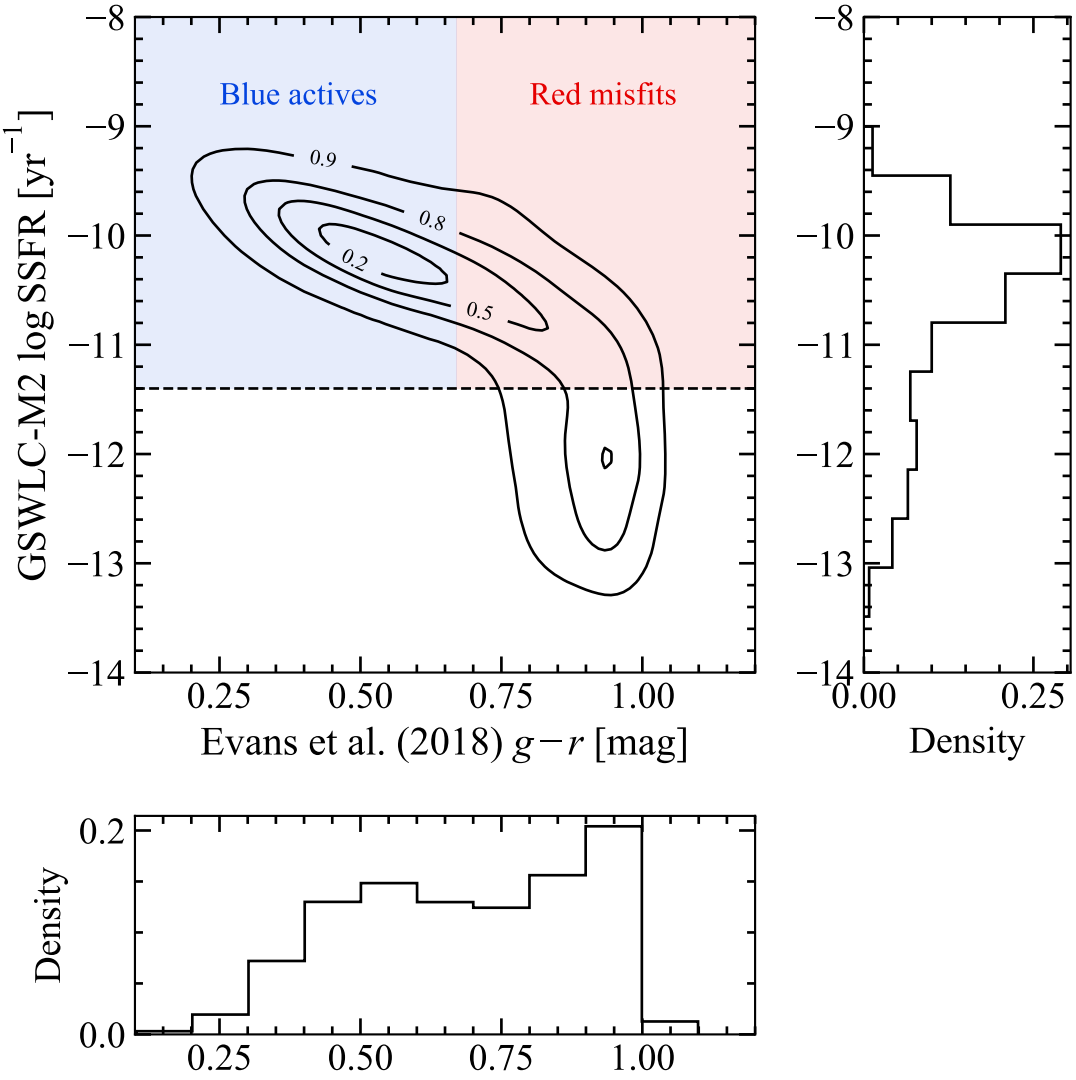

Figure 4.1: SSFR vs. $g - r$ colour of all 118,769 galaxies in the intersection of the Evans et al. (2018) and GSWLC-M2 catalogs. We used the GSWLC-M2 star formation rates and stellar masses to compute the dividing line between star-forming and passive galaxies (the horizontal line at log SSFR $[\mathrm{yr}^{-1}] = -11.3$). This cut was determined by fitting the log SSFR histogram with a double-Gaussian and calculating where the two Gaussians intersect. Red misfits are defined as galaxies that are star forming (above the horizontal line) and red in colour ($g-r \geq 0.67$; Evans et al. 2018).

where $\alpha_{\rm CO}$ is the CO-to-H_2 conversion factor (Bolatto et al. 2013) and r_{21} is the ratio of CO(2-1) to CO(1-0) intensities. Note that in this work we use the subscript "mol" to indicate total molecular gas (hydrogen and helium). In normal star-forming regions $\alpha_{\rm CO}$ is often assumed to be 4.35 $M_\odot$ (K km s^{-1} $pc^2)^{-1}$, which includes the contribution from helium (a factor of 1.36). For CO(2-1) measurements, one must assume a value of r_{21}. Variations from $r_{21} \sim 0.6$ (Yajima et al. 2021) to ~ 0.8 (Saintonge et al. 2017) have been observed, we use the commonly-used value of 0.7. The JINGLE analysis assumed a ratio of $r_{21} = 0.7$ and $\alpha_{\rm CO} = 4.35$ (Saintonge et al. 2018).

2. IRAM 30-m CO(2-1) and some CO(1-0) fluxes from the xCOLD GASS survey (Saintonge et al. 2017). xCOLD GASS is a representative sample of CO emission in nearby galaxies. These galaxies were primarily selected from the xGASS survey (Catinella et al. 2018). The molecular gas masses in the xCOLD GASS catalog were computed using a metallicity-dependent $\alpha_{\rm CO}$. To be consistent with the JINGLE catalog we recalculated these molecular gas masses using $\alpha_{\rm CO} = 4.35$.

3. Our own JCMT CO(2-1) measurements of red misfits. These galaxies are from the JINGLE sample that were not scheduled to be observed in CO(2-1), but had already been observed using SCUBA-2. These data were reduced and converted into molecular gas masses using JINGLE method [C. Wilson, private communication]. These measurements are shown in Table A1.

The number of galaxies with CO measurements, and the sources of these measurements are

Table 4.1: Numbers of galaxies with CO, H I, and 850 μm measurements, and the sources of these measurements.

Measurement	Source(s)	# Galaxies	# Non-Detections
CO	- JINGLE - xCOLD GASS - Our own observations from JCMT	427	61
H I 21 cm †	- xGASS - JINGLE/Arecibo - ALFALFA α.100	369	65
Dust (850 μm)	- JINGLE - Our own observations from JCMT	209	106

† Only galaxies with both CO and H I observations are used.

shown in the first row of Table 4.1.

4.2.3 H I observations

In addition to the molecular gas supply, we are interested in measuring the total gas mass

$$M_{\rm gas} = 1.36(M_{\rm H_2} + M_{\rm HI}), \tag{4.4}$$

where $M_{\rm H_2}$ is the molecular hydrogen mass and $M_{\rm HI}$ is the neutral hydrogen mass. Note that in this work, the subscript "gas" refers to the total molecular and atomic gas as shown in Equation 4.4. We collected H I measurements from the following sources:

1. The ALFALFA α.100 catalog (Haynes et al. 2018). We cross-matched the JINGLE sample with this catalog, which provided H I measurements for 99 galaxies from the JINGLE sample.

2. The xGASS representative sample (Catinella et al. 2018). This sample provides H I mea-

surements for most of the galaxies in the xCOLD GASS sample.

3. Observations of a subset of the JINGLE sample using the Arecibo telescope (obtained by private communication with M. Smith). This sample consists of 60 JINGLE galaxies which were not observed as part of the ALFALFA survey.

The number of galaxies with H I measurements, and the sources of these measurements are shown in the second row of Table 4.1.

4.2.4 Dust masses from sub-millimeter observations

We use SCUBA-2 850 μm flux densities $S_{850\ \mu\mathrm{m}}$ to estimate the cold dust mass of galaxies in our sample. These measurements are from the following sources:

1. SCUBA-2 850 μm measurements from the JINGLE survey Smith et al. (2019). These data are available at `http://www.star.ucl.ac.uk/JINGLE/data.html`. On that page is a catalog of far-infrared and sub-mm photometry, from which we obtained 850 μm flux measurements.

2. Our own SCUBA-2 850 μm measurements of a sample of red misfits. These galaxies were selected from the xCOLD GASS sample. xCOLD GASS does not overlap significantly with far-infrared surveys – this was the primary motivation for obtaining SCUBA-2 measurements of these galaxies. We present our 850 μm measurements in Table B2. These measurements were processed in the same way as in Smith et al. (2019) except we did not correct for CO(3-2) contamination.

The number of galaxies with SCUBA-2 850 μm measurements, and the sources of these measurements are shown in the third row of Table 4.1.

To convert 850 μm flux densities $S_{850\,\mu\mathrm{m}}$ into dust masses, first consider the relationship between specific flux and dust mass at wavelength λ assuming it emits as a modified blackbody

$$F_\lambda\ [\mathrm{W\ m^{-2}\ m^{-1}}] = M_{\mathrm{dust}} d_L^{-2} \kappa_\lambda(\beta) B_\lambda(T), \tag{4.5}$$

where M_{dust} is the dust mass in kg, d_L is luminosity distance in m, κ_λ is the dust opacity in $\mathrm{m^2\ kg^{-1}}$, and $B_\lambda(T)$ is the Planck function

$$B_\lambda(T) = \frac{2hc^2}{\lambda^5} \frac{1}{\exp(hc/k_B T\lambda) - 1}. \tag{4.6}$$

Following Lamperti et al. (2019), dust opacity is given by

$$\kappa_\lambda(\beta)\ [\mathrm{m^2\ kg^{-1}}] = \kappa_0 \left(\frac{\lambda_0}{\lambda}\right)^\beta, \tag{4.7}$$

where $\kappa_0 = 5.1 \times 10^{-2}\ \mathrm{m^2\ kg^{-1}}$ at 500 μm, $\lambda_0 = 500\ \mu$m, and β is the spectral index.

The 850 μm flux density $S_{850\,\mu\mathrm{m}}$ in units of Jy can be converted into units of specific intensity via

$$F_{850\,\mu\mathrm{m}} = 10^{-26} c \lambda^{-2} S_{850\,\mu\mathrm{m}}. \tag{4.8}$$

Finally we can rearrange Equation 4.5 for $M_{\rm dust}$ which gives

$$M_{\rm dust} = \frac{10^{-26} c \lambda^{-2} d_L^2 S_{850\,\mu{\rm m}}}{\kappa_\lambda(\beta) B_\lambda(T)}. \tag{4.9}$$

We use the scaling relation for β from Equation 35 in Lamperti et al. (2019)

$$\beta = a_1 \log M_* + a_2 \log A + a_3 \log[12 + \log({\rm O/H})] + a_4, \tag{4.10}$$

where $A = \pi r_{50}^2$ in kpc^2 is the surface area corresponding to the optical half-light radius r_{50}, $12 + \log({\rm O/H})$ is the gas-phase metallicity using the [O III]/[N II] calibration of Pettini & Pagel (2004), and the fit parameters are $a_1 = 0.27$, $a_2 = -0.33$, $a_3 = 0.71$, and $a_4 = -6.62$. The relation for dust temperature T in Kelvin is their Equation 37

$$T = b_1 \log {\rm SFR} + b_2 \log M_* + b_3, \tag{4.11}$$

where $b_1 = 2.91$, $b_2 = -2.27$, and $b_3 = 45.42$. We use these scaling relations to estimate β and T for each galaxy, and then estimate dust mass using Equation 4.9.

4.3 Analysis and Results

4.3.1 Comparing the gas and dust properties of red misfit and blue active galaxies

To better understand the nature of red misfits and their role in galaxy evolution, it is critical to understand their gas and dust properties. In Figures 4.2, 4.3, and 4.4, we show their gas mass properties, gas depletion times, and dust mass fractions. We show each quantity from two perspectives in order to compare between red misfits and blue active galaxies. The first perspective is a comparison of distributions of detected measurements, shown in the left panels, which allows us to compare the properties of the entire red misfit and blue active samples. We compare the two unbinned distributions using a two-sample Kolmogorov-Smirnov (KS) test implemented in `scipy.stats.ks_2samp`; if the resulting KS statistic is small or the p-value is large, then one cannot reject the null hypothesis that the two distributions are drawn from the same parent distribution. A "$\star$" in the upper left of these histograms indicates that the distributions are statistically different. The results of each KS test are shown in Table 4.2. In this table we also show the restricted mean and standard error of each quantity for red misfits and blue actives separately, taking non-detections into account. This was done using the Kaplan-Meier estimator (implemented in the "lifelines" Python package), from which we extract a restricted mean and standard error. The Kaplan-Meier estimator is a survival analysis algorithm which estimates the probability distribution of a quantity when measurements of this quantity contain both detections and non-detections. The "restricted mean" is the integral of the estimated survival function up to the largest detected data point. A recent application of the Kaplan-Meier estimator to molecular gas measurements of galaxies can be found in Mok et al. (2016). The

second perspective shows gas mass properties, depletion times, and dust mass fractions in the SFR-M_* plane. This allows us to compare the average properties of red misfits and blue actives in two-dimensional bins of log SFR and log M_*. For example, in the right panel of the first row of Figure 4.2, the colour of each bin shows the average $M_{\rm mol}/M_*$ for red misfits divided by that of blue actives in that bin. This helps to understand differences in gas and dust properties while controlling for the fact that red misfits and blue actives are distributed differently in the log SFR-log M_* plane.

First we compare the relative amount of cold gas in these two populations through two quantities: the molecular-to-stellar mass ratio $M_{\rm mol}/M_*$, and the total gas to stellar mass ratio $M_{\rm gas}/M_*$, shown in Figure 4.2. The distributions on the left and the KS test results (Table 4.2) indicate that red misfits tend to have lower gas mass fractions than blue active galaxies. In the middle two panels one can see that red misfits and blue actives are distributed differently in the log SFR-log M_* plane (red misfits tend to lie below the MS especially at high stellar masses), and that the gas fractions vary within this space. To compare the average properties as functions of position in the log SFR-log M_* plane, we computed the average gas fractions (detections only) in two-dimensional bins of log SFR and log M_* (right column). A minimum of three red misfits and three blue actives per bin were required. One can see that red misfits tend to have higher $M_{\rm mol}/M_*$ primarily at low stellar masses, while red misfits tend to have lower $M_{\rm gas}/M_*$ in most regions of the plane. The restricted mean gas fractions for red misfits and blue actives are shown in Table 4.2. The ratio of red misfit to blue active gas fractions are significantly less than unity, which supports our findings from detections alone. This indicates that red misfits have lower

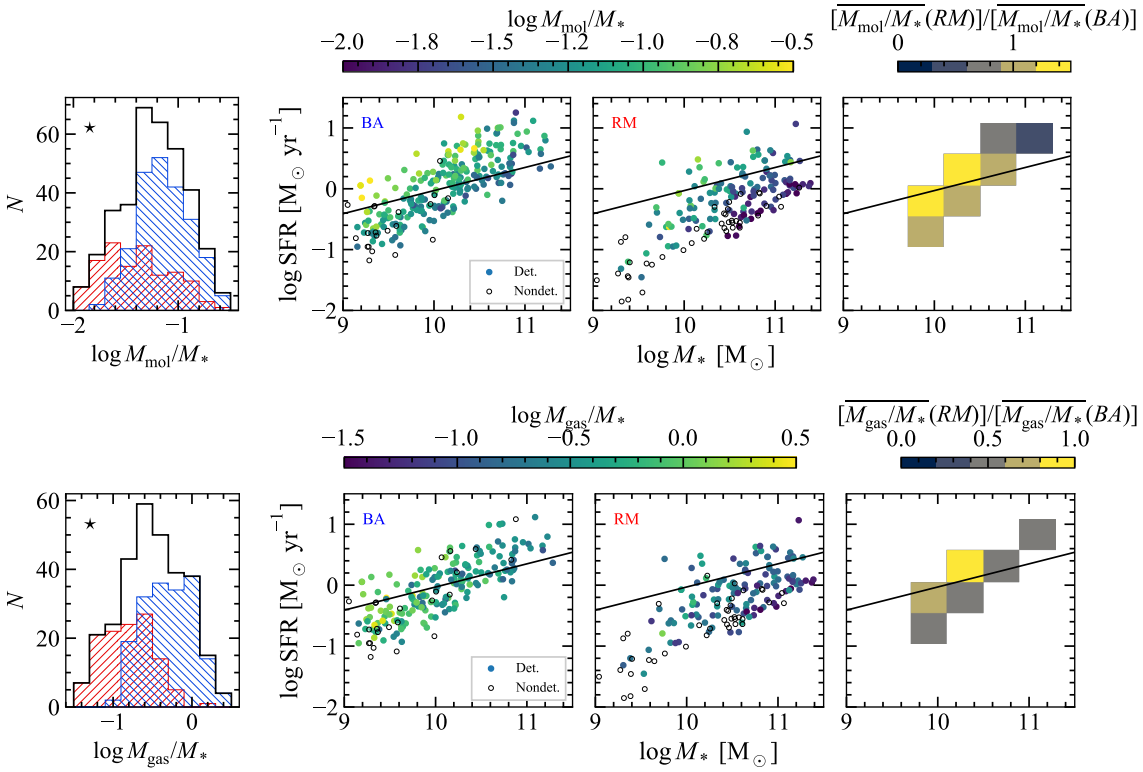

Figure 4.2: Left: Histograms of molecular (top) and total (bottom) gas mass fractions of all galaxies (black), red misfits (red histogram) and blue actives (blue histogram). Only detections are shown. The KS-test between the red misfit and blue active distributions are shown in Table 4.2; a "⋆" symbol in the upper left of a histogram indicates that the distributions are likely different. Restricted means and the ratio of restricted means of red misfits to blue actives are shown in Table 4.2. Middle panels: gas mass fractions of red misfits ("RM") and blue actives ("BA") and their relationships to host galaxy position on the SFMS diagram. Coloured circles are detected in H_2 (and H I where those measurements are used). Open circles were observed but not detected. The solid line is the star-forming main sequence from Table 1 of Popesso et al. (2019). The right panels show the ratio of the average gas mass fractions of red misfits to blue actives. Note that the ratios are in linear units and the colour scales are different in the two rows.

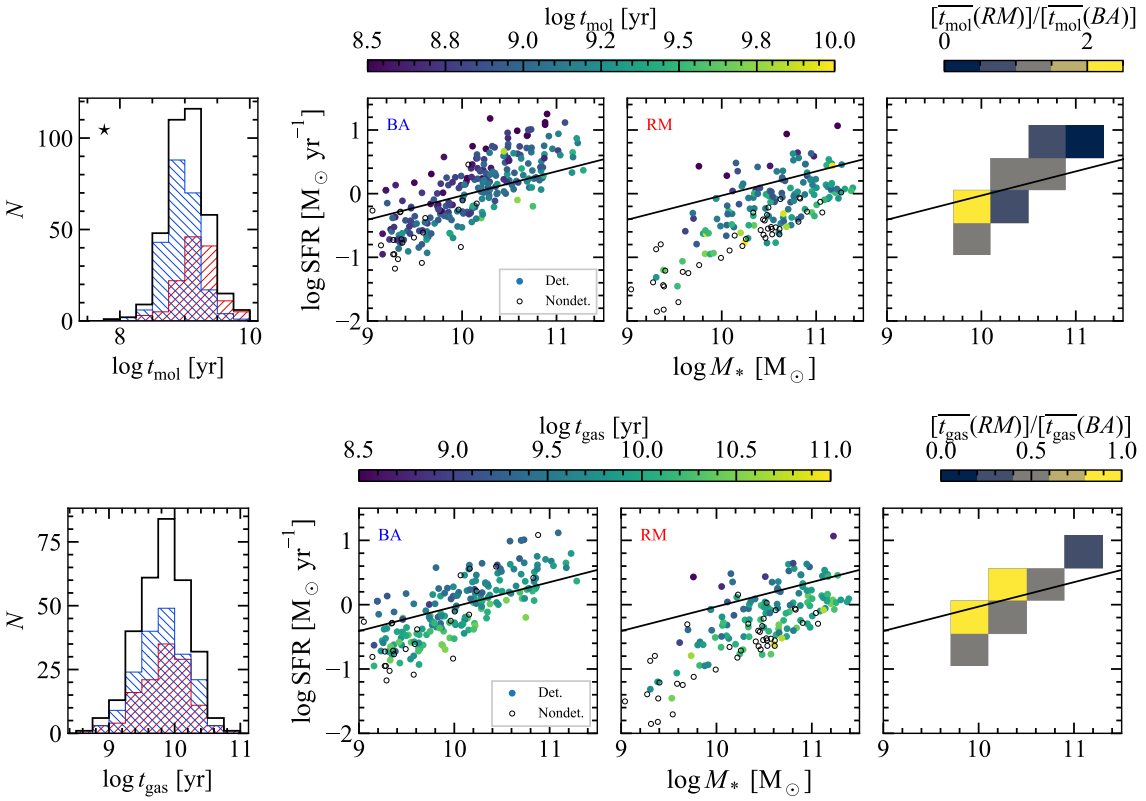

Figure 4.3: Same as Figure 4.2 except with molecular gas (top) and total gas (bottom) depletion times.

total gas content and molecular gas content relative to blue actives.

Next we compare the molecular and total gas depletion times (Figure 4.3). Based on the KS test between the red misfit and blue active distributions (Table 4.2), one can see that the t_{mol} distributions are significantly different, while the t_{gas} distributions are not. This is also supported by the ratios of the restricted means – compared to blue actives, the mean t_{mol} of red misfits is slightly larger but the difference is statistically significant. The mean t_{gas} of both populations are not significantly different. This indicates that the molecular gas will be depleted more slowly in red misfits than blue actives, but the total gas reservoirs deplete at nearly the same rates. From the other panels of Figure 4.3 there are no clear trends in the ratios of t_{mol} or t_{gas}. Thus overall,

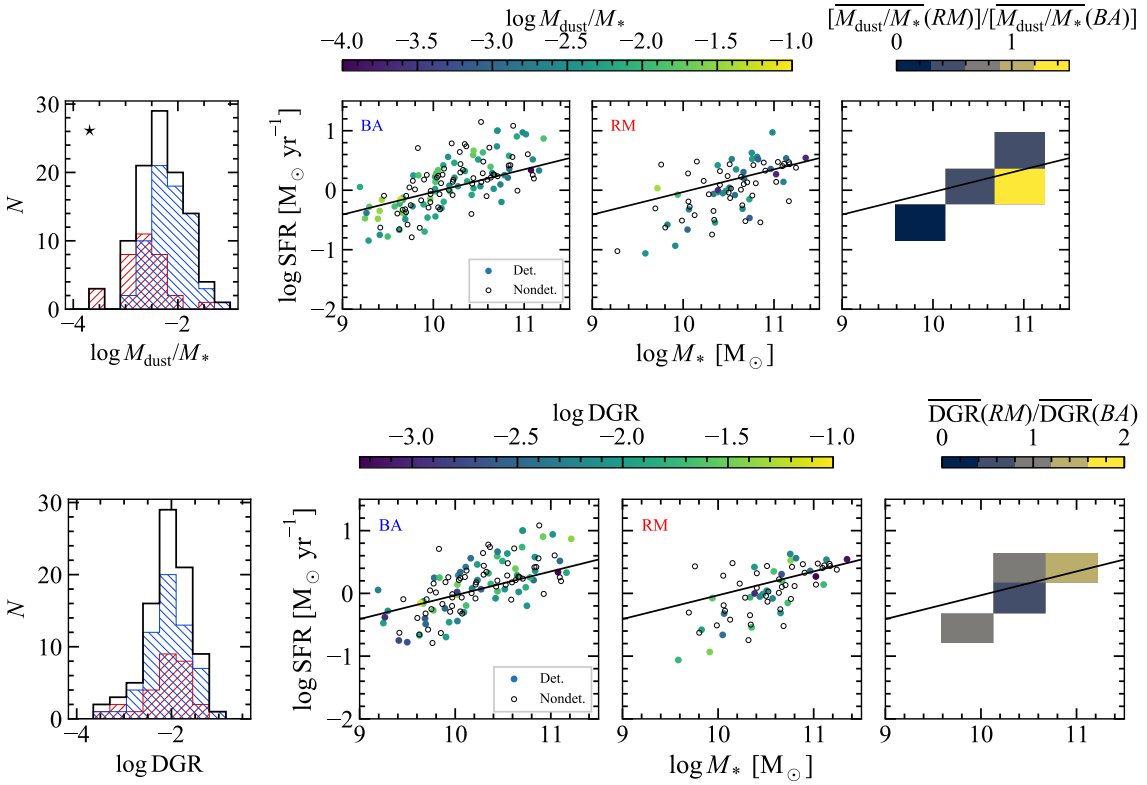

Figure 4.4: Same as Figure 4.2 except with dust-to-stellar mass shown in the top row and the dust-to-gas ratio (DGR; Equation 4.12) in the bottom row.

there are no strong trends in the ratio of depletion times with position in the SFMS.

Finally we show the dust-to-stellar mass ratios M_{dust}/M_* and the dust-to-gas ratios

$$\mathrm{DGR} \equiv \frac{M_{dust}}{M_{gas}}, \tag{4.12}$$

in Figure 4.4. In the top row one can see that M_{dust}/M_* distributions are different based on a KS test (Table 4.2), while the DGR distributions do not show a significant difference. This is also supported by the fact that red misfits have significantly lower restricted mean M_{dust}/M_* value than blue actives. Red misfits have a smaller restricted mean DGR than blue actives, but

this is not statistically significant (only 2σ). In the SFMS plane (middle panels of Figure 4.4), one can see that aside from a few bins with small number of galaxies in them, red misfits tend to have lower $M_{\rm dust}/M_*$ in all areas of this plane. Dust-to-gas ratios also do not show any strong differences between red misfits and blue actives in this plane. These results indicate that red misfits contain *less* dust than blue active galaxies, rather than more dust as one might initially expect based on their red colours.

Table 4.2: Statistical comparisons of gas- and dust-based quantities between red misfits and blue active galaxies.

Quantity	KS statistic[†]	p-value[††]	Different?[⋆]	Restricted mean[‡]		log(RM/BA)[‡‡]	Figure
				RM	BA		
log $M_{\rm mol}/M_*$	0.428	1.40×10^{-14}	Y	-1.61 ± 0.03	-1.16 ± 0.02	-0.46 ± 0.04	4.2
log $M_{\rm gas}/M_*$	0.592	3.33×10^{-16}	Y	-0.94 ± 0.03	-0.33 ± 0.02	-0.61 ± 0.04	4.2
log $t_{\rm mol}$ [yr]	0.409	2.70×10^{-13}	Y	9.10 ± 0.03	8.91 ± 0.02	0.20 ± 0.03	4.3
log $t_{\rm gas}$ [yr]	0.116	2.47×10^{-1}	N	9.76 ± 0.03	9.77 ± 0.03	-0.008 ± 0.042	4.3
log $M_{\rm dust}/M_*$	0.536	1.79×10^{-6}	Y	-2.87 ± 0.07	-2.20 ± 0.05	-0.67 ± 0.09	4.4
log DGR	0.112	9.44×10^{-1}	N	-2.32 ± 0.09	-2.07 ± 0.05	-0.2 ± 0.1	4.4

[†] Kolmogorov-Smirnov (KS) statistic comparing red misfits and blue actives. This includes detections only, by definition (§ 4.3.1).
[††] p-value corresponding to the KS statistic.
[⋆] Are the distributions statistically different based on the KS statistic (Y/N)? Y if KS ≥ 0.4 and $p \ll 1$.
[‡] Kaplan-Meier restricted mean and standard error (§ 4.3.1).
[‡‡] Ratio of the restricted mean of red misfits to blue actives, in logarithmic units.

4.3.2 Scaling relations

A key question in understanding the evolution of star-forming galaxies is what drives the scatter about the star forming main sequence (SFMS)? In recent work, assessing the relative importance of gas depletion time and gas mass fraction in driving the scatter about the SFMS has been a major focus (see, e.g., Saintonge et al. 2016; Lin et al. 2019b; Ellison et al. 2020; Feldmann 2020; Sánchez et al. 2021). Here we explore whether there are differences in how depletion times and gas mass fractions of red misfits and blue actives correlate with offset from the SFMS. To answer these questions, we plot $\log\ t_{\rm mol}$, $\log\ t_{\rm gas}$, $\log\ M_{\rm mol}/M_*$, and $\log\ M_{\rm gas}/M_*$ versus offset from the SFMS. The offset from the star forming main sequence is defined as

$$\Delta{\rm MS} = \log {\rm SFR}(M_*) - \log {\rm SFR}_{\rm MS}(M_*), \tag{4.13}$$

where $\log {\rm SFR}(M_*)$ is the SFR of a galaxy with stellar mass M_* and $\log {\rm SFR}_{\rm MS}(M_*)$ is the star forming main sequence (Popesso et al. 2019) at the same stellar mass

$$\log {\rm SFR}_{\rm MS}(M_*) = 0.38 \log M_* - 3.83. \tag{4.14}$$

We adopt this particular definition of the SFMS because it was derived from the same SFR and M_* measurements that we use here, namely those from the GSWLC-M2 catalog.

In Figure 4.5 we show molecular gas $t_{\rm mol}$ (left column) and total gas $t_{\rm gas}$ depletion times (right column) versus ΔMS. The restricted mean and standard error (see Section 4.3.1) of each quan-

tity is computed in bins of ΔMS. As a test of our method, in the top row we compare our relations with those from (Feldmann 2020), which shows good agreement. There are some notable differences between their study and ours: in Feldmann (2020) the xCOLD GASS sample was used, whereas here we are using a larger sample and a slightly different definition of the SFMS; they took non-detections into account using a method that is different than ours (LeoPy; Feldmann 2019). We also compare our log $t_{\rm mol}$-Δ MS relationship using the average of detections only with the relationship found by Tacconi et al. (2018) with the IRAM Plateau de Bure high-z blue sequence CO(3-2) survey (PHIBSS; Tacconi et al. 2013), who did not incorporate non-detections. Although their sample is notably different than ours in terms of redshift ($z \sim 1$ to 2 versus $z \sim 0$ in our work), this plot shows that our results are in good agreement with theirs. Overall, these relationships show that as galaxies move from above to below the main sequence their gas is used up more slowly.

Having confirmed that our results for the sample as a whole agree with previous work, we move on to study these trends for red misfits and blue actives separately in the middle and bottom rows of Figure 4.5. In the middle row, one can see that both populations follow similar trends to the population as a whole; however red misfits have elevated $t_{\rm mol}$ up to about Δ MS ~ 0.2 dex. This is in line with our previous result in Table 4.2, which showed that red misfits have longer $t_{\rm mol}$ and similar $t_{\rm gas}$ compared to blue actives. Here, however, we see that this difference is primarily coming from galaxies on and below the main sequence. In the bottom row we show the same as the middle row except only galaxies with $10 \leq \log M_* \leq 11$, which is where both red misfits and blue actives are well-sampled. One can see that the trends between

red misfits and blue actives become more similar. This result indicates that the differences seen in the middle left panel are coming from galaxies outside of this stellar mass range.

In Figure 4.6 we show molecular gas mass fractions $M_{\rm mol}/M_*$ and total gas $M_{\rm gas}/M_*$ mass fractions versus ΔMS. We use the same survival analysis approach as above to take non-detections into account in each ΔMS bin. Note that we do not have curves from the literature to show for comparison. In the top row one can see that $M_{\rm mol}/M_*$ decreases as galaxies move from above to below the main sequence, while $M_{\rm gas}/M_*$ remains roughly constant at $\sim$ 0.5 dex until offsets of about -0.5 dex are reached. In the middle row, one can see that the trends for red misfits and blue actives are different, especially below the main sequence. Red misfits have significantly lower $M_{\rm mol}/M_*$ and $M_{\rm gas}/M_*$ relative to blue active galaxies, although the differences become less significant on and above the main sequence. This indicates that red misfits are quite gas-poor, despite their relatively similar gas depletion times compared to blue actives. This result is echoed by the comparison of restricted means of these properties for red misfits and blue actives altogether (Table 4.2): red misfits have significantly lower gas mass fractions than blue actives. In the bottom row of Figure 4.6, we show the same as the middle row but only for galaxies with $10 \leq \log\ M_* \leq 11$. One can see in the that the relative differences between red misfits and blue actives remains. This indicates that the differences seen in the bottom row of Figure 4.6 are not being driven by galaxies outside of this stellar mass range.

4.3.3 The Kennicutt-Schmidt Law, and the Molecular Gas Main Sequences

Stellar mass, SFR, and molecular gas are correlated with each other, as shown by the star formation main sequence (SFR vs. stellar mass) and the Kennicutt-Schmidt relation (SFR vs. molec-

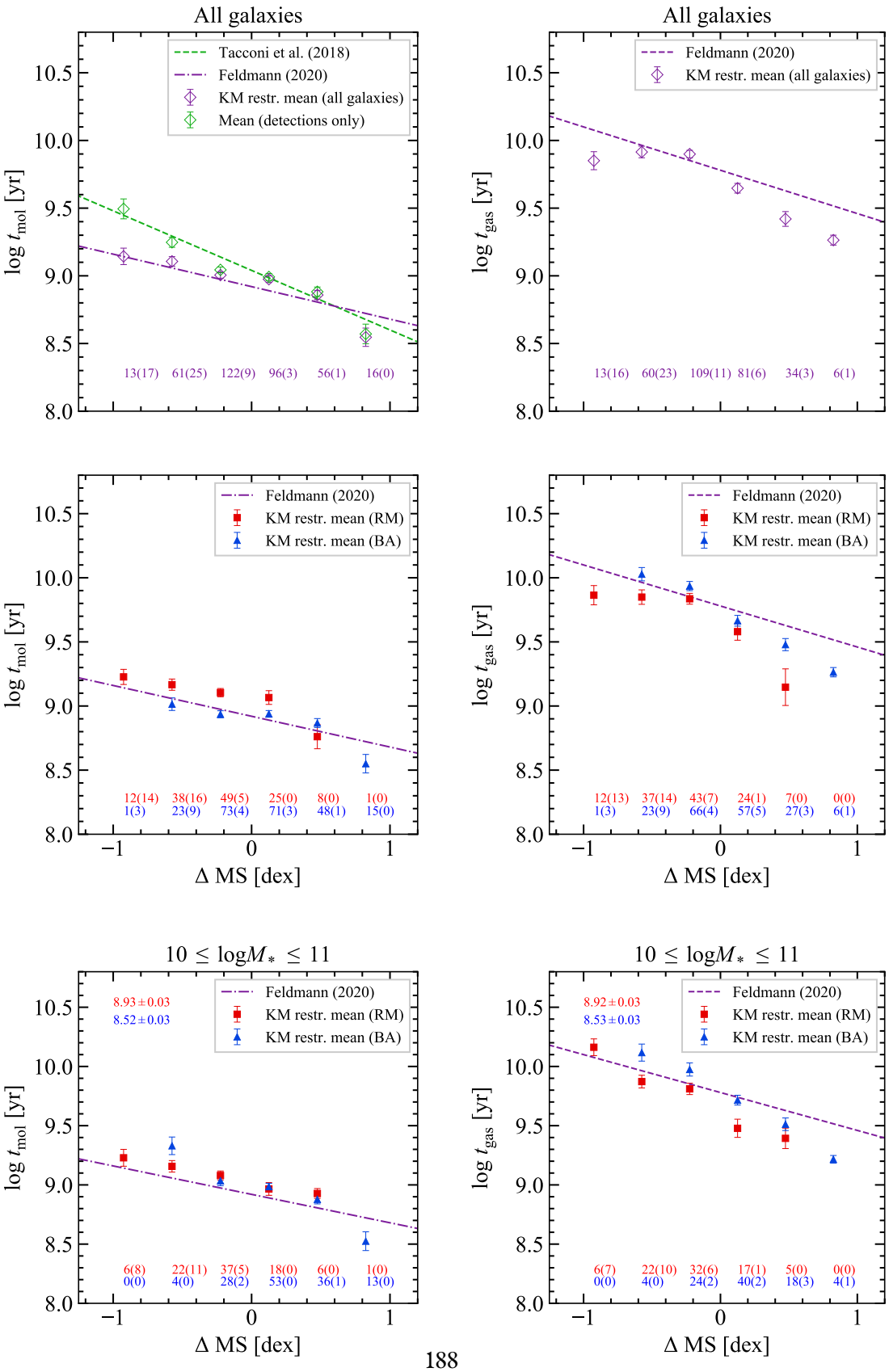

Figure 4.5: (Caption on following page.)

Figure 4.5: (Previous page.) Molecular (left) and total (right) gas depletion times versus offset from the star forming main sequence (Equation 4.13). The purple dot-dashed lines are from Feldmann (2020), which are fits to molecular (left) and total (right) gas depletion times from xCOLD GASS (+xGASS) after taking non-detections into account. The green dashed line is the fit to $z = 0 - 4$ galaxies from the PHIBSS survey (Tacconi et al. 2018) for comparison. The Kaplan-Meier median is the value where the cumulative distribution reaches 0.5. The top row shows all galaxies in our sample. One can see that our results agree well with (Tacconi et al. 2018) when we ignore non-detections and with Feldmann (2020) when we include non-detections. The middle row shows red misfits and blue actives separately. The number of detections in each bin and the number of non-detections in that bin are in brackets. One can see that, when there is enough data to compute a median ($\geq$ 5 points), the molecular and total gas depletion times of red misfits and blue actives are similar, although slightly (but statistically significantly) larger for red misfits. The bottom row is the same as the middle row except only showing galaxies with stellar masses between 10^{10} and 10^{11} $M_{\odot}$, where both depletion times become more similar between red misfits and blue actives.

ular gas mass). Recent work has introduced the "molecular gas main sequence" (MGMS; $\Sigma_{\rm mol}$ vs. Σ_{*}) as a companion to the aforementioned relationships (e.g. Lin et al. 2019a). By simultaneously examining these three correlations one can gain insight into the physical mechanisms that determine the observed appearance of the star formation main sequence. Here we compare the MGMS and KS relationships of red misfit and blue active galaxies (Figure 4.7). Each of these relationships shows strong correlations (Pearson-r of detections ranging from 0.68 to 0.86). We used LinMix (Kelly 2007) to fit lines to each of these plots, taking uncertainties in both variables and upper limits in $M_{\rm mol}$ into account. In the bottom row the fits were done with log SFR on the x-axis, and the best-fit equations were inverted to match how this relationship is usually shown with gas on the x-axis and SFR on the y-axis.

In the top row of Figure 4.7, by comparing the points and fits with lines of constant $M_{\rm mol}/M_{*}$ (dotted lines), one can see that red misfits have lower molecular fractions (between 1 and 10 per cent) than blue actives (mostly around 10 per cent). The fit to blue actives is nearly linear, and

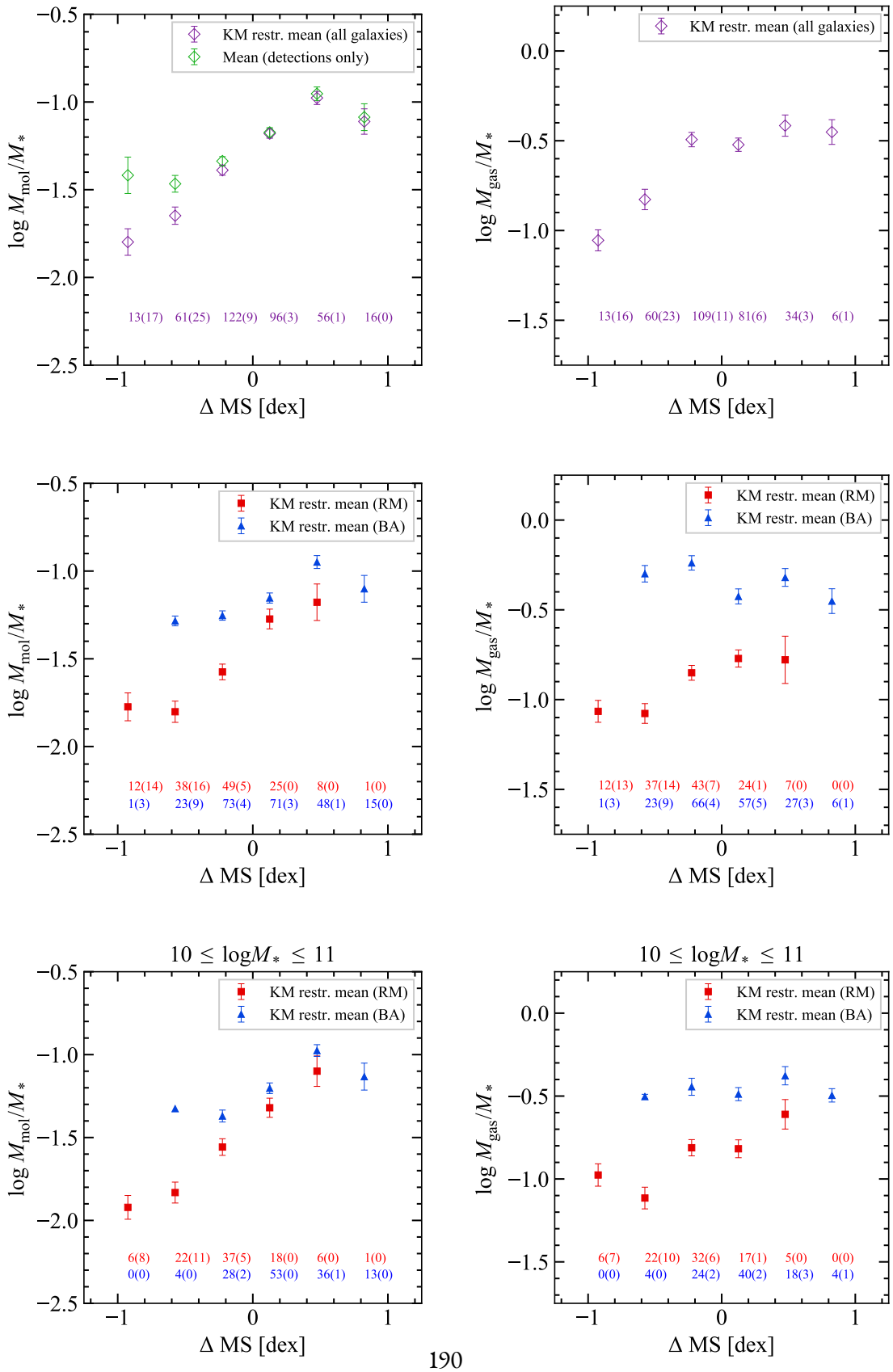

Figure 4.6: (Caption on following page.)

Figure 4.6: (Previous page.) Molecular (left) and total (right) gas mass fractions versus offset from the star forming main sequence (Equation 4.13). The top row shows all galaxies in our sample. One can see that across the main sequence, molecular gas mass fraction rises, while the total gas mass fraction rises and then remains constant. The middle row shows red misfits and blue actives separately. The number of detections in each bin and the number of non-detections in that bin are in brackets. One can see that, in contrast to Figure 4.5, red misfits tend to have lower molecular and total gas fractions below and on the main sequence. The bottom row is the same as the middle row except only showing galaxies with stellar masses between 10^{10} and 10^{11} $M_{\odot}$, where both gas mass fractions change slightly but remain significantly different between red misfits and blue actives.

the intercept is close to the value of the restricted mean from Table 4.2 (dashed line). Red misfits however show a significantly shallower (sub-linear) slope than blue actives (a difference of $\sim 6\sigma$), causing the best-fit intercept to differ more significantly from the restricted mean from Table 4.2 (dashed line). The difference between these populations is most striking at larger stellar masses. The shallower slope in the MGMS for red misfits suggests physical difference between these two populations – the molecular gas content of red misfits is lower on average, and is significantly less correlated with stellar mass.

In the bottom row of Figure 4.7, by comparing the data points and linear fits with lines of constant $t_{\rm mol}$, one can see that red misfits and blue actives have slightly longer $t_{\rm mol}$ (echoing our earlier results). In contrast to the MGMS plots, the slope of the red misfit and blue active KS relations are not significantly different ($\sim 1\sigma$). The KS slope of red misfits and blue actives are both slightly super-linear. This near-linearity results in the best-fit intercepts being close to the restricted means from Table 4.2 (dashed lines). The similarity of the gas depletion time relationships, combined with the MGMS results, and the fact that red misfits tend to lie below the SFMS (e.g., Figure 4.2) suggests that red misfits have lower than average star formation rates

due to a lack of molecular gas rather than inefficient star formation.

4.4 Discussion

Our findings show that red misfits and blue actives have different molecular and total gas mass fractions, and different dust mass fractions, slightly different molecular gas depletion times, but similar total gas depletion times, and similar dust-to-gas ratios. We showed that red misfits have lower $M_{\rm mol}/M_*$ and $M_{\rm gas}/M_*$ ratios than blue actives on average (Section 4.3.1) and as functions of offset from the main sequence (Section 4.3.2). We showed that red misfits tend to have lower $M_{\rm dust}/M_*$ ratios than blue actives (Section 4.3.1). We showed that red misfits have a significantly shallower slope than blue actives in the molecular gas main sequence (Section 4.3.3), and that red misfits and blue actives have consistent Kennicutt-Schmidt relations (Section 4.3.3).

We found that the dust content of red misfits is similar (based on the DGR) or lower than (based on $M_{\rm dust}/M_*$) that of blue actives, which supports the claims from Evans et al. (2018) that the red colours of red misfits are not due to dust reddening. Their red colours are therefore likely due to the presence of old stellar populations. However, $g-r$ colour is not as sensitive to young stellar populations as $u-r$ or NUV $-r$, and so a red $g-r$ colour does not necessarily indicate a red $u-r$ or NUV $-r$ colour. Indeed, by definition, red misfits are actively forming stars, and so they must host young stellar populations.

Our findings that red misfits have lower molecular gas fractions, and even lower total gas fractions, than blue actives, combined with the fact that red misfits tend to lie on or below the main sequence while blue actives tend to lie on or above the main sequence, and the fact that

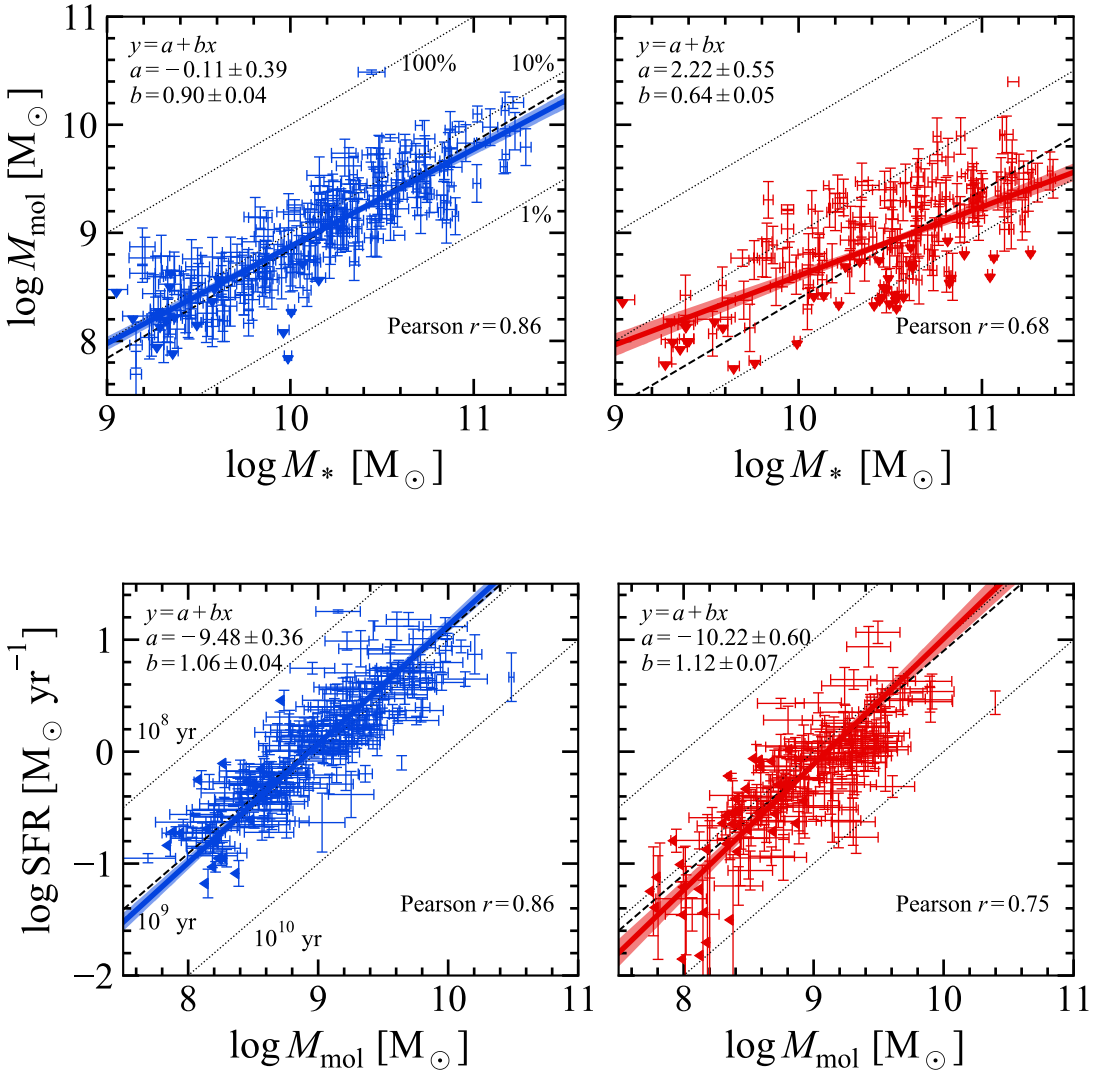

Figure 4.7: The molecular gas main sequence (top) and Kennicutt-Schmidt relation with molecular gas (bottom) for blue active (left) and red misfit galaxies (right). The linear fits in all panels were performed using LinMix (Kelly 2007) which incorporates uncertainties in x and y, and upper limits in y. In the bottom row the fits were done with log SFR on the x-axis, and the best-fit equations were inverted to match how this relationship is usually shown with gas on the x-axis and SFR on the y-axis. In the top row, the dotted lines represent constant $M_{\rm mol}/M_*$ (1, 10, and 100 per cent), and the dashed lines correspond to the restricted mean $M_{\rm mol}/M_*$ for blue actives and red misfits from Table 4.2. The bottom rows show lines of constant $t_{\rm mol}$, and the restricted means from Table 4.2. These plots show that red misfits tend to have lower $M_{\rm H_2}/M_*$ fractions, and slightly longer $t_{\rm mol}$. The slope of the MGMS is significantly flatter for red misfits than for blue actives.

$t_{\rm mol}$ and $t_{\rm gas}$ of red misfits and blue actives follow similar relationships, suggest that the lower star formation rates of red misfits are due to bottlenecks in the gas supply rather than reduced star formation efficiency. Our findings that the difference in total gas mass fraction is larger than that of molecular gas mass fraction suggests that the long-term fuel for star formation has been depleted or removed. The fact that the molecular gas mass fraction of red misfits is lowest compared to blue actives at high stellar masses suggests that red misfits have depleted their gas supply by forming stars and are on their way toward the red sequence.

One limitation of the present work is that we combined several datasets together, and so our sample has a complex selection function. Another limitation is that we only used 850 μm fluxes to estimate dust masses; a more optimal method would be to use infrared-to-submillimeter SED fitting. Unfortunately, our JCMT Semester 18B SCUBA-2 targets were selected from the xCOLD GASS sample and this sample does not overlap significantly with H-ATLAS and so the required infrared data do not exist like they do for JINGLE galaxies. In the interest of using the same method for all galaxies with SCUBA-2 data, we used the Lamperti et al. (2019) scaling relations to estimate a dust temperature and spectral index for each galaxy.

4.5 Conclusions

In summary, by analyzing trends of molecular and total cold gas mass fractions and depletion times, we have found that red misfit and blue active galaxies do not show strong differences in depletion times, but their gas mass fractions are significantly different, and exhibit significantly different scaling relations with offset from the main sequence and stellar mass. This suggests

that red misfits are more limited than blue actives by both their near term and long term gas supply rather than the rate at which they are turning the gas into stars. This is also likely due to the fact that red misfits below the main sequence tend to be more massive than blue actives. Thus red misfits have about the same amount of gas but are more massive. We also found that the dust-to-stellar ratios of red misfits are lower than that of blue actives, while their dust-to-gas ratios follow similar distributions.

Our results suggest that by selecting galaxies based on optical $g - r$ colour and specific star formation rate simultaneously, high mass galaxies that are classified as red and star forming (red misfits) are actively quenching after depleting their gas supply through star formation, while those with low stellar masses either had limited gas supply to begin with or had their gas removed prematurely (e.g. due to environmental effects such as ram pressure stripping).

Acknowledgements

We thank Fraser Evans for assistance and for providing the catalogue of red misfits. The James Clerk Maxwell Telescope is operated by the East Asian Observatory on behalf of The National Astronomical Observatory of Japan; Academia Sinica Institute of Astronomy and Astrophysics; the Korea Astronomy and Space Science Institute; Center for Astronomical Mega-Science (as well as the National Key R&D Program of China with No. 2017YFA0402700). Additional funding support is provided by the Science and Technology Facilities Council of the United Kingdom and participating universities and organizations in the United Kingdom and Canada. Additional funds for the construction of SCUBA-2 were provided by the Canada Foundation

for Innovation. The authors wish to recognize and acknowledge the very significant cultural role and reverence that the summit of Maunakea has always had within the Indigenous Hawaiian community. We are most fortunate to have the opportunity to conduct observations from this mountain.

A New JCMT CO(2-1) measurements of red misfits

Table A1: New JCMT CO(2-1) measurements of red misfits selected from the JINGLE sample.

RA (J2000)	Dec (J2000)	z	$\log M_*$	log SFR	$\log L_{\mathrm{CO}(1-0)}$	$\log M_{\mathrm{mol}}$
deg	deg		$M_\odot$	$M_\odot\ \mathrm{yr}^{-1}$	$\mathrm{K\,km\,s^{-1}\,pc^2}$	$M_\odot$
(1)	(2)	(3)	(4)	(5)	(6)	(7)
181.212	−2.438	0.0200	10.21	−0.08	8.55 ± 0.12	9.19 ± 0.75
131.119	2.064	0.0250	10.32	0.51	9.22 ± 0.07	9.86 ± 0.71
178.878	−1.261	0.0190	10.08	0.34	8.73 ± 0.12	9.37 ± 0.75
173.539	−1.595	0.0230	10.45	0.29	9.29 ± 0.06	9.93 ± 0.70
203.305	33.110	0.0240	10.78	0.25	9.40 ± 0.05	10.04 ± 0.68
179.693	−1.466	0.0210	9.72	0.03	< 8.49	< 9.13
175.912	−1.647	0.0430	10.46	0.60	< 9.03	< 9.67
201.313	32.671	0.0400	10.82	0.52	< 9.05	< 9.69
212.612	−0.832	0.0250	10.71	0.59	< 8.65	< 9.29
212.740	1.036	0.0250	10.58	0.24	< 8.64	< 9.28
182.575	−0.518	0.0350	11.02	0.27	< 8.94	< 9.57
132.804	1.062	0.0270	9.94	−0.10	< 8.55	< 9.19

(4) Stellar mass from the GSWLC-M2 or A2 catalog (if unavailable in M2).
(5) SFR from the GSWLC-M2 or A2 catalog (if unavailable in M2).
(6) Measured CO(1-0) luminosity (converted from 2-1 assuming $r_{21} = 0.7$).
(7) Measured molecular gas mass assuming $\alpha_{CO} = 4.35$.

B New SCUBA-2 measurements of red misfits

Table B2: New SCUBA-2 measurements of red misfits selected from the xCOLD GASS sample.

Name	d_L	T	β	Det?	$r_{\rm ap}$	r_{90}	$S_{850\ \mu{\rm m}}(r \leq r_{\rm ap})$	$\log M_{\rm dust}(r \leq r_{\rm ap})$
	Mpc	K			arcsec	arcsec	mJy	$M_\odot$
(1)	(2)	(3)	(4)	(5)	(6)	(7)	(8)	(9)
J142720.13+025018.1	115.53	22.64	1.94	Y	20.23	15.51	25.37 ± 3.95	8.18 ± 0.07
J104402.21+043946.8	116.29	22.25	1.65	Y	20.06	15.28	16.46 ± 2.90	7.95 ± 0.08
J101638.39+123438.5	138.88	22.14	1.86	Y	28.24	25.07	25.21 ± 4.36	8.34 ± 0.07
J100530.26+054019.4	196.55	20.16	1.94	Y	21.56	17.20	16.30 ± 2.51	8.53 ± 0.07
J095144.91+353719.6	117.99	22.93	1.93	Y	19.50	14.53	19.72 ± 3.98	8.08 ± 0.09
J235644.47+135435.4	159.92	22.81	1.82	Y	20.77	16.20	14.29 ± 2.98	8.19 ± 0.09
J105315.29+042003.1	184.23	22.54	1.91	Y	15.96	9.27	19.18 ± 3.68	8.46 ± 0.08
J100216.28+191256.3	71.90	21.88	1.92	Y	19.38	14.38	13.77 ± 3.51	7.52 ± 0.11
J080442.30+154632.6	128.22	21.32	1.86	Y	18.62	13.33	9.98 ± 2.94	7.89 ± 0.13
J112311.63+130703.7	208.32	22.26	1.90	Y	18.13	12.64	14.51 ± 4.23	8.45 ± 0.13
J094419.42+095905.1	44.09	20.38	2.03	N	16.58	10.28	< 9.82	< 7.02
J090923.67+223050.1	64.52	21.15	2.01	N	18.17	12.69	< 4.15	< 6.95
J135845.41+203942.7	69.95	22.29	2.00	N	16.56	10.26	< 8.18	< 7.28
J232326.53+152510.4	189.11	22.87	1.96	N	14.47	6.35	< 10.56	< 8.23
J151604.47+065051.4	162.09	22.99	1.93	N	21.02	16.52	< 10.37	< 8.08
J093953.62+034850.2	124.82	21.73	1.88	N	19.80	14.94	< 3.89	< 7.45
J104251.39+055135.5	146.88	20.90	1.94	N	23.48	19.55	< 7.69	< 7.92
J122006.47+100429.2	191.89	22.13	1.92	N	18.93	13.76	< 6.80	< 8.06
J152747.42+093729.6	136.77	21.57	2.02	N	17.33	11.46	< 6.99	< 7.82
J131934.30+102717.5	213.27	21.20	1.93	N	22.68	18.58	< 11.19	< 8.40
J102508.93+133605.1	80.82	21.56	1.72	N	19.07	13.96	< 7.17	< 7.30
J142846.66+271502.4	63.83	24.29	1.90	N	16.06	9.42	< 7.62	< 7.09
J021219.38+133645.6	182.82	22.01	1.89	N	16.66	10.42	< 4.80	< 7.87
J130035.67+273427.2	73.74	21.76	1.81	N	23.86	20.01	< 6.54	< 7.20
J001947.33+003526.7	76.84	22.52	1.70	N	17.88	12.28	< 6.84	< 7.21
J020359.14+141837.3	189.02	23.00	1.91	N	22.37	18.20	< 12.11	< 8.28
J130525.44+035929.7	193.31	22.13	1.87	N	15.77	8.93	< 4.17	< 7.85
J095439.45+092640.7	151.93	21.50	1.97	N	18.41	13.04	< 6.71	< 7.88
J111738.91+263506.0	210.84	22.38	2.07	N	13.61	4.03	< 7.26	< 8.20
J231816.95+133426.6	174.37	22.52	1.84	N	15.15	7.78	< 5.19	< 7.83
J011716.09+143720.5	167.65	19.62	1.98	N	15.68	8.76	< 4.66	< 7.87
J150926.10+101718.3	120.84	21.84	1.78	N	20.59	15.96	< 9.99	< 7.81
J150204.10+064922.9	204.97	21.47	1.75	N	16.90	10.79	< 5.99	< 8.04

(1) SDSS ID as shown in the xCOLD GASS catalog.
(2) Luminosity distance.
(3) Dust temperature estimated using Equation 4.11.
(4) Modified blackbody spectral index estimated using Equation 4.10.
(5) Flag for whether this galaxy is classified as a detection or not.
(6) Aperture radius over which the 850 μm flux density was measured.
(7) SDSS r-band 90 per cent Petrosian radius.
(8) 850 μm flux density within $r_{\rm ap}$.
(9) Dust mass within $r_{\rm ap}$ computed using Equation 4.9.

References

Belfiore F., et al., 2017, MNRAS, 466, 2570

Bolatto A. D., Wolfire M., Leroy A. K., 2013, ARA&A, 51, 207

Brownson S., Belfiore F., Maiolino R., Lin L., Carniani S., 2020, MNRAS, 498, L66

Catinella B., et al., 2018, MNRAS,

Coenda V., Martínez H. J., Muriel H., 2018, MNRAS, 473, 5617

Colombo D., et al., 2020, A&A, 644, A97

Eales S. A., et al., 2018, MNRAS, 481, 1183

Ellison S. L., et al., 2020, MNRAS, 493, L39

Evans F. A., Parker L. C., Roberts I. D., 2018, MNRAS, 476, 5284

Feldmann R., 2019, Astronomy and Computing, 29, 100331

Feldmann R., 2020, Communications Physics, 3, 226

Haynes M. P., et al., 2018, ApJ, 861, 49

Kelly B. C., 2007, ApJ, 665, 1489

Lamperti I., et al., 2019, MNRAS, 489, 4389

Leroy A. K., Walter F., Brinks E., Bigiel F., de Blok W. J. G., Madore B., Thornley M. D., 2008, AJ, 136, 2782

Li C., et al., 2015, ApJ, 804, 125

Lilly S. J., Carollo C. M., Pipino A., Renzini A., Peng Y., 2013, ApJ, 772, 119

Lin L., et al., 2017, ApJ, 851, 18

Lin L., et al., 2019a, ApJ, 872, 50

Lin L., et al., 2019b, ApJ, 884, L33

Lin L., et al., 2020, ApJ, 903, 145

Mancini C., et al., 2019, MNRAS, 489, 1265

Mok A., et al., 2016, MNRAS, 456, 4384

Popesso P., et al., 2019, MNRAS, 490, 5285

Saintonge A., et al., 2011, MNRAS, 415, 32

Saintonge A., et al., 2016, MNRAS, 462, 1749

Saintonge A., et al., 2017, ApJS, 233, 22

Saintonge A., et al., 2018, MNRAS, 481, 3497

Salim S., 2014, Serbian Astronomical Journal, 189, 1

Salim S., Boquien M., Lee J. C., 2018, ApJ, 859, 11

Sánchez S. F., et al., 2021, MNRAS, 503, 1615

Schawinski K., et al., 2014, MNRAS, 440, 889

Smethurst R. J., et al., 2015, MNRAS, 450, 435

Smith M. W. L., et al., 2019, MNRAS, 486, 4166

Tacconi L. J., et al., 2013, ApJ, 768, 74

Tacconi L. J., et al., 2018, ApJ, 853, 179

Yajima Y., et al., 2021, PASJ, 73, 257

York D. G., et al., 2000, AJ, 120, 1579

5

Summary and Future Work

I have presented three studies on star formation and the ISM in nearby galaxies. Molecular gas – the fuel for star formation – as traced by CO emission is a central component of each project. In this work I have taken an approach which uses data from a variety of wavelengths and resolutions, and the results have shown some of the advantages over approaches which use data from a narrower range of wavelengths, such as the ability to study star formation and the cold gas reservoir simultaneously. These projects tackled different science questions: the effects of galactic bars and interactions on molecular gas and star formation, the spatially-resolved relationship between mid-infrared emission and cold gas, and the nature of the ISM in red star-forming galaxies. This variety demonstrates the breadth of science that can be accomplished with a multi-wavelength approach. Chapters 2 and 3 utilized publicly available data, showing

the benefits of generating large, homogenous data sets for public use. Chapter 4, in contrast, utilized a heterogeneous sample consisting of public data from a variety of sources and data which I obtained from the JCMT. I was able to leverage existing data to motivate the need for further observations and to construct a sample not possible from current large surveys.

One of my overarching goals for each of these projects was to present each of them in a clear way so that every step of the analysis and all of my results can be reproduced by someone else. In each paper I have put a substantial amount of effort into clearly describing the steps of my procedures so that my results may be reproduced. Along with each paper I have also provided publicly-available data, code, and documentation which are available on the publisher's website (and additionally at `https://lig.astro.tsinghua.edu.cn/astrodata/publication/20/estimator-resolved-molecular/` for the data in Chapter 3). My hope is that the data products and analysis methods described in this thesis will be useful for others.

5.1 The role of bars and interactions

The investigations in Chapter 2 were aimed at tying together previous findings that the presence of a bar is a necessary but not sufficient condition for enhanced central star formation relative to the disk (Lin et al. 2017, 2020), and that barred galaxies tend to (but do not always) have high concentrations of molecular gas (e.g. Sheth et al. 2005). I found that both an elevated molecular gas concentration and the presence of a bar or an interaction are requirements for enhanced central star formation in isolated galaxies in our sample. None of the isolated, unbarred galaxies in the sample showed enhanced central star formation, regardless of cold gas concentration.

Thus, an elevated molecular gas concentration is the missing requirement to understand enhanced central star formation from Lin et al. (2017). The rest of the galaxies in the sample with enhanced central star formation were either interacting or merging, and with high gas concentrations. I found almost identical behaviour in all three star formation history indicators which were studied (Figure 7 of Chown et al. 2019), indicating that bar driven gas inflow and subsequent central star formation is a long-lived process ($\gtrsim 1$ Gyr). I also compared radial profiles of stellar age from one of the barred galaxies in our sample with that of a simulated barred galaxy with a similar stellar mass and bar length. The drop in stellar age with radius is evidence for the inside-out formation of the disk and bar. These results significantly improve our understanding of how bars and interactions affect the cold gas distributions and star formation histories of nearby galaxies. Chown et al. (2019) was the first EDGE science paper by authors outside of the EDGE collaboration.

5.2 The connection between CO and MIR emission

The investigations in Chapter 3 were aimed at extending previous work on the correlation between *WISE* 12 μm emission and CO emission (Jiang et al. 2015; Gao et al. 2019) to higher resolution. By smoothing the EDGE CO data to *WISE* 12 μm resolution (6.6 arcsec) and comparing H_2 surface densities with 12 μm surface densities in each pixel I found that 12 μm and CO(1-0) are strongly correlated at this resolution (1-2 kpc). I also found that the correlations vary from galaxy to galaxy. The presence of a strong spatially-resolved correlation between *WISE* 12 μm and CO(2-1), along with galaxy-to-galaxy offsets have recently been confirmed

in the PHANGS sample (Leroy et al. 2021).

My next goal was to develop an estimator of H_2 surface density ($\log \Sigma(H_2)$) based on *WISE* 12 μm. To do this, I used the machine learning techniques of ridge regression and cross-validation. I compiled all of the spatially-resolved measurements (EDGE CO, *WISE* 12 μm, resolved SFR, stellar mass, gas-phase metallicity from CALIFA IFU data) and global properties such as stellar mass, SFR, and NUV luminosity from *GALEX*. I performed ridge regression (with the regularization paramter chosen by cross-validation) on all possible combinations of parameters with $\log \Sigma(H_2)$ as the dependent variable, and measured the performance of each model (again using cross-validation). I selected models which had the best ability to predict $\Sigma(H_2)$, and we provided the best-fit relations in the paper. The correlation between $\Sigma(12\ \mu m)$ and $\Sigma(H_2)$ was the strongest of all correlations that were examined. I also found that $\Sigma(H_2)$ estimators which include $\Sigma(12\ \mu m)$ are able to predict $\Sigma(H_2)$ more accurately than estimators that include resolved optical properties instead of $\Sigma(12\ \mu m)$. These results suggest that 12 μm emission and H_2 as traced by CO emission are physically connected on kiloparsec scales, possibly due to a connection between the abundance of PAHs and the abundance of CO.

5.3 The nature of red star-forming galaxies

In Chapter 4 I investigated the interstellar medium of a unique sample of galaxies which are optically red yet star-forming, called "red misfits" (Evans et al. 2018). To trace the molecular gas content in these galaxies I combined CO data from the xCOLD GASS survey (Saintonge et al. 2018), the JINGLE survey (Saintonge et al. 2017), and my own JCMT P.I. science program. To

trace the H I content over much of this sample, I gathered together 21 cm H I data from the xGASS survey (Catinella et al. 2018), the ALFALFA 100 per cent catalog (Haynes et al. 2018), and an H I catalog for a subset of JINGLE (Saintonge et al. 2017) galaxies. Finally, to trace the dust content in many of these galaxies I used the SCUBA-2 850 μm measurements from JINGLE and my own JCMT P.I. science program. I used these data to compare the molecular gas, total gas, and dust properties of red misfits with those of blue star-forming galaxies ("blue actives"). I compared the properties of these two populations overall, versus offset from the star-forming main sequence, and versus position in the ($\log$ SFR, $\log$ M_*) plane. In comparison to blue actives, red misfits have longer molecular gas depletion times, similar total gas depletion times, lower gas mass fractions, lower dust-to-stellar mass ratios, and similar dust-to-gas ratios. These results suggest that the star formation process in red misfits is actively quenching.

5.4 Future Work

5.4.1 What is driving the correlation between *WISE* 12 μm and CO emission in galaxies?

My work on the *WISE* 12 μm-CO relationship in nearby galaxies has raised some key questions for future work. First, this correlation is very strong – it is the strongest resolved correlation between molecular gas and all other properties considered in Chown et al. (2021). The correlation is likely due to a connection between PAHs and molecular gas. Several recent results suggest that PAHs form in molecular clouds and are destroyed in a similar manner as CO (Li 2020). At molecular-cloud scales, Schinnerer et al. (2013) found that mid-infrared PAH emission features

correlate with CO emission in location but not in flux, while other works have found seemingly contradictory results that PAH flux *can* be used to predict CO flux (Regan et al. 2006; Cortzen et al. 2019). If *WISE* 12 μm emission is dominated by PAH emission (the 11.3 μm PAH feature), then why does it trace CO emission so well, and how does this relate to previous work? Furthermore, why is the 12 μm-CO correlation stronger than the Hα SFR-CO correlation? I would like to address these questions. In particular, some further examples are:

1. In Chown et al. (2021) I found no evidence for increased scatter at low surface densities. There must be a scale at which the correlation begins to show more scatter. This can be explored with higher-sensitivity, higher-resolution observations.

2. At fixed CO luminosity, the best-fit 12 μm-CO relation from Chown et al. (2021) yields lower 12 μm luminosities than Gao et al. (2019). Based on tests I performed, the source of this discrepancy appears to be the difference between 12 μm luminosities over the CO-detected area (which I did in Chown et al. 2021) versus that over the whole galaxy (which was done in Gao et al. 2019). However, it remains unclear whether there is truly no molecular gas in regions where 12 μm emission is detected but CO is not.

3. What is the dominant driver of the resolved 12 μm-CO correlation: warm dust? PAH emission, and if so, which PAH feature(s)? Does the 11.3 μm PAH feature in particular have a special connection to CO? In order to answer these questions, it is necessary to decompose the *WISE* 12 μm emission into its individual components in a spatially resolved manner.

4. How does *WISE* 12 μm emission correlate with H I? Given that PAH emission is believed to be coming from PDRs, which contain most of the neutral gas in the ISM (Hollenbach & Tielens 1997, 1999), perhaps the 12 μm-H I correlation may be stronger? Furthermore, it would be interesting to explore how dense gas tracers, such as HCN and CN, which are more closely associated with the gas that actually forms stars, scale with 12 μm emission.

5. How does the 12 μm-CO relationship evolve (if at all) when observing spatial scales that are only practically observable within the Milky Way (e.g. resolved regions of an individual molecular cloud), to galaxy-integrated scales?

6. Does the 12 μm-CO relationship evolve with redshift? PAH luminosities have been calibrated as a molecular gas tracer at moderate redshifts (e.g. Cortzen et al. 2019), but it would be interesting to study the 12 μm-CO and the PAH-CO relationships at fixed spatial resolution over a range of redshifts.

The directions of study proposed above are well-suited for the PHANGS survey (Leroy et al. 2021) – an ALMA survey of CO(2-1) emission in $\sim$90 nearby galaxies with cloud-scale resolution ($\sim$1 arcsec, corresponding to $\sim$100 pc). In the near future, detailed multi-wavelength data from *HST* and MUSE IFU for PHANGS galaxies will also be released. The wealth of high-resolution multi-wavelength data that is available for PHANGS galaxies enables one to construct experiments to understand the physics underlying the 12 μm-CO correlation. Other key data sets for studying the resolved *WISE* 12 μm-CO correlation are the Plateau de Bure inter-

ferometer Arcsecond Whirlpool Survey (PAWS) of CO(1-0) in M51 with molecular cloud scale resolution (Schinnerer et al. 2013), and the Berkeley-Illinois-Maryland Association Survey of Nearby Galaxies (BIMA SONG) which measured CO(1-0) in 44 nearby galaxies with ∼230 pc resolution (Regan et al. 2001). With these data sets one will be able to study the galaxy-to-galaxy offsets and their physical drivers.

For some of the questions above, one must estimate the spatially-resolved contributions of some PAH features to *WISE* 12 μm images. Spatially-resolved measurements of PAH emission in nearby galaxies have come from *Spitzer* (although this will change dramatically once *JWST* is launched). For example, *Spitzer* 8 μm and 24 μm images, matched in resolution to the CO data, can be used to roughly estimate the contributions of 7.7 μm PAH emission and warm dust respectively (Smith et al. 2007; Bendo et al. 2008, and references therein), to the *WISE* 12 μm emission. For a more precise comparison of resolved PAH emission and CO, one could use the recently-developed fitting routine for generating images of PAH emission from *Spitzer*/IRS spectral mapping-mode observations from Zhang et al. (2021). This method can be used to create maps of 11.3 μm PAH emission in BIMA SONG, PAWS, and PHANGS galaxies, and compare them with *WISE* 12 μm and CO images. Additionally, as part of the PAWS survey, there is an abundance of very high-quality multi-wavelength data (star formation and stellar mass indicators, PAH images) for M51 – these data will be important for testing the *WISE* 12 μm-CO correlation at high resolution. The results of these experiments will improve our understanding of the *WISE* 12 μm-CO correlation, and will motivate future *JWST* proposals to obtain 11.3 μm images of galaxies across a range of redshifts. Understanding the connections between

mid-infrared emission and molecular gas could have wide-ranging implications for the field of galaxy evolution – both practical (e.g. molecular gas tracers), and scientific (e.g. understanding the lives of PAHs).

I am currently leading a project to examine the 12 μm-CO relationship in Virgo cluster galaxies as part of The Virgo Environment Traced in CO (VERTICO) collaboration. VERTICO is an ALMA Large Program to measure CO(2-1) emission in Virgo galaxies (P.I.: T. Brown). The goal of this project is to push the limits of the correlation to better sensitivities and to study any dependence on galaxy environment. For this project, I am: 1) testing the Chown et al. (2021) estimators at higher physical resolution (0.5 to 1 kpc) and better sensitivity than EDGE, 2) determining whether the 12 μm-CO relationship at these scales varies with environment (e.g. in tails of stripped gas) and 3), developing an estimator of H_2 from CO(2-1) data. I already see strong correlations within galaxies and variations from galaxy to galaxy, qualitatively consistent with Chown et al. (2021).

5.4.2 How do bars and interactions affect the resolved cold gas distribution and star formation history of galaxies?

Large surveys of nearby galaxies with optical integral-field spectroscopy (such as MaNGA and CALIFA) combined with complementary surveys of spatially-resolved CO (such as EDGE and PHANGS) have opened up many new opportunities to study the relationships between the interstellar medium and star formation on a pixel by pixel basis. In particular, two-dimensional kinematics of the ionized gas extracted from optical IFU data allows one to measure quantities that determine the dynamics of galactic bars, such as pattern speed.

One could compile a sample of barred galaxies from the MaNGA survey from which important bar properties have been measured (e.g. Guo et al. 2019), together with spatially-resolved CO data from ALMA. With this sample, a detailed study of the kinematics of both the ionized gas and the molecular gas could be used to understand how bars and bar properties affect large scale gas motion and star formation history. Barred galaxies from the PHANGS sample could also be used to study this question with higher resolution than MaNGA sample – these galaxies have detailed morphological masks and measurements of bar properties based on data from the *Spitzer* Survey of Stellar Structure in Galaxies (S^4G; Sheth et al. 2010).

Galaxy-galaxy interactions have a similar effect as bars on the molecular gas distribution, and are known to trigger central star formation (Li et al. 2008; Patton et al. 2013) and increase the molecular gas mass and mass fraction (Pan et al. 2018). While archival data can address many issues, others need new observations. Due to the close proximity of galaxies in pairs, it is possible to efficiently observe both galaxies in the same track using ALMA or the Submillimeter Array (SMA). One could compile a sample of nearby galaxy pairs from the MaNGA sample based on Pan et al. (2019), and observe them in CO(2-1) using ALMA and/or the SMA. The gas kinematics and surface density distributions could be compared as functions of projected separation between galaxies and stellar mass ratios. This study will help us understand how tidal interactions affect the evolution of interacting galaxies. In particular, we will be able to learn where and how, within each galaxy, the star formation efficiency is affected by galaxy interactions.

Looking forward, the future of multi-wavelength studies of galaxies is promising. We now in an era of astronomy where high-sensitivity, high-resolution, multi-wavelength data sets are

available for large numbers of galaxies. I have demonstrated some of the capabilities of surveys like EDGE-CALIFA. The recently-released PHANGS survey provides even higher resolution and sensitivities for a similar number of galaxies, and opens opportunities for even more science. Furthermore, in the near future, one of the multi-wavelength data sets will come from the *JWST* – this will revolutionize astronomy. At the same time, unresolved surveys will always be larger than resolved ones, and it will be critical to compare the two to better understand results and to decide on future directions to pursue.

Bibliography

Aguerri J. A. L., Méndez-Abreu J., Corsini E. M., 2009, A&A, 495, 491

Aguilar L. A., White S. D. M., 1985, ApJ, 295, 374

Allamandola L. J., Tielens A. G. G. M., Barker J. R., 1985, ApJ, 290, L25

Allamandola L. J., Tielens A. G. G. M., Barker J. R., 1989, ApJS, 71, 733

Athanassoula E., 1992, MNRAS, 259, 345

Athanassoula E., 1994, in Shlosman I., ed., Mass-Transfer Induced Activity in Galaxies. p. 143

Athanassoula E., 2005, MNRAS, 358, 1477

Athanassoula E., Machado R. E. G., Rodionov S. A., 2013, MNRAS, 429, 1949

Bacon R., et al., 2010, in McLean I. S., Ramsay S. K., Takami H., eds, Society of Photo-Optical Instrumentation Engineers (SPIE) Conference Series Vol. 7735, Ground-based and Airborne Instrumentation for Astronomy III. p. 773508, doi:10.1117/12.856027

Baldry I. K., Glazebrook K., Brinkmann J., Ivezić Ž., Lupton R. H., Nichol R. C., Szalay A. S., 2004, ApJ, 600, 681

Baldry I. K., Balogh M. L., Bower R. G., Glazebrook K., Nichol R. C., Bamford S. P., Budavari T., 2006, MNRAS, 373, 469

Baldwin J. A., Phillips M. M., Terlevich R., 1981, PASP, 93, 5

Balogh M. L., Navarro J. F., Morris S. L., 2000, ApJ, 540, 113

Barnes J. E., Hernquist L. E., 1991, ApJ, 370, L65

Bekki K., Couch W. J., Shioya Y., 2002, ApJ, 577, 651

Bendo G. J., et al., 2008, MNRAS, 389, 629

Bigiel F., Leroy A., Walter F., Brinks E., de Blok W. J. G., Madore B., Thornley M. D., 2008, AJ, 136, 2846

Blanton M. R., Moustakas J., 2009, ARA&A, 47, 159

Blanton M. R., et al., 2001, AJ, 121, 2358

Bolatto A. D., Wolfire M., Leroy A. K., 2013, ARA&A, 51, 207

Bolatto A. D., et al., 2017, ApJ, 846, 159

Brinchmann J., Charlot S., White S. D. M., Tremonti C., Kauffmann G., Heckman T., Brinkmann J., 2004, MNRAS, 351, 1151

Calzetti D., Armus L., Bohlin R. C., Kinney A. L., Koornneef J., Storchi-Bergmann T., 2000, ApJ, 533, 682

Calzetti D., et al., 2007, ApJ, 666, 870

Cardelli J. A., Clayton G. C., Mathis J. S., 1989, ApJ, 345, 245

Casasola V., et al., 2020, A&A, 633, A100

Catinella B., Cortese L., 2015, MNRAS, 446, 3526

Catinella B., et al., 2018, MNRAS,

Chown R., et al., 2019, MNRAS, 484, 5192

Chown R., Li C., Parker L., Wilson C. D., Li N., Gao Y., 2021, MNRAS, 500, 1261

Chung A., van Gorkom J. H., Kenney J. D. P., Crowl H., Vollmer B., 2009, AJ, 138, 1741

Combes F., 2009, in Jogee S., Marinova I., Hao L., Blanc G. A., eds, Astronomical Society of the Pacific Conference Series Vol. 419, Galaxy Evolution: Emerging Insights and Future Challenges. p. 31 (arXiv:0901.0178)

Conroy C., 2013, ARA&A, 51, 393

Conselice C. J., Bershady M. A., Dickinson M., Papovich C., 2003, AJ, 126, 1183

Cortzen I., et al., 2019, MNRAS, 482, 1618

Cox T. J., Jonsson P., Somerville R. S., Primack J. R., Dekel A., 2008, MNRAS, 384, 386

Dabrowski I., 1984, Canadian Journal of Physics, 62, 1639

Davies J. I., et al., 2019, A&A, 626, A63

Devereux N. A., Young J. S., 1990, ApJ, 359, 42

Dobbs C. L., Pringle J. E., 2013, MNRAS, 432, 653

Dobbs C. L., Pringle J. E., Burkert A., 2012, MNRAS, 425, 2157

Dodelson S., 2003, Modern cosmology

Draine B. T., 1978, ApJS, 36, 595

Draine B. T., 2011, Physics of the Interstellar and Intergalactic Medium

Dressler A., 1980, ApJ, 236, 351

Eggen O. J., Lynden-Bell D., Sandage A. R., 1962, ApJ, 136, 748

Ellison S. L., Nair P., Patton D. R., Scudder J. M., Mendel J. T., Simard L., 2011, MNRAS, 416, 2182

Elmegreen B. G., 1997, in Franco J., Terlevich R., Serrano A., eds, Revista Mexicana de Astronomia y Astrofisica Conference Series Vol. 6, Revista Mexicana de Astronomia y Astrofisica Conference Series. p. 165

Elmegreen B. G., 2000, ApJ, 530, 277

Evans F. A., Parker L. C., Roberts I. D., 2018, MNRAS, 476, 5284

Farouki R., Shapiro S. L., 1981, ApJ, 243, 32

Feldmann R., 2020, Communications Physics, 3, 226

Ferland G. J., et al., 2013, Rev. Mex. Astron. Astrofis., 49, 137

Fernández X., et al., 2016, ApJ, 824, L1

Fisher D. B., Drory N., 2008, AJ, 136, 773

Fraternali F., Binney J. J., 2006, MNRAS, 366, 449

Galliano F., 2017, Planet. Space Sci., 149, 38

Galliano F., Dwek E., Chanial P., 2008, ApJ, 672, 214

Galliano F., Galametz M., Jones A. P., 2018, ARA&A, 56, 673

Gao Y., Solomon P. M., 2004, ApJ, 606, 271

Gao Y., et al., 2019, ApJ, 887, 172

Genzel R., et al., 2012, ApJ, 746, 69

Goodwin S. P., Whitworth A. P., 2004, A&A, 413, 929

Gunn J. E., Gott J. Richard I., 1972, ApJ, 176, 1

Guo Q., et al., 2019, Nature Astronomy, p. 493

Hao C.-N., Kennicutt R. C., Johnson B. D., Calzetti D., Dale D. A., Moustakas J., 2011, ApJ, 741, 124

Haynes M. P., et al., 2018, ApJ, 861, 49

Hildebrand R. H., 1983, QJRAS, 24, 267

Hollenbach D. J., Tielens A. G. G. M., 1997, ARA&A, 35, 179

Hollenbach D. J., Tielens A. G. G. M., 1999, Reviews of Modern Physics, 71, 173

Hopkins P. F., Hernquist L., 2006, ApJS, 166, 1

Hubble E. P., 1926, ApJ, 64, 321

Hubble E. P., 1936, Realm of the Nebulae

Jarrett T. H., et al., 2013, AJ, 145, 6

Jiang X.-J., Wang Z., Gu Q., Wang J., Zhang Z.-Y., 2015, ApJ, 799, 92

Kauffmann J., Goldsmith P. F., Melnick G., Tolls V., Guzman A., Menten K. M., 2017, A&A, 605, L5

Kennicutt R. C. J., 1983, ApJ, 272, 54

Kennicutt Robert C. J., 1989, ApJ, 344, 685

Kennicutt Jr. R. C., 1998, ARA&A, 36, 189

Kennicutt Robert C. J., De Los Reyes M. A. C., 2021, ApJ, 908, 61

Kennicutt R. C., Evans N. J., 2012, ARA&A, 50, 531

Kennicutt Robert C. J., et al., 2007, ApJ, 671, 333

Kitzbichler M. G., White S. D. M., 2008, MNRAS, 391, 1489

Koda J., et al., 2020, ApJ, 890, L10

Kormendy J., 2013, Secular Evolution in Disk Galaxies. p. 1

Kormendy J., Bender R., 2012, ApJS, 198, 2

Kormendy J., Ho L. C., 2013, ARA&A, 51, 511

Kormendy J., Kennicutt Jr. R. C., 2004, ARA&A, 42, 603

Kormendy J., Bender R., Cornell M. E., 2011, Nature, 469, 374

Kraljic K., Bournaud F., Martig M., 2012, ApJ, 757, 60

Larson R. B., Tinsley B. M., Caldwell C. N., 1980, ApJ, 237, 692

Leroy A. K., Walter F., Brinks E., Bigiel F., de Blok W. J. G., Madore B., Thornley M. D., 2008, AJ, 136, 2782

Leroy A. K., et al., 2009, AJ, 137, 4670

Leroy A. K., et al., 2011, ApJ, 737, 12

Leroy A. K., et al., 2013, AJ, 146, 19

Leroy A. K., et al., 2019, ApJS, 244, 24

Leroy A. K., et al., 2021, arXiv e-prints, p. arXiv:2104.07739

Li A., 2020, Nature Astronomy, 4, 339

Li C., Kauffmann G., Heckman T. M., Jing Y. P., White S. D. M., 2008, MNRAS, 385, 1903

Li Y., Calzetti D., Kennicutt R. C., Hong S., Engelbracht C. W., Dale D. A., Moustakas J., 2010, ApJ, 725, 677

Lin Y., Cervantes Sodi B., Li C., Wang L., Wang E., 2014, ApJ, 796, 98

Lin L., et al., 2017, ApJ, 851, 18

Lin L., et al., 2019, ApJ, 884, L33

Lin L., et al., 2020, MNRAS, 499, 1406

Liu L., Gao Y., Greve T. R., 2015, ApJ, 805, 31

Lotz J. M., Jonsson P., Cox T. J., Primack J. R., 2010, MNRAS, 404, 575

Lower S., Narayanan D., Leja J., Johnson B. D., Conroy C., Davé R., 2020, ApJ, 904, 33

Magdis G. E., Elbaz D., Daddi E., Morrison G. E., Dickinson M., Rigopoulou D., Gobat R., Hwang H. S., 2010, ApJ, 714, 1740

Maloney P., Black J. H., 1988, ApJ, 325, 389

Mancuso C., Lapi A., Shi J., Cai Z. Y., Gonzalez-Nuevo J., Béthermin M., Danese L., 2016, ApJ, 833, 152

Meurer G. R., Obreschkow D., Wong O. I., Zheng Z., Audcent-Ross F. M., Hanish D. J., 2018, MNRAS, 476, 1624

Mitchell P. D., Lacey C. G., Baugh C. M., Cole S., 2013, MNRAS, 435, 87

Mo H., van den Bosch F. C., White S., 2010, Galaxy Formation and Evolution

Moustakas J., Kennicutt Robert C. J., Tremonti C. A., 2006, ApJ, 642, 775

Murphy E. J., et al., 2011, ApJ, 737, 67

Noeske K. G., et al., 2007a, ApJ, 660, L43

Noeske K. G., et al., 2007b, ApJ, 660, L47

Osterbrock D. E., Ferland G. J., 2006, Astrophysics of gaseous nebulae and active galactic nuclei. University Science Books

Pan H.-A., et al., 2018, ApJ, 868, 132

Pan H.-A., et al., 2019, ApJ, 881, 119

Patton D. R., et al., 2002, ApJ, 565, 208

Patton D. R., Torrey P., Ellison S. L., Mendel J. T., Scudder J. M., 2013, MNRAS, 433, L59

Peeters E., Spoon H. W. W., Tielens A. G. G. M., 2004, ApJ, 613, 986

Pettini M., Pagel B. E. J., 2004, MNRAS, 348, L59

Piner B. G., Stone J. M., Teuben P. J., 1995, ApJ, 449, 508

Popesso P., et al., 2019, MNRAS, 483, 3213

Pringle J. E., Allen R. J., Lubow S. H., 2001, MNRAS, 327, 663

Privon G. C., Barnes J. E., Evans A. S., Hibbard J. E., Yun M. S., Mazzarella J. M., Armus L., Surace J., 2013, ApJ, 771, 120

Regan M. W., Thornley M. D., Helfer T. T., Sheth K., Wong T., Vogel S. N., Blitz L., Bock D. C. J., 2001, ApJ, 561, 218

Regan M. W., et al., 2006, ApJ, 652, 1112

Renzini A., Peng Y.-j., 2015, ApJ, 801, L29

Richstone D. O., 1976, ApJ, 204, 642

Saintonge A., et al., 2011, MNRAS, 415, 32

Saintonge A., et al., 2016, MNRAS, 462, 1749

Saintonge A., et al., 2017, ApJS, 233, 22

Saintonge A., et al., 2018, MNRAS, 481, 3497

Salim S., et al., 2007, ApJS, 173, 267

Salim S., et al., 2016, ApJS, 227, 2

Sánchez S. F., et al., 2012, A&A, 538, A8

Sánchez S. F., et al., 2016, A&A, 594, A36

Sánchez S. F., et al., 2021, MNRAS, 503, 1615

Sancisi R., Fraternali F., Oosterloo T., van der Hulst T., 2008, A&ARv, 15, 189

Sandstrom K. M., et al., 2013, ApJ, 777, 5

Schiminovich D., et al., 2007, ApJS, 173, 315

Schinnerer E., et al., 2013, ApJ, 779, 42

Schmidt M., 1959, ApJ, 129, 243

Schreiber C., et al., 2015, A&A, 575, A74

Scoville N., et al., 2016, ApJ, 820, 83

Sheth K., Vogel S. N., Regan M. W., Thornley M. D., Teuben P. J., 2005, ApJ, 632, 217

Sheth K., et al., 2010, PASP, 122, 1397

Shi Y., Helou G., Yan L., Armus L., Wu Y., Papovich C., Stierwalt S., 2011, ApJ, 733, 87

Shi Y., et al., 2018, ApJ, 853, 149

Silk J., 1997, ApJ, 481, 703

Smith J. D. T., et al., 2007, ApJ, 656, 770

Solomon P. M., Vanden Bout P. A., 2005, ARA&A, 43, 677

Solomon P. M., Downes D., Radford S. J. E., Barrett J. W., 1997, ApJ, 478, 144

Sormani M. C., Binney J., Magorrian J., 2015, MNRAS, 454, 1818

Speagle J. S., Steinhardt C. L., Capak P. L., Silverman J. D., 2014, ApJS, 214, 15

Strateva I., et al., 2001, AJ, 122, 1861

Tielens A. G. G. M., 2008, ARA&A, 46, 289

Toomre A., 1977, in Tinsley B. M., Larson Richard B. Gehret D. C., eds, Evolution of Galaxies and Stellar Populations. p. 401

Verheijen M., van Gorkom J. H., Szomoru A., Dwarakanath K. S., Poggianti B. M., Schiminovich D., 2007, ApJ, 668, L9

Walter F., Brinks E., de Blok W. J. G., Bigiel F., Kennicutt Robert C. J., Thornley M. D., Leroy A., 2008, AJ, 136, 2563

Wilson C. D., 1995, ApJ, 448, L97

Wilson C. D., 2018, MNRAS, 477, 2926

Wilson C. D., et al., 2012, MNRAS, 424, 3050

Wolfire M. G., Hollenbach D., McKee C. F., Tielens A. G. G. M., Bakes E. L. O., 1995, ApJ, 443, 152

Yajima Y., et al., 2021, PASJ, 73, 257

York D. G., et al., 2000, AJ, 120, 1579

Zhang L., Ho L. C., Xie Y., 2021, AJ, 161, 29

de los Reyes M. A. C., Kennicutt Robert C. J., 2019, ApJ, 872, 16

den Brok J. S., et al., 2021, MNRAS, 504, 3221